NANO & MACRO MECHANICS – NMM 2023

September 14, 2023, Prague, Czech Republic

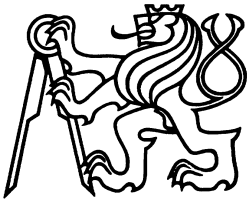

Book title: 14th annual Conference NANO & MACRO MECHANICS – NMM 2023.
Series title: Acta Polytechnica CTU Proceedings.
Volume: 49. **Date of issue:** November 21, 2024.
Published by: Czech Technical University in Prague,
Jugoslávských partyzánů 1580/3, 160 00 Praha 6 – Dejvice, Czech Republic.
IČ: 68407700

Editorial Office: CTU — Central Library,
Technická 6, 160 80 Praha 6, Czech Republic.
acta@cvut.cz

Print:
Powerprint (Brandejsovo nám. 1219/1, 165 00 Praha Suchdol).

Available on-line at https://ojs.cvut.cz/ojs/index.php/APP/issue/view/902
Each article is assigned a digital object identifier doi:10.14311/APP.2024.49.⟨*4-digit article page number*⟩

ISSN 2336-5382 (online) ISBN 978-80-01-07378-0 (online) Print on demand

13th annual Conference

NANO & MACRO MECHANICS NMM 2023

September 14, 2023, Prague, Czech Republic

Editor

Pavel Padevět

Preface

The 14th conference Nano & Macro Mechanics was held in Prague, in September 14, 2023. The conference was organized by Department of Mechanics, Faculty of Civil Engineering, Czech Technical University in Prague, Czech Republic.

The main objective of the conference is to bring together researchers, students and engineers devoting their work to comuting and experimental mechanics in different areas of engineering applications on a common platform.

The conference key topics were following:

- Testing of buildings materials at the nano, micro, mezzo and macro levels.
- Destructive and non-destructive methods for determining the mechanical properties of building materials.
- Relationships between material parameters.
- Computational and experimental dynamics and mechanics.
- Material research for steel, buildings materials, glass, woods, textiles, and composites.
- Analyses of constructions.
- Computational methods for analyses of constructions and materials.

We strongly believe that NMM 2023 has a significant impact on the development of contemporary analytical, numerical and experimental methods in mechanics and will also create an opportunity for opening a forum for discussion and collaboration among the participants.

This Issue of Acta Polytechnica Proceedings contains the papers presented in the topic of the conference on Nano & Macro Mechanics 2023. All papers were reviewed by two members of the conference scientific board.

We would like to express our special thanks to all members of scientific and organizing committee, session chairperson, reviewers of papers and conference participants for making this conference successful.

Pavel Padevět
On behalf of Scientific Committee

Contents

EXPERIMENTAL DYNAMIC ANALYSIS OF THE FOOTBRIDGE ACROSS JIZERA RIVER IN MLADÁ BOLESLAV

Miroslav Čáp[a,c], Vladimír Šána[b,*], Michal Polák[a], Tomáš Plachý[a]

[a] *Czech Technical University in Prague, Faculty of Civil Engineering, Department of Mechanics, Thákurova 7, 160 00 Prague, Czech Republic*

[b] *Czech Technical University in Prague, Faculty of Civil Engineering, Experimental Centre, Thákurova 7, 160 00 Prague, Czech Republic*

[c] *Pontex Consulting Engineers, Ltd., Bezová 1658, 147 14 Prague, Czech Republic*

[*] corresponding author: vladimir.sana@fsv.cvut.cz

Abstract. The text of this submitted paper is devoted to the experimental dynamic analysis of the newly designed footbridge across the Jizera River in Mladá Boleslav. Theoretical modal analysis has shown potential risk that some of the natural frequencies of the bridge deck will belong to the range which is typical for pacing frequencies induced by pedestrians. The resonance behaviour of this structure should be reduced by Tuned Mass Dampers (TMD), which would be tuned for separate natural frequencies of this structure. Therefore, the experimental dynamic analysis was performed on the footbridge in order to assess the effectiveness of installed TMDs. The experiment was divided into two stages, the first one was realized at the footbridge when TMDs were not yet installed, and the second one was carried out on the footbridge with installed and activated TMDs. Moreover, the authors have performed an experimental modal analysis in order to verify the aptness of the computational model and its results.

Keywords: Experimental dynamic analysis, dynamic load test, experimental modal analysis, human-induced vibration, vandalism.

1. Introduction

As can be seen from the number of contributions and participants, who regularly presents their papers at the international conferences dealing with the structural dynamics, such as EURODYN, IMAC, etc., and in technical journals, dynamic behaviour (obtained by either numerical predictions or in-situ experiments) of the footbridges is still at the foreground of international researchers community interest. The newly built structures are designed still more and more subtle thanks to the advanced computational procedures and modern materials. The effort to create more slender and subtle structures is caused in particular by a desire of architects to not break the view of the surrounding landscape. The combination of slenderness, low value of damping, physical properties of used materials, such as mass and stiffness, and static system of the superstructure lead very often to the fact, that some of the natural frequencies are scattered very closely in the region of the pacing frequencies induced by pedestrians. On the other hand, the artistic efforts of the architects create a natural pressure on designers (in the sense of numerical calculations and choice of a correct mathematical model of pedestrian, vandal, etc.), who must properly and with a reasonable measure of the accuracy determine the response of the individual members of the footbridge load-bearing structure. The final maximal level of vibration in the dimension of acceleration is used for structural assessment with respect to pedestrians' comfort. The maximal values are usually less suitable for a footbridge experimental assessment since their value can be significantly affected by sudden impulse loading, such as stamping in the close vicinity of the used accelerometers, etc. Therefore, some guidelines and standards recommend RMS (Root Mean Square) values of acceleration for assessing a comfort level of a footbridge structure with respect to pedestrians.

In literature, one can find a lot of sources, where authors designed TMD on existing or newly built structures. In [1], authors designed and assessed a TMD on the cable-stayed footbridge. Ferreira et al. in [2] proposed a design of a TMD and SATMD (semi-active tuned mass damper) on the Infinity bridge in Stockton, Great Britain, which is an arch footbridge across River Tees. The SATMD was used as an efficient tool to prevent the lock-in effect, which is in this case lateral instability of the footbridge induced by a critical number of synchronous pedestrians in the lateral direction. A numerical and experimental study of simple structure with friction TMD was addressed by Eliecer et al. in [3] in order to reduce the vibrations of the floor. The bridge deck vibration of the lively footbridge across Motlawa River (Gdansk, Poland) was reduced by high coefficient TMD, see [4]. The suspended footbridge Żabia kładka in Wrocław and cable-stayed footbridge in Poznań, which have been enriched by TMDs, were studied in [5]. Optimal parameters of TMDs, such as their mass, stiffness, and

Figure 1. A view of the investigated footbridge in the direction of stationing.

Figure 2. A view of the bridge deck in the direction of stationing.

damping properties, can be found e.g. in [6] or [7]. Sometimes, the situation requires and permits the usage of TLD (Tuned Liquid Damper), where the kinetic energy of the vibrating structure is absorbed by the inertia of moving liquid, see e.g. [8].

2. Description of the investigated structure

For the purposes of the presented paper, we have chosen the footbridge, which is located in Mladá Boleslav (Czech Republic) and serves to pedestrian and cycling traffic as a part of the cycling route A1. A view of the structure in the direction of stationing is depicted in Figure 1 and Figure 2. The experimentally investigated footbridge is steel trussed structure with an orthotropic bridge deck, see Figure 3, and with two simply-supported spans, which is mounted on two massive abutments and a reinforced-concrete pillar. The length of individual spans are $L_1 = 68.40$ m and $L_2 = 23.68$ m, see Figure 4. Width of the superstructure of 4.60 m is constant along the entire structure, see Figure 2.

The footbridge centreline is direct in the horizontal direction and curved in the vertical plane with a radius of $R = 811.541$ m, see Figure 1 and Figure 2.

The main beams have been constructed from two trussed beams made of S355J2+N and S355J2H category steel. Top and bottom box-sectional chords with outer dimensions of 250 × 200 mm are welded to an arc. The thickness of the flanges and webs at the bottom chord is 15 mm. The top chord has a thickness of webs 15 mm and flanges of 15 mm, 20 mm and 25 mm. Both truss beams are rigidly connected by horizontal box-sectional bracing with dimensions of 250 × 200 mm. The height of the main beams is variable with respect to the longitudinal axis. The webs of the trussed beams are a combination of rigid tubes, box-sectional rods, providing the shape stability of the top chords, and pair of prestressed rectifiable rods.

The bridge deck was designed from a 10 mm plate reinforced with a system of longitudinal and transversal stiffeners with plate profiles and inverted T profiles. The profiles were added to the places with the premised locations of Tuned Mass Dampers (TMDs).

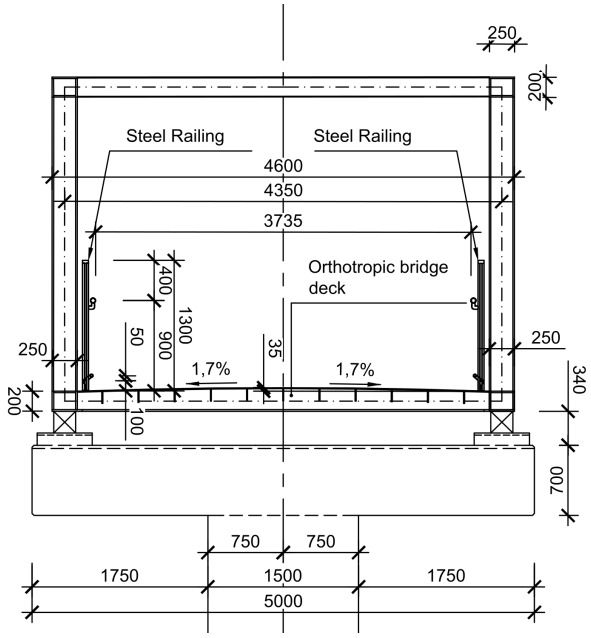

Figure 3. A cross-section of the investigated footbridge structure – support [10].

Generally, 8 TMDs were designed in the theoretical dynamic analysis, see [9]. The distance between separate cross-girders with inverted T profiles is 3000 mm and the mutual spacing of longitudinal plate stiffeners is 360 mm. The distance between inverted T profiles and plate stiffeners at the places, where the inverted T profiles were added, is 270 mm.

3. Experiment

The in-situ experiment was divided into two phases. While the first stage was focused on the determination of the natural frequencies, relevant mode shapes of the superstructure (experimental modal analysis, informative dynamic test), and the response of the superstructure without installed TMDs, the second stage was primarily aimed at verification of the effectiveness of the Tuned Mass Dampers (TMDs) after

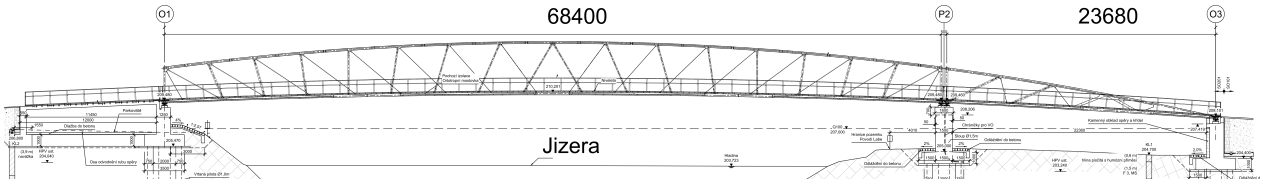

FIGURE 4. A longitudinal section of the investigated footbridge structure [10].

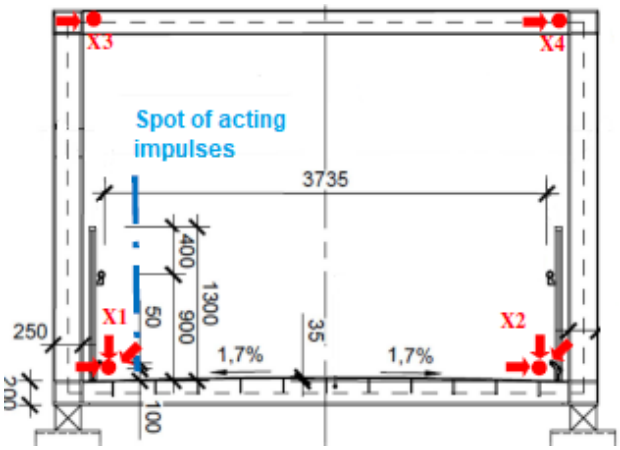

FIGURE 5. A view at sensor placement.

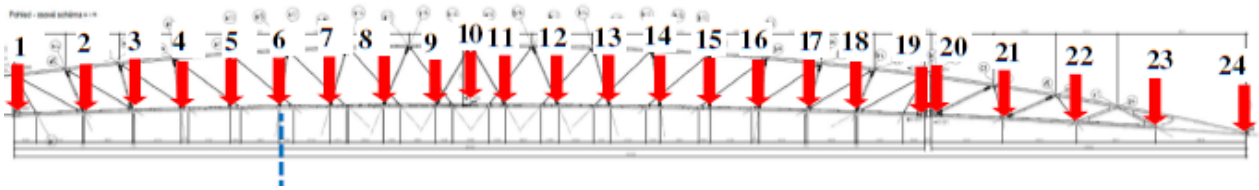

FIGURE 6. A view at sensor placement in a longitudinal section.

their installation and activation for a purpose of decreasing a level of vibration of the bridge deck. The dynamic forces were produced by diversely formed groups of pedestrians. The groups of pedestrians used in the second stage corresponded to the groups from the first stage. Thus the results from both stages were mutually comparable and we were able to determine the effect of activated TMDs.

Response of the structure was observed in the preselected mesh of points by accelerometers, which were adjusted by steel weights and placed in the correct position. These used accelerometers were piezoelectric seismic sensors of type 8344 (Brüel&Kjær). The sensors were adjusted to the top chord and on the steel weights directly by neodymium magnets, see Figure 5. Sensitivity of the accelerometers is 2500 mV g^{-1} with a frequency range of 0.2 Hz–3 kHz.

Eight-channel vibration control stations SIRIUS 6ACC – 2ACC+ and SIRIUS 8ACC have been used to collect seismic sensor data.

3.1. Experimental modal analysis

Experimental modal analysis (dynamic informative test within the meaning of standard ČSN 73 6209 [11]) was focused on the determination of natural vibration characteristics of the empty structure. The logarithmic decrement, dominant natural frequencies, and corresponding global mode shapes belong among these characteristics. The structure was excited by regularly jumping person – Ambient Vibration Test (AVT) in a predefined spot to excite all desired mode shapes.

The dash-and-dot line, depicted in Figure 5, represents the approximate spot of the jumping person. The eccentricity of this spot permitted the excitation of potential torsion mode shapes. Figure 6 represents the placement of individual measured sections in the longitudinal direction. Reference sensors were placed in points 62 and 102 (measurement in y and z directions) throughout the experimental modal analysis. Besides this, the next reference sensor was placed in point 104 (measurement in the y direction). During the experimental modal analysis of the second span, the reference sensors were located in point 222 (measurement in the y and the z directions).

Experimentally obtained data of the time behaviour of the oscillating bridge deck were stored on the hard drive and subsequently processed by Fast Fourier Transform (FFT), which transforms the original signal from the time domain to the frequency domain, and natural frequencies are depicted as local peaks. The width of the peak at a specific height is related to the damping connected with this natural frequency.

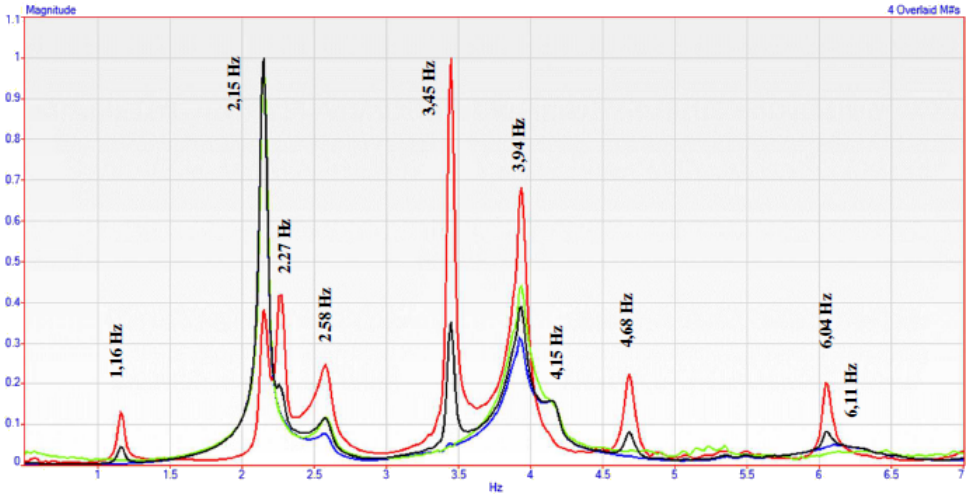

Figure 7. The example of Complex Mode Indicator Function (the black line – evaluated across all measured points in x, y, and z directions, the green curve in the x direction, the red line in the y direction, and the blue curve for the z direction).

Thanks to the fact, that the force of excitation was produced by a jumping person, Frequency Response Spectra in individual points on the bridge deck have been used for the determination of Operating Deflection Shapes Frequency Response Functions (ODSFRF or $\mathrm{ODSH}_{kR}(if)$). $\mathrm{ODSH}_{kR}(if)$ is generally a complex function consisting of real and imaginary part. Since the individual points have been fitted by sensors at different times and therefore the level of excitation force was not constant, the transmissibility functions $\mathrm{T}_{kR}(if)$ were determined as well. Transmissibility functions permit precise evaluation of the mode shapes. These functions were determined by the equation:

$$\mathrm{T}_{kR} = \frac{\ddot{w}_k(if)}{\ddot{w}_R(if)}, \tag{1}$$

where

i means an imaginary unit,

$\ddot{w}_k(if)$ stands for the response (acceleration) of the structure in point k in the frequency domain,

$\ddot{w}_R(if)$ denotes the response (acceleration) of the structure in reference point R in the frequency domain.

The natural frequencies and mode shapes were evaluated in the software ME'scope VES. The example of evaluated Complex Mode Indicator Function with depicted natural frequencies is presented in Figure 7.

3.2. Dynamic load test

According to the standard ČSN 73 6209 [11], we have tested such an arrangement of pedestrians, which was in accordance with the requirements of this standard. An ordinary traffic is usually simulated by:

- Random footbridge crossing with a pedestrian flow density of the same order as the density during standard use of the structure,
- excitation of torsional or bending vibration; two synchronized pedestrians stepping on the same foot at the same time; pacing frequency according to natural frequencies of empty structure,
- excitation of lateral vibration; two synchronized pedestrians stepping on the same foot at the same time; pacing frequency according to natural frequencies of empty structure.

In addition to the ordinary traffic, other form of pedestrian excitation of the footbridge (for example running joggers, swaying and bobbing vandals) were also investigated. The walking pedestrians, running joggers and swaying/bobbing vandals have been synchronized by digital metronome.

3.2.1. The first stage – inactivated TMD

On the basis of the previous experimental modal analysis, we have chosen the following pacing frequencies, which were the same as some of the natural frequencies:

The first span $\mathbf{L_1 = 68.40\,m}$

- $f_{(2)} = 2.15\,\mathrm{Hz}$ – the first shape of vertical bending vibration; $f_p = 2.15\,\mathrm{Hz}$, $f_v = 2.15\,\mathrm{Hz}$,
- $f_{(4)} = 2.58\,\mathrm{Hz}$ – the first shape of torsional vibration; $f_p = 2.58\,\mathrm{Hz}$,
- $f_{(5)} = 3.44\,\mathrm{Hz}$ – the third shape of lateral bending vibration (top chords of main beams); $f_p = 1.73\,\mathrm{Hz}$, $f_p = 3.44\,\mathrm{Hz}$ $f_v = 1.72\,\mathrm{Hz}$, $f_v = 3.44\,\mathrm{Hz}$,
- $f_{(6)} = 3.94\,\mathrm{Hz}$ – the shape of lateral bending vibration; $f_p = 1.97\,\mathrm{Hz}$, $f_v = 1.97\,\mathrm{Hz}$, $f_v = 1.95\,\mathrm{Hz}$,
- $f_{(7)} = 4.16\,\mathrm{Hz}$ – the second shape of vertical bending vibration (top chords of main beams); $f_p = 2.08\,\mathrm{Hz}$, $f_v = 2.08\,\mathrm{Hz}$.

The following compositions of loading groups have been used:

j	1st span $f_{(j)}$ [Hz]	2nd span $f_{(j)}$ [Hz]
1	1.16	5.27
2	2.15	5.92
3	2.27	7.31
4	2.58	8.42
5	3.45	11.46
6	3.94	11.92
7	4.15	13.87
8	4.68	15.59
9	6.04	17.21
10	6.11	-

TABLE 1. Natural frequencies of the first and the second spans during the first stage (inactivated TMD).

- Simulation of an ordinary traffic: 4 pedestrians (random crossing),
- synchronized walking/running: 2 pedestrians side by side,
- vandalism: 4 qualified vandals.

The second span $L_2 = 23.68$ m

- $f_{(1)} = 5.28$ Hz – the first shape of vertical bending vibration; $f_p = 1.76$ Hz, $f_p = 2.64$ Hz, $f_v = 1.76$ Hz, $f_v = 2.64$ Hz.

The following compositions of loading groups have been used:

- Simulation of ordinary traffic: 5 pedestrians (random crossing),
- synchronized walking/running: 2 pedestrians side by side,
- vandalism: 4 qualified vandals.

In the previous list, $f_{(k)}$ denotes k-th natural frequency, f_p stands for exciting frequency produced by pedestrians, and finally, f_v means exciting frequency produced by vandals.

3.2.2. The second stage – activated TMD

The first span $L_1 = 68.40$ m

- $f_{(2)} = 2.15$ Hz – the first shape of vertical bending vibration; $f_p = 2.15$ Hz, $f_v = 2.15$ Hz,
- $f_{(4)} = 2.47$ Hz – the first shape of torsional vibration; $f_p = 2.47$ Hz,
- $f_{(5)} = 3.42$ Hz – the third shape of lateral bending vibration (top chords of main beams); $f_p = 1.71$ Hz, $f_p = 3.42$ Hz $f_v = 1.71$ Hz, $f_v = 3.42$ Hz,
- $f_{(6)} = 3.94$ Hz – the shape of lateral bending vibration; $f_p = 1.95$ Hz, $f_p = 1.98$ Hz, $f_v = 1.95$ Hz, $f_v = 1.98$ Hz,
- $f_{(7)} = 4.16$ Hz – the second shape of vertical bending vibration (top chords of main beams); $f_p = 2.08$ Hz, $f_v = 2.08$ Hz.

The following compositions of loading pedestrian groups have been used:

- Simulation of ordinary traffic: 8–9 pedestrians (random crossing),
- synchronized walking/running: 2 pedestrians side by side,
- vandalism: 4 qualified vandals.

The second span $L_2 = 23.68$ m

- $f_{(1)} = 5.27$ Hz – the first shape of vertical bending vibration; $f_p = 1.76$ Hz, $f_p = 2.64$ Hz, $f_v = 1.76$ Hz, $f_v = 2.64$ Hz,
- $f_{(2)} = 5.92$ Hz – the first shape of vertical bending vibration; $f_p = 1.98$ Hz, $f_p = 2.97$ Hz, $f_v = 1.98$ Hz, $f_v = 2.97$ Hz,
- $f_p = 2.30$ Hz, $f_v = 2.30$ Hz.

The following compositions of loading groups have been used:

- Simulation of ordinary traffic: 4 pedestrians (random crossing),
- synchronized walking/running: 2 pedestrians side by side,
- vandalism: 3 qualified vandals.

4. Results

This text summarizes obtained and evaluated results from the in-situ experiment, which was focused on experimental modal analysis and forced vibration (dynamic load test). The Table 1 and Table 2 present evaluated natural frequencies of the footbridge during the first stage.

An example of the second mode shape of the first span is graphically depicted in Figure 8.

Table 3 summarizes the important values of damping. These values were determined for the first vertical bending frequency at the first span and for the first vertical bending frequency at the second span.

The following tables (Table 4, Table 5) present the results of maximal RMS values of acceleration at the first span because dominant values of measured dynamic response were observed right there.

j	1st span	2nd span
1	Lateral bending – top chords	Vertical bending – bridge deck
2	Vertical bending – bridge deck	Lateral bending – top chords
3	Lateral bending – top chords	Torsional – bridge deck
4	Torsional – bridge deck	Torsional – bridge deck
5	Lateral bending – top chords	Lateral bending – top chords
6	Lateral bending – bridge deck	Vertical bending – bridge deck
7	Vertical bending – bridge deck	Lateral bending – top chords
8	Lateral bending – top chords	Vertical bending – bridge deck
9	Lateral bending – top chords	Torsional – bridge deck
10	Vertical bending – bridge deck	-

Table 2. Description of the individual evaluated mode shapes (inactivated TMD).

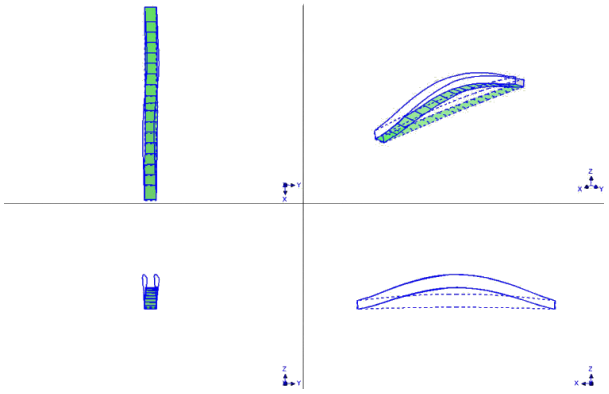

Figure 8. The second mode shape $f_{(2)} = 2.15$ [Hz] – The first span (inactivated TMD).

Span	f [Hz]	ϑ [-]	ξ [%]
1st	2.15	0.031	0.49
2nd	5.27	0.061	0.97

Table 3. Values of logarithmic damping decrement ϑ.

5. Conclusion

The submitted paper presents the results of the experimental dynamic analysis of the newly built footbridge across the Jizera River in Mladá Boleslav. The calculations, in the design phase, have shown that the structure must be supplemented by TMDs to decrease vibrations induced by pedestrians. The experiment should prove whether the installed absorbers are effective or not. As can be seen from Table 4 and Table 5, the absorbers helped significantly to decrease the level of vibration, which is the most noticeably evident for vandalism at a frequency of 1.95 Hz and synchronized running pedestrians at a frequency of 3.44 Hz.

Acknowledgements

The financial support has been provided by grant No. SGS22/089/OHK1/2T/11 of the Czech Technical University in Prague, which is gratefully acknowledged.

Description	Freq. [Hz]	Spot	Max [m s^{-2}]
Ordinary traffic	-	102-Z	0.170
Syn. ped.	1.73	102-Z	0.089
Syn. ped.	1.97	102-Z	0.123
Syn. ped.	2.08	102-Z	**0.258**
Syn. ped.	2.15	102-Z	0.245
Syn. ped.	2.58	102-Z	0.250
Syn. ped.	3.44	102-Z	**0.572**
Vandals	1.72	102-Z	0.117
Vandals	1.95	102-Z	**2.123**
Vandals	1.97	102-Z	1.376
Vandals	2.08	102-Z	0.340
Vandals	2.15	102-Z	0.491
Vandals	3.44	102-Z	0.205

Table 4. Maximal RMS values for individual exciting frequencies – the first stage (inactivated TMD).

Description	Freq. [Hz]	Spot	Max [m s^{-2}]
Ordinary traffic	-	102-Z	0.111
Syn. ped.	1.71	102-Z	0.062
Syn. ped.	1.79	102-Z	0.078
Syn. ped.	1.95	102-Z	0.086
Syn. ped.	1.98	102-Z	0.072
Syn. ped.	2.08	102-Z	**0.085**
Syn. ped.	2.15	102-Z	0.111
Syn. ped.	2.47	102-Z	0.158
Syn. ped.	3.42	102-Z	**0.276**
Vandals	1.71	102-Z	0.141
Vandals	1.79	102-Z	0.270
Vandals	1.95	102-Z	**0.193**
Vandals	1.98	102-Z	0.153
Vandals	2.08	102-Z	0.114
Vandals	2.15	102-Z	0.143
Vandals	2.47	102-Z	0.211
Vandals	3.42	102-Z	0.470

Table 5. Maximal RMS values for individual exciting frequencies – the second stage (activated TMD).

References

[1] D. Makovička, M. Studničková, D. Makovička, J. Korbelář. Dynamický tlumič na lávce pro chodce [In Czech; Dynamic absorber on a footbridge]. *Stavební obzor* **12**(5):149–155, 2003.

[2] F. Ferreira, C. Moutinho, Á. Cunha, E. Caetano. Use of semi-active tuned mass dampers to control footbridges subjected to synchronous lateral excitation. *Journal of Sound and Vibration* **446**:176–194, 2019. https://doi.org/10.1016/j.jsv.2019.01.026

[3] J. E. C. Carmona, S. M. Avila, G. Doz. Proposal of a tuned mass damper with friction damping to control excessive floor vibrations. *Engineering Structures* **148**:81–100, 2017. https://doi.org/10.1016/j.engstruct.2017.06.022

[4] K. Zoltowski, A. Banas, M. Binczyk, P. Kalitowski. Control of the bridge span vibration with high coefficient passive damper. Theoretical consideration and application. *Engineering Structures* **254**:113781, 2022. https://doi.org/10.1016/j.engstruct.2021.113781

[5] W. Fiebig. Reduction of vibrations of pedestrian bridges using tuned mass dampers (TMD). *Archives of Acoustics* **35**(2):165–174, 2010. https://doi.org/10.2478/v10168-010-0015-3

[6] J. Máca. Dynamic response of footbridges with tuned mass dampers. *IOP Conference Series: Materials Science and Engineering* **236**:012060, 2017. https://doi.org/10.1088/1757-899X/236/1/012060

[7] H. Bachmann, W. J. Ammann, F. Deischl, et al. *Vibration Problems in Structures: Practical Guidelines*. 1. Birkhäuser Basel, 2011. https://doi.org/10.1007/978-3-0348-9231-5

[8] M. Pirner, S. Urushadze. Liquid damper for suppressing horizontal and vertical motions – parametric study. *Journal of Wind Engineering and Industrial Aerodynamics* **95**(9–11):1329–1349, 2007. https://doi.org/10.1016/j.jweia.2007.02.010

[9] S. Hračov, D. Gregor, V. Janata, P. Nehasil. *Dynamické posouzení lávky [In Czech; Dynamic assessment of a footbridge]*. Excon a.s., 2021.

[10] T. Lindtner, D. Šindler, O. Dědek, V. Hvízdal. *SO201 Lávka přes Jizeru (000 – Přehledné výkresy) [In Czech; Plans (Cross sections and Lontitudinal sections)]*. Pontex, Ltd., 2022.

[11] Český normalizační institut. ČSN 73 6209. Zatěžovací zkoušky mostních objektů [In Czech; Loading tests on bridges], 2019.

DYNAMIC BEHAVIOR OF A CABLE-STAYED FOOTBRIDGE DEPENDING ON THE CALCULATION ACCURACY

Kristian D'Amico*, Jiří Máca

Czech Technical University in Prague, Faculty of Civil Engineering, Department of Mechanics, Thákurova 7, 166 29 Prague, Czech Republic

* corresponding author: kristian.d.amico@fsv.cvut.cz

Abstract. Footbridges are analyzed in terms of dynamic response for pedestrian comfort. This problem is solved mainly on light and at the same time rigid constructions, which are easily oscillated by pedestrian load. It is often solved on steel footbridges, but with the technological development of UHPC, we are capable nowadays to build relatively light and long span concrete footbridges. Behaviour of a thin concrete cross-section with its geometry is closer to steel structures, but at the same time we have to deal with rheological effects such as creep and shrinkage. There are many influences on the structure that can affect the dynamic behavior of the structure, including the non-linear behavior of the cable system. This paper presents an initial entry into the computational issues of more complex constructions that have more input influences.

Keywords: Dynamic characteristics, natural frequencies, footbridge, cable-stayed bridge, finite element method, UHPC, stiffness matrix, mass matrix.

1. Introduction

Dynamic analysis precedes the dynamic experiment in-situ, unfortunately construction companies are mostly forced to buy bridge dampers in advance, so calculation inaccuracy may lead to an uneconomical design and therefore an accurate model is required.

Critical freqency range in the vertical direction is between 1.25–2.3 Hz and for the horizontal natural frequences between 0.5–1.2 Hz. Footbridges with frequencies for vertical or longitudinal vibrations in range 2.5–4.5 Hz might be excited by resonanse by the 2nd harmonic of pedestrian load. In that case critical frequences range for vertical and longitudinal vibrations expands to 1.25–4.5 Hz. The frequencies are further analyzed more precisely, and the amount of oscillating mass in bridge engineering is also tracked. Dampers are designed into the locations, where the acceleration reaches critical values where the natural damping of the structure is insufficient. In practice, if there is an inaccuracy in the calculation, a damper can be designed in a place where it will not be needed [1].

2. Dynamic characteristics

The main dynamic characteristics that enter into the dynamic calculation of natural frequencies are stiffness matrix $[K]$ and mass matrix $[M]$. A two-dimensional model using the finite element method was chosen for monitoring changes in the behavior of the structure [2, 3].

2.1. Local stiffness matrix

The full stiffnes matrix of an element:

$$K_e = \frac{E}{L}\begin{pmatrix} A & 0 & 0 & -A & 0 & 0 \\ 0 & \frac{12I}{L^2} & \frac{6I}{L} & 0 & \frac{12I}{L^2} & \frac{6I}{L} \\ 0 & \frac{6I}{L} & 4I & 0 & -\frac{6I}{L} & 2I \\ -A & 0 & 0 & A & 0 & 0 \\ 0 & -\frac{12I}{L^2} & -\frac{6I}{L} & 0 & \frac{12I}{L^2} & -\frac{6I}{L} \\ 0 & \frac{6I}{L} & 2I & 0 & -\frac{6I}{L} & 4I \end{pmatrix}, \tag{1}$$

where

E is Young's modulus of the material [kPa],

I is the moment of inertia for the Y-axis in base of the cross-section [m^4],

A is the element area [m^2],

L is the lenght of the element [m].

This matrix belongs to the deck and the pilons, but the cables behaviour is different. The cables are non-linerar elements that can only be tensed and have zero bending stiffness. In this analysis, the effect of rope sag is neglected for simplification reasons.

To achieve the correct behavior of a cable-stayed structure, the geometric stiffness matrix of the element also needs to be included:

$$K_g = \frac{P}{30L}\begin{pmatrix} 0 & 0 & 0 & 0 & 0 & 0 \\ 0 & 36 & 3L & 0 & -36 & 3L \\ 0 & 3L & 4L^2 & 0 & -3L & -L^2 \\ 0 & 0 & 0 & 0 & 0 & 0 \\ 0 & -36 & -3L & 0 & 36 & -3L \\ 0 & 3L & -L^2 & 0 & -3L & 4L^2 \end{pmatrix}, \tag{2}$$

where

P is the stressing/tension force in the element [kN].

The axial force in the member is denoted by P, with the positive axial force in this case representing pressure. Combining the element stiffness and geometrical stiffness we recive the local matrix of stiffness:

$$K_L = K_e + K_g. \tag{3}$$

2.2. Local mass matrix

Normally, cables are considered intangible, because they oscillate at low frequencies and thus introduce a large amount of low frequencies into the calculation, which usually unnecessarily interfere the global assessment. For the academic purposes, the cables in the numeric model are considered to have weight for realistical results.

The weight of the structure is expressed often using the diagonal mass matrix, which expresses that the mass is equaly divided to end nodes:

$$M_d = \frac{\eta L}{2}\begin{pmatrix} 1 & 0 & 0 & 0 & 0 & 0 \\ 0 & 1 & 0 & 0 & 0 & 0 \\ 0 & 0 & 1 & 0 & 0 & 0 \\ 0 & 0 & 0 & 1 & 0 & 0 \\ 0 & 0 & 0 & 0 & 1 & 0 \\ 0 & 0 & 0 & 0 & 0 & 1 \end{pmatrix}, \tag{4}$$

where

η is weight per unit length [t m^{-1}].

A more accurate option is to evenly distribute the mass along the element by consistent mass matrix:

$$M_k = \frac{\eta L}{420}\begin{pmatrix} 140 & 0 & 0 & 70 & 0 & 0 \\ 0 & 156 & 22L & 0 & 54 & -13L \\ 0 & 22L & 4L^2 & 0 & 13L & -3L^2 \\ 70 & 0 & 0 & 140 & 0 & 0 \\ 0 & 54 & 13L & 0 & 156 & -22L \\ 0 & -13L & -3L^2 & 0 & -22L & 4L^2 \end{pmatrix}. \tag{5}$$

In the past, it has been proven that the difference in the calculation is in the order of a few percent, so the diagonal weight matrix is considered an acceptable input, the error is negligible. Commercial softwars often use diagonal form, difference with the consistent one will also be compared in this analysis.

Increment to the weight matrices is a mass matrix with the influence of the bending moment:

$$M_i = \frac{\rho I}{30L}\begin{pmatrix} 0 & 0 & 0 & 0 & 0 & 0 \\ 0 & 36 & 3L & 0 & -36 & 3L \\ 0 & 3L & 4L^2 & 0 & -3L & -L^2 \\ 0 & 0 & 0 & 0 & 0 & 0 \\ 0 & -36 & -3L & 0 & 36 & -3L \\ 0 & 3L & -L^2 & 0 & -3L & 4L^2 \end{pmatrix}, \tag{6}$$

where

I is material moment of inertia.

The mass moment of inertia is the inertia in rotation around the center of the cross-section. In the vast majority of cases, this has minimal effect. This must be taken into account in the case of very high beams or extremely fast loads.

Inertia in the stiffness matrix corresponding to the rotation of the cross-section. But it is related both to the inertia resulting from the transverse movement and to the inertia resulting from the rotation of the cross-sections. Inertia, related to the member tip rotation parameter, which will come out in a consistent cross-section matrix. If a consistent inertia matrix is considered, then this term generally cannot be neglected.

Combining the element mass and the mass with the influence of the rotational bending moment we recive the local mass matrix:

$$M_L = M_{\mathrm{d/k}} + M_i. \tag{7}$$

2.3. Transformation to global matrices

Using the transformation matrix $[A]$ the local matrix is transformed into the global coordinate system, and we get the global matrix of stiffness:

$$A = \begin{pmatrix} c & s & 0 & 0 & 0 & 0 \\ s & c & 0 & 0 & 0 & 0 \\ 0 & 0 & 1 & 0 & 0 & 0 \\ 0 & 0 & 0 & c & s & 0 \\ 0 & 0 & 0 & -s & c & 0 \\ 0 & 0 & 0 & 0 & 0 & 1 \end{pmatrix}, \tag{8}$$

where

c is cosine of the angle the element subtends from the global system,

s is sine of the angle the element subtends from the global system.

$$\begin{aligned} K_G &= A^T K_L A, \\ M_G &= A^T M_L A, \end{aligned} \tag{9}$$

where

K_G is the global stiffness matrix,

M_G is the global mass matrix.

3. FEM model

To verify the effects of the imputs, an already tested structure was needed, as such cable-stayed footbridge in Čelakovice was chosen. The two-dimensional finite element model was parametrized in MatLab by the project documentation, which was avaible including the static evaluation [4].

3.1. Geometry

This is the footbridge with field spans of 21.5 m + 156 m + 21.5 m, pylons are 36 m high each with 14 pairs of cables (Figure 1).

The bridge deck is supported at the crossing points with pylons and bridge abutments on the shores of the river Labe. The deck is made of UHPC with

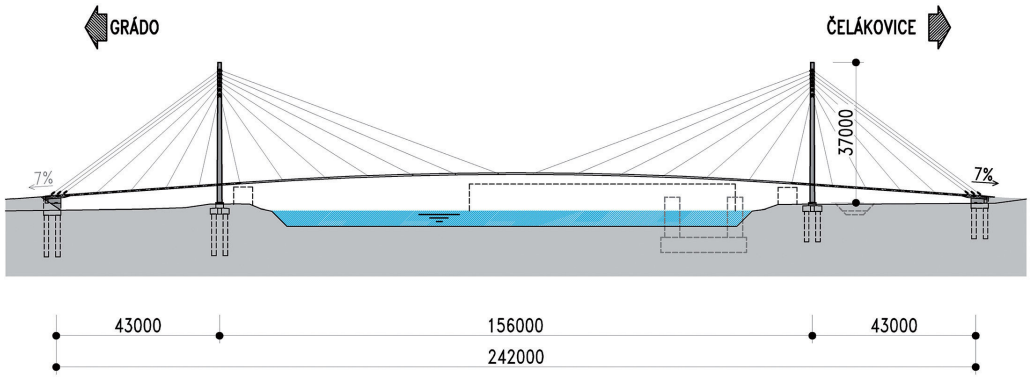

Figure 1. Sectional view.

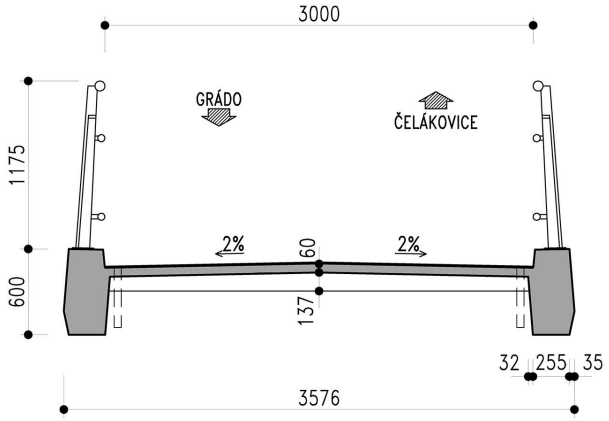

Figure 2. Cross section.

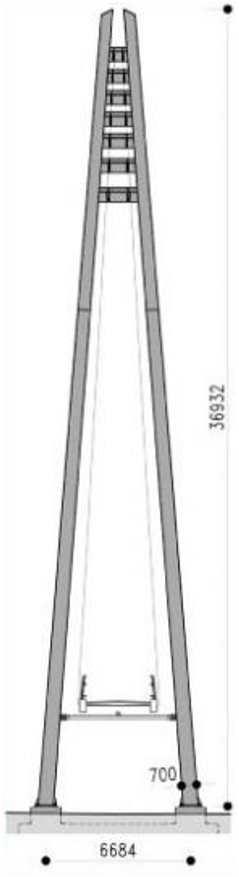

Figure 3. Pylon.

a strength C110/130 (Figure 2), the cables and pylons are made of steel (Figure 3).

The mathematical model is parameterized by dividing the construction into elements, where the end nodes at the beginning and end are assigned code numbers. The proposed 2D structure was designed in AutoCad (Figure 4).

3.2. Calculation

Elements were further divided so that material and physical characteristics could be assigned to them (Table 1). Each pair of cables was also assigned a prestressing force according to the static calculation (Table 2).

At the connection point of the cables between the pylon and the bridge plate, joints were defined. Where the bearings were supported, the bonds were loosened in the matrices so that the structure could move freely in the permitted directions. Numerically, this meant that at the support locations the rows and columns in the global matrices were zeroed/cleared because there is no unknown displacement but zero displacement/rotation.

For each finite element, the above-mentioned matrices were calculated in the local coordinate system, which were further transformed into the global coordinate system and global matrices K and M were formed. The natural shapes and natural frequences were calculated by direct solution by searching for eigenvalues on the diagonal, the correctness of the results was also verified by the method of inverse iterations. Another verification of the results was the modeling of the structure in the SCIA Engineer, which confirmed the correctness of the procedure (Figure 5).

Since the script is in MatLab (Figure 6), for final results the following command served the necessary outputs:

$$[V, D] = \mathrm{eig}(K, M), \tag{10}$$

where

V are the eigenform vectors,

D are eigenvalues – natural frequencies.

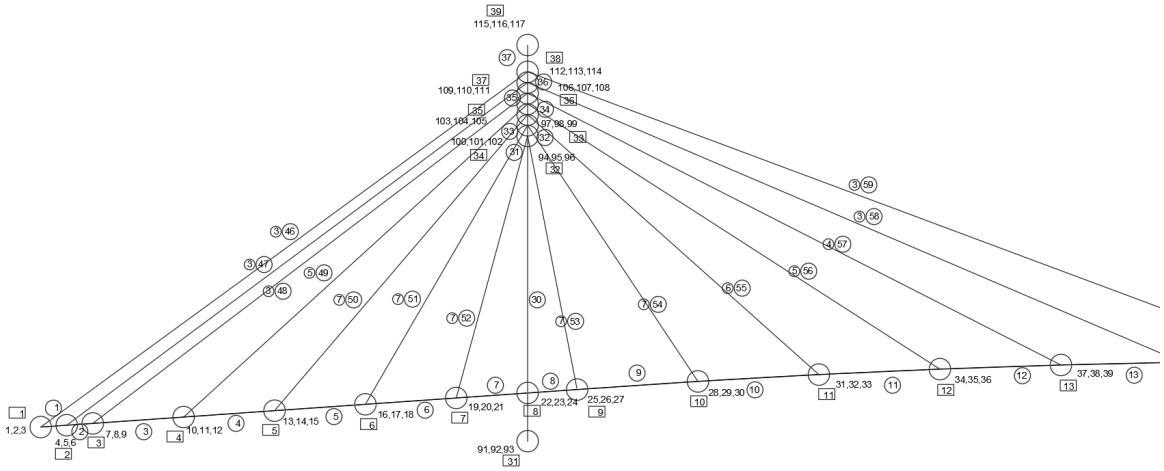

FIGURE 4. 2D drawing to determine code numbers on the lements.

Element type	E [MPa]	A [m^2]	I [m^4]	η [$t\,m^{-1}$]	ρ [$kN\,m^{-3}$]
Bridge deck	45 000	0.51368	0.012369	1.3356	26
Pylon	210 000	0.12478	0.0098726	0.9795	78.5
Cables	164464 – 165067	0.0053 – 0.00163	$1.12612 \times 10^{-8} - 1.0571 \times 10^{-7}$	0.0044 – 0.0136	82.53 – 83.70

TABLE 1. Material and geometric characteristics of the elements.

Cable number	Area [mm^2]	Area of doubled cable [mm^2]	Pre-stressing force [kN]
1 (101, 401)	266	532	75.6
2 (102, 402)	266	532	82.1
3 (103, 403)	266	532	87.1
4 (104 ,404)	521	1 042	133.6
5 (105, 405)	815	1 630	287.8
6 (106, 406)	815	1 630	287.8
7 (107, 407)	815	1 630	282.1
8 (201, 301)	266	532	90.7
9 (202, 302)	266	532	90.5
10 (203, 303)	416	832	117.8
11 (204, 304)	521	1 042	155.7
12 (205, 305)	639	1 278	185.1
13 (206, 306)	815	1 630	205.9
14 (207, 307)	815	1 630	276.8

TABLE 2. Cable parametres.

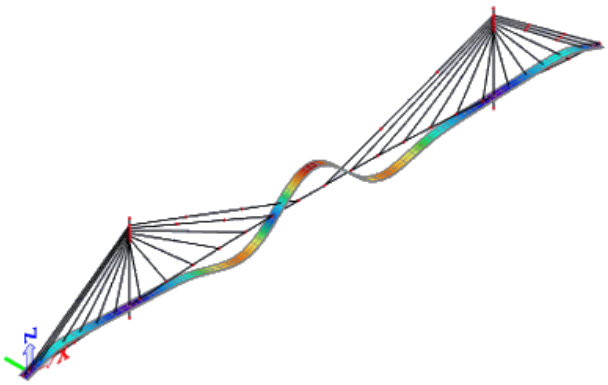

FIGURE 5. Numerical model verification in SCIA Engineer.

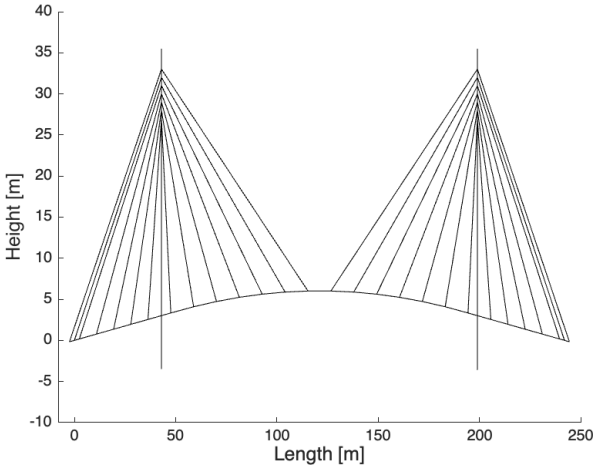

FIGURE 6. The shape of the structure ploted in MatLab.

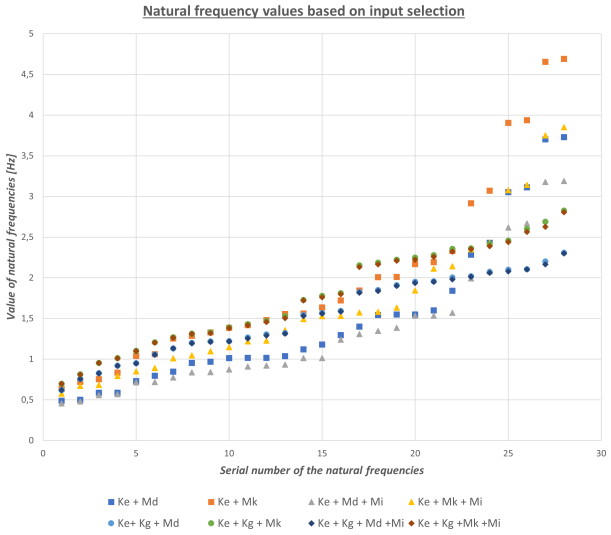

Figure 7. Comparison of calculation combinations.

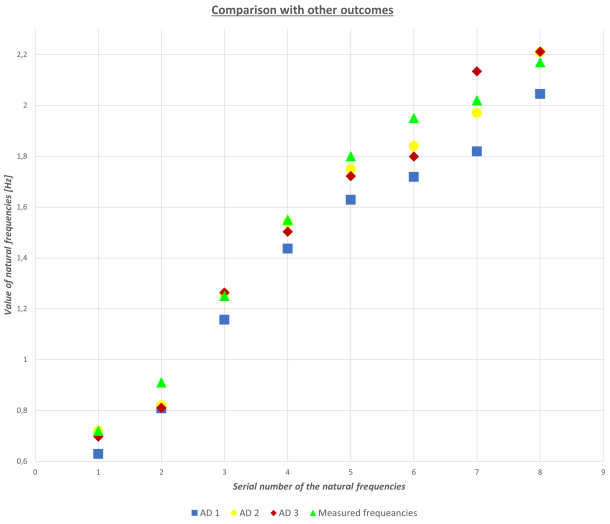

Figure 8. Comparison of vertical frequencies with other results on the same construction [5, 6].

4. Results

Various combinations of the stiffness and mass matrix were used in the dynamic calculation of the eigenshapes and eigenfrequencies. A comparison of individual combinations can be seen on the graph (Figure 7).

The biggest effect is noticeable at higher frequencies, where the curves move away from each other. As expected, the addition of the M_i global mass matrix has the least influence on the calculation, because it is a bridge deck with a low structural height. In the area around 1–2 Hz, which is observed in bridge structures, the difference between the results is up to a two-digit percentage number.

Furthermore, the results of this analysis were compared with the results of others who also calculated vertical frequencies on the same construction. The green curve is the actual measured frequencies on the structure (Figure 8), AD1 and AD2 are provided values from other mathematical models [5, 6], AD3 are the results from the most accurate form of this analysis, which is a combination of $K_e + K_g + M_k + M_i$.

The vertical frequencies are similar, but even if the results are based on the same project documentation, a difference of 5–10 % can be seen [5, 6].

5. Conclusion

The analysis helps for better understanding of the behaviour of cable-stayed bridges in terms of dynamics. In contrast with the commercial software, which are often black boxes, the hand-writed numerical code of a finite element model structure is much clearer in terms of changes in the influence on dynamic behavior. By testing different combinations of accuracy, it was proven that for such a complex construction, accuracy has a large effect on frequency results. It is important to continue to collect data from new UHPC constructions, for possible calibration of models, in order to achieve a correct prediction of the structure's behavior and avoid unnecessary design of dampers. The results confirm the sensitive behavior of such a complex non-linear construction, and with today's computer performance, where there is no need to save on computing memory, it is better to choose a more accurate form of calculation.

Acknowledgements

The authors gratefully acknowledge support from the Czech Technical University in Prague, project SGS23/032/OHK1/1T/11 Development and application of numerical algorithms for analysis and modelling in mechanics of structures and materials.

References

[1] European Commission, Joint Research Centre, A. Goldack, et al. *Design of lightweight footbridges for human induced vibrations – Background document in support to the implementation, harmonization and further development of the Eurocodes*. Publications Office, 2009. https://doi.org/doi/10.2788/33846

[2] Z. Bittnar, P. Řeřicha. *Metoda konečných prvků v dynamice konstrukcí [In Czech]*. SNTL, Praha, 1981.

[3] M. Baťa, V. Plachý, F. Trávníček. *Dynamika stavebních konstrukcí [In Czech]*. SNTL, Praha, 1987.

[4] M. Kalný, J. Komanec, V. Kvasnička, et al. Lávka přes Labe v Čelákovicích – první nosná konstrukce z UHPC v ČR [In Czech; Footbridge over the Elbe river in Čelakovice – the first UHPC superstructure in the Czech Republic]. *Beton* (4):10–18, 2014. [2023-09-01]. https://www.ebeton.cz/wp-content/uploads/2014-4-10_0.pdf

[5] J. Štěpánek. *Dynamická analýza lávky pro pěší [In Czech; Dynamic analysis of the footbridge]*. Bachelor's thesis, Czech Technical University in Prague, Faculty of Civil Engineering, 2016.

[6] V. Šáňa. *Vibration of footbridges human-structure interaction*. Ph.D. thesis, Czech Technical University in Prague, Faculty of Civil Engineering, 2016.

FRACTIONAL ORDER MODELS OF VISCOELASTIC POLYMERIC SOLIDS UNDERGOING LARGE DEFORMATIONS

Barbora Hálková[a,*], Michal Beneš[b]

[a] *Czech Technical University in Prague, Faculty of Civil Engineering, Department of Mechanics, Thákurova 7, 166 29 Prague, Czech Republic*

[b] *Czech Technical University in Prague, Faculty of Civil Engineering, Department of Mathematics, Thákurova 7, 166 29 Prague, Czech Republic*

[*] corresponding author: barbora.halkova@fsv.cvut.cz

Abstract. We present a fractional order model for nonlinear visco-hyperelastic solids taking into account large deformations. A three-field form of the Hu-Washizu principle is introduced to create a stable finite element method in the context of nearly incompressible dynamics. The β-method (a generalized midpoint rule) for time discretization is implemented into a variational finite element framework for efficient computing of numerical approximations to the initial boundary-value problem for hyperbolic equation of motion. Finally, a 2-D cantilever beam problem with a step end load is considered in order to demonstrate the algorithm.

Keywords: Fractional viscoelasticity, large deformations, springpot, fractional calculus, finite element, integration algorithm.

1. Introduction

Many polymers exhibit time dependent behavior somewhere between purely elastic and purely viscous materials. As a result, a large number of Kelvin-Voigt or Maxwell elements (and thus a large number of material parameters) are needed to be identified from experimental data to obtain a reasonably accurate description of mechanical response. On the other hand, a fractional calculus, i.e. the theory of derivatives and integrals of non-integer order, seems to be an efficient tool for the theoretical modelling of viscoelastic materials [1]. Theoretical models based on the fractional calculus allows us to describe viscoelastic materials with significantly less parameters than the standard approach. For a deeper discussion on this issue we refer the reader to [2]. The fractional viscoelastic model at small strains was introduced e.g. in [3–7]. On the other hand, although rubbery polymers typically exhibit large deformations in engineering applications, much less attention has been given to fractional viscoelasticity in combination with the finite strain theory [8]. The present work provides a computational framework for modelling the fractional viscoelastic behaviour of polymeric solids at finite strains in the context of nearly incompressible dynamics.

Let the open set Ω_0 be the reference configuration of a given (compressible or nearly incompressible) body at time t_0. Here, Ω_0 is described by a set of continuously distributed points X (particles or material points) which occupy a region within the Euclidean space $\mathbb{E}^3$. In the absence of displacement discontinuities, a one-to-one deformation map $\boldsymbol{\phi} : \Omega_0 \times [0,T] \to \mathbb{E}^3$ describing a motion exists,

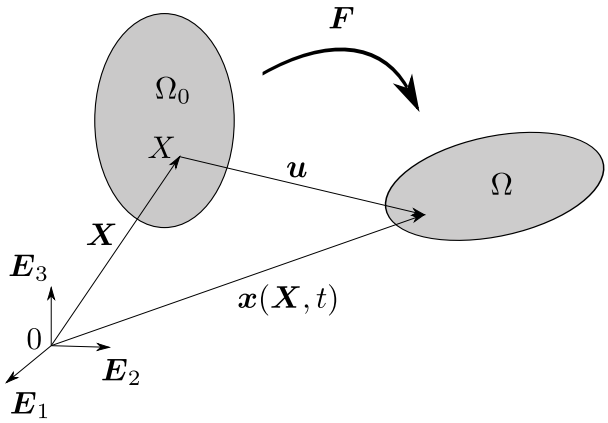

Figure 1. Motion of body Ω_0.

such that any displaced position at a current time $t \in [0,T]$, where $[0,T] \subset \mathbb{R}^+$ denotes the time of interest, is determined as $\boldsymbol{x} = \boldsymbol{\phi}(\boldsymbol{X},t)$ with the difference being the displacement field $\boldsymbol{u}(\boldsymbol{X},t) = \boldsymbol{x} - \boldsymbol{X}$. Here, the position vector $\boldsymbol{X} = (X_1, X_2, X_3)$ represents the particle X in the reference configuration Ω_0, $\boldsymbol{X} = X_1\boldsymbol{E}_1 + X_2\boldsymbol{E}_2 + X_3\boldsymbol{E}_3$, where $(\boldsymbol{E}_1, \boldsymbol{E}_2, \boldsymbol{E}_3)$ defines an orthogonal base system with origin 0. Hence, we have $\boldsymbol{x} = \boldsymbol{\phi}(\boldsymbol{X},t) = \boldsymbol{X} + \boldsymbol{u}(\boldsymbol{X},t)$, see Figure 1. The deformation gradient $\boldsymbol{F}(\boldsymbol{X},t)$ is obtained as the gradient of this deformation map $\boldsymbol{F} = \nabla_0\boldsymbol{\phi}$, where ∇_0 is the gradient with respect to $\boldsymbol{X}$, and the Jacobian of the deformation map is given by $J(\boldsymbol{X},t) = \det \boldsymbol{F}$. We also define the right Cauchy-Green deformation tensors $\boldsymbol{C}(\boldsymbol{X},t) = \boldsymbol{F}^T\boldsymbol{F}$.

Let Ω_0 be the reference configuration of the body of interest with the boundary $\partial\Omega_0$ and $T > 0$ be the time horizon. Let $\partial\Omega_u$, $\partial\Omega_P$ be smooth open disjoint subsets of $\partial\Omega_0$ such that $\overline{\partial\Omega_0} = \overline{\partial\Omega_u \cup \partial\Omega_P}$, $\partial\Omega_u \neq \emptyset$

and $\partial\Omega_u \cap \partial\Omega_P = \emptyset$. Let $\boldsymbol{f}_0$ be the body force per unit of mass, a given vector field defined on $\Omega_0 \times (0,T)$, $\boldsymbol{u}_0$ and $\boldsymbol{v}_0 : \Omega_0 \to \mathbb{R}^3$ be the prescribed initial position and velocity. Further, let $\breve{\boldsymbol{t}}_0$ be the given traction prescribed on $\partial\Omega_P \times (0,T)$ and let the displacement $\breve{\boldsymbol{u}}_0$ be prescribed on $\partial\Omega_u \times (0,T)$. The local form of the initial boundary value problem for the momentum equation is given by the following system [9]:

$$\rho_0 \frac{\partial^2 \boldsymbol{u}}{\partial t^2} = \nabla_0 \cdot \boldsymbol{P} + \boldsymbol{f}_0 \qquad \text{in } \Omega_0 \times (0,T), \tag{1}$$

$$\boldsymbol{u} = \breve{\boldsymbol{u}}_0 \qquad \text{in } \partial\Omega_u \times (0,T), \tag{2}$$

$$\boldsymbol{P} \cdot \boldsymbol{N}_0 = \breve{\boldsymbol{t}}_0 \qquad \text{in } \partial\Omega_P \times (0,T), \tag{3}$$

$$\boldsymbol{u}(\cdot,0) = \boldsymbol{u}_0 \qquad \text{in } \Omega_0, \tag{4}$$

$$\frac{\partial \boldsymbol{u}}{\partial t}(\cdot,0) = \boldsymbol{v}_0 \qquad \text{in } \Omega_0, \tag{5}$$

where

$\boldsymbol{N}_0$ is the field normal to $\partial\Omega_P$,

$\boldsymbol{P} = \boldsymbol{P}(\boldsymbol{X}, \boldsymbol{F}(\boldsymbol{X},t))$ is the first Piola-Kirchhoff stress.

2. Constitutive relationships

2.1. Hyperelastic material

In this contribution, we are interested to solve the system (1)–(5), in the context of nearly-incompressible material behavior (rubber like materials), which requires a special numerical treatment – like *mixed methods*. In particular, the deformation is split into a volumetric part represented by J and an isochoric part of the right Cauchy-Green deformation tensor $\widehat{\boldsymbol{C}}$, $\widehat{\boldsymbol{C}} = J^{-\frac{2}{3}}\boldsymbol{C}$. As a consequence, the split permits a different treatment of the incompressible part.

The deformation gradient $\boldsymbol{F}$ together with its conjugate first Piola-Kirchhoff stress measure $\boldsymbol{P}$, will be retained in order to defined the basic material relationship. The hyperelastic constitutive equation can be generally expressed as:

$$\boldsymbol{P}(\boldsymbol{F}) = \frac{\partial W(\boldsymbol{F})}{\partial \boldsymbol{F}}. \tag{6}$$

Typically for mixed methods [10, 11], the stored energy function W is additively decomposed into distortional part $\widehat{W}$ and dilatational part U, namely:

$$W(\boldsymbol{F}) = \widehat{W}(\boldsymbol{C}) + U(J). \tag{7}$$

Recall that $\boldsymbol{C} = \boldsymbol{F}^T\boldsymbol{F}$ and $J = \det \boldsymbol{F}$. A traditional nearly incompressible neo-Hookean potential $\widehat{W}(\boldsymbol{C}) = \frac{1}{2}\mu(\mathrm{tr}\widehat{\boldsymbol{C}} - 3)$ and a simple volumetric function $U(J) = \frac{1}{2}\kappa(J-1)^2$ are used in this work, where μ is the shear modulus and κ denotes the bulk modulus. These assumptions give us the possibility to decompose the stress tensor into pure shear and bulk responses. The calculation is straightforward, we get:

$$\boldsymbol{P}(\boldsymbol{F}) = 2\boldsymbol{F}\frac{\partial \widehat{W}}{\partial \boldsymbol{C}} + 2\boldsymbol{F}\frac{\partial U}{\partial J}\frac{\partial J}{\partial \boldsymbol{C}} \tag{8}$$

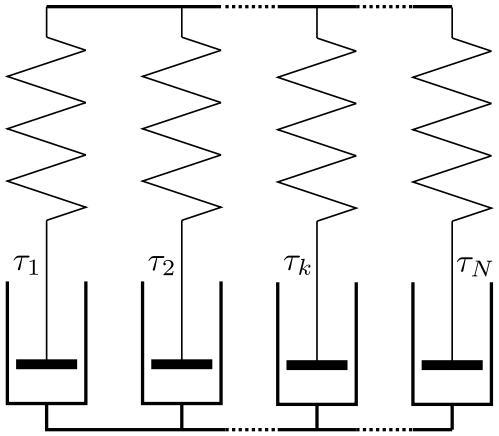

Figure 2. The standard viscoelastic model.

and

$$\frac{\partial J}{\partial \boldsymbol{C}} = \frac{\sqrt{\det \boldsymbol{C}}}{\partial \boldsymbol{C}} = \frac{1}{2} J \boldsymbol{C}^{-1}. \tag{9}$$

To account properly for nearly incompressible material response and to avoid difficulties concerning "locking" of the finite element procedure, we employ a three-field de Veubeke-Hu-Washizu principle [10]. Additional variables entering the *mixed* three-field formulation represent a strain variable θ which is equivalent to J:

$$\theta = J, \tag{10}$$

and the hydrostatic pressure:

$$p = \left.\frac{\partial U}{\partial J}\right|_{J=\theta}. \tag{11}$$

In the weak formulation of our problem and the subsequent finite element procedure, introduced hereafter, Equations (10) and (11) are satisfied in a weak sense.

2.2. Fractional viscoelasticity

In a viscoelastic model the stress depends not solely on the current strain (elastic model), but it also depends on the entire strain history. The standard viscoelastic model consists of N Maxwell chains coupled in parallel, see Figure 2. The present approach is based on the assumption that a viscous response is characterized by a set of rate constitutive equations, namely for a nonequilibrium stress $\boldsymbol{Q}_k$ (in chain k) as an internal variable, $k = 1, 2, \ldots, N$. The constitutive model can be written as a set of coupled equations [8, 9, 12]:

$$\boldsymbol{S} = 2\frac{\partial \mathcal{W}}{\partial \boldsymbol{C}} - \sum_{k=1}^{N} \boldsymbol{Q}_k, \qquad \boldsymbol{P} = \boldsymbol{F}\boldsymbol{S}, \tag{12}$$

$$\frac{\partial \boldsymbol{Q}_k}{\partial t} + \frac{1}{\tau_k}\boldsymbol{Q}_k = \frac{1}{\tau_k}\left(2\frac{\partial \widehat{W}_k}{\partial \boldsymbol{C}}\right), \quad \boldsymbol{Q}_k(0) = \boldsymbol{0}, \tag{13}$$

where

$k = 1, 2, \ldots, N$,

$\mathcal{W} = \sum_{k=1}^{N} W_k$,

$\boldsymbol{S}$ represents the second (or symmetric) Piola-Kirchhoff stress tensor,

W_k is the strain energy in chain k,

τ_k is the relaxation time associated with each Maxwell chain.

Classical theory of viscoelasticity employs the models composed of rheological elements such as elastic springs and viscous dampers. Meanwhile, the fractional viscoelasticity introduces the springpot element together with the principles of fractional calculus. The fractional derivative of order α of a function u is defined as:

$$D^{\alpha}u(t) = \frac{1}{\Gamma(1-\alpha)}\frac{\mathrm{d}}{\mathrm{d}t}\int_0^t \frac{u(s)}{(t-s)^{\alpha}}\mathrm{d}s, \tag{14}$$

where

$0 < \alpha < 1$,

Γ is the gamma function.

Replacing now the integer order derivative in (13) with a fractional order derivative we get:

$$D^{\alpha_k}\boldsymbol{Q}_k + \frac{1}{\tau_k^{\alpha_k}}\boldsymbol{Q}_k = \frac{1}{\tau_k^{\alpha_k}}\left(2\frac{\partial \widehat{W}_k}{\partial \boldsymbol{C}}\right), \tag{15}$$

$$\boldsymbol{Q}_k(0) = \boldsymbol{0}, \tag{16}$$

where

$k = 1, 2, \ldots, N$,

$\tau_k^{\alpha_k}$ can now be interpreted as the most probable relaxation time out of a continuous distribution of relaxation times.

The fractional order of differentiation α_k then plays the role of a distribution parameter for the corresponding distribution of relaxation times [13]. The fractional Maxwell chain is obtained as a parallel connection of N fractional Maxwell cells, see the scheme in Figure 3.

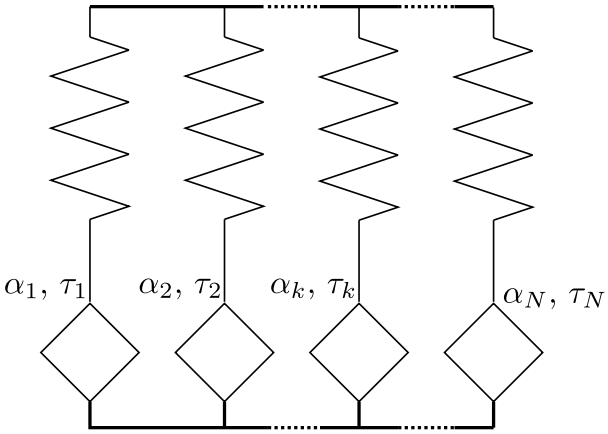

FIGURE 3. The fractional Maxwell chain.

3. The weak formulation

In the rest of the paper, just to simplify and shorten the presentation and avoid unnecessary technicalities, we will consider the case $N = 1$ (the fractional Maxwell cell). The simple model presented here can be straightforwardly extended to a setting with the parallel connection of N cells (in the fractional Maxwell chain).

Let $W^{1,2}(\Omega_0)$ denote the Sobolev space of functions possessing square integrable derivatives and $\mathbb{H}(\Omega_0) := W^{1,2}(\Omega_0)^3$. Let us denote by $\mathbb{S}_t$ the displacement solution space at time $t \in [0,T]$ defined as:

$$\mathbb{S}_t = \left\{ \boldsymbol{u}(\cdot,t) \in \mathbb{H}(\Omega_0) \,\middle|\, \boldsymbol{u}(\cdot,t) = \breve{\boldsymbol{u}}_0(\cdot,t) \text{ on } \partial\Omega_u \right\}.$$

Finally, we denote by $\mathbb{H}_u(\Omega_0)$ the linear space of admissible test functions or kinematically admissible variations, i.e., (virtual) displacements satisfying the homogeneous form of the essential boundary condition (2) as:

$$\mathbb{H}_u(\Omega_0) = \left\{ \boldsymbol{v} \in \mathbb{H}(\Omega_0) \,\middle|\, \boldsymbol{v} = \boldsymbol{0} \text{ on } \partial\Omega_u \right\}.$$

With these notations in hand, the weak form of our problem reads as follows:
For *sufficiently smooth* data $\boldsymbol{f}_0$, $\boldsymbol{u}_0$, $\boldsymbol{v}_0$, $\breve{\boldsymbol{t}}_0$ and $\breve{\boldsymbol{u}}_0$ find the displacement field $\boldsymbol{u}(\cdot,t) \in \mathbb{S}_t$, pressure $p(\cdot,t) \in L^2(\Omega_0)$, the volume filed $\theta(\cdot,t) \in L^2(\Omega_0)$ and the internal variable $\boldsymbol{Q}(\cdot,t) \in L^2(\Omega_0)^{3\times 3}$, such that $\boldsymbol{u}(\cdot,0) = \boldsymbol{u}_0$, $\frac{\partial \boldsymbol{u}}{\partial t}(\cdot,0) = \boldsymbol{v}_0$ and $\boldsymbol{Q}(0) = \boldsymbol{0}$ in Ω_0 and:

$$\begin{aligned}
&\int_{\Omega_0} \rho_0 \frac{\partial^2 \boldsymbol{u}}{\partial t^2} \cdot \boldsymbol{v}\,\mathrm{d}\Omega_0 \\
&+ \int_{\Omega_0} \widehat{\boldsymbol{S}} : [\boldsymbol{F}^T\nabla_0\boldsymbol{v}] + pJ\boldsymbol{C}^{-1} : [\boldsymbol{F}^T\nabla_0\boldsymbol{v}]\,\mathrm{d}\Omega_0 \\
&- \int_{\Omega_0} \boldsymbol{Q} : [\boldsymbol{F}^T\nabla_0\boldsymbol{v}]\,\mathrm{d}\Omega_0 \\
&= \int_{\Omega_0} \boldsymbol{f}_0 \cdot \boldsymbol{v}\,\mathrm{d}\Omega_0 + \int_{\partial\Omega_P} \breve{\boldsymbol{t}}_0 \cdot \boldsymbol{v}\,\mathrm{d}S_0
\end{aligned} \tag{17}$$

for all $\boldsymbol{v} \in \mathbb{H}_u(\Omega_0)$ and all $t \in [0,T]$,

$$\int_{\Omega_0} [p - \kappa(\theta-1)]\,\psi\,\mathrm{d}\Omega_0 = 0 \tag{18}$$

for all $\psi \in L^2(\Omega_0)$ and all $t \in [0,T]$ and:

$$\int_{\Omega_0} (J-\theta) q\,\mathrm{d}\Omega_0 = 0 \tag{19}$$

for all $q \in L^2(\Omega_0)$ and all $t \in [0,T]$. Finally:

$$D^{\alpha}\boldsymbol{Q} + \frac{1}{\tau^{\alpha}}\boldsymbol{Q} = \frac{1}{\tau^{\alpha}}\widehat{\boldsymbol{S}}, \quad \tau > 0,\ \alpha \in (0,1], \tag{20}$$

holds almost everywhere in Ω_0 and for all $t \in [0,T]$. Here:

$$\widehat{\boldsymbol{S}} = 2\frac{\partial \widehat{W}}{\partial \boldsymbol{C}}$$

denotes the computational deviatoric second Piola-Kirchhoff stress. The Equation (17) denotes the weak form of the Equation of motion (1). The second Equation (18) yields the constitutive equation for the pressure p, see also Equation (11), and the third Equation (19) reproduces the constraint condition (10).

4. Numerical algorithm

Here we outline a general numerical solution scheme for the viscoelastic problem (extended to fractional viscoelasticity) within the context of the finite-element method. The point of departure in our developments is the weak formulation introduced in the preceding section. For simplicity, we will assume that the displacement boundary conditions are homogeneous, i.e.:

$$\boldsymbol{u}(\cdot,t) = \breve{\boldsymbol{u}}_0(\cdot,t) \equiv \boldsymbol{0} \text{ on } \partial\Omega_u.$$

We begin by traditional discretization in space by the finite element method. Let us define:

$$\boldsymbol{u}^h = \boldsymbol{\Psi}_u^T \tilde{\boldsymbol{u}}, \quad \boldsymbol{u}^h\Big|_{\Omega_e} = \sum_{i=1}^{NN_u} \Psi_u^i(\boldsymbol{x})\tilde{\boldsymbol{u}}^i(t) \tag{21}$$

for all $\boldsymbol{u}^h \in \mathbb{H}_u^h \subset \mathbb{H}_u(\Omega_0)$,

$$\theta^h = \boldsymbol{\Psi}_\theta^T \tilde{\boldsymbol{\theta}}, \quad \theta^h\Big|_{\Omega_e} = \sum_{i=1}^{NN_\theta} \Psi_\theta^i(\boldsymbol{x})\tilde{\theta}^i(t) \tag{22}$$

for all $\theta^h \in L^h \subset L^2(\Omega_0)$,

$$p^h = \boldsymbol{\Psi}_p^T \tilde{\boldsymbol{p}}, \quad p^h\Big|_{\Omega_e} = \sum_{i=1}^{NN_p} \Psi_p^i(\boldsymbol{x})\tilde{p}^i(t), \tag{23}$$

for all $p^h \in L^h \subset L^2(\Omega_0)$ and:

$$\boldsymbol{Q}^h = \boldsymbol{\Psi}_Q^T \tilde{\boldsymbol{Q}}, \quad \boldsymbol{Q}^h\Big|_{\Omega_e} = \sum_{i=1}^{NN_Q} \Psi_Q^i(\boldsymbol{x})\tilde{\boldsymbol{Q}}^i(t) \tag{24}$$

for all $\boldsymbol{Q}^h \in [L^h]^{3\times 3} \subset L^2(\Omega_0)^{3\times 3}$. Here we denoted by $\mathbb{H}_u^h$ and L^h the finite element subspace of the space $\mathbb{H}_u(\Omega_0)$ and $L^2(\Omega_0)$, respectively.

Let now $0 = t_0 < t_1 < \cdots < t_R = T$ be an equidistant partitioning of the time interval $[0,T]$ with the discrete time step Δt, $\{t_n\}_{n=0}^R$, $\Delta t = \frac{T}{R}$. For any function, vector-valued function or tensor ζ, we will use the approximation $\zeta_n \approx \zeta(t_n)$ and introduce the notation:

$$\zeta_{n+\beta} = (1-\beta)\zeta_n + \beta\zeta_{n+1}, \quad \beta \in [0,1]. \tag{25}$$

Our goal is to develop time discretization schemes for which a discrete form of the problem (17)–(20) can be established. Replacing the second order derivative in (17) by the discrete derivative, $\frac{\partial^2 \boldsymbol{u}}{\partial t^2} \approx \frac{\boldsymbol{u}_{n+1}^h - 2\boldsymbol{u}_n^h + \boldsymbol{u}_{n-1}^h}{\Delta t}$, and incorporating the generalized midpoint rule (25) into the weak formulation (17)–(19), the final result is the generalized β-scheme of the form:

$$\begin{aligned}
\mathcal{R}_u = &-\int_{\Omega_0} \rho_0 \left(\frac{\boldsymbol{u}_{n+1}^h - 2\boldsymbol{u}_n^h + \boldsymbol{u}_{n-1}^h}{\Delta t}\right)\cdot \delta\boldsymbol{u}^h \,\mathrm{d}\Omega_0 \\
&- \beta\Delta t \int_{\Omega_0} \widehat{\boldsymbol{S}}_{n-1+\beta} : \left[\boldsymbol{F}_{n-1+\beta}^T(\nabla_0\, \delta\boldsymbol{u}^h)\right] \mathrm{d}\Omega_0 \\
&- \beta\Delta t \int_{\Omega_0} p_{n-1+\beta}^h\, J_{n-1+\beta}\boldsymbol{C}_{n-1+\beta}^{-1} : \left[\boldsymbol{F}_{n-1+\beta}^T(\nabla_0\, \delta\boldsymbol{u}^h)\right] \mathrm{d}\Omega_0 \\
&- \beta\Delta t \int_{\Omega_0} \boldsymbol{Q}_{n-1+\beta} : \left[\boldsymbol{F}_{n-1+\beta}^T(\nabla_0\, \delta\boldsymbol{u}^h)\right] \mathrm{d}\Omega_0 \\
&- (1-\beta)\Delta t \int_{\Omega_0} \widehat{\boldsymbol{S}}_{n+\beta} : \left[\boldsymbol{F}_{n+\beta}^T(\nabla_0\, \delta\boldsymbol{u}^h)\right] \mathrm{d}\Omega_0 \\
&- (1-\beta)\Delta t \int_{\Omega_0} p_{n+\beta}^h J_{n+\beta}\boldsymbol{C}_{n+\beta}^{-1} : \left[\boldsymbol{F}_{n+\beta}^T(\nabla_0\, \delta\boldsymbol{u}^h)\right] \mathrm{d}\Omega_0 \\
&- (1-\beta)\Delta t \int_{\Omega_0} \boldsymbol{Q}_{n+\beta} : \left[\boldsymbol{F}_{n+\beta}^T(\nabla_0\, \delta\boldsymbol{u}^h)\right] \mathrm{d}\Omega_0 \\
&+ \beta\Delta t \int_{\Omega_0} (\boldsymbol{f}_0)_{n-1+\beta}\cdot \delta\boldsymbol{u}^h \,\mathrm{d}\Omega_0 \\
&+ (1-\beta)\Delta t \int_{\Omega_0} (\boldsymbol{f}_0)_{n+\beta}\cdot \delta\boldsymbol{u}^h \,\mathrm{d}\Omega_0 \\
&+ \beta\Delta t \int_{\partial\Omega_P} (\breve{\boldsymbol{t}}_0)_{n-1+\beta}\cdot \delta\boldsymbol{u}^h \,\mathrm{d}S_0 \\
&+ (1-\beta)\Delta t \int_{\partial\Omega_P} (\breve{\boldsymbol{t}}_0)_{n+\beta}\cdot \delta\boldsymbol{u}^h \,\mathrm{d}S_0 = 0
\end{aligned} \tag{26}$$

for all $\delta\boldsymbol{u}^h \in \mathbb{H}_u^h$,

$$\begin{aligned}
\mathcal{R}_\theta = &-\Delta t \int_{\Omega_0} \big[\kappa\,\beta\,\left(\theta_{n-1+\beta}^h - 1\right) \\
&+ \kappa(1-\beta)\left(\theta_{n+\beta}^h - 1\right)\big]\,\delta\theta^h \,\mathrm{d}\Omega_0 \surd \\
&+ \Delta t \int_{\Omega_0} \left[\beta p_{n-1+\beta}^h + (1-\beta)p_{n+\beta}^h\right]\delta\theta^h \,\mathrm{d}\Omega_0 = 0
\end{aligned} \tag{27}$$

for all $\delta\theta^h \in L^h$ and:

$$\begin{aligned}
\mathcal{R}_p = &-\Delta t \int_{\Omega_0} \left[\beta J_{n-1+\beta} + (1-\beta)J_{n+\beta}\right]\delta p^h \,\mathrm{d}\Omega_0 \\
&+ \Delta t \int_{\Omega_0} \left[\beta\theta_{n-1+\beta}^h + (1-\beta)\theta_{n+\beta}^h\right]\delta p^h \,\mathrm{d}\Omega_0 = 0
\end{aligned} \tag{28}$$

for all $\delta p^h \in L^h$. Note that β serves as a parameter to control the implicitness of the algorithm. For $\beta = 0$ or $\beta = 1$ we get the explicit method. Setting $\beta = \frac{1}{2}$ we obtain the implicit method.

Next we present the algorithm for the integration of the rate Equation (20). First, the discrete fractional derivative of order α at time $(n+1)\Delta t$ can be approximated by [14]:

$$[D^\alpha \boldsymbol{Q}]_{n+1} = \frac{1}{(\Delta t)^\alpha}\sum_{j=0}^{n} w_j(\alpha)\boldsymbol{Q}_{n+1-j}, \tag{29}$$

where the weights can be identified and calculated by the recursion relation below:

$$\begin{aligned}
&w_0(\alpha) = 1, \\
&w_1(\alpha) = -\alpha, \\
&\qquad\cdots \\
&w_j(\alpha) = \frac{j-1-\alpha}{j} w_{j-1}(\alpha), \\
&\qquad\cdots .
\end{aligned}$$

Using (29) in the rate equation (20) we get:

$$[D^\alpha \boldsymbol{Q}]_{n+1} + \frac{1}{\tau^\alpha}\boldsymbol{Q}_{n+1} = \frac{1}{\tau^\alpha}\widehat{\boldsymbol{S}}_n. \tag{30}$$

Moreover, using (29) we can rewrite the approximation of the fractional derivative as:

$$\begin{aligned}[D^\alpha \boldsymbol{Q}]_{n+1} =& \frac{1}{(\Delta t)^\alpha}\boldsymbol{Q}_{n+1} \\ &+ \frac{1}{(\Delta t)^\alpha}\sum_{j=1}^{n} w_j(\alpha)\boldsymbol{Q}_{n+1-j}.\end{aligned} \tag{31}$$

Substituting (31) into (30) it is easy to see that $\boldsymbol{Q}_{n+1}$ can be computed as:

$$\begin{aligned}\boldsymbol{Q}_{n+1} =& (\Delta t)^\alpha [w_0(\alpha)\tau^\alpha + (\Delta t)^\alpha]^{-1}\widehat{\boldsymbol{S}}_n \\ &- \tau^\alpha [w_0(\alpha)\tau^\alpha + (\Delta t)^\alpha]^{-1}\sum_{j=1}^{n} w_j(\alpha)[\boldsymbol{Q}]_{n+1-j}.\end{aligned} \tag{32}$$

The disadvantage of the fractional viscoelasticity is the nonlocal character of fractional derivatives. Numerical approximation requires the whole history of the internal variables in the preceding time steps to be saved and included in the calculation of the new time step. Letting $\alpha = 1$ and the sum in Equation (32) simply becomes $-\boldsymbol{Q}_n$ and the classical model follows.

It is worth pointing out that the right hand side in (30) is taken from the preceding time step (a *semi*-implicit integrator). As a result, the discrete rate Equation (30) is *decoupled* from the system at the actual time step $n+1$ and the approximation of the internal variable $\boldsymbol{Q}_{n+1}$ can be computed first (at each discrete time step). Then, with $\boldsymbol{Q}_{n+1}$ in hand, the Newton-Raphson method is applied to solve the non-linear system (26)–(28). The derivation of a tangent stiffness tensor that is consistent with the integration procedure is essential to ensure a quadratic rate of convergence [15]. A consistent linearization for the set of non-linear equations given in Equations (26)–(28), about a configuration $\boldsymbol{u}$, θ and p, is given by:

$$\boldsymbol{J}_g(\boldsymbol{y}^{(i)})\Delta\boldsymbol{y}^{(i)} = -\boldsymbol{g}(\boldsymbol{y}^{(i)}), \tag{33}$$

$$\boldsymbol{y}^{(i+1)} = \boldsymbol{y}^{(i)} + \Delta\boldsymbol{y}^{(i)}, \tag{34}$$

where

$$\boldsymbol{y}^T = (\tilde{\boldsymbol{u}}_{n+1}, \tilde{\boldsymbol{\theta}}_{n+1}, \tilde{\boldsymbol{p}}_{n+1}),$$

$$\boldsymbol{g}^T = (\boldsymbol{\mathcal{R}}_u, \boldsymbol{\mathcal{R}}_\theta, \boldsymbol{\mathcal{R}}_p),$$

$$\boldsymbol{J}_g = \begin{pmatrix} \boldsymbol{C}_{uu} & \boldsymbol{0} & \boldsymbol{C}_{pu}^T \\ \boldsymbol{0} & \boldsymbol{C}_{\theta\theta} & \boldsymbol{C}_{p\theta}^T \\ \boldsymbol{C}_{pu} & \boldsymbol{C}_{p\theta} & \boldsymbol{0} \end{pmatrix}, \quad \boldsymbol{C}_{\square\triangle} = \frac{\partial \boldsymbol{\mathcal{R}}_\square}{\partial \triangle_{i+1}}.$$

5. Numerical example

To illustrate the performance of the model, we consider a 2-D cantilever beam 1.0×0.4 m with a step end load, see Figure 4 and Figure 5. The beam is meshed uniformly with 4-node quadrilateral elements and partitioned as shown. The parameters used for this problem are: Young's modulus $E = 1.0 \times 10^4$ Pa, density

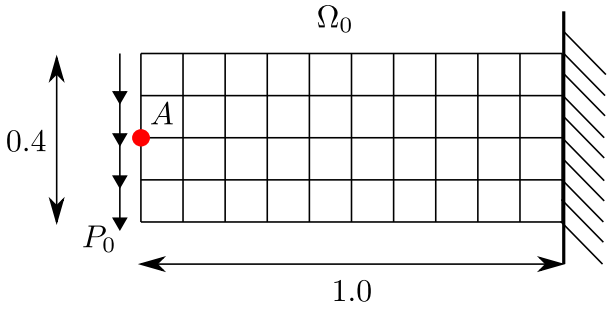

Figure 4. 2-D cantilever beam.

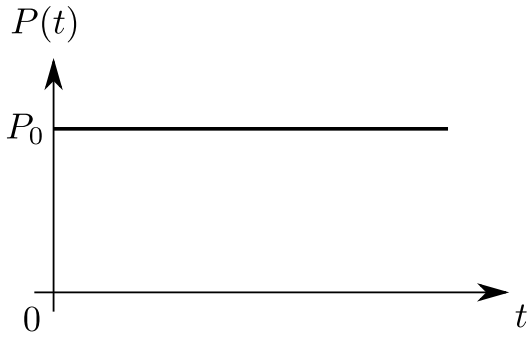

Figure 5. A step end load.

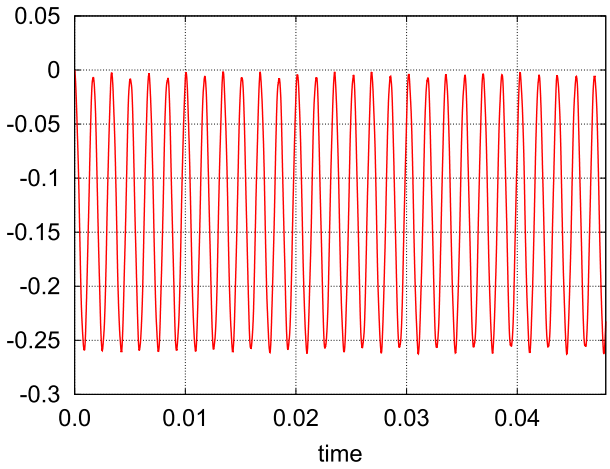

Figure 6. Vertical displacement of the mid-point A on the free edge. Hyperelastic material was considered in this case (neglecting viscous effects, i.e. $\tau \to +\infty$).

$\rho_0 = 1.0 \times 10^{-4}\,\mathrm{kg\,m^{-3}}$, end load $P_0 = 20.0\,\mathrm{N\,m^{-1}}$ distributed over the free edge. The problem was integrated with a time step $\Delta t = 2.0 \times 10^{-6}$ s. First, we considered the *purely* hyperelastic material neglecting viscous effects ($\tau \to +\infty$). Figure 6 shows the motion of point A. Note that our results are in very close agreement with the results presented in [16].

In Figure 7 the vertical displacement of the mid-point A versus time is displayed for different values of α. As can be observed, the value of α clearly affects the results. Vertical displacements seem to decay faster with higher values of α. Figures 8 and 9 show the deformed cantilever for parameter $\alpha = 0.5$.

Due to the fact that the time step is limited by

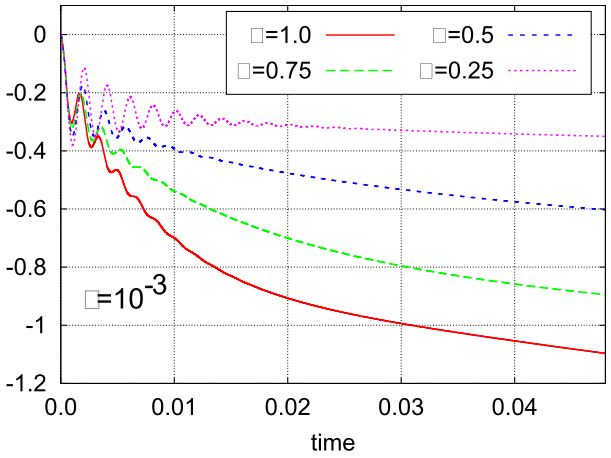

Figure 7. Vertical displacement of the point A. The influence of different values of α for fixed $\tau = 10^{-3}$ s.

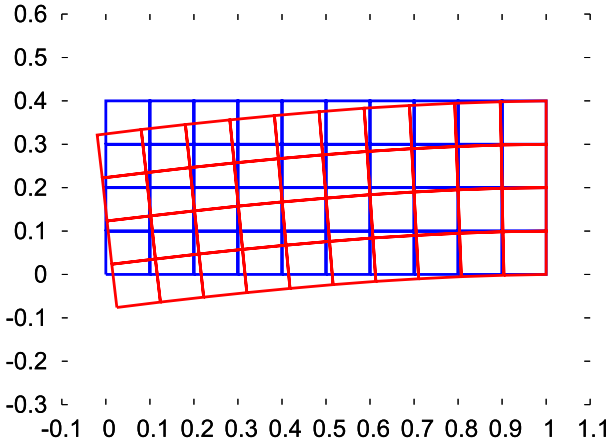

Figure 8. Motion of the beam at time $t = 3.0 \times 10^{-4}$ s.

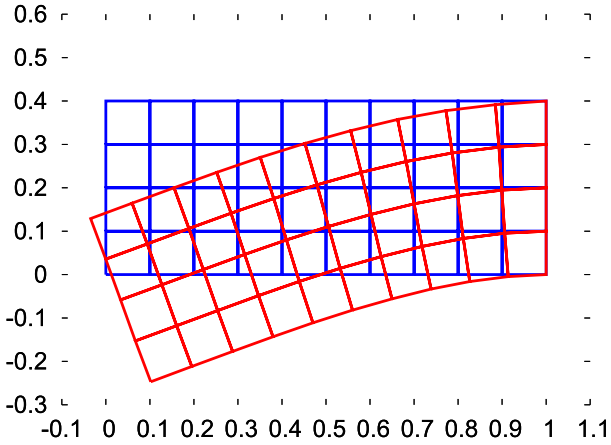

Figure 9. Motion of the beam at time $t = 8.9 \times 10^{-4}$ s.

accuracy requirements rather than stability conditions, the explicit algorithm was used in our simulations (which is significantly faster as no iterations in each time step are needed).

6. Conclusion

A fractional derivative visco-hyperelastic model for large and nearly incompressible deformations has been formulated based on irreversible thermodynamics with internal variables. The finite element framework is based on a three-field form of the Hu-Washizu principle to create a stable finite element method. The β-method (the generalized midpoint rule) for time discretization of the equation of motion and a specific semi-implicit approximation of fractional ODEs governing the evolution of the internal variables enable us to partially decouple the elastic and viscous response to simplify and speed up the numerical algorithm. The consistent linearization of the resulting system of nonlinear equations is also briefly presented.

The present work is our first step toward linking the fractional calculus and hyperelasticity. The dynamic response of a 2-D cantilever beam is computed, including both geometrically and materially nonlinear effects.

Acknowledgements

This research was supported by SGS, project number SGS23/001/OHK1/1T/11, and the Czech Science Foundation, the grant No. 22-15553S.

References

[1] R. C. Koeller. Applications of fractional calculus to the theory of viscoelasticity. *Journal of Applied Mechanics* **51**(2):299–307, 1984. https://doi.org/10.1115/1.3167616

[2] B. Hálková. *Experimentální a numerické modelování PVB folie [In Czech; Experimental and numerical modelling of PVB foil]*. Master's thesis, Czech Technical University in Prague, 2024.

[3] S. W. J. Welch, R. A. L. Rorrer, J. R. G. Duren. Application of time-based fractional calculus methods to viscoelastic creep and stress relaxation of materials. *Mechanics of Time-Dependent Materials* **3**(3):279–303, 1999. https://doi.org/10.1023/A:1009834317545

[4] J. Padovan. Computational algorithms for FE formulations involving fractional operators. *Computational Mechanics* **2**(4):271–287, 1987. https://doi.org/10.1007/BF00296422

[5] M. Enelund, L. Mähler, K. Runesson, B. L. Josefson. Formulation and integration of the standard linear viscoelastic solid with fractional order rate laws. *International Journal of Solids and Structures* **36**(16):2417–2442, 1999. https://doi.org/10.1016/S0020-7683(98)00111-5

[6] S. Müller, M. Kästner, J. Brummund, V. Ulbricht. A nonlinear fractional viscoelastic material model for polymers. *Computational Materials Science* **50**(10):2938–2949, 2011. https://doi.org/10.1016/j.commatsci.2011.05.011

[7] A. Schmidt, L. Gaul. Finite element formulation of viscoelastic constitutive equations using fractional time derivatives. *Nonlinear Dynamics* **29**(1):37–55, 2002. https://doi.org/10.1023/A:1016552503411

[8] K. Adolfsson, M. Enelund. Fractional derivative viscoelasticity at large deformations. *Nonlinear Dynamics* **33**(3):301–321, 2003. https://doi.org/10.1023/A:1026003130033

[9] J. C. Simo, T. J. R. Hughes. *Computational Inelasticity*. Interdisciplinary Applied Mathematics Volume 7. Springer New York, USA, 1998. https://doi.org/10.1007/b98904

[10] J. C. Simo, R. L. Taylor, K. S. Pister. Variational and projection methods for the volume constraint in finite deformation elasto-plasticity. *Computer Methods in Applied Mechanics and Engineering* **51**(1–3):177–208, 1985. https://doi.org/10.1016/0045-7825(85)90033-7

[11] S. N. Atluri, E. Reissner. On the formulation of variational theorems involving volume constraints. *Computational Mechanics* **5**(5):337–344, 1989. https://doi.org/10.1007/BF01047050

[12] J. C. Simo. On a fully three-dimensional finite-strain viscoelastic damage model: Formulation and computational aspects. *Computer Methods in Applied Mechanics and Engineering* **60**(2):153–173, 1987. https://doi.org/10.1016/0045-7825(87)90107-1

[13] M. Enelund, G. A. Lesieutre. Time domain modeling of damping using anelastic displacement fields and fractional calculus. *International Journal of Solids and Structures* **36**(29):4447–4472, 1999. https://doi.org/10.1016/S0020-7683(98)00194-2

[14] C. Lubich. Discretized fractional calculus. *SIAM Journal on Mathematical Analysis* **17**(3):704–719, 1986. https://doi.org/10.1137/0517050

[15] J. C. Simo, R. L. Taylor. Consistent tangent operators for rate-independent elastoplasticity. *Computer Methods in Applied Mechanics and Engineering* **48**(1):101–118, 1985. https://doi.org/10.1016/0045-7825(85)90070-2

[16] A. Prakash, K. D. Hjelmstad. A FETI-based multi-time-step coupling method for Newmark schemes in structural dynamics. *International Journal for Numerical Methods in Engineering* **61**(13):2183–2204, 2004. https://doi.org/10.1002/nme.1136

EFFECT OF GEOMETRY ON HOMOGENISED PROPERTIES OF SELECTED AUXETIC METAMATERIALS

Nataša Jošková*, Martin Doškář

Czech Technical University in Prague, Faculty of Civil Engineering, Department of Mechanics, Thákurova 7, 166 29 Prague, Czech Republic

* corresponding author: joskonat@cvut.cz

Abstract. Our study investigates the influence of geometrical parameters of two types of auxetic metamaterials on their effective properties. In particular, we focus on three-dimensional lattice structures, which we represent with discrete beam models of their respective Periodic Unit Cells (PUCs). Limiting the scope of the study to linear elasticity, we compute the effective response of PUCs by plugging the kinematic ansatz of the first-order numerical homogenisation into the strain energy expression arising from the Direct Stiffness Method and minimising the energy with respect to the periodic fluctuation field. The obtained effective stiffness matrices are post-processed to arrive at elastic parameters as Poisson's ratios coefficients, that are reported in different directions with respect to the key geometrical parameters.

Keywords: Auxetic metamaterial, first-order homogenisation, periodic unit cell, effective Poisson's ratio.

1. Introduction

Metamaterials are artificial materials with properties beyond those of materials found in nature. These properties are mainly determined by their microstructure rather than by the chemical or physical parameters of the bulk constituents from which they are made [1]. Due to technological advances in recent decades, complex microstructures of these metamaterials can be produced by manufacturing techniques such as 3D and even 4D printing [2], optical lithography [3], or electrospinning. Mathematical modelling is then needed for efficient design of metamaterials by circumventing lenghty experimental search for their optimal design.

Our study of the influence of geometry on the effective Poisson's ratio focuses on two variants of a three-dimensional auxetic metamaterial (cubic and hexagonal) proposed by Bückmann et al. [3] and shown in Figure 1. Both designs exhibit a periodic microstructure allowing us to investigate only the response of a Periodic Unit Cell (PUC) as their Representative Volume Element (RVE).

2. Geometry of investigated metamaterial

The microstructure of metamaterial is composed of arranged bow-tie structures, the geometry of which is controlled by the angle δ located between the diagonal beam of the central bow-tie structure in the upper left quadrant and the yz plane passing through its initial node, see insets on the right-hand side in Figure 2. The 3D metamaterial is created by rotating the central bow-tie structure located in the xz plane around its vertical centre beams, as shown in Figure 2. The cubic microstructure is obtained by rotation by 90°, from

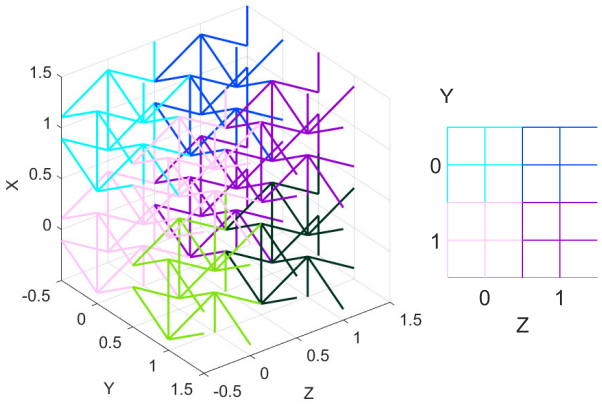

(a). Cubic variant.

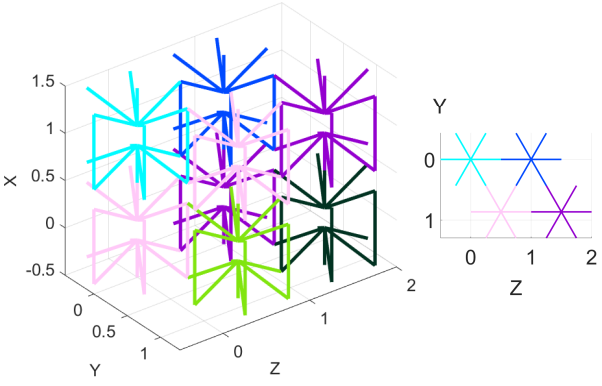

(b). Hexagonal variant.

Figure 1. Two investigated auxetic metamaterials. Insets on the right-hand side show a top view of the microstructures.

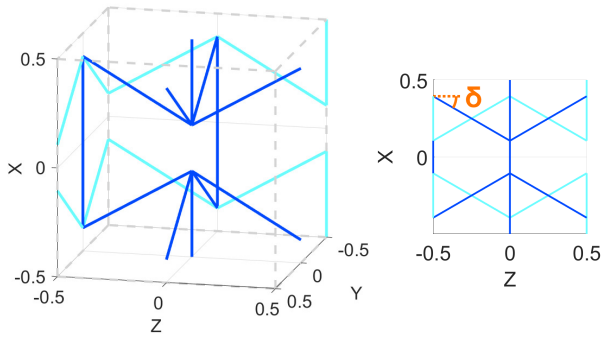

(A). Cubic microstructure.

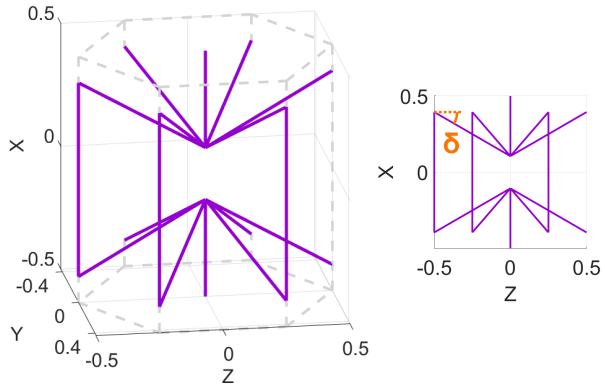

(B). Hexagonal prismatic microstructure.

FIGURE 2. Periodic Unit Cell of cubic and regular hexagonal prismatic microstructure along with their corresponding side view including angle δ, which controls the geometry of the metamaterial.

which the central structure is formed (dark blue). This central structure is complemented by a similar one (cyan) shifted by half a period in yz plane. To create the PUC of regular hexagonal prism with equal height and long base diagonal length, we perform 60° and 120° rotations of the bow-tie structure (purple). The height H of both PUCs will be considered as a single unit height.

Here, we model PUC with discrete beams; we know the position of each node and the orientation of the beams that connect them. For this study, we assume a circular beam cross-section with diameter $d = 0.1H$. Consequently, cross-sectional characteristics follow as:

$$\begin{aligned} A &= \frac{\pi}{4} \cdot d^2, \\ I &= \frac{\pi}{64} \cdot d^4, \\ J &= 2I = \frac{\pi}{32} \cdot d^4, \end{aligned} \tag{1}$$

where A is the cross-section area, I is the second moment of inertia, and J is the polar moment of inertia. The volume of PUC is for the cubic variant $V_c = H^3$ and $V_h = \frac{3\sqrt{3}}{8} \cdot H^3$ for the hexagonal one.

3. Direct stiffness method

To compute a mechanical response of the PUC model, we use a linear discrete beam model that can be described by a linear relation:

$$\mathsf{F} = \mathsf{K}\mathsf{u}, \tag{2}$$

where the vector F contains the forces and moments applied on all nodes, K is the stiffness matrix – assembled from individual submatrices K_i for each beam – and u is the displacement vector that successively contains subvectors of displacements u_i, v_i, w_i and rotations $\varphi_{x,i}$, $\varphi_{y,i}$, $\varphi_{z,i}$ of individual nodes i.

3.1. Local stiffness matrix

The local stiffness matrix K_i^l for the i^{th} beam follows from the Bernoulli-Euler beam theory [4, 5] and has size 12×12, due to the 6 unknowns located at the beginning (index b) and the end (index e) node of the beam. Individual parts that contribute to the stiffness matrix can be divided into 4 submatrices pertinent to:

(1) membrane behaviour:

$$\begin{bmatrix} X_b^l \\ X_e^l \end{bmatrix} = \frac{EA}{L_i} \begin{bmatrix} 1 & -1 \\ -1 & 1 \end{bmatrix} \begin{bmatrix} u_b^l \\ u_e^l \end{bmatrix}, \tag{3}$$

(2) bending in xy plane:

$$\begin{bmatrix} Y_b^l \\ M_{z,b}^l \\ Y_e^l \\ M_{z,e}^l \end{bmatrix} = \frac{2EI_z}{L_i} \begin{bmatrix} \frac{6}{L_i^2} & \frac{3}{L_i} & -\frac{6}{L_i^2} & \frac{3}{L_i} \\ \frac{3}{L_i} & 2 & -\frac{3}{L_i} & 1 \\ -\frac{6}{L_i^2} & -\frac{3}{L_i} & \frac{6}{L_i^2} & -\frac{3}{L_i} \\ \frac{3}{L_i} & 1 & -\frac{3}{L_i} & 2 \end{bmatrix} \begin{bmatrix} v_b^l \\ \varphi_{z,b}^l \\ v_e^l \\ \varphi_{z,e}^l \end{bmatrix}, \tag{4}$$

(3) bending in xz plane:

$$\begin{bmatrix} Z_b^l \\ M_{y,b}^l \\ Z_e^l \\ M_{y,e}^l \end{bmatrix} = \frac{2EI_y}{L_i} \begin{bmatrix} \frac{6}{L_i^2} & -\frac{3}{L_i} & -\frac{6}{L_i^2} & -\frac{3}{L_i} \\ -\frac{3}{L_i} & 2 & \frac{3}{L_i} & 1 \\ -\frac{6}{L_i^2} & \frac{3}{L_i} & \frac{6}{L_i^2} & \frac{3}{L_i} \\ -\frac{3}{L_i} & 1 & \frac{3}{L_i} & 2 \end{bmatrix} \begin{bmatrix} w_b^l \\ \varphi_{y,b}^l \\ w_e^l \\ \varphi_{y,e}^l \end{bmatrix}, \tag{5}$$

(4) torsion:

$$\begin{bmatrix} M_{x,b}^l \\ M_{x,e}^l \end{bmatrix} = \frac{GJ}{L_i} \begin{bmatrix} 1 & -1 \\ -1 & 1 \end{bmatrix} \begin{bmatrix} \varphi_{x,b}^l \\ \varphi_{x,e}^l \end{bmatrix}. \tag{6}$$

In the equations above, L_i refers to the length of a corresponding beam, E denotes Young's modulus, G stands for the shear modulus, and moments of inertia I_y, I_z are equal to I due to the circular cross-section of the beam. The local stiffness matrix K_i^l is obtained by combining the submatrices from Equations (3)–(6), each contributing to its specific degrees of freedom (DOFs).

3.2. Global stiffness matrix

The beams constituting the PUC's microstructure have different orientations. Hence, it is necessary to transform local displacements, rotations and end forces from Equations (3)–(6) into a global coordinate system. In our study, we took the approach of building a rotation matrix R_i for the i^{th} beam with Euler angles.

The beam's initial position is established by aligning its local coordinate system with the global one. Afterwards, we execute an extrinsic rotation around the global coordinate axes until the desired position is achieved. Rotation matrices:

$$\mathsf{R}_x = \begin{bmatrix} 1 & 0 & 0 \\ 0 & \cos\alpha & -\sin\alpha \\ 0 & \sin\alpha & \cos\alpha \end{bmatrix}, \tag{7}$$

$$\mathsf{R}_y = \begin{bmatrix} \cos\beta & 0 & \sin\beta \\ 0 & 1 & 0 \\ -\sin\beta & 0 & \cos\beta \end{bmatrix}, \tag{8}$$

$$\mathsf{R}_z = \begin{bmatrix} \cos\gamma & -\sin\gamma & 0 \\ \sin\gamma & \cos\gamma & 0 \\ 0 & 0 & 1 \end{bmatrix}, \tag{9}$$

determine rotation around global x, y, z axes by angles α, β, γ, respectively, while each angle stands for rotation from the latest beam's position.

To obtain the rotation matrix R_i, we perform matrix multiplication:

$$\mathsf{R}_i = \mathsf{R}_z \cdot \mathsf{R}_y \cdot \mathsf{R}_x, \tag{10}$$

where the sequence of the elements is based on order in which the beam is rotated, starting with rotation around the global x axis.

The nodal displacements and rotations are transformed on each side of the beam equally, so we can create a transformation matrix T_i by arranging the rotation matrix R_i on its diagonal:

$$\mathsf{T}_i = \begin{bmatrix} \mathsf{R_i} & 0 & 0 & 0 \\ 0 & \mathsf{R_i} & 0 & 0 \\ 0 & 0 & \mathsf{R_i} & 0 \\ 0 & 0 & 0 & \mathsf{R_i} \end{bmatrix}. \tag{11}$$

The local stiffness matrix is then transformed into a global coordinate system using the relation:

$$\mathsf{K}_i^g = \mathsf{T}_i^{\mathsf{T}} \mathsf{K}_i^l \mathsf{T}_i, \tag{12}$$

from which we obtain the global stiffness matrix K_i^g for each beam and localise them to the stiffness matrix K using Boolean localisation matrices L_i:

$$\mathsf{K} = \sum_i \mathsf{L}_i^{\mathsf{T}} \mathsf{K}_i^g \mathsf{L}_i. \tag{13}$$

4. Homogenisation

The homogenisation process substitutes a heterogeneous PUC at the microscopic level with a corresponding macroscopic constitutive model, allowing us to study the effective behaviour of the PUC when treated as a material considering its microstructure. In our study, we are using the first-order numerical homogenisation to obtain effective metamaterial properties.

4.1. Displacement decomposition

In the first-order homogenisation, the total displacement field $\vec{u}(\vec{x})$ is assumed in the form:

$$\vec{u}(\vec{x}) = \vec{u}^{\,\mathbf{E}}(\vec{x}) + \vec{u}^{\,*}(\vec{x}), \tag{14}$$

where $\vec{u}^{\,\mathbf{E}}$ denotes the macroscopic and $\vec{u}^{*}$ is the fluctuation part of the displacement field caused by the heterogeneity of the metamaterial [6]. The macroscopic part $\vec{u}^{\,\mathbf{E}}$ of the displacement field corresponds to a situation under which an entire cell composed of homogeneous material would be subjected to a constant macroscopic strain tensor $\mathbf{E}$:

$$\mathbf{E} = \begin{bmatrix} E_{xx} & E_{xy} & E_{xz} \\ E_{yx} & E_{yy} & E_{yz} \\ E_{zx} & E_{zy} & E_{zz} \end{bmatrix}, \tag{15}$$

which results in a displacement field $\mathbf{u}^{\mathbf{E}}$ given as:

$$\vec{u}^{\,\mathbf{E}}(x_i) = \mathbf{E} \cdot \mathbf{x}_i = \begin{bmatrix} u_i^{\mathbf{E}} \\ v_i^{\mathbf{E}} \\ w_i^{\mathbf{E}} \end{bmatrix}. \tag{16}$$

For the first-order homogenisation, it is further assumed that the volumetric average of the gradient of the entire displacement field $\vec{u}(\vec{x})$ corresponds to the prescribed macroscopic deformation $\mathbf{E}$. By applying the symmetric gradient operator $\nabla^s = \frac{1}{2}(\nabla + \nabla^{\mathsf{T}})$ and averaging the result over a unit cell Ω, we obtain:

$$\begin{aligned} \mathbf{E} &= \frac{1}{|\Omega|} \int_\Omega \nabla^s \vec{u}(\vec{x}) \,\mathrm{d}\vec{x} \\ &= \frac{1}{|\Omega|} \int_\Omega \nabla^s \vec{u}^{\,\mathbf{E}}(\vec{x}) + \nabla^s \vec{u}^{\,*}(\vec{x}) \,\mathrm{d}\vec{x}, \end{aligned} \tag{17}$$

where Ω represents the microscale domain of interest, being the metamaterial's macroscopic point [7].

The macroscopic part of the deformation $\vec{u}^{\,\mathbf{E}}(\vec{x})$ in Equation (16) is defined such that:

$$\mathbf{E} = \frac{1}{|\Omega|} \int_\Omega \nabla^s \vec{u}^{\,\mathbf{E}}(\vec{x}) \mathrm{d}\vec{x}. \tag{18}$$

Consequently, the fluctuation part $\vec{u}^{\,*}(\vec{x})$ of the displacement field $\vec{u}(\vec{x})$, must have a zero volumetric average gradient, i.e.:

$$\frac{1}{|\Omega|} \int_\Omega \nabla^s \vec{u}^{\,*}(\vec{x}) \mathrm{d}\vec{x} = \mathsf{0}. \tag{19}$$

For our discrete beam model, Equation (16) in a matrix form reads as:

$$\begin{aligned}\mathsf{u}_i^{\mathsf{E}} &= \begin{bmatrix} x_i & 0 & 0 & 0 & \frac{1}{2}z_i & \frac{1}{2}y_i \\ 0 & y_i & 0 & \frac{1}{2}z_i & 0 & \frac{1}{2}x_i \\ 0 & 0 & z_i & \frac{1}{2}y_i & \frac{1}{2}x_i & 0 \\ 0 & 0 & 0 & 0 & 0 & 0 \\ 0 & 0 & 0 & 0 & 0 & 0 \\ 0 & 0 & 0 & 0 & 0 & 0 \end{bmatrix} \mathsf{E} \\ &= \mathsf{Q}_i^{\mathsf{E}}\,\mathsf{E},\end{aligned} \tag{20}$$

and couples nodal DOFs with the macroscopic deformation E, which is the vectorial representation of a symmetric second-order tensor:

$$\mathsf{E} = \begin{bmatrix} E_x & E_y & E_z & \Gamma_{yz} & \Gamma_{xz} & \Gamma_{xy} \end{bmatrix}^{\mathsf{T}}. \tag{21}$$

Now we can write the original degrees of freedom u depending on the macroscopic deformation E and the fluctuation unknowns u^*. Let's define the extended displacement vector:

$$\widehat{\mathsf{u}} = \begin{bmatrix} \mathsf{E} \\ \mathsf{u}^* \end{bmatrix}, \tag{22}$$

then we can express degrees of freedom of our discrete beam model as:

$$\mathsf{u} = \begin{bmatrix} \mathsf{Q}^E & \mathsf{I} \end{bmatrix} \begin{bmatrix} \mathsf{E} \\ \mathsf{u}^* \end{bmatrix} = \mathsf{Q}\,\widehat{\mathsf{u}}, \tag{23}$$

where I is the square identity matrix and Q^E is composed of the blocks $\mathsf{Q}_i^{\mathsf{E}}$ corresponding to the expression (20).

4.2. Periodic boundary conditions

To satisfy the constraint (19), we introduce Periodic Boundary Conditions (PBC), which is a natural model assumption for materials with periodic microstructures. Let's denote $\Pi(x)$ the mapping from the source part Γ^s of the boundary Γ onto its periodic image. The fluctuation DOFs at a periodic point, denoted as $\mathsf{u}^*(\Pi(x))$, are then equivalent to the corresponding DOFs $\mathsf{u}^*(x)$ at the boundary of the unit cell Γ^s:

$$\mathsf{u}^*(\Pi(x)) = \mathsf{u}^*(x) \quad \forall\, x \in \Gamma^s. \tag{24}$$

To this end, we established a new vector a, containing unknown periodic fluctuation DOFs, which maps to u^* through the Boolean matrix P^*:

$$\mathsf{u}^* = \mathsf{P}^*\mathsf{a}. \tag{25}$$

This step significantly reduces the number of unknowns in our equations.

To prevent the PUC from moving as a whole unit during deformation, we prescribe zero fluctuation displacements at the node in the centre of the top edge of the PUC, illustrated with a black node in Figure 3, while rotations remain free. Due to the periodicity, the fluctuation displacements must also vanish at the node in the centre of the bottom face of the PUC.

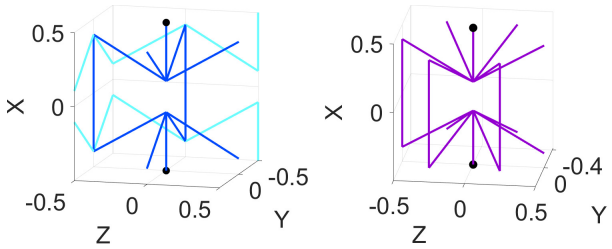

Figure 3. Fixed fluctuation displacements at nodes in the centre of the top and bottom face of the PUC, marked down with the black dots.

Similarly to Equation (23), the matrix $\widehat{\mathsf{P}}$ connects the macroscopic deformation E and the fluctuation unknowns a, to the extended DOFs $\widehat{\mathsf{u}}$:

$$\widehat{\mathsf{u}} = \begin{bmatrix} \mathsf{E} \\ \mathsf{u}^* \end{bmatrix} = \begin{bmatrix} \mathsf{I} & \mathsf{P}^* \end{bmatrix} \begin{bmatrix} \mathsf{E} \\ \mathsf{a} \end{bmatrix} = \widehat{\mathsf{P}}\,\widehat{\mathsf{a}}. \tag{26}$$

By connecting the macroscopic and fluctuation parts of the displacement field from Equation (26) and considering Equation (23) we get an expression for full-field displacement DOFs u based on unknown $\widehat{\mathsf{a}}$:

$$\mathsf{u} = \mathsf{Q}\widehat{\mathsf{P}}\,\widehat{\mathsf{a}}. \tag{27}$$

4.3. Energy minimisation

For every macroscopic deformation E, there is a certain state into which the cell deforms, because it naturally attempts to reach the state with the lowest energy.

The energy $\mathcal{E}$ of a discrete beam model, which represents our PUC composed of beams and nodes, can be written as:

$$\mathcal{E} = \frac{1}{2}\mathsf{u}^{\mathsf{T}}\mathsf{K}\mathsf{u}. \tag{28}$$

Similarly, for a linear elastic material of volume V that is subjected to a uniform deformation E at the macroscopic level, the relation for the energy can be expressed as:

$$\mathcal{E}_M = V\frac{1}{2}\mathsf{E}^{\mathsf{T}}\mathsf{D}^{\mathrm{hom}}\mathsf{E}, \tag{29}$$

where $\mathsf{D}^{\mathrm{hom}}$ is the material stiffness matrix of the desired homogenised metamaterial and vector E contains the individual macroscopic components of the deformation tensor in the vectorial form introduced in Equation (21).

Plugging the unknowns from Equation (27) into Equation (28) yields an expression for PUC's energy based on macroscopic deformations E and fluctuation unknowns a:

$$\begin{aligned}\mathcal{E}(\mathsf{E},\mathsf{a}) &= \frac{1}{2}\begin{bmatrix} \mathsf{E} \\ \mathsf{a} \end{bmatrix}^{\mathsf{T}} \begin{bmatrix} \widehat{\mathsf{K}}_{\mathsf{EE}} & \widehat{\mathsf{K}}_{\mathsf{Ea}} \\ \widehat{\mathsf{K}}_{\mathsf{aE}} & \widehat{\mathsf{K}}_{\mathsf{aa}} \end{bmatrix} \begin{bmatrix} \mathsf{E} \\ \mathsf{a} \end{bmatrix} \\ &= \frac{1}{2}\,\widehat{\mathsf{a}}^{\mathsf{T}}\widehat{\mathsf{K}}\,\widehat{\mathsf{a}},\end{aligned} \tag{30}$$

where stiffness matrix $\widehat{\mathsf{K}}$, and its four submatrices $\widehat{\mathsf{K}}_{\mathsf{ij}}$ pertinent to E and a, follow from:

$$\widehat{\mathsf{K}} = \widehat{\mathsf{P}}^{\mathsf{T}}\mathsf{Q}^{\mathsf{T}}\mathsf{K}\,\mathsf{Q}\,\widehat{\mathsf{P}}. \tag{31}$$

Since we are interested in the response of the homogenised PUC to a prescribed macroscopic deformation E and not in displacement of its individual nodes, we express a with respect to the macroscopic deformation E of the cell. To this end, we keep the macroscopic deformation E fixed and determine the fluctuation displacements a as the solution $\widetilde{\mathsf{a}}(\mathsf{E})$ that minimizes the energy $\mathcal{E}(\mathsf{E},\mathsf{a})$ for the given deformation E as:

$$\widetilde{\mathsf{a}}(\mathsf{E}) = \underset{\mathsf{a}\in\mathbb{R}^n}{\operatorname{argmin}} \frac{1}{2}(\mathsf{E}^\mathsf{T}\widehat{\mathsf{K}}_{\mathsf{EE}}\mathsf{E} + \mathsf{E}^\mathsf{T}\widehat{\mathsf{K}}_{\mathsf{Ea}}\mathsf{a} + \mathsf{a}^\mathsf{T}\widehat{\mathsf{K}}_{\mathsf{aE}}\mathsf{E} + \mathsf{a}^\mathsf{T}\widehat{\mathsf{K}}_{\mathsf{aa}}\mathsf{a}), \tag{32}$$

where n represents the number of unknown fluctuation DOFs. As a result of the matrix $\widehat{\mathsf{K}}$ being both symmetric and positive definite, the quadratic form (30) attains a global minimum at the point of its zero gradient:

$$\nabla_\mathsf{a}\mathcal{E}(\mathsf{E},\mathsf{a})\big|_{\mathsf{a}=\widetilde{\mathsf{a}}(\mathsf{E})} = \mathsf{K}_{\mathsf{aE}}\mathsf{E} + \mathsf{K}_{\mathsf{aa}}\widetilde{\mathsf{a}}(\mathsf{E}) = \mathsf{0}. \tag{33}$$

This provides us with the expression for the minimizer:

$$\widetilde{\mathsf{a}}(\mathsf{E}) = -\mathsf{K}_{\mathsf{aa}}^{-1}\mathsf{K}_{\mathsf{aE}}\mathsf{E}. \tag{34}$$

Substituting the expression above into Equation (30) yields an energy dependent entirely on the macroscopic deformations E:

$$\widetilde{\mathcal{E}}(\mathsf{E}) = \mathcal{E}(\mathsf{E},\widetilde{\mathsf{a}}(\mathsf{E})), \tag{35}$$

$$\begin{aligned}\widetilde{\mathcal{E}}(\mathsf{E}) &= \frac{1}{2}\,\mathsf{E}^\mathsf{T}(\widehat{\mathsf{K}}_{\mathsf{EE}} - \widehat{\mathsf{K}}_{\mathsf{Ea}}\widehat{\mathsf{K}}_{\mathsf{aa}}^{-1}\widehat{\mathsf{K}}_{\mathsf{aE}})\,\mathsf{E} \\ &= \frac{1}{2}\,\mathsf{E}^\mathsf{T}\mathsf{K}^{\mathrm{eff}}\mathsf{E}.\end{aligned} \tag{36}$$

Comparing the expression (36) with the formula for the energy of a homogeneous material of volume $V = |\Omega|$ subjected to a constant deformation E in the form in Equation (29), we arrive at the relation for the homogenised material stiffness of the auxetic metamaterial as:

$$\mathsf{D}^{\mathrm{hom}} = \frac{1}{V}\mathsf{K}^{\mathrm{eff}}. \tag{37}$$

4.4. Effective Poisson's ratio

The procedure introduced in the previous sections yields the whole effective stiffness matrix. However, comparing and discussing the entire stiffness matrix is cumbersome. Here, we focus on the homogenised Poisson's effect as it is the primal objective of the auxetic metamaterial.

Because our structures are symmetric in three mutually perpendicular directions, we can expect the overall orthotropic response. Consequently, there are three different values of the Poisson's ratio depending on the direction of the prescribed relative deformation. Clearly, the Poisson's ratios ν in the xy and xz planes, ν_{xy} and ν_{xz}, will be the same due to the symmetry of PUC. Furthermore, ν_{yz} and ν_{zy} should be equal for the same reason.

We will refer to the stress in the metamaterial Σ to distinguish the macroscopic level from the microscopic one. The stress-strain relation is linear because we work in the range of Hooke's law, so macroscopic stress can be written as:

$$\Sigma = \mathsf{D}^{\mathrm{hom}}\mathsf{E}, \tag{38}$$

which can be broken down into individual components as follows:

$$\begin{bmatrix}\Sigma_x\\ \Sigma_y\\ \Sigma_z\\ \Sigma_{yz}\\ \Sigma_{xz}\\ \Sigma_{xy}\end{bmatrix} = \begin{bmatrix}D_{xx} & D_{xy} & D_{xz} & 0 & 0 & 0\\ D_{yx} & D_{yy} & D_{yz} & 0 & 0 & 0\\ D_{zx} & D_{zy} & D_{zz} & 0 & 0 & 0\\ 0 & 0 & 0 & G_{yz} & 0 & 0\\ 0 & 0 & 0 & 0 & G_{xz} & 0\\ 0 & 0 & 0 & 0 & 0 & G_{xy}\end{bmatrix}\begin{bmatrix}E_x\\ E_y\\ E_z\\ \Gamma_{yz}\\ \Gamma_{xz}\\ \Gamma_{xy}\end{bmatrix}. \tag{39}$$

To determine the Poisson's ratio ν_{ij}, we perform a virtual uniaxial tension/compression experiment in which we prescribe the macroscopic strain in the i^{th} direction and compute the strain in the j^{th} direction for the requirement of zero macroscopic stress in the j^{th} and k^{th} direction. This experiment results in the following relation:

$$\widetilde{E}_j^{E_i} = \frac{D_{ik}D_{jk} - D_{ij}D_{kk}}{D_{jj}D_{kk} - D_{jk}^2}E_i. \tag{40}$$

Using (40) we can express Poisson's ratio for any direction, following its definition as a negative ratio of the derived and prescribed macroscopic strain. Consequently, the effective Poisson's ratio of an auxetic metamaterial is given by:

$$\nu_{ij} = -\frac{\widetilde{E}_j^{E_i}}{E_i} = \frac{D_{ik}D_{jk} - D_{ij}D_{kk}}{D_{jk}^2 - D_{jj}D_{kk}}. \tag{41}$$

5. Results

We parameterised the two microstructural geometries (cubic and hexagonal) from Section 2, recall Figures 1 and 2, with an angle $\delta \in (0°, 45°\rangle$. This range was chosen to avoid beams' overlaps. The numerical results comply with our assumptions of equal Poisson's ratio values in following directions:

$$\begin{aligned}\nu_{xy} &= \nu_{xz},\\ \nu_{yx} &= \nu_{zx},\\ \nu_{yz} &= \nu_{zy},\end{aligned} \tag{42}$$

see also overlapping lines in Figure 4. We observed auxetic behaviour in the whole range of δ with cubic PUC, while the metamaterial with hexagonal PUC exhibits pure auxetic properties only for angles $\delta \in \langle 10.56°, 45°\rangle$. For the lower values of δ, the metamaterial is auxetic only in the xy and xz planes, with the highest Poisson's ratio value of $\nu_{yz} = 0.33$, which leads to the lateral contraction during stretching in the yz plane.

Poisson's ratios ν_{yx} and ν_{zx} are the most influenced by the metamaterial's geometry and attain their minimum, within the investigated range of δ, from which

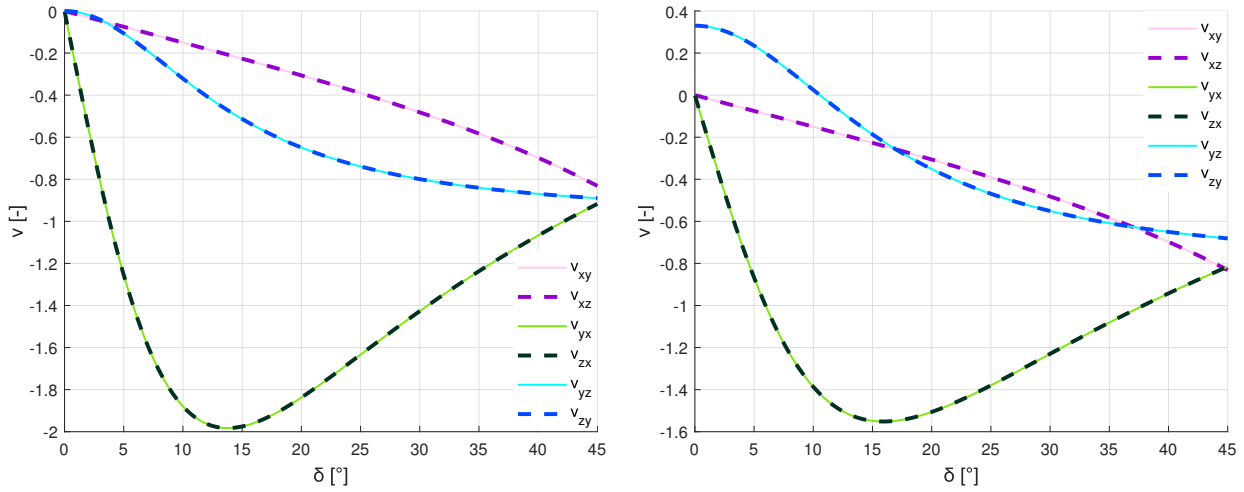

(A). Cubic microstructure. (B). Hexagonal prismatic microstructure.

FIGURE 4. Poisson's ratio as a function of angle δ for cubic and regular hexagonal prismatic microstructure.

their value starts increasing and slowly approaching remaining Poisson's ratios. Specifically, for the cubic PUC, the global minimum $\nu_{yx} = -1.98$ is achieved by the geometry of angle $\delta = 13.78°$. Hexagonal PUC exhibits its minimal Poisson's ratio of value $\nu_{yx} = -1.55$ by the angle $\delta = 15.92°$. The remaining pairs of Poisson's ratios, i.e. ν_{xy}, ν_{xz} and ν_{yz}, ν_{zy}, on the other hand, tend to decrease with the increasing angle δ across the entire range.

Additionally, we observe certain values of δ, where some Poisson's ratios coincide. In the cubic PUC, ν_{xy} and ν_{yz} attain the same value of -0.05 for $\delta = 3.32°$. The hexagonal PUC exhibits two such values of δ, $\delta = 16.96°$ and $\delta = 36.98°$, for which Poisson's ratios are equal to $\nu_{xy} = \nu_{yz} = -0.26$ and -0.63, respectively.

In addition, the hexagonal PUC have equal Poisson's ratios ν_{xy} and ν_{yx} of value $\nu_{xy} = -0.82$ at the angle $\delta = 44.71°$.

6. Conclusion

We investigated the influence of the geometry controlled by the angle δ in the bow-tie part of the microstructure on the effective Poisson's ratios of two three-dimensional metamaterials. Their PUCs were modelled with discrete beam elements, and the effective metamaterial properties were determined using Direct Stiffness Method and the first-order numerical homogenisation, resulting in a connection between their microstructure and macroscopic behaviour.

Given the symmetries of both investigated microstructural geometries, we obtain three distinct values of Poisson's ratios as functions of angle δ. Two of these values are monotonously decreasing with increasing angle δ, while the remaining value (same for ν_{yx} and ν_{zx}) exhibits a minimum within the studied range of ν. The cubic PUC features the minimum value $\nu_{yx} = -1.98$ for $\delta = 13.78°$, while the hexagonal PUC attains the minimum $\nu_{yx} = -1.55$ for $\delta = 15.92°$.

In conclusion, only the cubic PUC delivers auxetic behaviour in all directions for all investigated values of δ. The hexagonal PUC shares the same trait only for $\delta \geq 10.56°$.

Acknowledgements

This work was supported by the Grant Agency of the Czech Technical University in Prague, grant No. SGS23/032/OHK1/1T/11.

References

[1] E. Barchiesi, M. Spagnuolo, L. Placidi. Mechanical metamaterials: A state of the art. *Mathematics and Mechanics of Solids* **24**(1):212–234, 2019. https://doi.org/10.1177/1081286517735695

[2] X. Zhou, L. Ren, Z. Song, et al. Advances in 3D/4D printing of mechanical metamaterials: From manufacturing to applications. *Composites Part B: Engineering* **254**:110585, 2023. https://doi.org/10.1016/j.compositesb.2023.110585

[3] T. Bückmann, N. Stenger, M. Kadic, et al. Tailored 3D mechanical metamaterials made by dip-in direct-laser-writing optical lithography. *Advanced Materials* **24**(20):2710–2714, 2012. https://doi.org/10.1002/adma.201200584

[4] A. Kassimali. *Matrix analysis of structures*. Cengage Learning, Stamford, Australia, 2nd edn., 2012. ISBN 978-1-111-42620-0.

[5] W. McGuire, R. H. Gallagher, R. D. Ziemian. *Matrix structural analysis*. John Wiley, New York, 2nd edn., 2000. ISBN 9781507585139.

[6] J. C. Michel, H. Moulinec, P. Suquet. Effective properties of composite materials with periodic microstructure: A computational approach. *Computer Methods in Applied Mechanics and Engineering* **172**(1–4):109–143, 1999. https://doi.org/10.1016/S0045-7825(98)00227-8

[7] M. Doškář, J. Novák. A jigsaw puzzle framework for homogenization of high porosity foams. *Computers & Structures* **166**:33–41, 2016. https://doi.org/10.1016/j.compstruc.2016.01.003

PROPERTIES OF CEMENT SCREEDS USING RECYCLED FINE AGGREGATES WITH RESPECT TO CEMENT PERCENTAGE

Leoš Joura[a], Zdeněk Prošek[a,b,*]

[a] *Czech Technical University in Prague, Faculty of Civil Engineering, Department of Mechanics, Thákurova 7, 166 29 Prague, Czech Republic*

[b] *Czech Technical University in Prague, University Centre for Energy Efficient Buildings, Třinecká 1024, 273 43 Buštěhrad, Czech Republic*

[*] corresponding author: zdenek.prosek@fsv.cvut.cz

Abstract. This article deals with the effect of 100 % replacement of natural aggregate by recycled aggregate and at the same time the effect of cement percentage on the observed properties of cement screeds. For these purposes, concrete and brick recycled aggregate is used in combination with CEM I 42.5R Portland cement, constituting 10 %, 15 %, 20 % and 25 % of the mixtures weight. To determine the properties of the cement screeds, test intervals of 3, 7, 14, 21 and 28 days are set, during which changes in bulk density are monitored. Simultaneously, destructive tests are carried out on test beams of $4 \times 4 \times 16$ cm in size. The results found that the use of recycled fine aggregates allows the production of lighter cement screeds, for example, for reconstruction. Potentially usable mixes appear to be those containing 15 %, 20 % and 25 % cement compared to recycled aggregate. For the contaminated recyclate fine fraction, the flexural strength has been shown to improve. However, this improvement is not reflected in an increase in compressive strength.

Keywords: Recycled aggregate, cement screed, concrete recyclate, brick recyclate, Portland cement.

1. Introduction

Over the last few years, people's attitudes towards recycling have changed significantly. The same applies to using recycled materials and products that are becoming part of everyday life. Unfortunately, in the construction sector, the use of it is problematic. This may be due to a lack of knowledge, insufficient standards, financial disadvantages, deteriorated properties, and people's attitudes towards building materials made from recycled materials. These barriers need to be overcome as the amount of construction waste is increasing every year. At the same time, landfill space is diminishing, and the storage of recyclable waste should be banned in the Czech Republic from 2030 [1]. On the other hand, it is very problematic to meet the high demand with the existing quarries and natural aggregate deposits. Thus, the pressure to find efficient uses for construction waste is increasing. Concrete, brick, and mixed recyclates are the most commonly encountered and can be further divided into coarse (> 4 mm) and fine (0.063–4.0 mm) recycled aggregates (RFA). Coarse aggregates are already starting to be used for recycled concrete and the number of researches looking into this application is increasing [2]. However, there is very little research on the fine fraction, even though its representation in the construction waste recycling process is significant. For this reason, this article focuses specifically on the use of the fine recycled fraction for use in cement screeds, where there is some hidden potential. These screeds currently use natural sand as a filler and are used as leveling and spreading layers for floors in hall and apartment buildings. They are applied in small thicknesses, reaching a maximum thickness of 50 mm [2]. They can be distributed as dry bagged mix, wet mix, or as liquid cement screed [2]. Many manufacturers modify the properties of these screeds with various additives and admixtures to achieve faster strength increases and better workability [3].

Cement screeds are defined by ČSN EN 13318 [4]. Production is governed by EN 13892-1 [5] and the most common tests are described in ČSN EN 13892-2 [6]. In their studies of fresh mixtures using RFA, researchers also look at the following properties: air content, consistency of the mixture, and onset and end of solidification. In the case of hardened mortars, the most commonly monitored properties are: bulk density, flexural strength, compressive strength, and water absorption [7]. For the use of cement screed, a minimum safe flexural strength of 2 MPa is defined [3], and standard ČSN EN 13813 [8] separates cement screeds from 1 MPa. In the case of compressive strength, the lowest compressive strength is specified by the standard from 5 MPa [8]. For the use of cement screed as a contact leveling layer with the use of an additional floor covering, the minimum compressive strength is set at 12 MPa. For use in residential construction as a floating layer, the strength is set at 20 MPa, and for heavy use up to 30 MPa [9].

Existing research in the investigation of the fine recycled fraction uses the term cement screeds and mortars. The mixtures themselves in these investigations tend to be very similar and consist of aggregate,

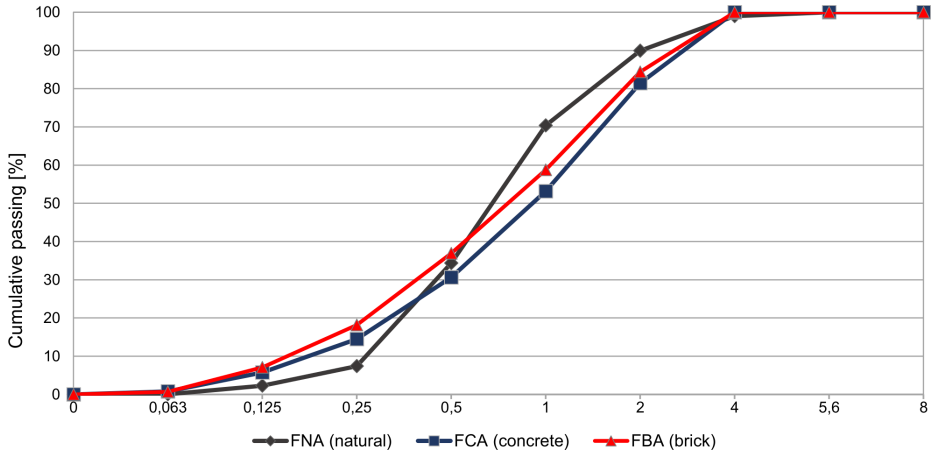

FIGURE 1. Cumulative passing.

cement, and water. For this reason, the properties of the two also agree in many respects on similar conclusions and are presented in this article. In the research carried out by Katz [7] focusing on the effect of FRA on mortars, it was found that FRA is more absorbent and therefore affects the amount of water added and thus workability. Furthermore, the quality and purity of FRA also affects the final properties, as it may contain clays, glass, and other impurities [2, 7]. More research points to deteriorating tensile and compressive strengths when using RFA [2, 7, 10, 11].

Further, some researchers agree on the conflicting results, with some studies saying that fine recycled aggregates affect the resulting mix positively and others negatively. This may be due, for example, to different approaches to incorporating absorbed water into the recycled aggregate [2, 7, 12], production process [2, 7], and the method of crushing [11].

2. MATERIALS

The recycled aggregates used in this research were supplied by company Moravostav. These are concrete recyclate (FCA) and brick recyclate (FBA). FCA was produced from clean concrete waste that was delivered from a separate demolition site and crushed using a RESTA jaw crusher. The FBA came from crushing brick rubble that was obtained from separate demolition. All these recyclates were supplied with a maximum grain size of 4 mm for production. For the reference mix, natural fine aggregate (NFA) was used, which came from the Dobříň gravel pit. For all these aggregates, their grain size curve was known (Figure 1) and also the content of pollution by washable particles (< 0.063 mm) (Figure 2). Portland cement with the designation CEM I 42.5 R from the Radotín plant was used as a binder.

3. SAMPLE PRODUCTION

Based on the mixture knowledge for cement screeds with NFA, the production ratios for mixtures using recycled fillers are shown in Table 1. This is a volume

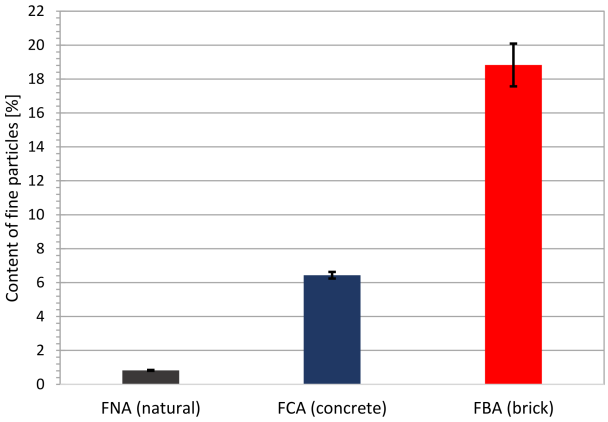

FIGURE 2. Content of fine particles.

replacement of the filler and the effect of the different percentages of cement in the mix, which was set at 10 %, 15 %, 20 % and 25 % by volume of the filler. The amount of water contained in each mixture was individually adjusted to achieve a similar consistency, which was set at 170 mm ±5 mm. For this purpose, a shaking table was used which complies with the standard ČSN EN 1015-3.

The forms used for the test beams were $40 \times 40 \times 160$ mm in size. A total of 108 beams were produced, so 3 of each mix were allocated for each test. The test dates were set at 3, 7, and 28 days for destructive tests. The actual manufacture was carried out in accordance with the procedures described in the ČSN EN 13892-1 [5]. After fabrication, the test beams were stored for 7 days in containers of water at 20 °C. They were then left in the air at 21 °C and 65 % humidity to ensure that the curing conditions were suitable for use on site.

4. EXPERIMENTAL METHODS

4.1. BULK DENSITY

Before each non-destructive and destructive test, the test beams were weighed, and their dimensions measured. From this knowledge, the wet and dry bulk

Set	Cement [kg m^{-3}]	Fine natural aggregate [kg m^{-3}]	Fine concrete aggregate [kg m^{-3}]	Fine brick aggregate [kg m^{-3}]	Water [kg m^{-3}]
REF 10	210	1 890			331
REF 15	315	1 785			307
REF 20	420	1 680			284
REF 25	525	1 575			272
C 10	210		1 531		301
C 15	315		1 446		293
C 20	420		1 361		305
C 25	525		1 276		310
B 10	210			1 531	396
B 15	315			1 446	390
B 20	420			1 361	399
B 25	525			1 276	399

Table 1. Overview of mixtures.

weights were calculated according to the scheduled test dates using the formula:

$$D = \frac{m}{V}, \tag{1}$$

where

D bulk density of saturated sample [kg m^{-3}],

m mass of the fully saturated test body [kg],

V volume of the test body [m^3].

4.2. Flexural strength

This test is based on the ČSN EN 196-1. Laboratory hydraulic press from STRASSENTEST was used for this test. The beams were placed on 2 supports spaced 140 mm apart and loaded at a speed of 3 mm min^{-1} using a non-moving part located above the center of the beam until they broke. From the force required to break the beam, flexural strength was calculated according to the formula:

$$f_t = \frac{3F_{b,\max}L_s}{2ab^2}, \tag{2}$$

where

f_t flexural strength [MPa],

$F_{b,\max}$ maximum breaking force [N],

L_s distance of supports [mm],

a beam width [mm],

b beam height [mm].

A total of 108 beams were tested in this way, from which 216 halves were created for the next test.

4.3. Compressive strength

The broken beams from the previous test were further used for the compressive strength test, which was also performed according to ČSN EN 196-1. For this test, a test press was used, which was supplemented with an insert that defined 2 areas of 40 × 40 mm. The 216 beam halves were inserted between these sections until final failure. After deduction of the maximum achieved force, the compressive strength was calculated according to equation:

$$f_c = \frac{F_{c,\max}}{A_c}, \tag{3}$$

where

f_c compressive strength [MPa],

$F_{c,\max}$ force at the moment of breakage [N],

A_c loaded area [mm^2].

5. Results and discussion

The bulk density results (Figure 3) show a gradual decrease in the bulk density of the cement mortar over time. The significant differences between the initial and final measurements are due to the decreasing amount of water in the mortar due to drying and hydration of the cement. Linear increases in the bulk weights of the mixtures with increasing cement percentage can be observed. This is due to the higher bulk density of cement, which proportionally replaces the lighter filler. The decreasing bulk density of cement mortar when substituting filler is also confirmed by Hubáček [2] in his research at FCA and also Mora-Ortiz [12], who researched the FBA.

When comparing REF, C and B mixtures, we can conclude the suitability of mixtures with recycled fine aggregate, as the differences reach values up to 300 kg m^{-3}. This is due to the higher porosity and lower bulk density of the recyclates used compared to the natural aggregate. This could be used, for example, in the reconstruction of old buildings where overloading of the structure is undesirable.

From the results on Figure 4, there is a linear increase in flexural strength for all mixes with increasing time and percentage of cement, which is the expected result. For short-term strengths, mixes using C and B with 10 and 15 % cement are even more resistant to failure compared to mixes with FNA filler. From the

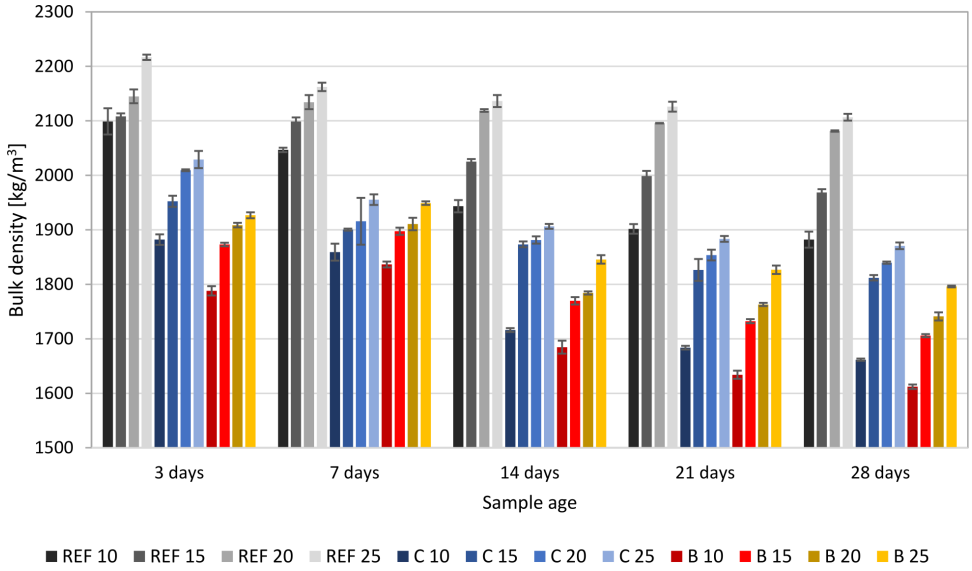

FIGURE 3. Bulk density.

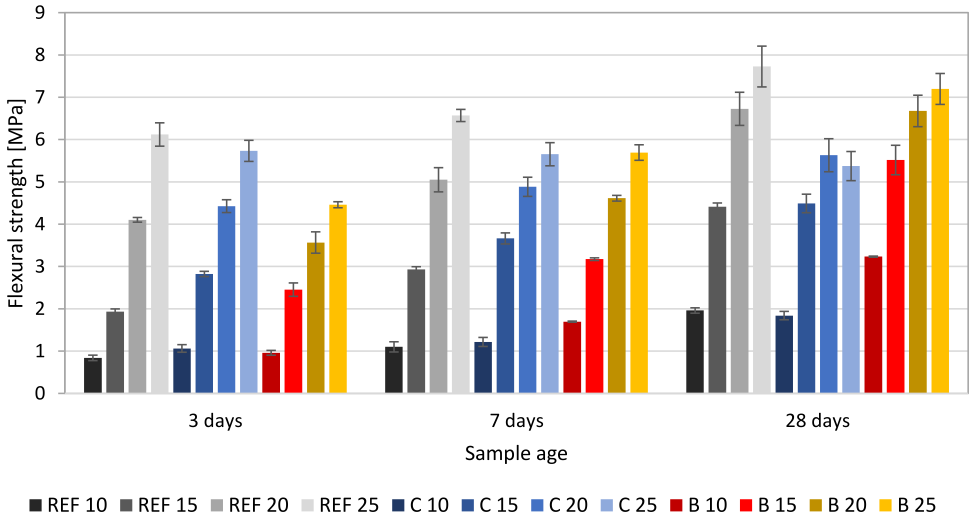

FIGURE 4. Flexural strength.

point of view of allowing light loads, mixes with B 20, B 25, C 20, and C 25 appear to be suitable after only 3 days. Looking at the strengths after 28 days, there is a more significant increase in strength for C 15, C 20, and C 25 compared to B mixes. This may be due to the higher proportion of finer grains in the delivered FBA, which is evident from Figure 2. Similar trends in the use of FCA have been achieved by Katz [7] and Hubáček [2], who also describe decreasing flexural strengths compared to reference mixtures.

Figure 5 shows the compressive strength results after 3, 7, and 28 days. The results show a linear increase in strength over time for all aggregates used. During the first 3 days, the C 15 and C 20 mixes achieve higher or equal strengths compared to the reference mixes. Mixture B achieves noticeably poorer strengths during the first 7 days compared to the others. Of note are mixes B 15 and B 25 at 28 days, which have comparable strengths to mixes C 15 and C 25. One possible explanation also according to Hubáček [2] is the effect of a higher proportion of washable particles on the filling of the space between the individual grains in the cement mortar. The effect of 100 % replacement of aggregate with fine recyclates on the inferior strengths compared to the reference mixes is also consistent with research conducted by Katz [7] and Fan [11] for concrete recyclate and Mora-Ortiz [12] for brick recyclate.

6. CONCLUSION

This article investigated the effect of fine recycled aggregate (concrete and brick) on the performance of cement screeds at 10, 15, 20, and 25 % cement content in the mix with full replacement of natural fine aggregate. Cement screeds with recycled fine aggregates have the great advantage of a lower bulk density compared to natural aggregates and can therefore be used in applications requiring low weight.

For the flexural strength, the concrete recyclate has worse strengths after 28 days compared to brick with

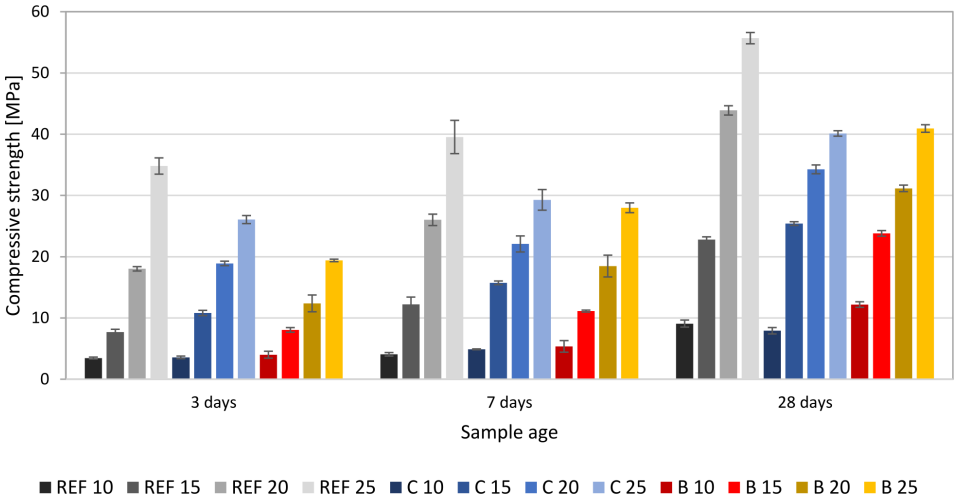

Figure 5. Compressive strength.

the same cement content. Furthermore, mixes with recyclates and at least 20 % cement content appear to be suitable for light loads within 3 days of placement. The flexural strength itself is positively influenced by the higher fraction < 0.063 mm.

The compressive strength has a negative effect when using the recycled fines fraction and the resulting strength compared to the reference mixes. Mixes containing concrete and brick recyclate and at least 25 % cement and achieving approximately the same strengths, but not the strengths of the reference mixes. Mixtures C 15, C 20, C 25, B 15, B 20, and B 25 meet the requirements for use as leveling and base layers for residential construction, as they reach compressive strengths higher than 20 MPa and flexural strength higher than 2 MPa.

Acknowledgements

This paper was financially supported by Czech Technical University in Prague under No. SGS project SGS22/089/OHK1/2T/11 and by Technology Agency of the Czech Republic under No. SS03010302. The authors also thank Moravostav for the supplied samples and materials.

References

[1] D. Vološinová, R. Kořínek, J. Kučera. Nakládání s komunálním odpadem ve světle nových předpisů [In Czech; Municipal waste management in light of new regulations]. *Vodohospodářské technicko-ekonomické informace* **63**(5):47–53, 2021. https://doi.org/10.46555/VTEI.2021.07.004

[2] A. Hubáček, L. Boehme, I. Nováková. Possibilities of recycled concrete aggregate in cement-based flowscreed. *Advanced Materials Research* **897**:247–251, 2014. https://doi.org/10.4028/www.scientific.net/AMR.897.247

[3] T. V. Oliveira, L. de Nazaré Pinheiro Cordeiro, S. A. L. Bessa. Experimental study of self-leveling mortars produced with recycled concrete aggregates. *Case Studies in Construction Materials* **17**:e01294, 2022. https://doi.org/10.1016/j.cscm.2022.e01294

[4] Úřad pro technickou normalizaci, metrologii a státní zkušebnictví. ČSN EN 13318. Potěrové materiály a podlahové potěry – Definice [In Czech; Screed materials and floor screeds – Definitions], 2001.

[5] Úřad pro technickou normalizaci, metrologii a státní zkušebnictví. ČSN EN 13892-1. Zkušební metody potěrových materiálů – Část 1: Odběr vzorků, zhotovení a ošetřování zkušebních těles [In Czech; Test methods for screed materials – Part 1: Sampling, making and curing specimens], 2003.

[6] Úřad pro technickou normalizaci, metrologii a státní zkušebnictví. ČSN EN 13892-2. Zkušební metody potěrových materiálů – Část 2: Stanovení pevnosti v tahu za ohybu a pevnosti v tlaku [In Czech; Test methods for screed materials – Part 2: Determination of flexural and compressive strength], 2003.

[7] A. Katz, D. Kulisch. Performance of mortars containing recycled fine aggregate from construction and demolition waste. *Materials and Structures* **50**(4):199, 2017. https://doi.org/10.1617/s11527-017-1067-x

[8] Úřad pro technickou normalizaci, metrologii a státní zkušebnictví. ČSN EN 13813. Potěrové materiály a podlahové potěry – Potěrové materiály – Vlastnosti a požadavky [In Czech; Screed materials and floor screeds – Screed materials – Properties and requirements], 2003.

[9] VýrobkyProStavbu.cz. Podlahové potěry II: Cementový potěr [In Czech; Floor screeds II: Cement screed], 2014. [2022-05-05]. https://www.vyrobkyprostavbu.cz/podlahove-potery-ii-cementovy-poter/

[10] H.-J. Chen, T. Yen, K.-H. Chen. Use of building rubbles as recycled aggregates. *Cement and concrete research* **33**(1):125–132, 2003. https://doi.org/10.1016/S0008-8846(02)00938-9

[11] C.-C. Fan, R. Huang, H. Hwang, S.-J. Chao. The effects of different fine recycled concrete aggregates on the properties of mortar. *Materials* **8**(5):2658–2672, 2015. https://doi.org/10.3390/ma8052658

[12] R. S. Mora-Ortiz, S. A. Díaz, E. Del Angel-Meraz, F. Magaña-Hernández. Recycled fine aggregates from mortar debris and red clay brick to fabricate masonry mortars: Mechanical analysis. *Materials* **15**(21):7707, 2022. https://doi.org/10.3390/ma15217707

LABORATORY VERIFICATION OF THE PROPERTIES OF RECYCLED FINE AGGREGATES AND THE EFFECT OF DIFFERENT REPLACEMENT PERCENTAGES ON CONCRETE PROPERTIES

Leoš Joura[a], Zdeněk Prošek[a,b,*], Aleš Palička[a]

[a] *Czech Technical University in Prague, Faculty of Civil Engineering, Department of Mechanics, Thákurova 7, 166 29 Prague, Czech Republic*

[b] *Czech Technical University in Prague, University Centre for Energy Efficient Buildings, Třinecká 1024, 273 43 Buštěhrad, Czech Republic*

[*] corresponding author: zdenek.prosek@fsv.cvut.cz

Abstract. This research work deals with the issue of laboratory testing of commonly available recycled fine aggregates, namely concrete recyclate, mixed recyclate and brick recyclate. Their geometrical properties: granulometric composition and fine particle content, including physical properties: bulk density and water absorption are investigated. The tests themselves are carried out according to available standards, which are currently mainly standards for testing natural aggregates, and it is necessary to assess the suitability of these tests for recycled aggregates as well. The results found for concrete recyclates confirm the use of these standards to obtain the properties mentioned, but the bulk density and absorption tests are inconclusive in the case of mixed and brick recyclates. Subsequently, test concrete specimens were produced in which natural fine aggregate and concrete recyclate were substituted at 33, 66 and 100 %. A series of tests were performed on the hardened concrete: bulk density, absorption, porosity and compressive strength. From the results obtained, the use of concrete recyclate in concretes with the replacement of natural fine aggregate at 33 % is suitable, without a significant reduction in the observed properties.

Keywords: Recycled fine aggregate, concrete recyclate, mixed recyclate, brick recyclate, utility properties.

1. Introduction

Nowadays, the use of recycled materials is becoming more and more popular and recycling itself is taking its place in various areas of our lives. For this reason, it is an ideal time to expand public awareness of recycled materials that can also be used in construction. The construction industry itself is a major producer of raw materials that are generated by recycling construction and demolition waste. The recycling of this waste most often results in recycled aggregates, for which it is now necessary to find a place in modern construction, where we can see, for example, concrete structures for which recycled aggregates could serve as an alternative to natural aggregates. This aggregate can be divided into a fine fraction and a coarse fraction. The coarse fraction is now often used in the production of new concrete and is supported by standards [1]. The use of recycled fine aggregate is also possible in the production of new concrete. According to the available literature, concrete [2], brick [3] or mixed recyclate from brick and concrete [4] can be used as recycled fine aggregate.

An important process in this replacement is to define the properties of the recyclate itself, which include its granulometric composition, content of washable particles, bulk density and water absorption, as it is necessary to know the material that enters the concrete production process. For this reason, CSN standards that specify test procedures for natural aggregates in concrete are used in this paper and it is necessary to evaluate the suitability of these standards for these recyclates.

Scientific studies [5, 6] have addressed the effect of concrete recyclates on concrete properties, specifically porosity, water absorption and compressive strength were tested. Another study led by Jagan Sivamani [7] investigated the effect of concrete recyclate on concrete properties. The results of this study indicated deteriorating properties with increasing percentage of replacement.

2. Materials and samples

The recycled aggregates were supplied by Moravostav a.s., which used RESTA jaw crushers for crushing construction and demolition waste. Three basic recyclates are investigated in this paper. Concrete recyclate (REC1) came from highly segregated concrete waste, Mixed recyclate (REC2) consisted of a mixture of concrete, brick waste combined with soil and Brick recyclate (REC3) consisted of pure brick waste. REC1 was selected to replace the natural fine aggregate in 33, 66 and 100 weight percent replacements for the

Set	Cement	Fine natural aggregate 0/4	Coarse natural aggregate 4/8	Coarse natural aggregate 8/16	REC1	Water
REF	300	700	538	601	0	165
R1_33	300	466	538	601	233	165
R1_66	300	233	538	601	466	165
R1_100	300	0	538	601	700	165

Table 1. Summary of concrete mix design in $\mathrm{kg\,m^{-3}}$.

impact of the recycled fine aggregate, and reference concrete (REF) was produced at the same time. Three test specimens were produced for each test set. The detailed compositions of the concretes are described in Table 1. Concrete cubes with an edge of 150 mm were used as test specimens. The concrete itself contained Portland cement with the designation CEM I 42.5 R, which came from the Mokrá plant. In addition, natural fine aggregate, defined by the 0/4 fraction, from the Dobříň gravel pit, managed by Cemex, was used. The coarse aggregate came from the Zbraslav quarry with fractions 4/8 and 8/16 used.

3. Testing recycled aggregates

The dried recyclates were weighed and then soaked in water for 24 hours. After this time, this aggregate was placed on a set of sieves where the smallest sieve was 0.063 mm and with the vibration on, the aggregate was sieved while continuously adding water. The test itself is described by EN 933-1[8] and the desired result was the percentage of washable particles. The aggregate was then dried again in an oven at 110 °C, ready for the next stage of the test described in the previously mentioned standard. In this case, this involved the determination of the granulometric composition, which resulted in a grain size curve. Furthermore, it was necessary to carry out a test to determine the bulk density and water absorption of the recycled fine aggregates, for which the standard EN 1097-6 [9] was used. The standard described the procedure for carrying out the pycnometric method to obtain several types of bulk weights (apparent, surface dried and fully saturated) and percentage of absorption of the recyclates.

4. Testing of concrete samples

The produced test specimens were unmolded after solidification and stored in containers with water. They were subsequently tested after 7 and 28 days. The first test carried out on the test specimens was the bulk density, which was measured on the fully water-saturated solids according to EN 12390-7 [10], and it was necessary to measure the dimensions of the solids themselves to obtain their volume. This was followed by a test to determine the compressive strength of the concrete, which was based on EN 12390-3 [11]. The individual specimens were surface dried and placed in a test press. The loading was carried out by a constant

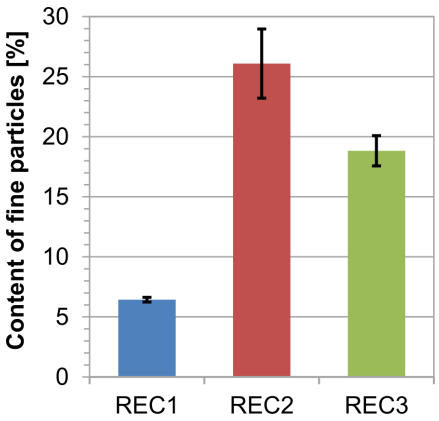

Figure 1. Content of fine particles.

increase in force until the resulting failure. The compressive strength was calculated from the maximum force achieved during the test $F_{c,\max}$ as:

$$f_c = \frac{F_{c,\max}}{ab}, \tag{1}$$

where

f_c is the compressive strength [Pa],

$F_{c,\max}$ is the maximum force [N],

a is the width of the sample [m],

b is the height of the sample [m].

5. Results and discussion

The results of the amount of fine particles can be seen in Figure 1 and, as expected, the lowest percentage of contamination came out for REC1. In the case of REC2 and REC3, the percentage of contamination already reaches significant values, indicating that these recyclates are very contaminated and their use is all the more complicated. In Figure 2 we can observe the resulting grain size curves for the tested recyclates. REC1 shows uniform gradients of the different fractions, but contains the smallest proportion of finer aggregates compared to the other two recyclates. In the case of REC2 and REC3, a more pronounced representation of grain sizes of 0.063–0.25 mm can be seen, which may be due to the higher content of fines.

In Figure 3, the results of the bulk weights can be observed. In the case of REC1, the resulting values are conclusive and very similar to, for example, the study by Cheng-Chih Fan [2]. For the other two recyclates

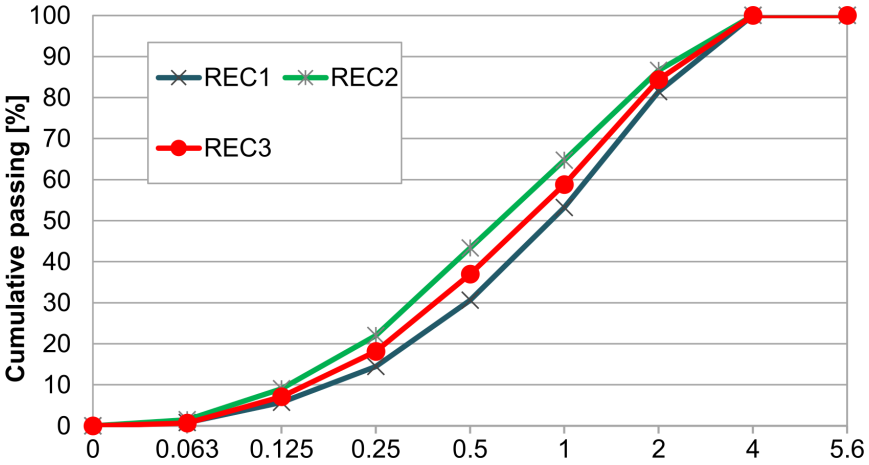

FIGURE 2. Particle size distribution.

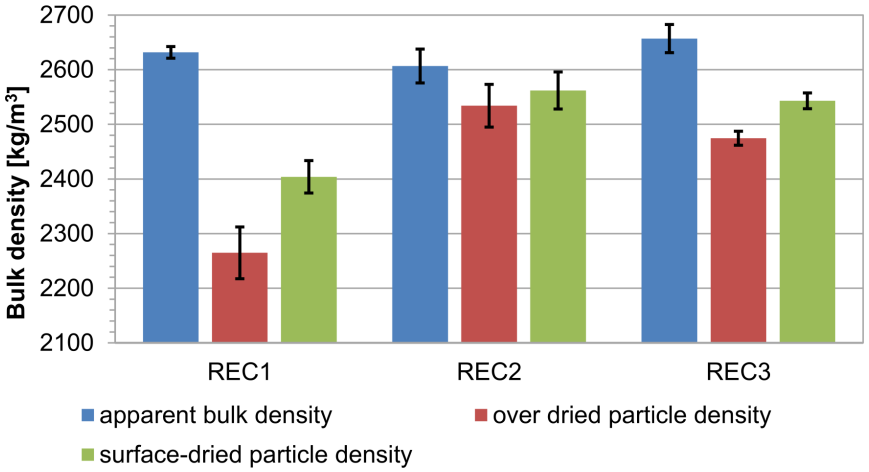

FIGURE 3. Bulk density of testing fine recycled aggregate.

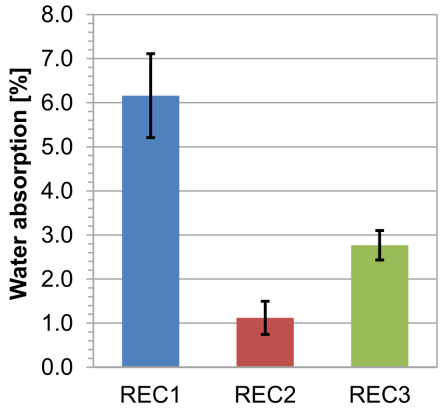

FIGURE 4. Water absorption of testing fine recycled aggregate.

REC2 and REC3, the results are considerably high, indicating the unsuitability of this test for these types of aggregates. The problem itself may be due to the difficulty in achieving the surface dried condition of the aggregate, which is the main variable of this test. Also related to the results of the bulk weights are the results of the absorption of the recyclates, which are shown in Figure 4. In relation to the previously mentioned problem, the results for REC2 and REC3 are completely inconclusive as their absorption rates are very low compared to reality. In the case of REC1, the absorption is assumed and is based on a similar basis as in the study by Gómez-Soberón [12] and therefore this recyclate can theoretically be tested according to the existing CSN standards for aggregates for concrete.

The results of the bulk weights of hardened concrete in the saturated state are shown in Figure 5. It is possible to observe a significant reduction in the bulk weights of the R1 set concretes compared to REF, and there is a linear relationship between the replacement and the bulk weight reduction itself. The same conclusion was also reached by Cheng-Chih Fan [2].

In Figure 6, the results of the compression test after 7 and 28 days can be seen. The resulting strength of REF concrete at 7 days shows lower strengths than the concrete with 33 % replacement. This may have been due to the small number of test specimens or to indiscipline in production. After 7 and 28 days, there is a rule of thumb which indicates that the compressive strength of concrete decreases as a function of replacement size, which is also confirmed by Jagan Sivamani [7].

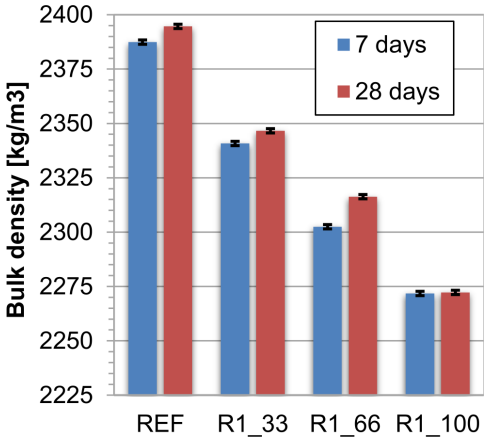

Figure 5. Bulk density of concrete specimens.

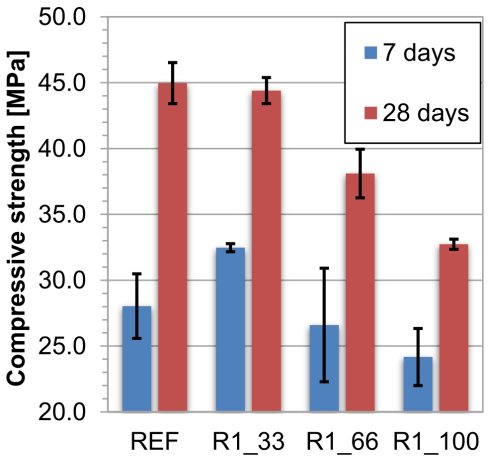

Figure 6. Compressive strength of concrete specimens.

6. Conclusion

This work was concerned with the determination of the basic properties of recycled fine aggregates, according to the available standards that apply to natural fine aggregates. At the same time, REC1 was selected, for which test bodies with 33, 66 and 100 % substitutions for natural fine aggregate were produced and the effect of these substitutions on the properties of the concrete itself was investigated. In the case of fine aggregates, it can be said that REC1 (concrete recyclate) can be tested according to current standards for aggregates in concrete. However, REC2 and REC3 are unsuitable for the application of these standards as it is difficult to achieve a surface dried condition of aggregates which affects the determination of their bulk density and water absorption. Concretes with a higher proportion of recycled fine aggregates have been shown to reduce the bulk density of concrete, which is also related to the resulting strength of the concrete. Concrete using 33 % recycled aggregate replacement is the closest approximation to the properties of the reference concrete. The 66 % and 100 % replacements are already far from the reference concrete in terms of properties.

Acknowledgements

This paper was financially supported by Czech Technical University in Prague under No. SGS project SGS22/089/OHK1/2T/11 and by Technology Agency of the Czech Republic (TA ČR) research project SS03010302. The authors also thank Moravostav for the supplied samples and materials.

References

[1] Úřad pro technickou normalizaci, metrologii a státní zkušebnictví. ČSN EN 206 +A1. Beton – Specifikace, vlastnosti, výroba a shoda [In Czech; Concrete – Specification, properties, production, and conformity], 2018.

[2] C.-C. Fan, R. Huang, H. Hwang, S.-J. Chao. Properties of concrete incorporating fine recycled aggregates from crushed concrete wastes. *Construction and Building Materials* **112**:708–715, 2016. https://doi.org/10.1016/j.conbuildmat.2016.02.154

[3] F. Debieb, S. Kenai. The use of coarse and fine crushed bricks as aggregate in concrete. *Construction and building materials* **22**(5):886–893, 2008. https://doi.org/10.1016/j.conbuildmat.2006.12.013

[4] H.-J. Chen, T. Yen, K.-H. Chen. Use of building rubbles as recycled aggregates. *Cement and concrete research* **33**(1):125–132, 2003. https://doi.org/10.1016/S0008-8846(02)00938-9

[5] L. Evangelista, J. De Brito. Mechanical behaviour of concrete made with fine recycled concrete aggregates. *Cement and concrete composites* **29**(5):397–401, 2007. https://doi.org/10.1016/j.cemconcomp.2006.12.004

[6] L. Evangelista, J. De Brito. Durability performance of concrete made with fine recycled concrete aggregates. *Cement and Concrete Composites* **32**(1):9–14, 2010. https://doi.org/10.1016/j.cemconcomp.2009.09.005

[7] J. Sivamani, N. T. Renganathan. Effect of fine recycled aggregate on the strength and durability properties of concrete modified through two-stage mixing approach. *Environmental Science and Pollution Research* **29**:85869–85882, 2022. https://doi.org/10.1007/s11356-021-14420-5

[8] Úřad pro technickou normalizaci, metrologii a státní zkušebnictví. ČSN EN 933-1. Zkoušení geometrických vlastností kameniva – Část 1: Stanovení zrnitosti – Sítový rozbor [In Czech; Tests for geometrical properties of aggregates – Part 1: Determination of particle size distribution – Sieving method], 2012.

[9] Úřad pro technickou normalizaci, metrologii a státní zkušebnictví. ČSN EN 1097-6. Zkoušení mechanických a fyzikálních vlastností kameniva – Část 6: Stanovení objemové hmotnosti zrn a nasákavosti [In Czech; Tests for mechanical and physical properties of aggregates – Part 6: Determination of particle density and water absorption], 2001.

[10] Úřad pro technickou normalizaci, metrologii a státní zkušebnictví. ČSN EN 12390-7. Zkoušení ztvrdlého betonu – Část 7: Objemová hmotnost ztvrdlého betonu [In Czech; Testing hardened concrete – Part 7: Density of hardened concrete], 2009.

[11] Úřad pro technickou normalizaci, metrologii a státní zkušebnictví. ČSN EN 12390-3. Zkoušení ztvrdlého betonu – Část 3: Pevnost v tlaku zkušebních těles [In Czech; Testing hardened concrete – Part 3: Compressive strength of test specimens], 2009.

[12] J. M. V. Gómez Soberón. Relationship between gas adsorption and the shrinkage and creep of recycled aggregate concrete. *Cement, Concrete & Aggregates* **25**(2):1–7, 2003. https://doi.org/10.1520/CCA10442J

MEASUREMENT OF TENSILE PROPERTIES OF SELECTED ROVINGS

Věra Kabíčková[a,b,*], Jakub Hájek[a,b], Jan Macháček[a,b], Eliška Kafková[a], Tomáš Vlach[a,b]

[a] *Czech Technical University in Prague, Faculty of Civil Engineering, Department of Architectural Engineering, Thákurova 7, 166 29 Prague, Czech Republic*

[b] *Czech Technical University in Prague, University Centre for Energy Efficient Buildings, Třinecká 1024, 273 43 Buštěhrad, Czech Republic*

[*] corresponding author: vera.kabickova@fsv.cvut.cz

Abstract. This article is focused on measuring the tensile properties of chosen fibre materials, such as flax, alkali resistant glass or viscose. All selected materials were tested both pure and impregnated using epoxy resin. In this article, the tensile strength and the Young's modulus were observed. Young's modulus was measured using Digital Image Correlation. The suitability of the location of small speckle pattern targets, which are used for measurements of deformations, was first verified on the viscose fiber samples. Targets were applied directly to the roving and further to the sleeves made of epoxy resin used to fix samples in the test equipment. After the evaluation, the selected location was then applied to the selected types of rovings. Finally, the measured results were compared.

Keywords: Roving, tensile strength, modulus of elasticity, digital image correlation.

1. Introduction

Civil engineering in general and especially cement production remains as one of the highest CO_2 emitters in the industrial sector. Significant efforts need to be made on promoting material efficiency and innovation in order to limit its negative impact on the environment [1]. This goes hand in hand with the development of alternative reinforcements in the form of composite and various fibers. Fiber-reinforced polymer (FRP) rebars as an alternative composite reinforcement have been considered as a non-corrosive alternative, but they are also associated with specific disadvantages [2]. Synthetic fibers such as carbon, basalt or alkali-resistant glass reach high mechanical properties, FRP rebars as a combination of epoxy resin with these fibers are logically less stiff and significantly less ductile when compared to steel rebars [3]. For the FRP reinforcements, there are several rovings (yarn) together in one rebar. Finer reinforcement from individual roving woven into technical textiles is also used as an alternative reinforcement for subtle concrete elements or in combination with traditional steel reinforcement for constructions. This type of reinforced concrete is called textile reinforced concrete (TRC). Technical textiles are usually applied without any impregnation, only with surface alkali-resistant coating, or impregnated using epoxy or polyester resin. The basic material parameter of this reinforcement in addition to the linear density of the yarn, interaction conditions and other basic information is the tensile strength of the reinforcement (single roving) and a Young's modulus of elasticity in tension. This article deals with these two basic material parameters.

For this article, which is focused on the basic tensile parameters, the procedure according to ACI 440.3R-04 about the test methods for fibre-reinforced polymers (FRP) for reinforcing or strengthening concrete structures was chosen and adapted, but due to the smaller cross-sectional area, it was more inspired by [4]. This method was developed for multi-filament yarns without any impregnation, but the same testing procedure was applied to the tensile testing of single roving with epoxy polymer matrix. To secure the samples to the testing machine epoxy sleeves on both sides of roving were used. Comparison of different methods for the determination of the modulus of elasticity of composite reinforcement produced from roving was also described in [5], the tensile strength and static modulus of elasticity were measured and calculated in [6].

2. Materials and methods

2.1. Materials and samples

For the experiment, three different fiber materials were chosen – alkali resistant glass, flax and viscose (Figure 1). Alkali resistant glass is already commonly used as a reinforcement in concrete structures, but research shows that natural fibers can also be considered as an alternative concrete reinforcement [7]. Flax has the best mechanical parameters of natural fibers. On the other hand, viscose, which is produced from natural material and is industrially compostable, has a great ductility. These materials were mutually compared.

The alkali resistant glass fibres roving CemFIL® 5325 had the length weight of 2 400 tex

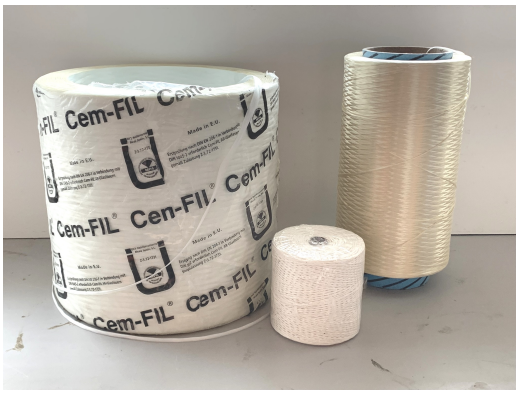

(A). Alkali resistant glass, flax and viscose fibers.

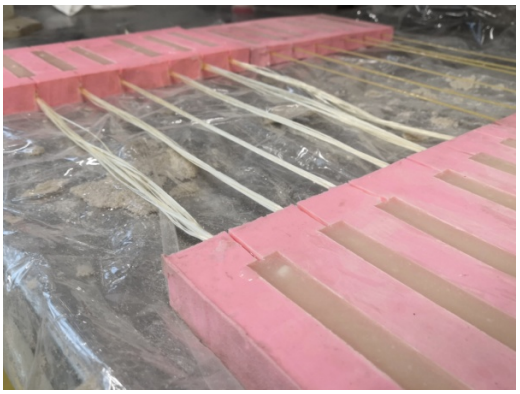

(B). Preparation of samples.

FIGURE 1. Rovings used.

Fiber type	**Specific gravity [g/cm³]**	**T [tex]**	**Tensile strength [MPa]**	**Elastic modulus [GPa]**
AR glass (Cem-FIL® 5325)	2.68	2 400	>1 000	72.0
Flax	1.40–1.50	1 680	343–2 000	27.6–103.0
Viscose	1.51	1 840	210–530	3.0–4.5

TABLE 1. Material characteristics of used roving [8–13].

(=2 400 g km^{-1}), the specific gravity of 2.68 g cm^{-3}, the tensile strength of more than 1 000 Mpa and the modulus of elasticity of 72 GPa. The theoretical maximum tensile force before breaking of all fibers at one time calculated from the technical data sheet is more than 896 N [8].

Another material used is flax. The chosen roving had the length weight of 840 tex, so two rovings were laid next to each other to reach a value of approximately 1 600 tex for better comparison [9] The primary use of natural flax roving is in the food industry, which means that there are not many mechanical properties available. In addition, its mechanical properties vary depending on many conditions, such as the production process (growth conditions, harvesting, etc.) or relative humidity. In literature, it can be found that the specific gravity is around 1.5 g cm^{-3}, the tensile strength is between 343–2 000 Mpa and the modulus of elasticity varies between 27.6–103 GPa [10, 11].

The last selected material was viscose. The viscose fibres roving Viscord® had the length weight of 1 840 tex. Viscose fibers have the specific gravity of 1.51 g cm^{-3} and usually reach the modulus of elasticity of 34 Mpa. There is a certain scatter of tensile strength, which varies between 210–530 Mpa [12, 13]. The characteristics of the materials can also be seen in Table 1.

Some rovings were impregnated with 2-part epoxy resin Sikafloor 150. The mixing ratio of Part A and Part B was 74:26 by weight [14].

To ensure fixation of the samples to the testing machine, both ends were fitted with the epoxy prisms 15 × 15 × 100 mm, as seen in Figure 1. The distance between these prisms was 300 mm. This method of preparation followed A novel tensile test device for effective testing of high-modulus multi-filament yarns by R. Rypl et al. [4].

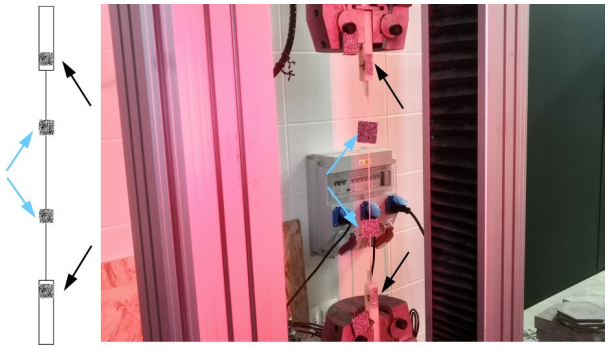

FIGURE 2. The location of the small speckle pattern targets.

2.2. EXPERIMENT

For the experiment, GALDABINI Quasar 100 hydraulic testing machine was used. The samples are fitted with small speckle pattern targets, which allows the area to be tracked, and the deformations are then calculated. For this experiment, two locations of the targets were chosen – directly to the roving (Figure 2, blue arrows) and further to the epoxy prisms (Figure 2, black arrows). The suitability of the location of these targets was first verified on the viscose fiber samples and the selected location was then applied to the other types of rovings. Especially in the case of samples without epoxy resin (pure roving), the small speckle pattern targets may rotate during the experi-

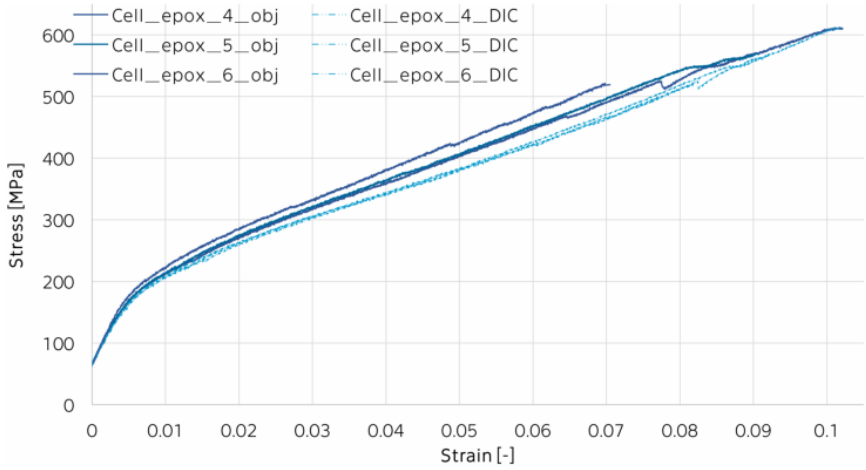

Figure 3. Comparison of chosen viscose data (DIC_obj – the targets on the prisms, DIC – the targets on the roving).

Fiber type	σ_{max} **[MPa]**	E_{DIC_roving} **[GPa]**	E_{DIC_prisms} **[GPa]**	**Deviation [%]**
Cell epox_2	610	6.93	7.67	10.8
Cell epox_3	621	7.50	8.68	15.7
Cell epox_4	612	7.21	8.18	13.4
Cell epox_5	569	6.38	7.28	14.1
Cell epox_6	521	5.42	6.80	25.3
Average	587	6.69	7.72	15.5

Table 2. Data of Tensile strength and Young's modulus of elasticity measured on the viscose samples using DIC.

ment. This may cause deviations in results, or even interruption of measurement. Speckle pattern targets on the edge of epoxy prisms do not rotate and are easily applied, but apparently will be influenced by a change of the stiffness.

The samples were tested in tension with a constant loading speed of $1\,\mathrm{mm\,min^{-1}}$ and the force and displacement were recorded. Another observed value was the Young's modulus. For the measurement of this value, DIC (Digital Image Correlation) was used. Photos taken during the experiment are then evaluated by the Istra4D software. The photos for the DIC analysis were taken in an interval of 0.5 seconds. As mentioned in the introduction, the test method was inspired by standard of American Concrete Institute ACI 440.3R-04 and adapted due to the smaller cross-sectional area. This adjustment was mostly inspired by [4] for multi-filament yarns without any impregnation and used also for the homogenized ones.

3. Results and discussion

First, the effect of the location of small speckle pattern targets was measured. In previous measurements an extensometer was used for the alkali resistant glass roving and results were similar [15]. Using extensometer is more reliable, because it does not matter whether the roving rotates during the loading process. But also it is more demanding and can't be used at pure rovings because of the damage of fibers during the installation. In contrast with extensometer, using DIC is easier, but the setup of the experiment must be more thorough. One the other hand, it is possible to measure a larger number of samples in a short time. But there is another problem associated with DIC and that is the location of the targets – when the targets are on the roving, as previously mentioned, they tend to rotate during the experiment (as seen in Figure 2 on the upper target) and there is a risk that the DIC camera would stop measuring due to the loss of the targets. Placing the targets on the epoxy prisms would solve this problem ever since it cannot rotate, on the other hand final results can be affected by many other influences (such as the effect of the supports). In this part of the article, the impact of targets' location was first verified on the viscose fibers rovings. According to the technical data sheet, the viscose has the highest elongation and seems to be the best for this verification.

Figure 3 shows that the courses of the curves are similar, but the slopes of the curves measured from prisms are steeper. In Table 2, the results of measurements are presented. We can see a comparison of the Young's modulus and the deviation from the values measured from rovings despite the fact that the targets were placed on the edge of the epoxy prism. The values measured from prisms are higher than from roving and the average deviation is 15.5 %. This deviation is caused by higher stiffness of the prisms. It can also be seen Table 2 that the deviation fluctuates

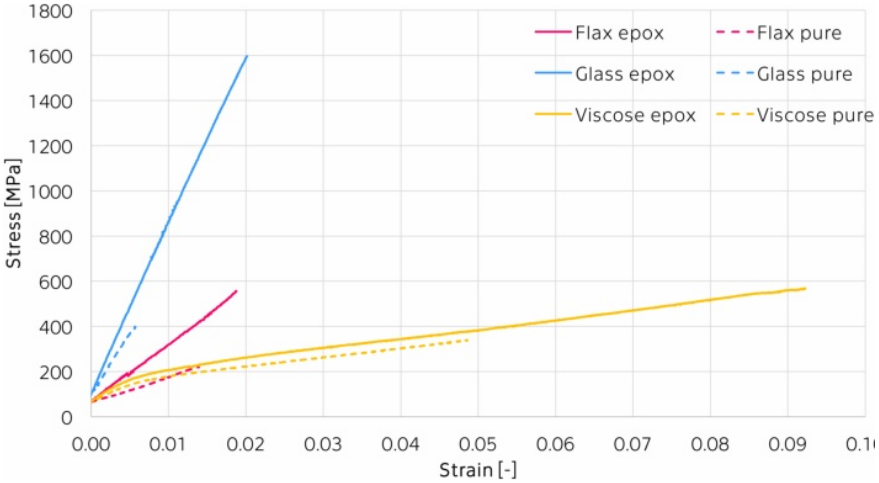

FIGURE 4. Stress-strain chart of chosen samples of pure and impregnated rovings.

Fiber type	σ_{max} **[MPa]**	**E [GPa]**
Flax epox	522	25.93
Flax pure	126	8.10
Glass epox	1 534	75.03
Glass pure	390	52.05
Viscose epox	587	6.69
Viscose pure	389	5.86

TABLE 3. Average data of Tensile strength and Young's modulus of elasticity.

significantly. Placing the targets on the epoxy prisms is therefore not very reliable.

Afterwards, all types of rovings, both pure and impregnated, were measured using DIC and, according to the results above, the targets were placed directly to the rovings. The results in the Figure 4 and Table 3 shows that the pure rovings reach lower strength and stiffness than the impregnated rovings. It is caused by the fact, that the stress cannot be transmitted through the whole cross-section of roving as in the case of the impregnated roving. All fibrils, thanks to the epoxy resin homogenization, then collapse at once.

It was also found that values of impregnated alkali resistant glass rovings are closer to those in the literature compared to the pure ones (measured Young's modulus of pure glass roving is 52 GPa, measured Young's modulus of impregnated glass roving is 75 GPa and the value of the Young's modulus in the literature is 72 GPa). However, this conclusion cannot be applied to all types of fibers. Since mechanical properties of natural fibers depend on many conditions (in addition, in the case of viscose fibers, many mechanical properties are not available), most of the measured values fit within the range of values in the literature.

The highest Young's modulus reach glass fibers with the value of 75 GPa, the lowest reach viscose fibers with the value of 6.7 GPa. This seems to be significantly lower, on the other hand, viscose fibers show by far the highest ductility, which may be useful in terms of reinforced concrete.

4. CONCLUSION

As expected, pure rovings without epoxy resin have significantly worse results, because there are gradual violations of individual fibrils. Similar behavior like presented results happens inside of the concrete matrix with textile reinforcement produced from rovings. In the textile reinforcement without impregnation, there is no full saturation of roving by cementitious particles and the fibrils collapse gradually. This leads to a reduction in load-bearing capacity, but to an increase and better behavior in ductility. The suitability of the use of pure, partially, or fully homogenized roving is determined by the specific applications and requirements.

Presented comparison of the selected materials was also more or less expected. The best potential as a reinforcement of concrete has alkali resistant glass roving, which has a relatively high Young's modulus of elasticity and is able to capture a possible crack initiation in concrete quickly. Also, flax has an interesting value of the elastic modulus, which is approximately similar to the static modulus of traditional concrete. This means that a large amount of reinforcement would have to be in the cross-section of the bend stressed element to bridge the crack. Due to the very low modulus of elasticity, viscose has almost no potential as a reinforcement in concrete elements, although the value of tensile strength is satisfactory.

ACKNOWLEDGEMENTS

The work on this paper was supported by Czech Science Foundation Grant No. 22-14942K entitled "Possibilities of using natural fibers for the production of hybrid textile reinforcement in concrete". The authors would like to acknowledge all financial assistance provided to support this research.

References

[1] E. Benhelal, G. Zahedi, E. Shamsaei, A. Bahadori. Global strategies and potentials to curb CO_2 emissions in cement industry. *Journal of Cleaner Production* **51**:142–161, 2013. https://doi.org/10.1016/j.jclepro.2012.10.049

[2] L. Yan, N. Chouw. Natural FRP tube confined fibre reinforced concrete under pure axial compression: A comparison with glass/carbon FRP. *Thin-Walled Structures* **82**:159–169, 2014. https://doi.org/10.1016/j.tws.2014.04.013

[3] Z. Achillides. *Bond behaviour of FRP bars in concrete*. Ph.D. thesis, University of Sheffield, 1998. [2023-07-27]. https://etheses.whiterose.ac.uk/14698/

[4] R. Rypl, R. Chudoba, U. Mörschel, et al. A novel tensile test device for effective testing of high-modulus multi-filament yarns. *Journal of Industrial Textiles* **44**(6):934–947, 2015. https://doi.org/10.1177/1528083714521069

[5] T. Vlach, L. Laiblová, A. Chira, et al. Comparison of different methods for determination of modulus of elasticity of composite reinforcement produced from roving. *Advanced Materials Research* **1054**:104–109, 2014. https://doi.org/10.4028/www.scientific.net/amr.1054.104

[6] T. Bittner, P. Bouška, M. Kostelecká, M. Vokáč. Experimental investigation of mechanical properties of textile glass reinforcement. *Applied Mechanics and Materials* **732**:45–48, 2015. https://doi.org/10.4028/www.scientific.net/AMM.732.45

[7] M. S. Ahamed, P. Ravichandran, A. R. Krishnaraja. Natural fibers in concrete – A review. In *IOP Conference Series: Materials Science and Engineering*, vol. 1055, p. 012038. 2021. https://doi.org/10.1088/1757-899X/1055/1/012038

[8] Owens Corning Composites. Cem-fil® 5325. [2023-01-02]. https://www.owenscorning.com/en-us/composites/product/cem-fil-5325

[9] JUTA Zemědělství/zahrada. Lněné potravinářské motouzy – cívky [In Czech]. [2023-01-02]. https://www.juta-zemedelstvi-zahrada.cz/obalove-materialy/komercni-motouzy/lnene-potravinarske-civky

[10] L. Yan, N. Chouw, K. Jayaraman. Flax fibre and its composites – A review. *Composites Part B: Engineering* **56**:296–317, 2014. https://doi.org/10.1016/j.compositesb.2013.08.014

[11] D. B. Dittenber, H. V. S. Gangarao. Critical review of recent publications on use of natural composites in infrastructure. *Composites Part A: Applied Science and Manufacturing* **43**(8):1419–1429, 2012. https://doi.org/10.1016/j.compositesa.2011.11.019

[12] N. Graupner, F. Sarasini, J. Müssig. Ductile viscose fibres and stiff basalt fibres for composite applications – An overview and the potential of hybridisation. *Composites Part B: Engineering* **194**:108041, 2020. https://doi.org/10.1016/j.compositesb.2020.108041

[13] H. Faulstich, A. Mally. *Textile Faserstoffe: Beschaffenheit und Eigenschaften*, chap. Mechanische Eigenschaften, pp. 157–230. Springer, Germany, 1993. https://doi.org/10.1007/978-3-642-77655-7_5

[14] SIKA. *Sikafloor®-150 [In Czech]*. [2022-12-04]. https://cze.sika.com/cs/produkty-pro-stavebnictvi/podlahy/penetrace/sikafloor-150.html

[15] J. Hájek, T. Vlach, J. Řepka, V. Žďára. Verification of material characteristic of natural fibers for concrete reinforcement. In *Acta Polytechnica CTU Proceedings*, vol. 47, p. 42–46. Czech Technical University in Prague, 2024. https://doi.org/10.14311/app.2024.47.0042

NUMERICAL MODELING OF CONCRETE BEAMS SUBJECTED TO PARTIAL WETTING AND DRYING CYCLES

Štěpán Krátký*, Petr Havlásek

Czech Technical University in Prague, Faculty of Civil Engineering, Department of Mechanics, Thákurova 7, 166 29 Prague, Czech Republic

* corresponding author: 1kratkystepan@gmail.com

Abstract. Concrete structures are commonly subjected to cycles of wetting and drying, which can have a significant impact on their behavior. However, experimental data on the effects of wetting and drying on concrete beams are scarce. This study presents the results of a 4-year experimental program on 2.5 m span concrete beams with heights of 100 mm, 150 mm, and 200 mm subjected to one-sided wetting and drying cycles. Vertical deflection of the beams was monitored throughout the experiment, and moisture mass balance was measured on companion specimens.

The behavior of the specimens was experimentally assessed, and subsequently numerical models using coupled hygromechanical finite element simulations were developed. The purpose of the simulations was to verify the prediction capabilities of the established constitutive models for moisture transport and creep and shrinkage of concrete and, if needed, to propose necessary corrections to the constitutive models.

Keywords: Concrete, creep, shrinkage, drying, cyclic temperature, modeling.

1. Introduction

Although the effects of moisture on the time-dependent behavior of concrete have been studied for decades, existing data are typically limited to cases where the concrete element is exposed to constant air humidity uniformly across the whole surface [1–4]. However, in reality, structural members are frequently subjected to cycles of highly variable ambient conditions. Data are scarce for cycles of contact with water and subsequent exposure to air, and/or the influence of sunlight [5–7], and focus primarily on axial strain.

In 2019, an extensive experimental campaign was initiated at the CTU in Prague to study the time-dependent behavior of structural concrete exposed to drying conditions [8]. All samples were prepared from a single concrete batch and cured for one month. The key component was a set of simply supported plain concrete beams of various sizes $L = 1.75$–3.0 m, $h = 0.05$–0.2 m and sealing setups which influenced not only the drying rate, and the development of vertical deflection, but also the degree of internal restraint and thus the extent of damage.

A set of spare specimens was used to investigate the effects of one-sided wetting and drying cycles. Within the experiment, deflection of simply supported beams with heights of 100, 150, and 200 mm and a span of 2.5 m was measured. After one year of drying, beams were placed inside a tank and repeatedly partially immersed (≈ 25 mm). The measurement results revealed that the response in the individual cycles varies depending on the number of previous cycles and the moisture content of the specimens. The data suggest that the members may undergo irreversible changes.

This paper summarizes the methods and results of the first author's master's thesis [9]. The first part describes the computational models, the second part presents the results of the blind prediction and the constitutive models employed, which aimed to understand the modeled problem and assess the predictive capabilities of the material models. The final part shows selected results from the refined simulations, which were designed to replicate the course of the experiment more accurately, and to identify potential causes of the variable behavior of the specimens between individual cycles.

2. Numerical modeling

A weakly coupled computational approach was used to model the moisture-induced structural response. Two sets of computational models were created for simulations:

(1.) Beams with different heights (as shown in Figures 1 and 2),

(2.) companion specimens used to measure the moisture content that did not consider the structural response.

The OOFEM finite element solver [10] was used to run all numerical simulations.

A finite element mesh of the beams and accompanying specimens represents a symmetric quarter of the real specimen. Suitable boundary conditions are defined on the symmetry planes to impose symmetric behavior (zero moisture flux and zero out-of-plane displacement). The mesh is finer near the surfaces, with an edge element thickness of 2 mm, to improve the convergence of computation and to capture the

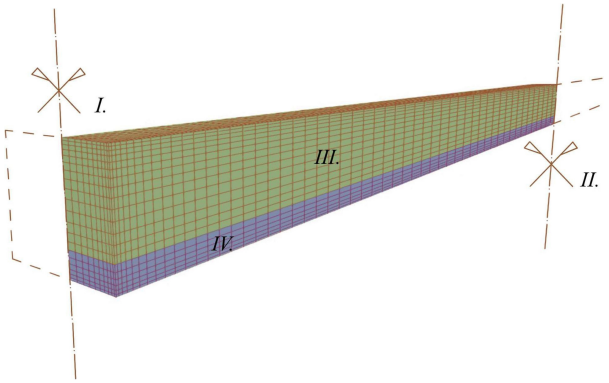

(I.) Longitudinal plane of symmetry,
(II.) mid-span plane of symmetry,
(III.) continuously exposed area to air,
(IV.) cyclically submerged area.

Figure 1. Outline of the moisture transport (MT) model.

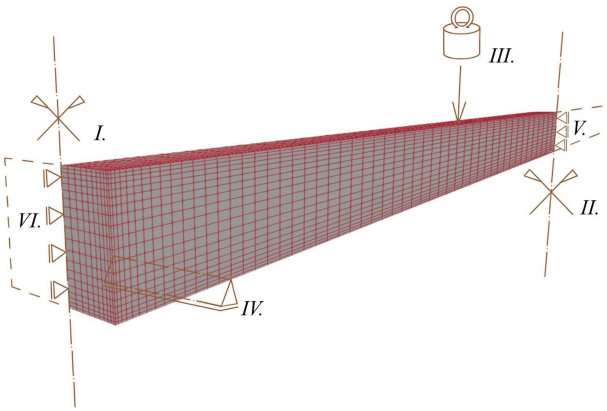

(I.) Longitudinal plane of symmetry,
(II.) mid-span plane of symmetry,
(III.) auxiliary weight,
(IV.) pin support,
(V.) mid-span symmetry BC,
(VI.) longitudinal symmetry BC.

Figure 2. Outline of the mechanical response (SM) model.

expected strong nonlinear behavior of the moisture profile.

For numerical simulations, the primary time step length is chosen to be 0.5 days. To improve convergence at the beginning of the simulations and humidity cycles, the step length is substantially reduced to 10^{-4} days and then gradually increased with a geometric progression until it reaches the primary step length.

The evolution of ambient humidity is shown in Figure 3. Experimental data indicate that the rate of wetting is much higher than the rate of drying. To realistically capture this phenomenon, during wetting cycles, the surface factor f, which appears in the mixed boundary condition for moisture transfer, is set to a large number to effectively become a Dirichlet boundary condition. Otherwise, its value is set to 1 mm/day.

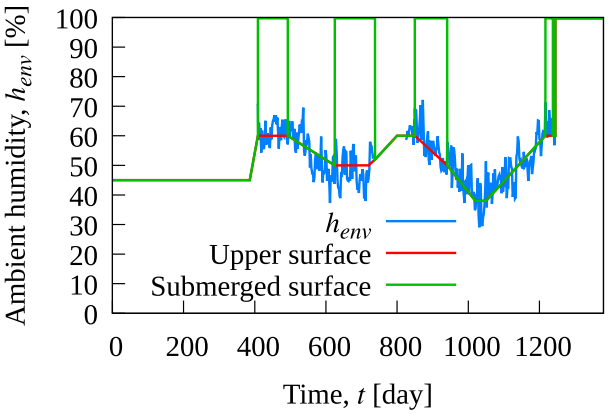

Figure 3. Measured (blue) and simplified (red) evolution of ambient relative humidity, wetting cycles assigned to the immersed portion are shown in green.

3. Blind prediction

3.1. Constitutive models

In the blind prediction, the transport of moisture in concrete is described by a widely accepted model proposed by Bažant and Najjar [11] that assumes a linear sorption isotherm. In the present case, the moisture capacity is set to 130 kg m^{-3} (see Figure 4). With this assumption, the governing equation for a diffusion of water vapor simplifies to:

$$\frac{\partial h}{\partial t} = \nabla \cdot (C(h) \nabla h)\,, \tag{1}$$

where

$\nabla\cdot$ is the divergence operator,

∇h is the gradient of relative humidity,

$C(h)$ is the humidity-dependent diffusivity.

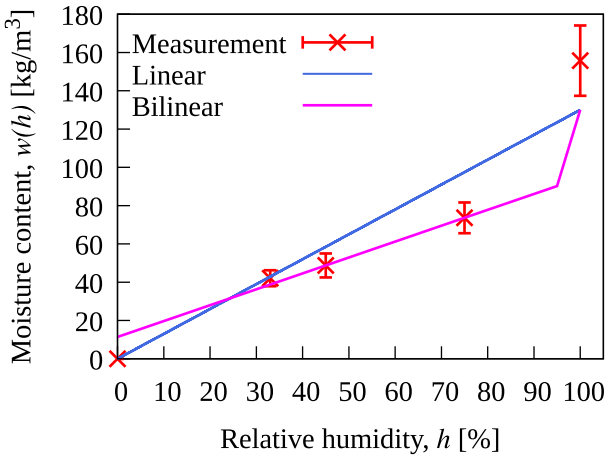

Figure 4. Experimental data of the sorption isotherm and its linear and bilinear approximation used in the blind prediction and calibrated model, respectively.

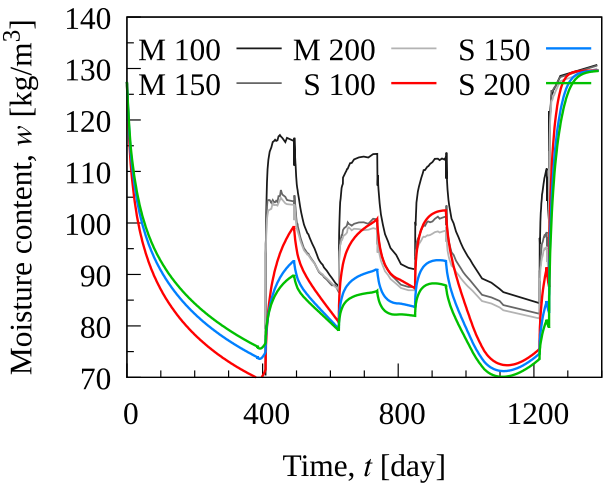

FIGURE 5. Evolution of the average moisture content in the companion specimens (M – measurement in grey scale) and in the blind prediction (S – simulation in colors). The numbers in the legend denote the height of the specimens. The time t corresponds to the material age.

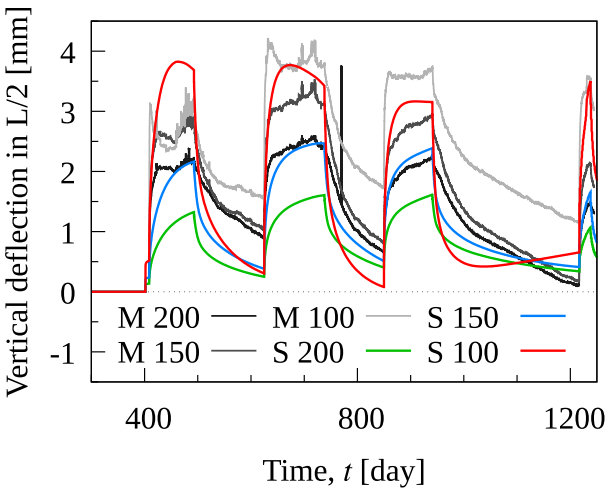

FIGURE 6. Evolution of vertical mid-span deflection of beams in the experiment (grey scale) and in the blind prediction (colors). The numbers in the legend denote the height of the beams. The time t corresponds to the material age.

The model parameters are prescribed according to the recommended values in the *fib* Model Code 2010 [12] from the compressive strength of concrete.

The mechanical behavior of concrete is described by a Microprestress-solidification (MPS) theory [13] modified to diminish the size-effect on drying shrinkage [14]. Under hygrally sealed conditions and constant room temperature, this model reduces to the basic creep compliance function of the B3 model [15] whose parameters $q_1 - q_4$ were estimated from the composition of the concrete mixture.

Changes in relative humidity give rise not only to volume changes (shrinkage/swelling) but also to further creep (Pickett effect). This additional creep is primarily controlled by the parameter k_3 [14]. Shrinkage strain and relative humidity are linearly linked via their rates:

$$\dot{\varepsilon}_{\mathrm{sh}} = k_{\mathrm{sh}} \dot{h}, \tag{2}$$

where k_{sh} is a material parameter usually treated as a humidity- and age-independent constant. In the initial blind prediction, the parameters of the MPS model k_3 and k_{sh} were calibrated to match the evolution of shrinkage and drying creep given by the (cross-sectional) B3 model.

3.2. Evolution of moisture content

Figure 5 shows the measured and predicted evolution of the average moisture content related to the total volume of the individual specimens. Since the initial state is not known exactly, the vertical offset of the experimental measurements is determined by setting the last part of this evolution (which corresponded to a fully submerged condition and almost saturated state) to $130\,\mathrm{kg\,m^{-3}}$. Comparison of the blind prediction to the experimental data demonstrates that even though the drying rate is captured quite accurately, the rate of moisture intake during the wetting stages is significantly underestimated. Additionally, the moisture balance in the individual drying and wetting cycles is less than the measured values. This implies that the moisture capacity and/or the portion of the specimen that experiences wetting is underestimated. The latter statement is supported by the distribution of relative humidity over the cross section (not presented here), which shows that the fully saturated state is only at the boundary. Only 2 mm from the surface, the humidity drops to 97.9 %.

3.3. Mechanical response

Figure 6 presents the evolution of the mid-span deflection of the concrete beams subject to drying and wetting cycles. The readings are zeroed with respect to the instant just before applying the self-weight whose contribution to the overall deflection is negligible compared to the swelling- and shrinkage- induced strains. The positive sign corresponds to downward deflection. In the figure, the experimental measurements (series M) on the three beams with different heights of 100, 150, and 200 mm are shown in gray scale while the blind prediction of the FEM simulation (series S) is drawn in colors.

Considering the fact that the presented results are truly the results of a blind prediction, the agreement with the experimental data can be considered promising. During wetting cycles, graphical postprocessing revealed that the evolution of the moisture field in the lower part of the cross section is very similar for all three cross-section heights, which in turn implies that the swelling action is also similar.

The computed data series are in correct order and correspond with the experiment; the highest deflection

is observed in the specimen with the smallest height of the cross section (and thus bending stiffness) and vice versa. A stiffer cross section providing stronger internal restraint produces higher magnitudes of self-equilibrated internal stresses.

Since the moisture intake rate was underestimated in the transport model, the mechanical response is also lagging behind the experiment. However, during drying, the computed deflection tends to return faster to the initial position than what is observed in the experiment. The contribution of creep to the total deflection is rather small, as demonstrated by the computed deflections at the end of the drying cycle.

Graphical post-processing of the mechanical analysis also revealed that shortly after the onset of wetting or drying, tensile stresses that exceed the tensile strength develop. The origin of these stresses stems from a highly variable field of eigenstrains produced by swelling or shrinkage which need to be balanced by a self-equilibrated normal stresses. The results obtained from an additional analysis in which tensile cracking was introduced using the concept of damage mechanics have shown that cracking leads to an increase in irreversible deformation at the end of the drying cycles.

4. Improved modeling approach

The results of the blind prediction with Bažant-Najjar model have shown that this approach does not give a realistic response when modeling drying and wetting cycles in which the concrete is in direct contact with the water. The primary reason for insufficient variation in moisture content is the presence of a linear sorption isotherm, which might be sufficient when modeling monotonous drying. To alleviate this problem, a nonlinear isotherm with a higher moisture capacity needs to be considered when approaching free saturation. However, the combination of Bažant-Najjar model with nonlinear isotherm would have led to an unrealistic response. For this reason, a more advanced constitutive model proposed by Künzel [16] is adopted instead. This model was developed and validated for transport tasks similar to those in the case of the experiment presented.

With the assumption of constant temperature and zero moisture sink, the moisture balance equation reads:

$$\frac{\partial w}{\partial h}\cdot\frac{\partial h}{\partial t}=\nabla\cdot\left[\left(D_w\frac{\partial w}{\partial h}+\delta_p p_{\mathrm{sat}}\right)\nabla h\right], \quad (3)$$

where

w is the moisture content,

D_w is the capillary transport coefficient [$\mathrm{m^2\,s^{-1}}$],

δ_p is the water vapor permeability,

p_{sat} is the saturation vapor pressure.

The expression for the transport coefficient that is dominant at higher values of relative humidity – and so in the present case – reads:

$$D_w=3.8\left(\frac{A}{w_f}\right)^2 1000^{\frac{w}{w_f}-1}, \quad (4)$$

where

A is the water absorption coefficient, with typical values ranging between 0.1–1.0 $\mathrm{kg\,m^{-2}\,day^{-0.5}}$,

w_f is the moisture content at free saturation.

The water vapor permeability of the building material that becomes more significant than the capillary transport at lower levels of relative humidity is defined as:

$$\delta_p=\frac{\delta}{\mu}, \quad (5)$$

where

δ is the water vapor permeability in air,

μ is the water vapor diffusion resistance factor.

4.1. Evolution of moisture content

The calibration procedure of the model for moisture transport was complicated by the fact that the evolution moisture content was unknown during the first 408 days of drying when the short companion specimen was cut from the beam, which was then used to measure vertical deflection. For this reason, the calibration can be based only on the moisture balance during the three wetting and drying cycles and the final stage when the companion specimens were immersed in water until their weight stabilized.

The best agreement was obtained with the bilinear sorption isotherm shown in Figure 4 and parameters $A=0.85\,\mathrm{kg\,m^{-2}\,day^{-0.5}}$ and $\mu=250$. It should be noted that the measured data were adjusted to compensate for the rather high content of macropores estimated as 10 %. The three sizes of companion specimens were used for calibration, but a higher weight was given to the smallest size 100 mm (Figure 7) as it was represented by three samples. Compared to the blind prediction, the rate of moisture uptake became significantly accelerated with the Künzel model.

Several snapshots of the graphical postprocessing showing the distribution of relative humidity over the symmetric half of the cross-section with height of 100 mm is shown in Figure 8. The state at the beginning and end of the first wetting cycle is shown in the first two pictures, the red color corresponds to the relative humidity 100 % and the blue color to 45 %. Initially, the relative humidity profile is extremely non-linear and the progress of wetting is very fast. At the end of the wetting cycle, the bottom half of the 100 mm cross-section is almost saturated. The wetting process is much more dominant than drying, the relative humidity has risen to $\approx 70\,\%$ even in the vicinity of the drying surfaces. At the end of the first drying cycle the distribution of relative humidity changes to nicely symmetric with $\approx 65\,\%$ in the core.

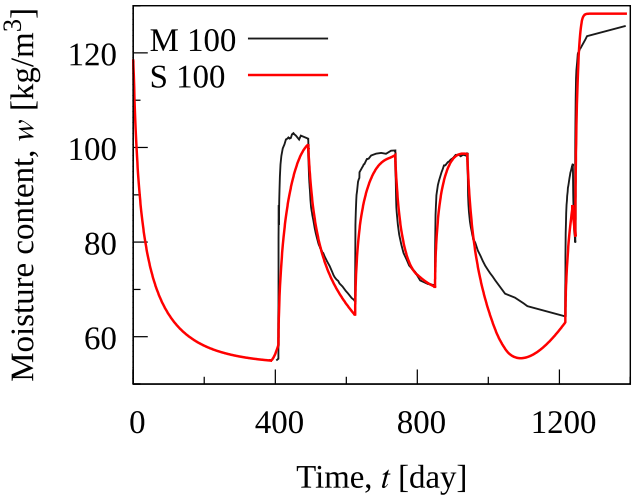

FIGURE 7. Evolution of the average moisture content of the accompanying prism with height of 100 mm. Response of the calibrated model is shown in red, measurement in grey.

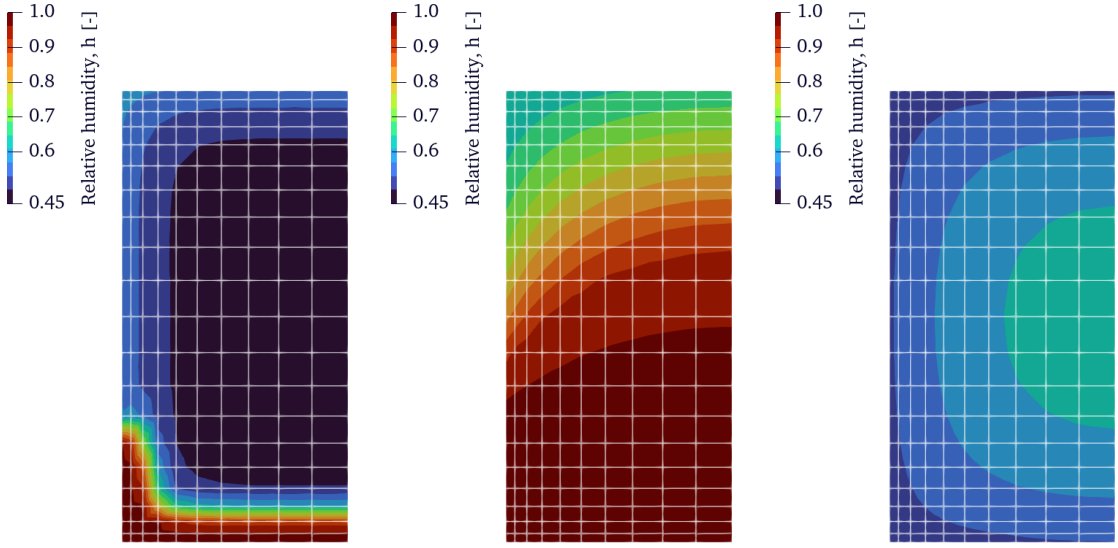

(A). 1st day of wetting. (B). 80th day of wetting. (C). 130th day of drying.

FIGURE 8. Distribution of relative humidity over a the symmetric half of a cross-section (height = 100 mm).

4.2. MECHANICAL RESPONSE

Several modifications of the MPS model for concrete creep were used to compute the response induced by the changing moisture field and by the sustained loading produced by the self-weight. The objective of this study was to identify the governing mechanisms responsible for the behavior observed in the experiments. A detailed discussion can be found in [9].

Graphical postprocessing of the results obtained with the model previously used in the blind prediction shown in Figure 9 illustrates the magnitude of normal stresses in the axial direction of the beam that develop as a response to changing moisture field. The black areas indicate surprisingly high compressive stresses exceeding 8 MPa produced by restrained swelling strain shortly after exposure to wetting, while the gray color shows regions where the tensile stress has exceeded the uniaxial tensile strength 3.38 MPa. Such stresses are produced only shortly after the onset of drying/wetting cycles when the distribution of eigenstrain is extremely nonlinear and the tensile stresses have not been relieved by relaxation. On the basis of these results, it can be concluded that creep can be treated as linear, but the incorporation of a softening behavior in tension is essential.

The evolution of the mid-span deflection obtained with the MPS model with tensile damage extension is shown in Figure 10. The Figure clearly shows that the acceleration in moisture transport has led to a significant acceleration in deflection rate, which is desired for the wetting phase but unintended for all drying phases. In the wetting phases, the computed response for beams with 150 mm and 200 mm height (shown in blue and green lines) is realistic, but the computed deflections reach only approx. $\frac{2}{3}$ of the experimental values. On the other hand, the maximum values for the smallest beam with 100 mm cross section (red line in Figure 10) are correct, but premature equilibra-

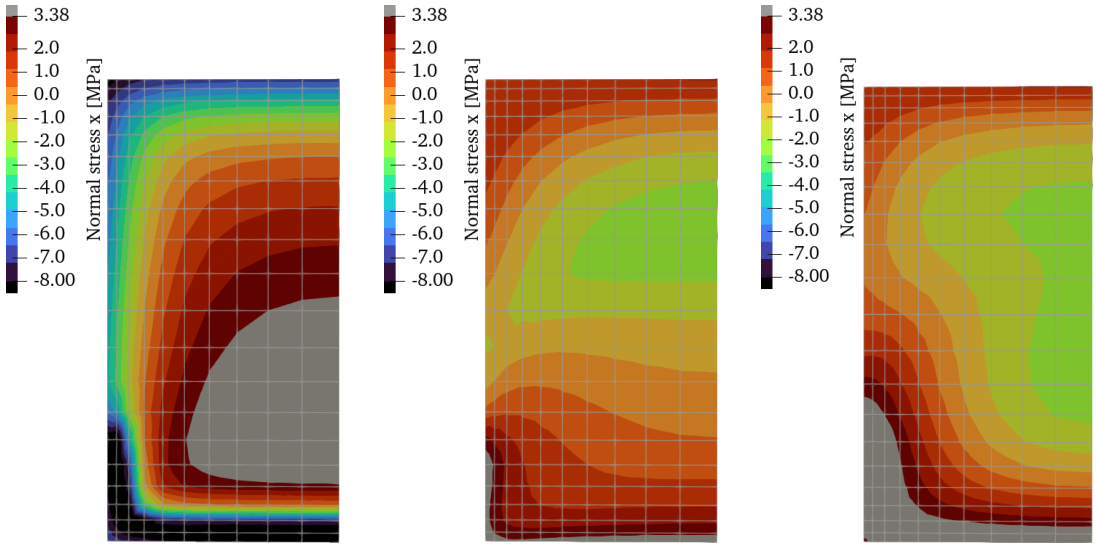

(A). 1st day of wetting. (B). 80th day of wetting. (C). 130th day of drying.

Figure 9. Distribution of normal stress in the axial direction over a the symmetric half of a cross-section at the midspan (height = 100 mm). The gray areas highlight the region where the tensile strength of concrete has been exceeded.

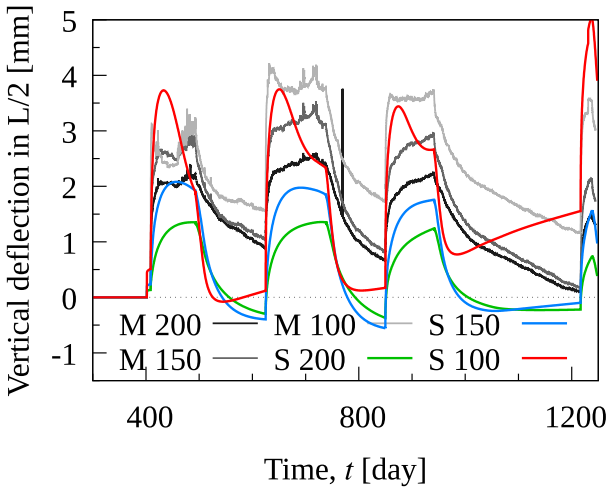

Figure 10. Evolution of vertical mid-span deflection of beams in the experiment (grey scale) and in the calibrated model (colors). The numbers in the legend denote the height of the beams.

tion of the moisture profile has caused an too early decrease in deflection which is not observed in the experiment until the onset of drying.

The rate of the structural response to drying is grossly overestimated. In the experiments, the deflection gradually decreases and would have continued if it had not been terminated by another wetting cycle. Although it is not apparent from the computed results in Figure 10, the contribution to tensile damage is substantial, without it the deflection at the end of the wetting cycles would have been much smaller (negative), which is a consequence of unrealistic creep strains triggered by moisture changes.

5. Conclusion

This paper investigated the influence of partial wetting and drying cycles on the mechanical response of plain concrete beams. The study has shown that a crucial element is a correct description of a moisture transport and that the constitutive model in the subsequent structural analysis is secondary.

The results of the blind predictions demonstrated that the widely used Bažant-Najjar model for transport cannot accurately capture the evolution of the moisture content when the concrete is in direct contact with water. Despite that, the prediction of the structural response which was driven by the (incorrect) moisture field was quite realistic both qualitatively and quantitatively.

Replacing the constitutive model for moisture transport and incorporating the bilinear sorption isotherm has significantly improved the agreement with the measured moisture balance. Despite the effort to calibrate the MPS model and introduce several improvements, the response was similar or worse to that of the blind prediction.

Based on the experimental and numerical results, the following statements can be formulated:

(1.) The influence of tensile damage is significant and cannot be ignored in the analysis.

(2.) At the onset of wetting, damage develops in the core area of the cross section occurring as a result of the expansion of the surface layer of the cross section. This effect increases with decreasing height of the cross section.

(3.) The extent and depth of tensile cracking that develops after sudden exposure to drying increases with cross-sectional height.

Acknowledgements

The authors gratefully acknowledge financial support from the Czech Science Foundation (GA ČR), project number 21-03118S, and from the Grant Agency of the Czech Technical University in Prague, project number SGS23/032/OHK1/1T/11.

References

[1] P. Li, S. He. Effects of variable humidity on the creep behavior of concrete and the long-term deflection of RC beams. *Advances in Civil Engineering* **2018**(1):8301971, 2018. https://doi.org/10.1155/2018/8301971

[2] H. Cagnon, T. Vidal, A. Sellier, et al. Drying creep in cyclic humidity conditions. *Cement and Concrete Research* **76**:91–97, 2015. https://doi.org/10.1016/j.cemconres.2015.05.015

[3] L. Vandewalle. Concrete creep and shrinkage at cyclic ambient conditions. *Cement and Concrete Composites* **22**(3):201–208, 2000. https://doi.org/10.1016/S0958-9465(00)00004-4

[4] G. Pickett. The effect of change in moisture-content on the creep of concrete under a sustained load. In *Journal Proceedings of the American Concrete Institute*, vol. 38, pp. 333–356. 1942. https://doi.org/10.14359/8607

[5] Y. Song, Q. Wu, F. Agostini, et al. Concrete shrinkage and creep under drying/wetting cycles. *Cement and Concrete Research* **140**:106308, 2021. https://doi.org/10.1016/j.cemconres.2020.106308

[6] S. Asamoto, A. Ohtsuka, Y. Kuwahara, C. Miura. Study on effects of solar radiation and rain on shrinkage, shrinkage cracking and creep of concrete. *Cement and Concrete Research* **41**(6):590–601, 2011. https://doi.org/10.1016/j.cemconres.2011.03.003

[7] R. L'Hermite, M. Mamillan. Nouveaux résultats de recherches sur la déformation et la rupture du betón [In French; New research results on deformation and failure of concrete]. *Annales de L'Institut Technique du Batiment et des Travaux Publics* **18**(207):325–359, 1965.

[8] L. Dohnalová, P. Havlásek, V. Šmilauer. Behavior of predried mature concrete beams subject to partial wetting and drying cycles. In *Acta Polytechnica CTU Proceedings*, vol. 34, pp. 1–5. 2022. https://doi.org/10.14311/APP.2022.34.0001

[9] Štěpán Krátký. *Chování betonových nosníků vystavených cyklům částečného namáčení a vysychání: numerické modelování a experiment [In Czech; Behavior of concrete beams subject to partial wetting and drying cycles: numerical modeling and experiment]*. Master's thesis, Czech Technical University in Prague, 2023.

[10] B. Patzák. OOFEM home page, 2000. [2023-01-01]. http://www.oofem.org

[11] Z. P. Bažant, L. J. Najjar. Nonlinear water diffusion in nonsaturated concrete. *Materials and Structures* **5**(1):3–20, 1972. https://doi.org/10.1007/BF02479073

[12] Fédération Internationale du Béton. *Model Code 2010 – Final draft, Volume 2*. No. 66 in fib Bulletin. 2012. ISBN 978-2-88394-106-9.

[13] Z. P. Bažant, A. B. Hauggaard, S. Baweja, F.-J. Ulm. Microprestress-solidification theory for concrete creep. I: Aging and drying effects. *Journal of Engineering Mechanics* **123**(11):1188–1194, 1997. https://doi.org/10.1061/(ASCE)0733-9399(1997)123:11(1188)

[14] P. Havlásek. *Creep and shrinkage of concrete subjected to variable environmental conditions*. Ph.D. thesis, Czech Technical University in Prague, 2014.

[15] Z. P. Bažant, S. Baweja. Creep and shrinkage prediction model for analysis and design of concrete structures: Model B3. In *Adam Neville Symposium: Creep and Shrinkage – Structural Design Effects*. 2000.

[16] H. M. Künzel. *Simultaneous heat and moisture transport in building components: One- and two-dimensional calculation using simple parameters*. Ph.D. thesis, University of Stuttgart, 1995.

THE CONCEPT OF FRACTURED ROCK-MASS MODELING USING DFN-BASED STATISTICAL VOLUME ELEMENTS

Martin Lebeda*, Petr Kabele

Czech Technical University in Prague, Faculty of Civil Engineering, Department of Mechanics, Thákurova 7, 166 29 Prague, Czech Republic

* corresponding author: martin.lebeda@fsv.cvut.cz

Abstract. The overall mechanical response of a fractured rock mass is, to a large extent, affected by naturally occurring fractures that exhibit sizes from millimeters to kilometers. Thus, in analysis of underground structures, such as tunnels, it is required that the fractures' influence on the stress and deformation state in the vicinity of the structure is taken into account. In the present work, we examine the applicability of the statistical volume element (SVE) approach to determining the apparent stiffness tensor of an equivalent continuum representation of the fractured rock, which is then used in the framework of the finite element method. The equivalent continuum properties are determined by volume-averaging the effect of individual fractures that intersect the SVE, while the fractures are represented using the "parallel plate model". Stochastically generated discrete fracture networks are used to represent the fractures' geometry. Presently, we solve the problem linearly for an incremental change of the stress state. An application of the concept is demonstrated on simulation of tunnel excavation.

Keywords: Fractured rock mass, discrete fracture network (DFN), finite element method (FEM), statistical volume element (SVE).

1. Introduction

Rock masses generally exhibit material heterogeneity at multiple scales. At the level of microscale, the heterogeneity can be associated with variable properties of mineral grains and microstructural defects. On the other hand, on the macroscale the behavior of rock mass is dominated by the stiffness of the rock matrix, presence of different types of discontinuities (generally called fractures) and the filling material or fluids inside the fractures. Considering the typical dimensions of underground structures, such as tunnels, their analysis and design generally correspond with the macroscale. Hence, when these structures are excavated in fractured rock, the effect of fractures must be taken into account [2]. The finite element method (FEM) is often used for the analyses. Then, one efficient way is to include only a few largest fractures as discrete discontinuities in the model, while the rest of the fractures is substituted by an equivalent continuum with effective or apparent properties of the rock mass. These overall parameters are evaluated by averaging or homogenization procedure [3]. In this paper, we focus on the equivalent continuum modeling and follow up on our previous work [4], where stochastically generated discrete fracture network (DFN) models [5, 6] provide a geometrical description of the fracture system in the rock mass. Note that this approach makes it possible to utilize data from geological survey to statistically describe the fractured rock mass.

The equivalent continuum methods are commonly used in conjunction with the concept of the representative volume element (RVE) [7–9]. In principle, the RVE is the smallest volume, which encompasses a sufficient sample of the substructures (e.g., fractures), so as to provide effective constitutive properties, which are nearly invariable with respect to the RVE placement. On the other hand, on the scale of the whole analyzed problem (e.g., tunnel), RVE must be small enough with respect to the spatial variation of macroscopic stress to represent a material point. Our previous research [4] shows that, for DFNs with power-law fracture size distribution (with minimum fracture size on the order of decimeters), the RVE size should be on the order of tens of meters. However, in the case of tunnel analysis, this RVE size does not meet the second criterion, as the stress shows high gradients in the close proximity of the excavation (units of meters). In this regard, La Pointe et al. [10] questioned the applicability of the continuum simulations on the scale of 10 to 100 meters, while fracture sizes occurring in the rock mass may range from millimeters to kilometers. Furthermore, Ostoja-Starzewski [11] pointed out the spatial randomness of the rock material and incorporated the concept of statistical volume element (SVE) on the level of mesoscale, separating the microscale of heterogeneities from the macroscale that is usually connected with the RVE approach. The procedure of determination of overall properties using volume elements smaller than representative is in agreement with widely accepted study presented by Kanit et al. [12], which suggests the evaluation of the effective properties as mean values of apparent properties of rather small volumes considering sufficient number of realizations. Against this background,

Fracture set	1	2	3	4	5	6	7	8	9
Fisher distribution									
Mean dip [°]	85.365	36.871	3.360	87.507	62.308	88.629	78.236	88.629	83.253
Mean strike [°]	222.949	49.597	313.665	316.780	133.438	346.277	1.040	269.482	85.957
κ [-]	35.056	2.704	28.633	25.351	2.913	18.730	3.815	17.300	3.962
Power law distribution									
$a_{\min}$ [m]	0.3	0.3	0.3	0.3	0.3	0.3	0.3	0.3	0.3
$a_{\max}$ [m]	1 000	1 000	1 000	1 000	1 000	1 000	1 000	1 000	1 000
α [-]	3.328	3.062	3.800	3.789	3.382	3.042	3.000	3.607	3.296
P_{30} [m^{-3}]	0.269	0.220	0.061	0.246	0.427	0.232	0.146	0.581	0.380

TABLE 1. Parameters of DFNs [1].

we adopt the SVE approach to simulations of tunnel excavation, while taking into account the spatial, orientational, and dimensional randomness of rock fractures.

In this study, we present ongoing work on development of the 3D FE stress and displacement analysis that incorporates parameters of equivalent continuum obtained by averaging procedure in conjunction with the 3D stochastic DFN. We use the averaging method based on the approach proposed by Oda et al. [9] that treats individual fractures by the "parallel plate model", which means that the deformation response of a fracture to normal and shear stress is represented by two dimensionless stiffness parameters. At present stage, we have implemented the FE analysis linearly with constant fractures' stiffness for an incremental change of stress state. Although the linear solution is admissible only for small stress changes, the applicability of the SVE concept can be demonstrated.

2. DFN model of fractures' geometry

The description of the rock-mass inherent fracturing state represents the crucial part of underground structures' analysis. The stochastically generated DFN approach provides an adequate balance between the computational efficiency and the accuracy [5, 6]. The quantitative input information about simulated fracture network is often obtained by geological survey that usually consists of structural-geological mapping of fracture traces on rock outcrops or tunnel walls and of inspection of boreholes (observation windows). As the survey provides only a limited information about fractures deep in the rock mass volume, the data are used in the framework of so-called stochastic DFN modeling. In this approach, individual fractures are idealized as polygons, whose size, orientation, and spatial placement are assumed to follow certain probabilistic distributions. The distributions' parameters are identified so as to match (in a statistical sense) the traces' sizes, directions, and density within the observation windows. Based on the calibrated probabilistic distributions any desired number of DFN realizations can be generated [13].

In the following parts of this study we use fracture network models generated by in-house software *DFN_toolbox* [14]. Parameters of these DFNs were calibrated based on data collected in the past by the Czech Geological Survey at the underground research facility Bukov, which is located at a depth of 550 metres below the Earth's surface. Detailed description of the used measurement procedures and the acquired data are presented in report [1].

Positioning of fractures' centers in the model volume is ruled by Poisson random generation process. The abundance of fractures is defined by volumetric density P_{30} (number of fractures per unit volume). Fractures are modeled as squares, whose sizes a (radii of circumscribed circles) are controlled by the power law distribution with parameters $a_{\min}$, which is the minimum fracture size (location parameter), and α, which is the law's exponent (shape parameter). For practical reasons, only fractures smaller than chosen value $a_{\max}$ are generated. The orientation of fractures is determined by Fisher distribution, with parameters mean dip and mean strike (from which the mean unit normal vector $\boldsymbol{\mu}$ can be determined), and κ, which is the concentration parameter.

The whole network consists of nine fracture sets, where each of them is defined by individual density, orientation, and size parameters. All of the parameters are listed in Table 1. Note that steeply dipping fractures prevail (namely sets 1, 4, 6, 8, 9) while subhorizontal (set 3) and mildly dipping fractures are less abundant.

3. Averaging procedure

The overall effective properties of fractured rock mass are calculated by averaging procedure that was originally proposed by Oda et al. [9]. The main Equation (1) of the procedure represents the relation between macroscopic stress σ_{kl} and the corresponding strain ε_{ij} that are connected by the fourth order compliance tensor C_{ijkl}:

$$\varepsilon_{ij} = \frac{1}{2G}\left(\frac{1}{2(\delta_{ik}\delta_{jl}+\delta_{il}\delta_{jk})} - \frac{\nu}{1+\nu}\delta_{ij}\delta_{kl}\right)\sigma_{kl} + \frac{1}{E}\left[\left(\frac{1}{k_n}-\frac{1}{k_s}\right)F_{ijkl} + \frac{1}{4k_s}(\delta_{ik}F_{jl}+\delta_{jk}F_{il} + \delta_{il}F_{jk}+\delta_{jl}F_{ik})\right]\sigma_{kl} = C_{ijkl}\sigma_{kl}, \tag{1}$$

where

G is the shear modulus,

E is the Young's modulus,

ν is the Poisson's ratio of the intact rock,

k_n is the nondimensional parameter related to the fracture's normal,

k_s is the nondimensional parameter related to the tangent stiffness,

δ_{ij} is Kronecker's delta,

F_{ij} and F_{ijkl} are so-called second and fourth rank crack tensors, respectively:

$$F_{ij} = \frac{1}{V}\sum_{k=1}^{M} S^{(k)}L^{(k)}n_i^{(k)}n_j^{(k)}, \tag{2}$$

$$F_{ijlm} = \frac{1}{V}\sum_{k=1}^{M} S^{(k)}L^{(k)}n_i^{(k)}n_j^{(k)}n_l^{(k)}n_m^{(k)}, \tag{3}$$

where

V is the volume of the domain over which averaging is performed,

$S^{(k)}$ is the area of k-th fracture inside the sampling volume,

$L^{(k)}$ is a typical size of the fracture (equal to the diameter of a circle with the same area),

$n_i^{(k)}$ are the components of a unit vector normal to the fracture.

Note that, the typical fracture size L is evaluated using the whole area of the fracture and not of the part inside the sampling volume because it is a property of the fracture independent on the size of the sampling volume.

The dimensionless stiffness parameters k_n and k_s are, in this study, set while considering fractures' mechanical response in the depth of hundreds of meters below the ground level, which corresponds, for example, to the potential location of a deep underground radioactive waste repository. It is assumed that the rock mass is geostatically compressed to the point that all fractures are closed, and their normal stiffness is nearly infinite. On the contrary, fractures are assumed to be vulnerable to slip in the case of changing stress state due to, for example, tunnel excavation, meaning that the shear stiffness is almost nil. In that sense, the parameters are set as $k_n = 10\,000$, $k_s = 1.0$. Further investigation of this assumption is needed, however the present study deals with the applicability of the SVE concept, which is feasible regardless of stiffnesses choice.

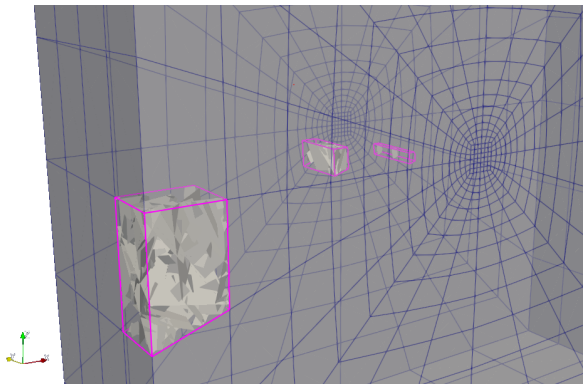

Figure 1. Illustration example of three SVEs corresponding to finite elements. In each SVE, only the intersecting portions of the underlying DFN fractures are shown.

3.1. Statistical volume element

The concept of using the SVE to obtain averaged mechanical properties of fractured and heterogenous materials has already been studied by other authors at the level of microscale, for example, [15, 16]. The most frequently used shapes of SVE are square and circle in the case of 2D models and cube or sphere for 3D models. The size of the statistical sampling element should be chosen regarding coefficient of variation of the monitored variable [17].

In this study, we use either cubical SVEs with a fixed side size (in the concept verification stage, Section 4) or SVEs, whose shape, size, and position correspond with those of the finite elements (for the FE simulations, Section 5) to obtain the apparent stiffness tensor of the fractured rock mass. To this end, each SVE's compliance tensor is first calculated using Equations (1) to (3), $S^{(k)}$, $L^{(k)}$, $n_i^{(k)}$ in which are determined from all fractures of the underlaying DFN, which intersect the SVE (Figure 1). Subsequently, the stiffness tensor is obtained by inverting the compliance. Note that, in general, this procedure yields fully anisotropic tensors. Finally, the stiffness tensors are assigned to the corresponding finite elements, which generally means that each finite element is composed of a unique material (Figure 2). The whole process has been implemented by means of Python API in the open-source FE code OOFEM [18].

4. The SVE concept verification

First, we need to verify that the SVE concept is applicable to analyses, such as, FE simulation of a tunnel excavation in a fractured rock modelled by DFN with parameters given in Table 1. The verification is inspired by the study presented by Kanit et al. [12]. In particular, we investigate, whether, when averaging

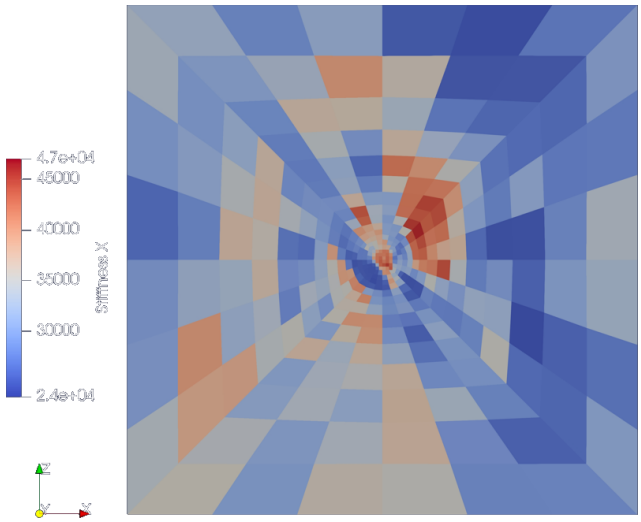

(A). Distribution of the apparent modulus E_x obtained by SVEs. For comparison, the value of E_x calculated by averaging over large AV on the same underlaying DFN is 27 100 MPa.

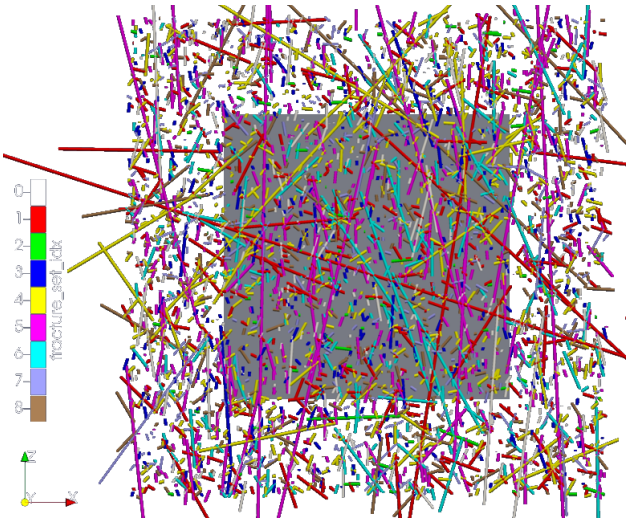

(B). Section view of the underlaying DFN (right).

FIGURE 2. Distribution of the apparent modulus E_x obtained by SVEs and section view of the underlaying DFN.

is performed on volumes smaller than RVE, similar apparent moduli are obtained when samples are taken from multiple locations of one realization of the DFN as well as by sampling one location in multiple DFN realizations.

To this end, we use 10 different statistical realizations of the DFN model with parameters described in the Section 2. The fractures are generated with centers in a cubical domain with the side size of 50 m. As a reference, we firstly calculate the effective moduli for all DFN realizations by volume-averaging over a sub-domain of $30 \times 30 \times 30\,\mathrm{m}^3$. The sub-domain is placed at the center of the larger DFN to reduce the boundary effect. Based on a previous study [19], this sub-domain, denoted as *large averaging volume* (AV) should be large enough to serve as RVE. Secondly, moduli are calculated from 10 SVEs with dimensions of $2 \times 2 \times 2\,\mathrm{m}^3$, which are placed randomly far apart but all in the central portion of *one realization* of the DFN. Thirdly, moduli are obtained for *one SVE* with dimensions of $2 \times 2 \times 2\,\mathrm{m}^3$, which is placed at the same location near the center in all 10 realizations of the DFN. The SVE size was chosen so as to roughly correspond with the size of typical finite elements used in the subsequent simulations.

Although the complete stiffness tensors are calculated, we use Young's moduli E_x, E_y, E_z, which correspond to the tensor elements D_{1111}, D_{2222}, D_{3333}, respectively, to illustrate the results. The data shown in Figures 3–5 confirm the expected difference between values obtained by using the SVEs and by using the large averaging volume. When moduli are evaluated over the large AV, the results from 10 realizations show coefficient of variation (COV) of 5.2 % or less. In the case of the SVE calculations, the results are more dispersed with COV ranging between 15.8 and

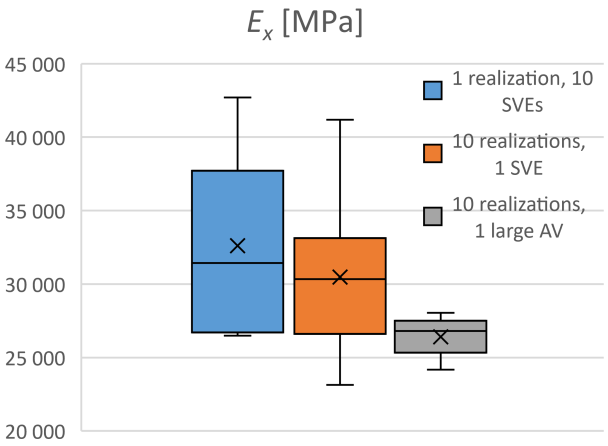

FIGURE 3. Comparison of stiffness E_x. The boxes indicate the quartiles, the whiskers indicate the minimum and maximum and the cross indicates the mean.

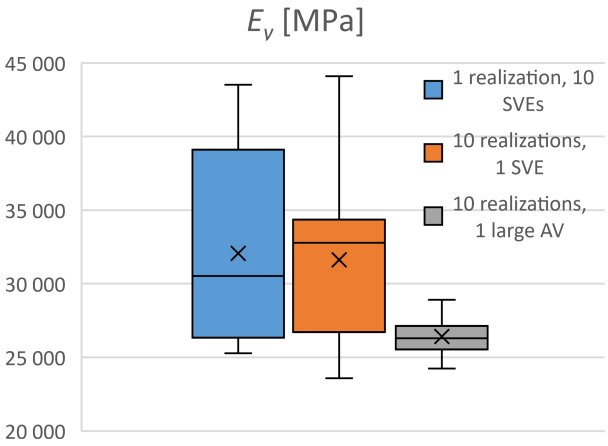

FIGURE 4. Comparison of stiffness E_y. The boxes indicate the quartiles, the whiskers indicate the minimum and maximum and the cross indicates the mean.

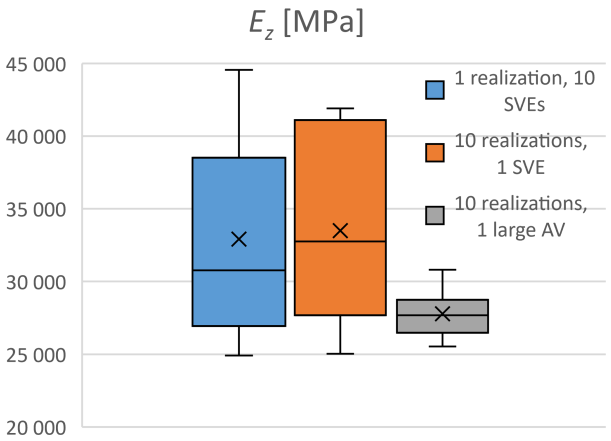

Figure 5. Comparison of stiffness E_z. The boxes indicate the quartiles, the whiskers indicate the minimum and maximum and the cross indicates the mean.

19.7 % and the mean values of apparent moduli are higher. Furthermore, both SVEs approaches (spatial sampling and multiple realizations) are in a fair agreement. Especially, in the case of the E_y and E_z, the mean values differ by less than 2 %. In the case of the difference is approximately 7 %.

5. Numerical simulation of tunnel excavation

To demonstrate the use of the SVE modeling approach, 3D simulation of tunnel excavation is performed. The modelled rock domain consists of $30 \times 30 \times 10\,\mathrm{m}^3$ prism, where the short dimension is parallel to the tunnel axis. The tunnel passes through the center of the domain and has a diameter of 3 m. The displacement of the rock body is constrained by statically determinate supports. The excavation problem is solved in two calculation steps, see Figure 6. In the first step the initial stress state is induced and in the second step the excavation of the tunnel is simulated by removal of elements.

To impose the initial stress state, the FE model is loaded by normal stresses that are applied to the outer surface of the rock body. The initial loading stress tensor is based on field measurements from Rožná mine [20], which is a part of the underground research facility Bukov. The data from vertical boreholes showed that the directions of the principal stresses are vertical and horizontal. The vertical principal stress is calculated as:

$$S_v = -\rho \cdot g \cdot h, \tag{4}$$

where

ρ is volumetric weight,

g is gravity acceleration,

h is depth beneath the ground level.

The parameters for calculation of the vertical principal stress (Table 2) are adopted from [21]. As the major

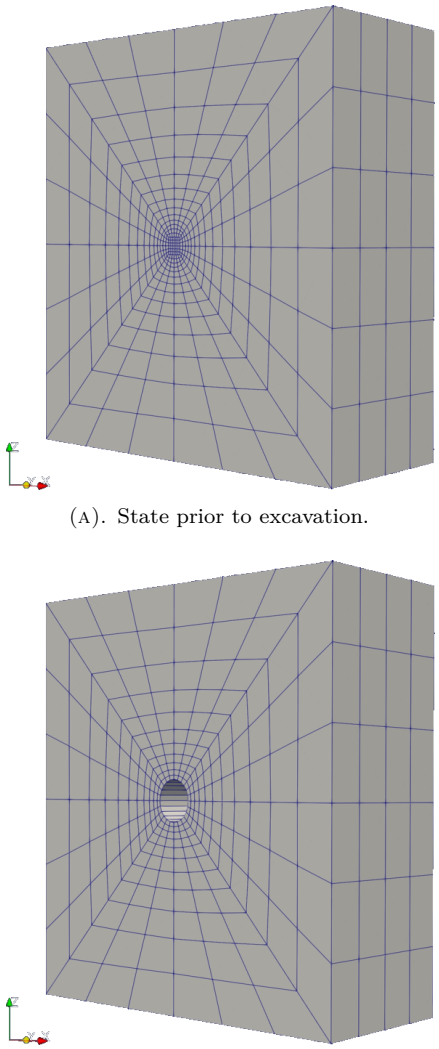

(a). State prior to excavation.

(b). State after excavation.

Figure 6. The finite element mesh.

Parameter	Value
Major horizontal principal stress S_H [MPa]	−22.8
Major horizontal principal stress S_h [MPa]	−14.6
Volumetric weight ρ [kg m^{-3}]	28 000
Depth of the mine beneath the gnd level [m]	550
Vertical principal stress S_v [MPa]	−15.4

Table 2. The initial loading stress parameters.

and minor horizontal principal stresses, S_H and S_h, respectively, we use the average of the values measured on different levels of the mine. The values of the initial stress are listed in Table 2. Orientation of the model is set so, that the tunnel axis is parallel with the minor horizontal principal stress, which means that the direction of S_h corresponds to the global axis y.

For the purpose of comparison, simulations are calculated, firstly, using the uniform effective stiffness tensor, obtained by averaging over the large volume, in all finite elements. Secondly, the concept of SVE is applied with the same underlaying DFNs. In the latter case, the stiffness tensor is calculated by averag-

ing over SVEs that coincide with the finite elements, which yields nonuniform stiffness over the analyzed domain, as illustrated in Figure 2. Specifically, the values of modulus E_x are plotted over individual elements along the front cross-section perpendicular to the tunnel axis located at $y = -3.75\,\mathrm{m}$. The figure also shows the section of the underlaying DFN.

It is noted that the case of uniform stiffness, the stress state prior to the tunnel excavation is also uniform within the modelled domain. On contrary, the calculations using the SVE concept exhibit nonuniform initial stress state, which is caused by different material stiffness in each finite element (see Figure 2).

5.1. Results of the study

The calculations were performed for 10 realizations of the stochastic DFN. The main monitored result values are horizontal and vertical convergences of the tunnel walls measured on the cross sections passing through the tunnel center, see Figure 7 and Figure 8.

The results show that the absolute values of tunnel walls convergences are lower in the case of the SVE approach, which is in agreement with Section 4, where higher stiffnesses were obtained while using SVEs. However, the variances of the results are comparable regardless of the size of the averaging volume. Further investigation of this phenomenon is needed since it may be caused by various effects, e.g., low number of statistical realizations or the specific spatial, orientational, and dimensional characteristics of the DFN fracture sets.

6. Conclusion

The applicability of the SVE concept incorporated in the 3D FEM simulation of tunnel excavation using overall rock-mass parameters obtained by averaging procedure based on DFN has been examined. The results of the study lead to the following conclusions:

- The variance of the overall moduli obtained by averaging over SVEs (COV = 15.8–19.7 %) is higher compared to averaging over large volume (COV = 5.2 %), which is an expected outcome.
- The agreement of the two different SVE evaluation methods (spatial sampling and multiple realizations) is fairly good with the highest difference of 7 %.
- Lower convergences of tunnel walls appear while using the SVE approach compared to large averaging volume, which is in agreement with the higher stiffnesses obtained in case of SVEs.
- On the other hand, the variance of convergences of tunnel walls are comparable regardless of the size of the averaging volume. This phenomenon requires further investigation since it is not an expected outcome.

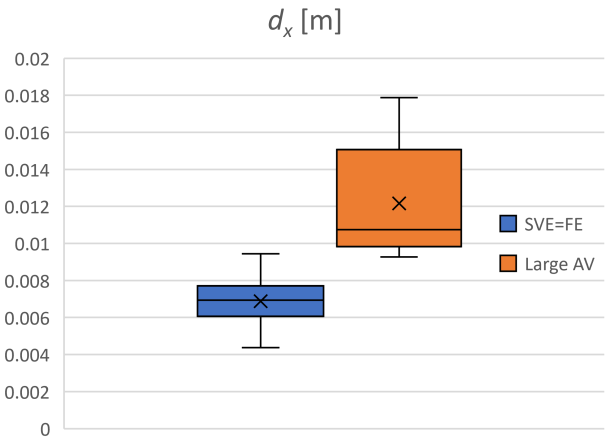

Figure 7. Horizontal convergence of tunnel walls. The boxes indicate the quartiles, the whiskers indicate the minimum and maximum and the cross indicates the mean for 10 realizations of stochastic DFN.

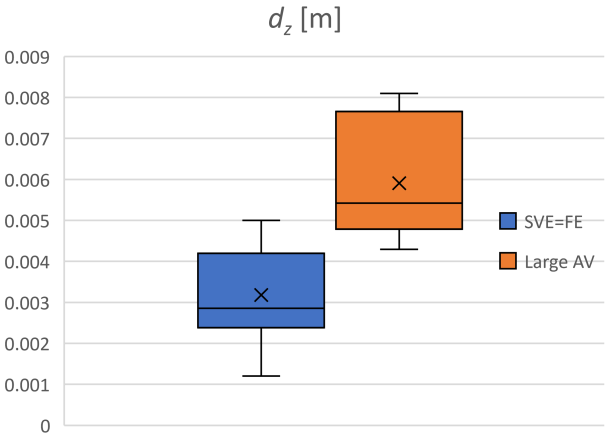

Figure 8. Vertical convergence of tunnel walls. The boxes indicate the quartiles, the whiskers indicate the minimum and maximum and the cross indicates the mean for 10 realizations of stochastic DFN.

Acknowledgements

This paper was financially supported by Czech Technical University in Prague under SGS project no. SGS23/032/OHK1/1T/11.

References

[1] L. Gvoždík, P. Kabele, J. Říha, et al. Transport of radionuclides from deep geological repository/testing of conceptual and numeric models. Tech. rep., Progeo s. r. o., 2020.

[2] L. Jing. A review of techniques, advances and outstanding issues in numerical modelling for rock mechanics and rock engineering. *International Journal of Rock Mechanics and Mining Sciences* **40**(3):283–353, 2003. https://doi.org/10.1016/S1365-1609(03)00013-3

[3] M. Hori, S. Nemat-Nasser. On two micromechanics theories for determining micro-macro relations in heterogeneous solids. *Mechanics of Materials* **31**(10):667–682, 1999. https://doi.org/10.1016/S0167-6636(99)00020-4

[4] M. Lebeda, P. Kabele. Analysis of tunnel excavation based on linear DFN-FEM modelling. *Acta Poytechnica CTU Proceedings* **40**:61–68, 2023. https://doi.org/10.14311/APP.2023.40.0061

[5] J. Andersson, A. M. Shapiro, J. Bear. A stochastic model of a fractured rock conditioned by measured information. *Water Resources Research* **20**(1):79–88, 1984. https://doi.org/10.1029/wr020i001p00079

[6] C. Darel, P. Davy, O. Bour, J.-R. De Dreuzy. Discrete fracture network for the Forsmark site. Tech. rep., SKB – Svensk Kärnbränslehantering AB Swedish Nuclear Fuel and Waste Management Co, 2006. [2023-08-22]. http://www.iaea.org/inis/collection/NCLCollectionStore/_Public/38/013/38013872.pdf

[7] M. Kachanov. Continuum model of medium with cracks. *Journal of the Engineering Mechanics Division* **106**(5):1039–1051, 1980. https://doi.org/10.1061/JMCEA3.0002642

[8] M. Cai, H. Horii. A constitutive model of highly jointed rock masses. *Mechanics of Materials* **13**(3):217–246, 1992. https://doi.org/10.1016/0167-6636(92)90004-W

[9] M. Oda, T. Yanabe, Y. Ishizuka, et al. Elastic stress and strain in jointed rock masses by means of crack tensor analysis. *Rock Mechanics and Rock Engineering* **26**(2):89–112, 1993. https://doi.org/10.1007/BF01023618

[10] P. R. La Pointe, P. C. Wallmann, S. Follin. Continuum modelling of fractured rock masses: Is it useful? In *Prediction and performance in rock mechanics and rock engineering*, vol. 2, pp. 343–350. 1996.

[11] M. Ostoja-Starzewski. Material spatial randomness: From statistical to representative volume element. *Probabilistic Engineering Mechanics* **21**(2):112–132, 2006. https://doi.org/10.1016/j.probengmech.2005.07.007

[12] T. Kanit, S. Forest, I. Galliet, et al. Determination of the size of the representative volume element for random composites: statistical and numerical approach. *International Journal of Solids and Structures* **40**(13–14):3647–3679, 2003. https://doi.org/10.1016/S0020-7683(03)00143-4

[13] P. Kabele, O. Švagera, et al. Mathematical modeling of brittle fractures in rock mass by means of the DFN method. Tech. rep., Czech Technical University in Prague, 2017.

[14] P. Kabele. *DFN_toolbox*, 2023. [2023-08-22]. https://gitlab.com/pkabele/DFN_toolbox

[15] J. M. Garrard, R. Abedi. Statistical volume element averaging scheme for fracture of quasi-brittle materials. *Computers and Geotechnics* **117**:103229, 2020. https://doi.org/10.1016/j.compgeo.2019.103229

[16] K. Acton, J. Garrard, R. Abedi. Geometric partitioning schemes to reduce modeling bias in statistical volume elements smaller than the scale of isotropic and homogeneous size limits. *Computer Methods in Applied Mechanics and Engineering* **393**:114772, 2022. https://doi.org/10.1016/j.cma.2022.114772

[17] D. Trias, J. Costa, A. Turon, J. E. Hurtado. Determination of the critical size of a statistical representative volume element (SRVE) for carbon reinforced polymers. *Acta Materialia* **54**(13):3471–3484, 2006. https://doi.org/10.1016/j.actamat.2006.03.042

[18] B. Patzák. OOFEM project home page, 2000. [2023-08-22]. http://www.oofem.org

[19] M. Lebeda, P. Kabele. The effect of sampling volume size on the apparent stiffness of jointed rock mass. *Acta Poytechnica CTU Proceedings* **34**:38–42, 2022. https://doi.org/10.14311/APP.2022.34.0038

[20] Z. Bukovská, et al. SÚRAO TZ 464/2020. Získání dat z hlubokých horizontů dolu Rožná [In Czech; Data acquisition from the deep horizons of the Rožná mine]. Tech. rep., SÚRAO – Správa úložišť radioaktivních odpadů, 2020.

[21] K. Souček, M. Vavro, L. Staš, et al. SÚRAO ZZ 221/2018. Komplexní geologická charakterizace prostorů PVP Bukov – část II geotechnická charakterizace [In Czech; Complex geological characterization of the Bukov URF – part II geotechnical characterization]. Tech. rep., SÚRAO – Správa úložišť radioaktivních odpadů, 2018.

A SIMPLIFIED DESIGN OF A CONCRETE SANDWICH STRUCTURE CONTAINING A REINFORCING RIB

Jan Macháček[a,*], Eliška Kafková[a], Věra Kabíčková[a,b], Tomáš Vlach[a,b]

[a] *Czech Technical University in Prague, Faculty of Civil Engineering, Department of Architectural Engineering, Thákurova 7, 166 29 Prague, Czech Republic*

[b] *Czech Technical University in Prague, University Centre for Energy Efficient Buildings, Třinecká 1024, 273 43 Buštěhrad, Czech Republic*

[*] corresponding author: jan.machacek@fsv.cvut.cz

Abstract. This article presents the use of a strut and tie analogy for modelling the behaviour of a concrete sandwich structure, which is formed by thin outer concrete layers made of high-performance concrete and reinforcing ribs. The beams transmitting shear are made of a rigid material with low thermal conductivity (Purenit) in combination with a carbon fibre reinforced polymer. The purpose of these ribs is to ensure reliable shear interaction of the outer concrete layers regardless of the thermal insulation of the sandwich structure. A simplified model using the truss analogy in the Scia Engineer software was used for the design of this structure. Furthermore, this design was verified experimentally on a section of the sandwich panel where the feasibility and functionality were tested by a four-point bending test. Finally, the theoretical values from the model were compared with the experimental results. This also includes a simple evaluation of whether this simplified modelling of the structure's behaviour is appropriate. The paper contains a summary of the conditions that could have affected the results.

Keywords: High performance concrete, precast concrete, sandwich panels, composite reinforcement, shear reinforcement, rigid heat insulation, strut-and-tie model.

1. Introduction

Precast concrete sandwich panels are formed from two thin outer layers made of concrete (nowadays from high performance concrete) which are connected by some kind of shear connectors between which is placed thermal insulation. The connectors where historically from steel [1] but due to high thermal conductivity of steel which resulted in significant heat bridges, which depreciated value of heat transfer coefficient (U-value) of construction, we are trying to replace them. So nowadays they are mostly from some kind of fibre reinforced polymers like for example CFRP, GFRP etc. or is used only rigid thermal insulation placed between concrete layers. The shear connections methods are investigated by many scientists all over the world, for example Richard O'Hegarty [2, 3], Abdelghani Benayoune [4], Kamil Hodicky [5], Mathias Flansbjer [6] and many others [7, 8]. In this case is the shear connection solved by reinforcing ribs composed from rigid heat insulation (specially from purenit) and braids from CFRP. The problem is that it is very hard to predict behaviour of panels during loading because of panels composition from many components which have different properties. This article deals with the use of strut and tie model for modelling of precast sandwich concrete panel behaviour. The first step was to test mechanical properties of materials which are used in sandwich panel. Then was created strut and tie model in Scia Engineer with values gained from material tests and was created panel section sample. In the last step the panel section was tested by a four-point bending test and the theoretical values from the model were compared with the experimental results.

Mix content	**kg m^{-3}**
Cement I 42.5R	650
Technical silica sand	1 200
Elkem microsilica 940 U-S	100
Technical quartz powder ST 6	235
Superplasticizer based on PCE	18
Water	190
Total	2 393

Table 1. HPC mix design.

2. Materials used in panel section sample and properties tests

2.1. High performance concrete

Thin outer layers of PCSP are from HPC in this case specifically from the HPC who's mix design is listed below. This mixture was developed in department of civil engineering at CTU in Prague and later improved in UCEEB at Buštěhrad. For determining panel's behaviour during loading test as accurately as possible was necessary to test concrete's properties. 6 samples were tested in total. 3 cubes with

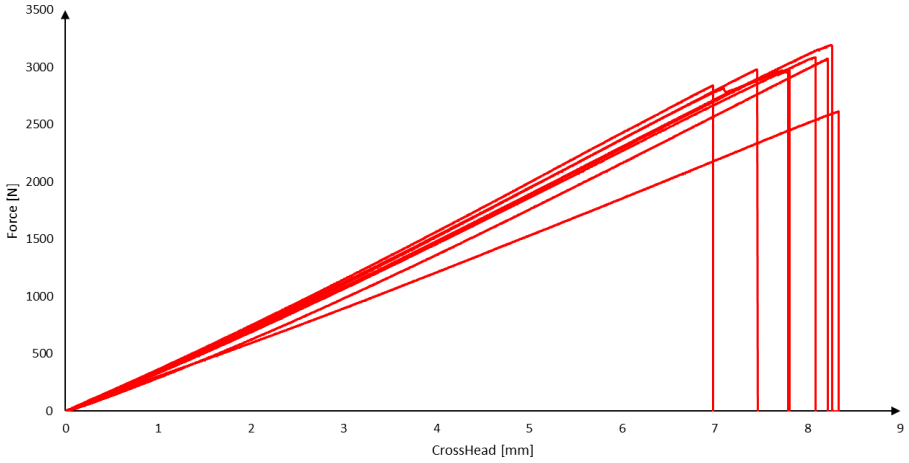

Figure 1. Tensile test of carbon composite reinforcement.

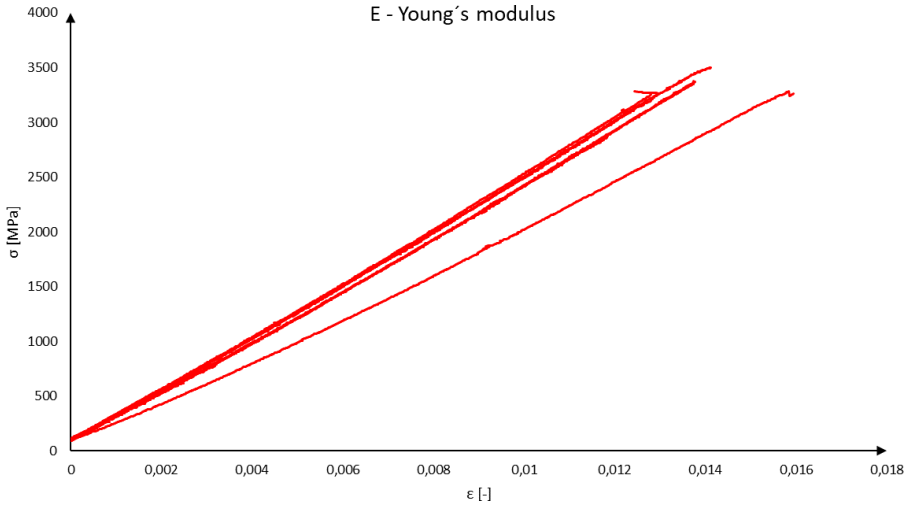

Figure 2. Young's modulus of carbon composite reinforcement.

an edge of 100 mm and 3 beams with the dimensions $40 \times 40 \times 160$ mm. The cubes were tested in compression according to ČSN EN 12390-3 [9] and the beams were subjected to three-point bending test according to ČSN EN 12390-5 [10].

The test measured the average strength of concrete in central pressure at cube 97.42 MPa according to ČSN EN 12390-3 [9] and the average tensile strength of the concrete under bending measured on beams at 15.51 MPa according to ČSN EN 12390-5 [10]. Modulus of elasticity was known from previous tests which was done in UCEEB during developing of the mixture and its value is 45.00 GPa. These values were used for calculations.

2.2. Carbon fibre reinforced polymer

As a shear reinforcement of the panel which is subject of this article is used a composite reinforcement consisting of epoxy resin and carbon fibres TenaxTH – E STS40 F13 24k 1600 tex from TEIJIN. Before creation of panel were created 8 samples of this reinforcement which were tested by uniaxial simple tension on the test equipment. The maximum force at material failure was monitored (bearing capacity) and the dependence of the relative deformation on stress (approximate Young's modulus of elasticity). The results of test are presented in the Figure 1: Tensile test of carbon composite reinforcement and Figure 2: Young's modulus of carbon composite reinforcement.

Tensile tests of carbon composite reinforcement revealed that the rovings achieve average tensile strength of 2 968.30 N which corresponds to a stress of 3.28 GPa and that the average Young's modulus is 237.60 GPa. These values were used in the following calculations.

2.3. Purenit

As part of this work the behaviour of purenit under pressure loading was tested, specifically 3 samples of width 100 mm, thickness 30 mm and height 180 mm. These dimensions were accurately measured by caliper at 3 locations and from the measured values the average value was calculated. After measure the samples were loaded at a speed of 1 mm per minute until failure. From the loading tests was obtained the working diagram of purenit which were used in following calculations.

Based on the results of loading tests the average breaking strength of purenit is 8.25 MPa as presented

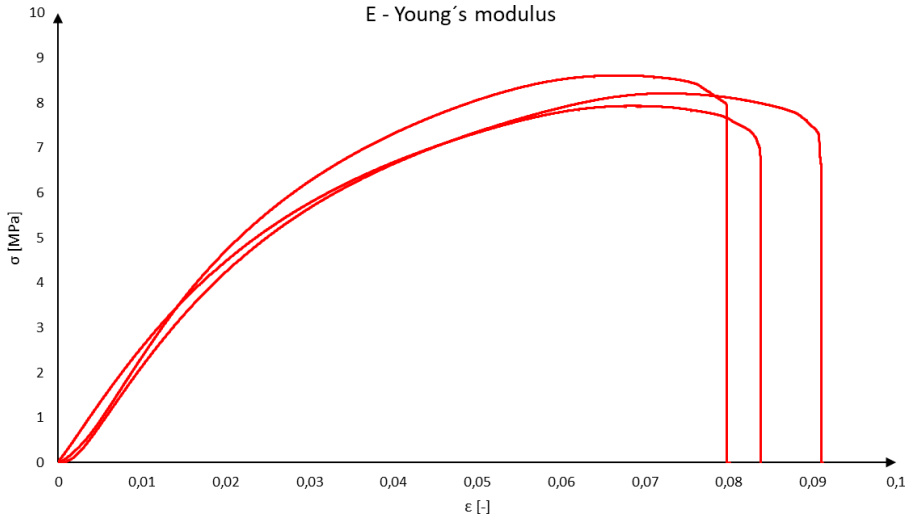

FIGURE 3. Young's modulus of purenit.

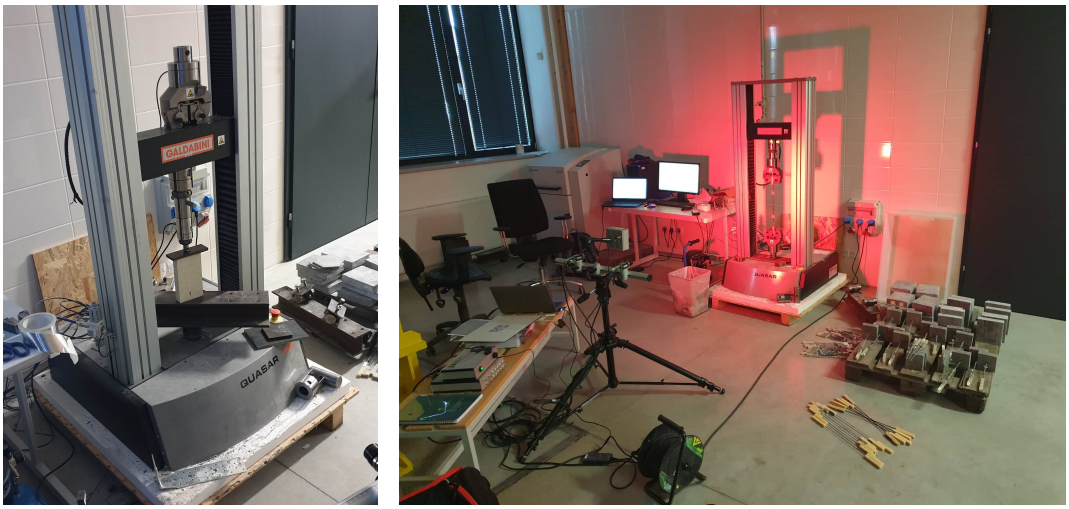

FIGURE 4. Photos from materials tests.

in Figure 3 and the modulus of elasticity is 226.28 MPa, which approximately corresponds to the data in the technical sheet from manufacturer [11]. After exceeding the load-bearing capacity, the material literally flew to pieces. To the value of 3.50 MPa the material's behaviour was elastic.

3. STRUT-AND-TIE MODEL

For the calculation purpose the entire panel was significantly simplified. In calculation model the panel construction is represented by strut-and-tie model which is essentially a rib's longitudinal section. The strut-and-tie model works as follow: the upper compression bar and lower tension member represents outer concrete layers, so in the calculation model they are from concrete profiles which are 2 cm high, 50 cm wide and have properties which were measured on concrete samples. The diagonals represent shear reinforcement, so their area and properties correspond to area and measured properties of the used reinforcement from CFRP and the shafts represent purenit.

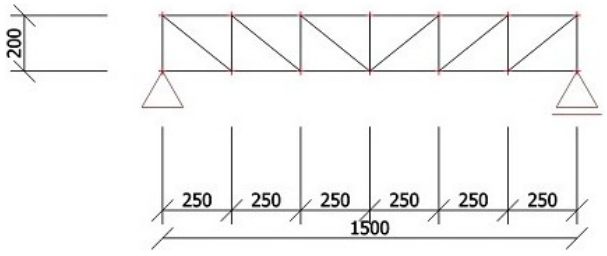

FIGURE 5. Strut-and-tie model.

The model as presented in Figure 5 and Figure 6 has been loading by 2 forces operating in thirds of the truss beam until the calculated stress in diagonals has the breaking strength value [12].

Because strut-and-tie model represent only one rib and experimental panel has two, the forces must be summarized and multiplicated by two. So, the prediction based on the strut-and-tie model is that after force on the press reaches 36.52 kN the shear reinforcement will break and then the panel collapses due to shear failure of the rib from purenit.

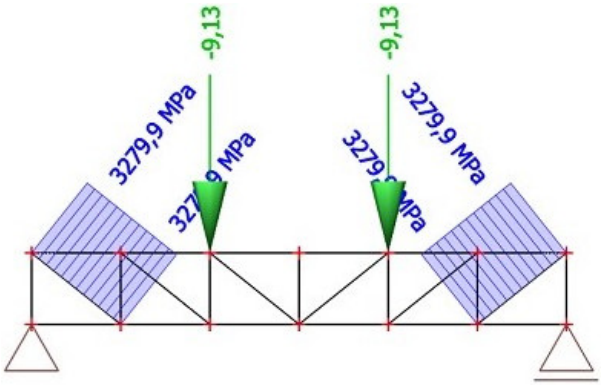

Figure 6. The breaking strength.

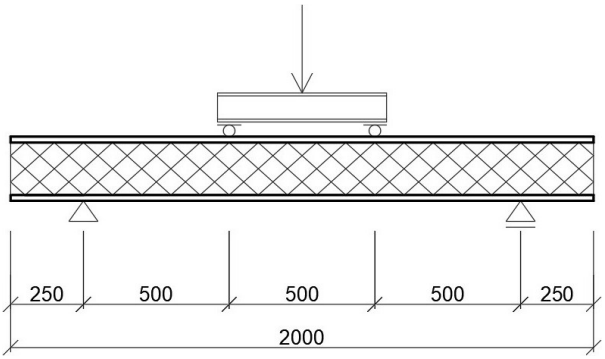

Figure 7. Schema of four-point bending test.

4. Experiment

The load test of the panel took place at UCEEB and were carried out using a press from which the force was transmitted through a pair of welded I-sections to achieve a four-point bending load. Scheme of four-point bending test is presented in Figure 7 and photo from testing procedure in Figure 8. Loading was carried out at a rate of 3 mm per minute, and it continued until the structure failed.

The first shear reinforcement failed when the force on the press was 30.00 kN, after that panel's behaviour stopped being linearly elastic and composite reinforcement gradually began to fail until finally the structure collapsed due to the shear failure of the purenit ribs as presented in Figure 9. The maximum force on the press was 54.58 kN.

5. Comparison

As you can see in presented Figure 10 below, the strut-and-tie model predicted, that the panel will collapse when the force on the press will be 36.52 kN due to failure of the shear reinforcement. It is very close to the real force 30.00 kN at which the shear reinforcement started to fail but strut-and-tie model didn't deal with plastic reserve. Panel collapsed when the force on the press was 54.58 kN which is much more than was expected. The same we can say about deformation which were smaller than was expected, because purenite with a large cross-sectional area also has large effect.

Figure 8. Photo from four-point bending test.

Figure 9. Detail of the purenit rib shear failure.

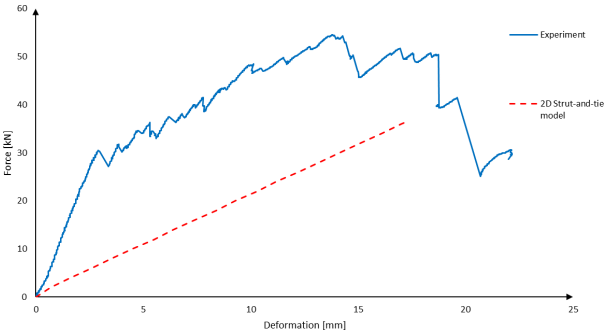

Figure 10. Experiment vs. strut-and-tie model.

6. Conclusion

The strut-and-tie model provides results which are "on the safe side" so this model could be used for the approximate design of the precast concrete sandwich panels but doesn't perfectly describe the real behaviour. To achieve more accurate results could be useful to use some software for nonlinear analysis like ATENA etc. The results could be affected by geometric differences between strut-and-tie model and the real panel. In the real panel the angle of shear reinforcement was 45°, in the model it was 38.65°. The results also could be affected by violation of the shear reinforcement during the creation of the panel which could lead to former shear reinforcement failure than expected. There is also a problem with small number of samples because the only one sample was tested which means that the result isn't statistically significant.

Acknowledgements

The work on this paper was supported by Czech Science Foundation Grant No. 22-14942K entitled "Possibilities of using natural fibers for the production of hybrid textile reinforcement in concrete". The authors would like to acknowledge all financial assistance provided to support this research.

References

[1] A. Einea, D. C. Salmon, G. J. Fogarasi, et al. State-of-the-art of precast concrete sandwich panels. *PCI journal* **36**(6):79–98, 1991. https://doi.org/10.15554/pcij.11011991.78.98

[2] R. O'Hegarty, O. Kinnane, M. Grimes, et al. Development of thin precast concrete sandwich panels: Challenges and outcomes. *Construction and Building Materials* **267**:120981, 2021. https://doi.org/10.1016/j.conbuildmat.2020.120981

[3] R. O'Hegarty, R. West, A. Reilly, O. Kinnane. Composite behaviour of fibre-reinforced concrete sandwich panels with FRP shear connectors. *Engineering Structures* **198**:109475, 2019. https://doi.org/10.1016/j.engstruct.2019.109475

[4] A. Benayoune, A. A. Abdul Samad, D. N. Trikha, et al. Flexural behaviour of pre-cast concrete sandwich composite panel – experimental and theoretical investigations. *Construction and Building Materials* **22**(4):580–592, 2008. https://doi.org/10.1016/j.conbuildmat.2006.11.023

[5] K. Hodicky, T. Hulin, J. W. Schmidt, H. Stang. Structural performance of new thin-walled concrete sandwich panel system reinforced with BFRP shear connectors. In *Proceedings of the 4th Asia-Pacific Conference on FRP in Structures*. 2013. https://doi.org/10.25916/sut.26269924.v1

[6] M. Flansbjer, N. Williams Portal, D. Vennetti, U. Mueller. Composite behaviour of textile reinforced reactive powder concrete sandwich façade elements. *International Journal of Concrete Structures and Materials* **12**(1):71, 2018. https://doi.org/10.1186/s40069-018-0301-4

[7] A. Shams, M. Horstmann, J. Hegger. Experimental investigations on textile-reinforced concrete (TRC) sandwich sections. *Composite structures* **118**:643–653, 2014. https://doi.org/10.1016/j.compstruct.2014.07.056

[8] J.-Q. Huang, J.-G. Dai. Direct shear tests of glass fiber reinforced polymer connectors for use in precast concrete sandwich panels. *Composite structures* **207**:136–147, 2019. https://doi.org/10.1016/j.compstruct.2018.09.017

[9] Czech Office for Standards, Metrology and Testing. ČSN EN 12390-3. Zkoušení ztvrdlého betonu – Část 3: Pevnost v tlaku zkušebních těles [In Czech], 2020.

[10] Czech Office for Standards, Metrology and Testing. ČSN EN 12390-5. Zkoušení ztvrdlého betonu – Část 5: Pevnost v tahu ohybem zkušebních těles [In Czech], 2020.

[11] Izolace-info.cz. Purenit – přesvědčivý funkční materiál s rozmanitým využitím [In Czech]. https://www.izolace-info.cz/technicke-informace/zateplovanifasady-1/22656-purenit-presvedcivy-funkcni-material-s-rozmanitym-vyuzitima.html

[12] J. Macháček. *Vliv smykové kompozitní výztuže na únosnost betonových sendvičových panelu [In Czech; Influence of composite shear reinforcement on bearing capacity of concrete sandwich panels]*. Master's thesis, Czech Techical University in Prague, 2022.

EXPERIMENTAL OF VERIFICATION OF ALTERNATIVE HYDRAULIC BINDERS FLEXURAL AND COMPRESSIVE STRENGTH

Aleš Palička[a,*], Zdeněk Prošek[a,b], Pavel Tesárek[a]

[a] *Czech Technical University in Prague, Faculty of Civil Engineering, Department of Mechanics, Thákurova 7, 166 29 Prague, Czech Republic*

[b] *Czech Technical University in Prague, University Centre for Energy Efficient Buildings, Třinecká 1024, 273 43 Buštěhrad, Czech Republic*

[*] corresponding author: ales.palicka@fsv.cvut.cz

Abstract. The paper deals with the investigation of alternative binders, namely the two available samples N6 and N7 with comparison from the reference sample CEM I 42.5R. Both testing binders are provided by company Destro. It is a product that contains different ratios of fly ash and slag. By examining the properties, the mix was compared in different proportions and subsequently tested for flexural strength and compressive strength. The results showed the effect of curing time and cement to binder ratio after 28 and 84 days.

Keywords: Alternative binder, fly ash, cement pastes, compressive strength, flexural strength.

1. Introduction

Nowadays, the use of alternative binders is becoming more and more popular in the construction industry as a replacement for cement. The use is more mainstream among the main objectives is to reduce CO_2 emissions that are produced in the production of cement with the high energy requirement for the creation. Individual introduction to alternative binders such as fly ash, which can be characterized as a fine-grained powder with a glassy structure that is produced as a waste material from the combustion of anthracite, lignite, and hard coal, where it is captured from the resulting gases by electrostatic or mechanical separators. Due to the numerous production processes using different types of boilers, combustion techniques, separation methods, and types of coal burned, the resulting ash can have quite variable chemical, mineralogical, and granulometric compositions. In the concrete industry, more use is made of fly ash produced from hard coal, as it is not as variable as brown coal fly ash. Slag is a coarse-grained substance of black to gray shade that may be of natural origin, i.e., volcanic or a product of the metallurgical industry, where it is produced as a waste product of iron or steel production. Previous scientific findings with the implementation of alternative concepts have shown promising results as described by A. Mohamed in his scientific work, where he observes the evolution of strength and rapid reactivity of the slag, where the results of the S1F1 (composed of slag and fly ash in a 50/50 ratio) pattern obtained remarkable results [1], A closer scientific evaluation is described by the scientific work of V. Shobeiri., where it relies on minimization of GWP (global warming potential) in concrete and replacement of SCM (supplied cementitios material) depending on OPC (ordinary portland cement) by supplementary materials [2]. Unfortunately, experimental methods require extensive experimentation and archiving so that we can meet the Paris Agreement on CO_2 reduction, and these experiments are often on a trial-and-error [3]. The experiment deals with selected N6 and N7 binders from different suppliers as replacement cement:

(1.) Binder N6 – Destrocement (fly ash),

(2.) Binder N7 – Destrocement (slag and fly ash).

Another reason is the cost per mix and the approximation of the same or better properties to Portland concrete at a reduced price due to alternative binders that can be recovered from recycled material or incorporated as waste material. Subsequently, the use of this waste material significantly reduces the price of the mix.

2. Materials and samples

The test specimens with dimensions $40 \times 40 \times 160$ mm were manufactured according to EN 196-1 [4], using moulds. A total of 5 mixtures were created for testing purposes, and 6 specimens were created for each mixture. The total number of specimens produced was 30.

The actual production of the sample consisted of weighing the necessary raw materials in the given ratio of water, cement, and fine aggregate 0/2 and crushed slag in a laboratory balance with an accuracy of ± 1 g, which can be seen in the Table 1. For all formulations, a water coefficient of 0.718 was established and the workability of the fresh mix was measured, using a cone spill after 15 blows. After the raw materials were weighed, the individual materials were added to the mixing vessel. First cement with an alternative

Marking	CEM I 42.5R [kg]	Destrocement (fly ash) [kg]	Destrocement R [kg]	Fine aggregate (0/2 mm) [kg]	Water [kg]
REF	0.825	-	-	2.475	0.592
N6 30	0.578	0.248	-	2.475	0.592
N6 50	0.413	0.413	-	2.475	0.592
N7 30	0.578	-	0.248	2.475	0.592
N7 50	0.413	-	0.413	2.475	0.592

TABLE 1. Overview of mixtures.

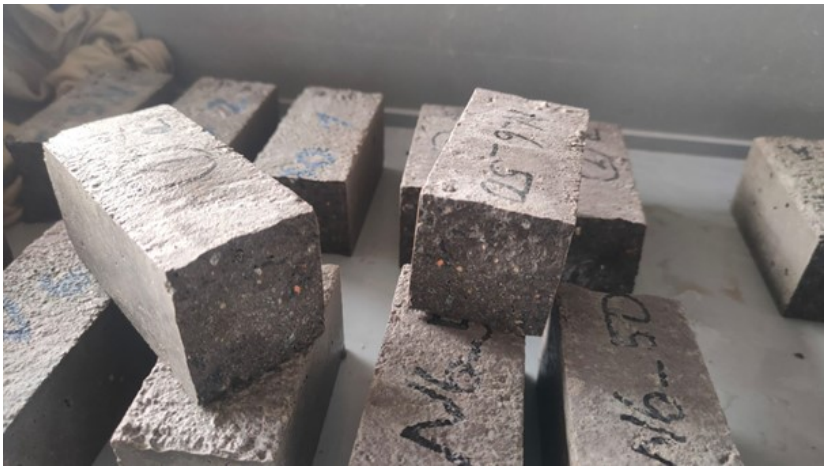

FIGURE 1. Detail of sample after destructive test.

binder due to mixing and losses. The third ingredient was water and the last was fine aggregate 0/2 and crushed slag. After all the ingredients were mixed, the material was filled into molds that were greased with a layer of forming oil for better removal of the sample after hardening. Immediately after the mixing was completed, the prepared steel triforms were filled about halfway with mortar using a spatula and the inner surface was painted with a thin layer of mineral oil. This first layer of mortar was further compacted. Finally, the mortar surface was aligned with the edges of the triforms using a spatula sawing motion and the samples were stored at an ambient temperature of $21 \pm 2\,°C$. After expiration of the time, the samples were and removed from the molds followed by marking the sample and placing it in a water bath at $20 \pm 5\,°C$ until testing time. Storage was carried out for half of the samples for 28 days and the other half for 84 days.

3. Experimental methods

The experiment was tested for flexural strength on the basis of EN 196-1 [4], on specimens of $40 \times 40 \times 160$ mm beams. After measuring and weighing, the specimen was placed on two hydraulic press supports spaced 100 mm apart. Using the software, the measurement was started by moving the hydraulic press at a speed of $1\,\text{mm}\,\text{min}^{-1}$ until the specimen was destroyed into two parts, which were further used for compressive strength measurements according to EN 196-1 [4]. Figure 1 shows the result after destructive testing, the main indicator being the resulting fracture and visible structure of the recycled compound used. This method investigated the introduction of compressive stress up to the time of specimen destruction. The specimen was used from the remaining two parts of the previous flexural strength test using a three-point arrangement. The body of the specimen was placed on the compression of the 40×40 mm machine. Then the hydraulic press displacement was started by the upper part displacement being constant throughout the test.

4. Results and discussion

The consistencies of the different mixtures in Figure 2 show us that as the cement values decrease, the spillage decreases. In Figure 3, we can see the bulk mass of each sample, which shows us the minimum variation with respect to the pore filling. From the measurements of the experiment using the three-point loading method to measure the flexural strength of the test specimens after a period of 28 and 84 days, the values shown in the Figure 4. The graph shows the strength range compared to the reference sample. The lower the cement content of the sample, the strength decreases. Interestingly, the destructiveness values at 50 % were like those of the reference sample after 84 days. For the N7 mixture, these values are even identical in strength at 30 % and 50 % of the mixture. For Fly ash N6 the reaction was confirmed after a longer curing time. Samples were tested using the uniaxial test after three points of testing. The highest and lowest compressive strength values were removed

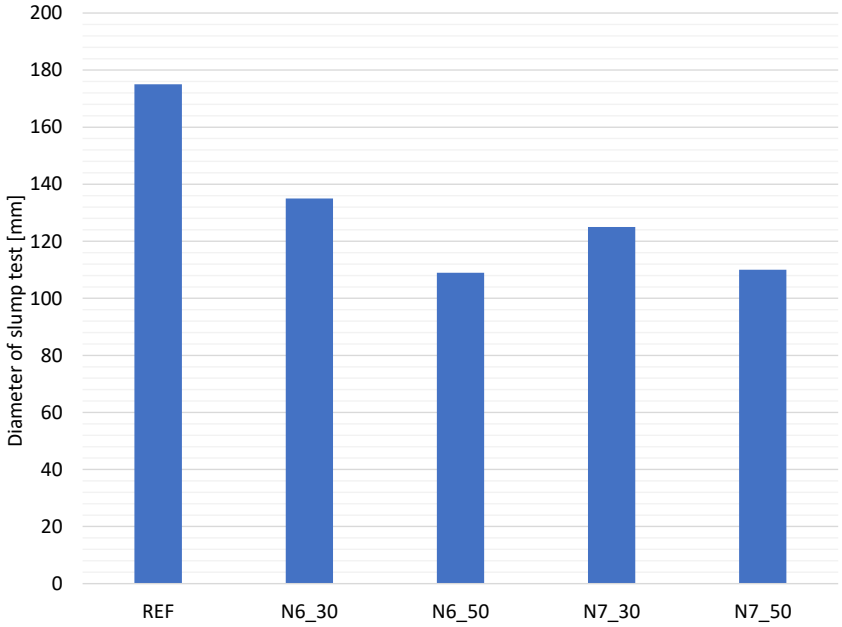

Figure 2. Spilling fresh mixture.

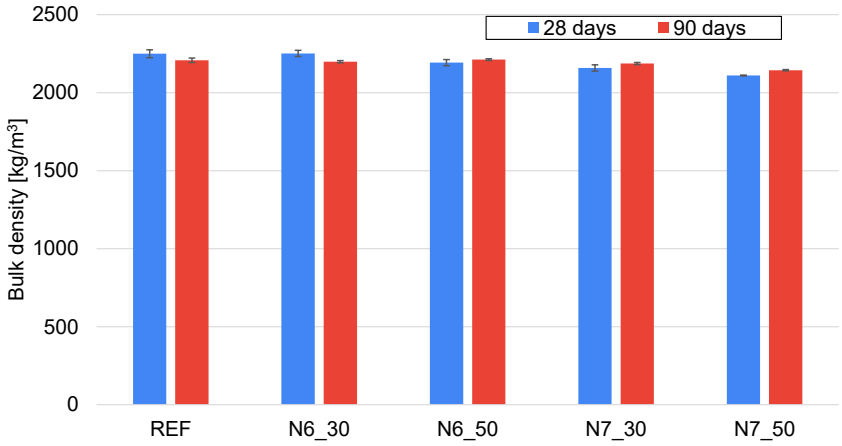

Figure 3. Bulk density of testing speciement with plotted standard deviations.

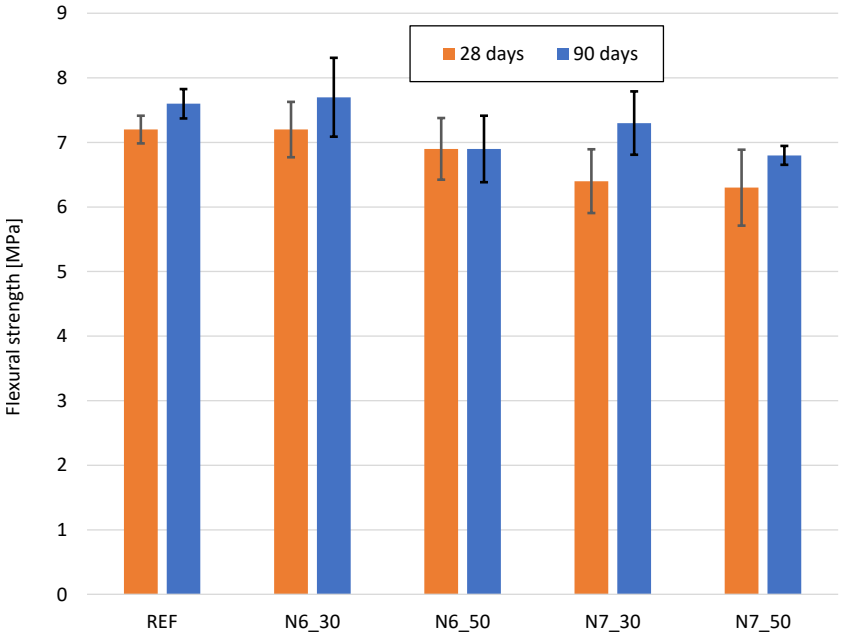

Figure 4. Flexural strength with plotted standard deviations.

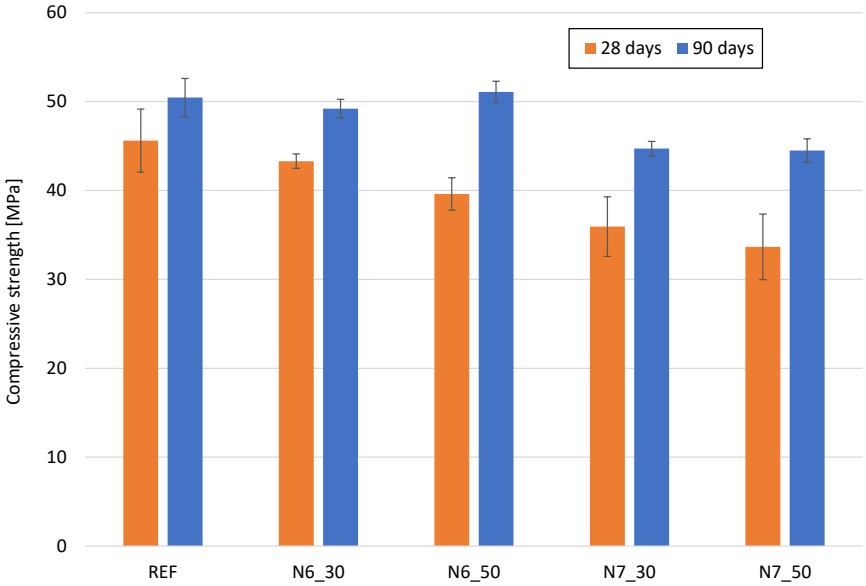

FIGURE 5. Compressive strength with plotted standard deviations.

from the obtained values and the arithmetic mean was removed from the remaining values, which can be seen in Figure 5. The result shows how the solidification time affects the strength of the samples and after 84 days the strength approaches the reference values. It is remarkable that for specimens N6 50 and N6 30 the values after 84 days are close. Similarly, for specimens N7 30 and N7 50 after 84 days, the values are in little difference.

Historically, although many studies have been conducted to quantify the effect of alternative binders on mechanical properties in concrete, the results were in mass agreement and had similar results. When alternative binders are applied as a partial replacement for CEM I, 42.5R materials such as slag and fly ash respond best after a longer curing time and therefore a higher strength increase can be observed after 90 days or more. Another factor affecting the individual mixes is the increase in the specific surface area due to the fineness of the material [5–7].

5. Conclusion

This work focuses on the effect of waste supplementary cementitious materials on the mechanical properties of cement pastes. Cement pastes are composed of mixed cement, where suplementary cementitious materials replaces Portland clinker. In our case, we used fly ash and slag. Supplementary cementitious materials were used in two different concentrations, namely: 30 wt. % and 50 wt. %. For our testing, the values for specimens N6 50 came out best in terms of replacement and applicability of alternative binders. For better observation and evaluation of the result, the curing time is a priority, which has a great influence on the properties of the different mixtures. A positive indicator is the reduction of hydration heat, which can be positively utilized. However, among the unpredictable factors in the application of an alternative binder, it is important to understand the origin of the material a qestion will be. Where the material was used, the method by which it was recycled and shredded, and the storage of the material. The aforementioned factors have implications for unforeseen admixtures that were not included. Therefore, it is worthwhile to establish a prescription for each future material to be recycled before use and recycling, so that it is appropriate for approximate laboratory conditions.

Considering all the results, the material can be used for construction works of a small nature, small weirs, walls, where the load is mainly caused by natural influences and high loads are not expected. The main limiting factor is the failure to guarantee the same properties of the alternative binder.

Acknowledgements

This paper was financially supported by Czech Technical University in Prague under No. SGS project GS24/037/OHK1/1T/11 and by the GA CR research a project under the number GA23-05500S. The authors also thank DESTRO for the supplied samples and materials.

References

[1] O. A. Mohamed, O. Najm, E. Ahmed. Alkali-activated slag & fly ash as sustainable alternatives to OPC: Sorptivity and strength development characteristics of mortar. *Cleaner Materials* **8**:100188, 2023. https://doi.org/10.1016/j.clema.2023.100188

[2] V. Shobeiri, B. Bennett, T. Xie, P. Visintin. Mix design optimization of concrete containing fly ash and slag for global warming potential and cost reduction. *Case Studies in Construction Materials* **18**:e01832, 2023. https://doi.org/10.1016/j.cscm.2023.e01832

[3] Beyond Zero Emissions. *Zero carbon industry plan: Rethinking cement*. Beyond Zero Emissions, 2017. ISBN 978-0-9923580-2-0.

[4] Úřad pro technickou normalizaci, metrologii a státní zkušebnictví. ČSN EN 196-1. Metody zkoušení cementu – Část 1: Stanovení pevnosti [In Czech; Methods of testing cement – Part 1: Determination of strength], 2016.

[5] J. Skibsted, R. Snellings. Reactivity of supplementary cementitious materials (SCMs) in cement blends. *Cement and Concrete Research* **124**:105799, 2019. https://doi.org/10.1016/j.cemconres.2019.105799

[6] L. E. Burris, M. C. Juenger. Effect of calcination on the reactivity of natural clinoptilolite zeolites used as supplementary cementitious materials. *Construction and Building Materials* **258**:119988, 2020. https://doi.org/10.1016/j.conbuildmat.2020.119988

[7] M. M. A. Elahi, C. R. Shearer, A. Naser Rashid Reza, et al. Improving the sulfate attack resistance of concrete by using supplementary cementitious materials (SCMs): A review. *Construction and Building Materials* **281**:122628, 2021. https://doi.org/10.1016/j.conbuildmat.2021.122628

VALIDATION OF GEOTECHNICAL LABORATORY TESTS DATA OBTAINED FROM VARIOUS SOURCES

Veronika Pavelcová[a,*], Tomáš Janda[b]

[a] *Czech Technical University in Prague, Faculty of Civil Engineering, Department of Geotechnics, Thákurova 7, 166 29 Prague, Czech Republic*

[b] *Czech Technical University in Prague, Faculty of Civil Engineering, Department of Mechanics, Thákurova 7, 166 29 Prague, Czech Republic*

[*] corresponding author: veronika.pavelcova@fsv.cvut.cz

Abstract. Data validation is a critical step in every data analysis. It is a well-known fact that the results of any data analysis are directly dependent on the input values. This paper works with a worldwide database of laboratory tests collected during four year operation of web calibration application ExCalibre and elaborates on the data correctness. ExCalibre application enables automatic calibration of three critical state models based on data from standard laboratory tests. The paper presents the rules and overall methodology for checking the validity of laboratory tests data and summarises the obtained results.

Keywords: Geotechnical laboratory test, data validation, data processing, error, warning, database.

1. Introduction

General observation of usage non-linear geotechnical material models for soils shows that the majority of practical engineers limit themselves to the use of basic non-linear soil models of the Mohr-Coulomb or Drucker-Prager type when solving standard geotechnical tasks. Although these models are sufficient when describing approximate interaction of the structure and the subsoil, some complex tasks require more sophisticated solutions. Critical state models allow for more accurate behaviour prediction, however, they are not as widely used as they could be. The general lack of knowledge of these advanced material models among practical engineers may be one of the reasons.

The second reason is the significantly higher difficulty of determination of advanced non-linear models input parameters in comparison to the basic models. Critical state models require prescription of parameters describing the behaviour of the given material under isotropic compression along with parameters characterising the current state of the soil.

Presented and previous work presented in *Extracting General Knowledge of Model Parameters for Clays out of Numerous Laboratory Tests* [1] is motivated by this non-straight-forward determination of input parameters and works forward to simplify the determination process by using knowledge extracted out of all of the data collected during four year operation of web calibration application ExCalibre [2–4]. This application enables automatic calibration of three advanced constitutive soil models based on detailed data from triaxial and oedometric tests [5]. After finishing all data preparation steps, Bayesian inference methods [6] will be used to set confidence intervals for each material parameter that governs critical state models.

2. ExCalibre

As mentioned before, ExCalibre web application laboratory test database is the main source of data processed in presented research. The application was developed by Faculty of Civil Engineering of CTU in Prague in cooperation with the Faculty of Science of Charles University. It runs from 2018 and performs automatic deterministic calibration of the hypoplastic model for sands [7], hypoplastic model for clays [8, 9] and modified Cam-clay model [10]. A typical workflow of model calibration using ExCalibre is the following:

(1.) Downloading a laboratory protocol template which is prepared in the form of an MS Excel file. The template differs for fine-grained and coarse-grained soils.

(2.) Filling in the results of laboratory tests. A minimum of one isotropically consolidated undrained (CIUP) triaxial test with pore pressure measurement for clay soils or one isotropically consolidated drained (CID) triaxial test for sandy soils must be filled in for successful calibration. In addition, one standard oedometric (OED) test is necessary.

(3.) Uploading the laboratory protocol spreadsheet to the ExCalibre web application. As a result, the application proposes optimal model parameters and graphs comparing the course of measured and simulated laboratory tests.

(4.) Manual modification of individual model parameters by user if required.

The main advantage of all these critical state models is that they distinguishes between material parameters that are constant for all possible states of a particular soil and state variables that evolve during straining. In this sense critical state models are fundamentally

Parameter	Data type	Note
USCS	string	
Specific gravity	float	[g cm^{-3}]
Liquid limit	float	[%]; only fine-grained soils
Plastic limit	float	[%]; only fine-grained soils
Angle of repose	float	[°]; only coarse-grained soils
Soil gradation	2D array	size (2, n); sieve size [mm] – passing [%]

Table 1. Data extracted from IDX AND GRAD worksheet.

Parameter	Data type	Note
Initial void ratio	float	[-]
Oedometric test data record	2D array	dimension (2, n); axial stress [kPa] – axial deformation [-]

Table 2. Data extracted from OED-NAT-n or OED-REC-n worksheet.

different from the Mohr-Coulomb model which employs distinct values of its material parameters for the same soil in different density states.

3. Protocol structure

As mentioned above, laboratory tests uploaded to ExCalibre application are all in the form of pre-prepared template file in MS Excel. This means that all protocols should contain the same type of data and should keep the same structure. Although template differs for fine-grained and coarse-grained soils, the majority of data worksheets remains the same. The only difference is the type of prescribed triaxial test. The content of the individual worksheets of the workbook will be described gradually.

3.1. NOTES worksheet

The introductory worksheet of any laboratory protocol is named NOTES and it contains basic information about sampling: soil type, sampling location, sampling depth, sampling method and possible notes of the laboratory technician. This worksheet is the same for both fine-grained and coarse-grained soils and no data from this worksheet are currently being further processed.

3.2. IDX AND GRAD worksheet

Another type of the laboratory protocol worksheet is named IDX AND GRAD. This worksheet contains soil classification, index characteristics and grain size analysis. This worksheet is the same for both fine-grained and coarse-grained soils. Extracted data to further statistical processing from this worksheet are summarised in Table 1.

3.3. OED-NAT-n worksheet or OED-REC-n worksheet

The laboratory protocol worksheet named OED-NAT-n contains a record of an oedometric test of naturally consolidated soil. The laboratory protocol worksheet named OED-REC-n contains a record of an oedometric test of the reconstituted soil sample. The symbol n in the label of the worksheet indicates the order of the oedometric test, in other words, it represents an increasing integer sequence. This worksheet is the same for both fine-grained and coarse-grained soils. Extracted data to further statistical processing from this worksheet are summarised in Table 2.

3.4. CIUP-NAT-n worksheet or CIUP-REC-n worksheet

The first type of triaxial laboratory protocol worksheet is named CIUP-NAT-n or CIUP-REC-n. CIUP-NAT-n laboratory protocol worksheet contains a record of a consolidated isotropically undrained triaxial test with pore pressure measurement of a naturally consolidated soil. The laboratory protocol worksheet named CIUP-REC-n contains a record of a consolidated isotropically undrained triaxial test with the measurement of the pore pressure of the reconstituted soil sample. The symbol n in the label of the worksheet indicates the order of the CIUP triaxial test, same as in the case of an oedometric test. This worksheet is used only for fine-grained soils. Extracted data to further statistical processing from this worksheet are summarised in Table 3.

3.5. CID-REC-n worksheet

The other, and last described, type of laboratory protocol worksheet is named CID-REC-n. It contains a record of a consolidated isotropically drained triaxial test of the reconstituted soil sample. The template does not assume the possibility of performing CID triaxial test of naturally consolidated test as soil sampling usually disrupts soil integrity. The symbol n in the label of the worksheet again indicates the order of the triaxial test. This worksheet is used only for coarse-grained soils and extracted data to further statistical processing from this worksheet are summarised in Table 4.

Parameter	Data type	Note
Initial void ratio	float	[-]
Initial mean effective stress	float	[kPa]
Triaxial test data record	2D array	dimension (3, n); axial deformation [-] – mean effective stress [kPa] – axial deviatoric stress [kPa]

TABLE 3. Data extracted from CIUP-NAT-n or CIUP-REC-n worksheet.

Parameter	Data type	Note
Initial void ratio	float	[-]
Radial effective stress	float	[kPa]
Triaxial test data record	2D array	dimension (4, n); axial deformation [-] – radial effective stress [kPa] – axial deviatoric stress [kPa] – volumetric deformation [-]

TABLE 4. Data extracted from CID-NAT-n or CID-REC-n worksheet.

4. Data validation

Data validation is a critical step in data preparation for statistical processing as the results of any data analysis are directly dependent on the input values. Even though pre-prepared templates for laboratory protocols uploaded to ExCalibre calibration application help prevent users error inputs, it cannot be assumed that the uploaded data are free of errors. ExCalibre itself does not implement a data validation at this time. Due to this fact and worldwide variability of users it was necessary to validate all data inputs that will be further statistically processed.

A set of rules that should catch all types of error data was created. All rules has been consulted with the head of the geotechnical laboratory at the Faculty of Science of Charles University, the lab technician with many years of practical experience. Created algorithm works on first-catch principle and distinguishes between two levels of error severity. So called *warnings* draw attention to values that are physically possible but not probable to occur and therefore require increased attention. On the other hand, *errors* notify values that should not occur under any circumstances. However, these rules are not strict. They were created based on years of experience not statistical observation. Another important note is the fact that the rules described below are created for soils which physical behaviour can be represented using Modified Cam-Clay, hypoplastic clay or hypoplastic sand model for soils. They do not consider, for example, highly organic soils, which are not suitable for ExCalibre calibration and would not comply with most of the stated rules.

All controls are performed cyclically in a predetermined logical order for all uploaded laboratory protocols. Then it forms two additional dataframe columns, one with a possible caught warning and the other with a caught error. In the algorithm described, the key of mentioned dataframe corresponds to the name of one laboratory protocol. Key values are assigned so that one line of the dictionary represents characteristic data of one laboratory protocol presented in Section 3. Any automated interventions into protocols are avoided. All necessary data corrections or protocol discarding will be done individually and manually with respect to all laboratory protocol data.

4.1. Warning rules

Overall 19 warning rules were created. Individual rules are listed below. The order in which the rules are listed corresponds to the order in which they are implemented in the script.

4.1.1. IDX AND GRAD worksheet

(1.) Specific gravity is out of 2.5–2.9 $\mathrm{g\,cm^{-3}}$ interval.

(2.) Liquid limit is greater than 150.0 %.

(3.) Plastic limit is greater than 60.0 %.

(4.) Angle of repose is lower than 30.0° or greater than 40.0°.

(5.) Angle of repose exists but soil consists of more than 10.0 % of fine grains (smaller than 0.063 mm).

(6.) Number of soil gradation inputs is lower than 5.

(7.) The first soil gradation passing is lower than 100 % but greater than 95.0 %.

(8.) Soil gradation sieve for the first non 100.0 % passing is out of 0.001–63.0 mm interval.

4.1.2. OED-NAT-n worksheet or OED-REC-n worksheet

(1.) Number of oedometric test data inputs is lower than 5.

(2.) Axial deformation is negative.

4.1.3. CIUP-NAT-n worksheet or CIUP-REC-n worksheet

(1.) Number of CIUP test data inputs is lower than 50.

(2.) Maximal axial deformation is lower than 1.0 %.

(3.) Initial mean effective stress is out of 20.0–2 000.0 kPa interval.

(4.) Initial axial deviatoric stress is greater than 10.0 kPa.

4.1.4. CID-REC-n worksheet

(1.) Number of CID test data inputs is lower than 50.

(2.) Maximal axial deformation is lower to 1.0 %.

(3.) Initial radial effective stress is out of 20.0–2 000.0 kPa interval.

(4.) Initial deviatoric stress is greater than 10.0 kPa.

(5.) Absolute value of maximal volumetric deformation is greater than 0.5 %.

4.2. Error rules

Overall 24 error rules were created. Individual rules are listed below. The order in which the rules are listed corresponds to the order in which they are implemented in the script.

4.2.1. IDX AND GRAD worksheet

(1.) Specific gravity is out of 2.0–3.2 g cm^{-3} interval.

(2.) Plastic limit is greater than or equal to liquid limit.

(3.) Liquid limit is greater than 500.0 %.

(4.) Plastic limit is greater than 80.0 %.

(5.) Angle of repose is lower than 25.0° or greater than 45.0°.

(6.) Angle of repose exists but soil consists of more than 20.0 % of fine grains (smaller than 0.063 mm).

(7.) Number of soil gradation inputs is 0.

(8.) The first soil gradation passing is lower than 95.0 %.

(9.) Soil gradation passing is increasing.

(10.) Any soil gradation passing is negative.

4.2.2. OED-NAT-n worksheet or OED-REC-n worksheet

(1.) Number of oedometric test data inputs is 0.

(2.) Initial void ratio is out of 0.2–3.5 interval.

(3.) Axial stress is out of 1.0–10 000.0 kPa interval.

(4.) Initial axial deformation is non-zero.

4.2.3. CIUP-NAT-n worksheet or CIUP-REC-n worksheet

(1.) Number of CIUP test data inputs is 0.

(2.) Initial axial deformation is non-zero.

(3.) Axial deformation is decreasing (tolerating noise).

(4.) Axial deviatoric stress is negative.

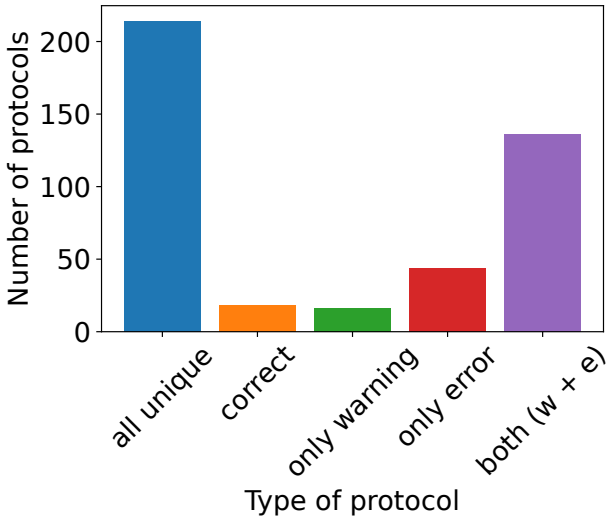

Figure 1. Summary of correct and incorrect laboratory protocols.

4.2.4. CID-REC-n worksheet

(1.) Number of CID test data inputs is 0.

(2.) Initial axial deformation is non-zero.

(3.) Axial deformation is decreasing (tolerating noise).

(4.) Radial effective stress is not constant.

(5.) Axial deviatoric stress is negative (tolerating noise).

(6.) Initial volumetric deformation is non-zero.

Soil index characteristics and granular analysis depend only on the type of soil. Therefore, it was possible to determine the limit values for individual parameters. On the other hand, the data record of oedometric, and especially triaxial, tests can vary greatly depending on the tested soil and the chosen test procedure. For this reason, it was usually impossible to determine error limits for the individual parameters that govern these tests. Thus, the control rules for these tests were mainly limited to the detection of erroneously entered units of measurement and evident physically impossible results rather than the definition of individual limit values.

5. Results

Out of 214 unique laboratory protocols, only 18 seem to be correct as they passed data validation check without any findings. Another 16 protocols have only warnings, no errors and conversely, 44 protocols have only errors and no warnings. Finally, there are 136 protocols left that have both warning's and error's detection. This observation is clearly summarised in Figure 1. However, this figure does not say anything about the amount of errors that each protocol contains.

Figure 2 shows the total detection of invalid data for each protocol, warnings (Figure 2a) and errors (Figure 2b) separately. These counts are related to an

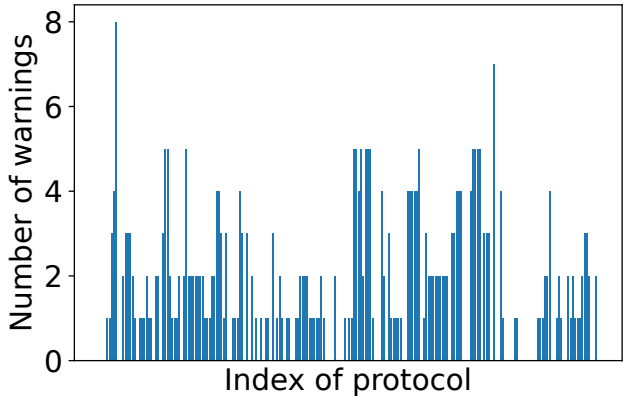

(A). Warnings.

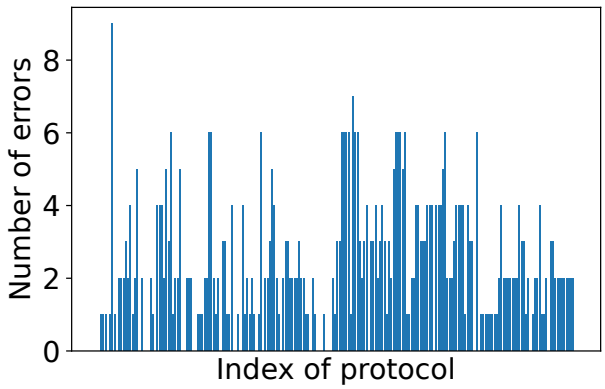

(B). Errors.

FIGURE 2. Number of warnings and errors detected in each laboratory protocol.

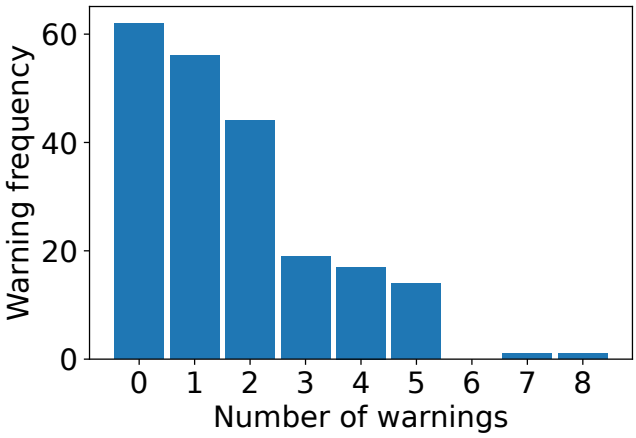

(A). Warnings.

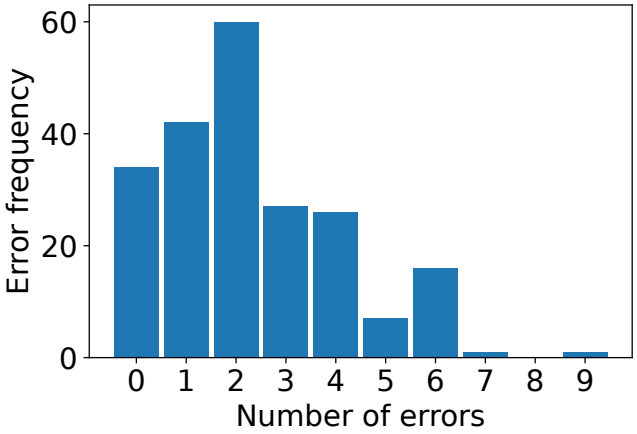

(B). Errors.

FIGURE 3. Histograms of warnings and errors detected in laboratory protocols.

index that is unique to each laboratory protocol and with which the protocol is identified. It can be seen that no more than 8 warnings or 9 errors were found in any of the protocols. Majority of protocols reports about 0–2 warnings and 0–4 errors. Histograms in Figure 3 clearly demonstrates this trends.

Table 5 and Table 6 summarise total number of occurrences of individual warnings and errors across all protocols. It can be observed that the most erroneous data were captured in data characterising sandy soils, namely existence of angle of repose for clay soils (control rule 4.1.1.5 and 4.2.1.6) or invalid record of CID triaxial test (control rules 4.1.4 and 4.2.4). Another recurring error are non-zero deformations or unsecured contact of piston and soil sample at the beginning of the deformation tests, most observed during oedometric tests (control rule 4.2.2.3 and 4.2.2.4).

It should be mentioned that the absolute counts of invalid data can be distorted by the repetition of individual problems as part of the control rules are interconnected, meaning that if one data is entered incorrectly and multiple rules are created to check its properties, an error will be displayed for multiple rules, although only one data value is missing or incorrect.

6. CONCLUSION

The paper introduced the reader to the origin of the researched laboratory protocols, their original use for the calibration of advanced material models in the ExCalibre web application, and the possibility of their future use in statistical analysis. The importance of checking any input data before statistical processing and the effect of invalid data on the results of statistical analysis was pointed out. The content of the geotechnical laboratory test template for ExCalibre application was presented by individual sheets of the Excel workbook in detail. The paper described the methodology chosen by the authors for data validation and specifically states all control rules applied during the control to individual characteristic of laboratory protocol. Finally, the results of the application of the control mechanism to the given data were summarised.

The specific purpose of this work was to give an initial estimation of how the real data collected in the laboratory protocols are realistic and physically possible. A manual control by a natural person is the necessary next step in data control. Attention will be paid only to individual data detected by the control rules listed in Section 4. The correction or removal of

	4.1.1. IDX AND GRAD								4.1.2. OED	
No. warning	1.	2.	3.	4.	5.	6.	7.	8.	1.	2.
Frequency	14	1	0	5	56	21	25	4	2	6

	4.1.3. CIUP				4.1.4. CID				
No. warning	1.	2.	3.	4.	1.	2.	3.	4.	5.
Frequency	40	11	4	19	28	35	3	44	38

Table 5. Frequency of each warning detected in laboratory protocols.

	4.1.1. IDX AND GRAD										4.1.2. OED			
No. error	1.	2.	3.	4.	5.	6.	7.	8.	9.	10.	1.	2.	3.	4.
Frequency	0	0	1	0	0	50	18	22	5	0	0	0	77	87

	4.1.3. CIUP				4.1.4. CID					
No. error	1.	2.	3.	4.	1.	2.	3.	4.	5.	6.
Frequency	0	26	2	12	17	43	17	49	13	55

Table 6. Frequency of each error detected in laboratory protocols.

values marked as invalid will always be decided with regard to the overall properties of the tested soil. It is possible that in the course of manual corrections some rules will have to be modified or new rules added. However, the rules presented here are based on years of practical experience in the laboratory and as such they can provide guidance to other researchers dealing with similar issues of validation of standard geotechnical laboratory test records.

This paper, together with previously published *Extracting General Knowledge of Model Parameters for Clays out of Numerous Laboratory Tests* [1], presents in detail one of the options for dealing with the task of preparation of data originating from an MS Excel file for statistical processing using automatic scripts. The further progress of statistical data processing will be presented in the future.

Acknowledgements

The support provided by the SGS project No. SGS23/032/OHK1/1T/11 and the GAČR project No. 22-12178S is gratefully acknowledged.

References

[1] V. Pavelcová, T. Janda. Extracting general knowledge of model parameters for clays out of numerous laboratory tests. In *Acta Polytechnica CTU Proceedings*, vol. 40, pp. 76–82. 2023. https://doi.org/10.14311/APP.2023.40.0076

[2] T. Kadlíček, T. Janda, M. Šejnoha, et al. Automated calibration of advanced soil constitutive models. Part I: hypoplastic sand. *Acta Geotechnica* **17**(8):3421–3438, 2022. https://doi.org/10.1007/s11440-021-01441-0

[3] T. Kadlíček, T. Janda, M. Šejnoha, et al. Automated calibration of advanced soil constitutive models. Part II: hypoplastic clay and modified Cam-Clay. *Acta Geotechnica* **17**(8):3439–3462, 2022. https://doi.org/10.1007/s11440-021-01435-y

[4] ExCalibre. SoilModels Automatic Calibration. [2023-07-26]. https://soilmodels.com/excalibre-cs/

[5] T. Janda, D. Mašín. General method for simulating laboratory tests with constitutive models for geomechanics. *International Journal for Numerical and Analytical Methods in Geomechanics* **41**(2):304–312, 2017. https://doi.org/10.1002/nag.2558

[6] J. Kruschke. *Doing Bayesian data analysis: A tutorial with R, JAGS, and Stan*. Academic Press, 2014. ISBN 978-0-12-405888-0.

[7] P.-A. von Wolffersdorff. A hypoplastic relation for granular materials with a predefined limit state surface. *Mechanics of Cohesive-frictional Materials* **1**(3):251–271, 1996. https://doi.org/10.1002/(sici)1099-1484(199607)1:3<251::aid-cfm13>3.0.co;2-3

[8] D. Mašín. A hypoplastic constitutive model for clays. *International Journal for numerical and analytical methods in Geomechanics* **29**(4):311–336, 2005. https://doi.org/10.1002/nag.416

[9] D. Mašín. Clay hypoplasticity with explicitly defined asymptotic states. *Acta Geotechnica* **8**(5):481–496, 2013. https://doi.org/10.1007/s11440-012-0199-y

[10] K. H. Roscoe, J. B. Burland. On the generalized stress-strain behaviour of wet clay. In *Engineering plasticity*, pp. 535–609. Cambridge University Press, 1968.

QCT/FEA ANALYSES OF PALATELESS SPLINTED AND UNSPLINTED MAXILLARY ALL-ON-4 SYSTEMS

Luboš Řehounek[a,*], Mária Frolo[b], Aleš Jíra[a]

[a] *Czech Technical University in Prague, Faculty of Civil Engineering, Department of Mechanics, Thákurova 7, 166 29 Prague, Czech Republic*

[b] *Charles University, Faculty of Medicine in Pilsen, Department of Stomatology, Alej Svobody 1655/76, 323 00 Pilsen, Czech Republic*

[*] corresponding author: lubos.rehounek@fsv.cvut.cz

Abstract. The goal of the presented study was to determine the viability of using splinted and unsplinted maxillary implant-supported overdentures. The main physical quantity used to evaluate their differences was compressive stress in bone and equivalent (von Mises) stress in the implant and overdenture components. We took a 3D X-ray scan of the maxilla and imported the data into a QCT/FEA (Quantitative Computed Tomography-based Finite Element Analysis) software. The loading was done in three load cases. We designed both models of the overdentures in CAD, included the polyetheretherketone (PEEK) overdenture and analyzed the whole model of the reconstructed maxilla with implants. The results show worse (more concentrated) compressive stress distributions for the unsplinted locator variant. The splinted, bar-retained variant shows lower values of stress in all load cases. These findings and their potential for real-time selection of the optimal variant are then further discussed.

Keywords: QCT/FEA, implant-supported overdenture, splinted, unsplinted, all-on-4.

1. Introduction

Alongside conventional methods including removable dentures, there has been a growing share of implant-based solutions since the formal acceptance of dental implants for tooth loss rehabilitation in 1978. These implants can either serve in fixed restorations or to stabilize complete removable dentures, as shown by an implant-supported overdenture (IOD) [1]. It is vital for this treatment option to have thorough assessment, with its indications initially outlined in the 1990s [2]. This option proves to be advantageous for patients with limited bone quality [3]. Edentulousness has been following a downward trend for over 10 years, but there is still a global concern due to demographic shifts towards an aging population.

Connecting the overdenture to the supporting dental implants can be done by various types of attachments including both unsplinted and splinted designs (bars and clips) [5–7]. To date, consensus has not been reached regarding the superior option [8]. Bar-supported (splinted) restorations offer better retention and show improved stability for dentures [9]. Bars can withstand lateral motion and rotation during function, facilitating a more even distribution of force across fixtures [7, 10]. However, their application may elevate the likelihood of mucosal issues and hyperplasia due to suboptimal oral hygiene [11].

While the unsplinted design may have its advantages in terms of treatment simplicity, duration, hygiene, and cost [12], evidence regarding the impact of splinting versus non-splinting on the load distribution of upper jaw overdentures remains relatively limited and sometimes contradictory [13]. In a literature review with a comparable follow-up duration, survival rates are 88.9 % for unsplinted implants in the upper jaw, whereas splinted attachments showed an implant survival rate exceeding 97 % [14].

The absence of standardized techniques, implant quantities, differing measurements of marginal bone and loading conditions in studies may contribute to the subjective preference for unsplinted or splinted attachments for maxillary overdentures [2]. Therefore, a more precise assessment of the biomechanical distinctions between these two alternatives is needed.

To simplify complex problems into a system of algebraic equations, we can use the finite element method (FEM) that provides insights into the behavior of the analyzed system. FEM proves beneficial in solving intricate geometries, achieving numerical solutions for highly complicated stress problems via finite element analysis (FEA) [15]. This technique has been effectively applied in examining stress and strain in implant dentistry [16]. With the increasing availability of 3D imaging techniques, such as quantitative computed tomography (QCT), accurate reconstruction of the upper jaw bone is now possible, enabling QCT/FEA for analyses of stress distributions at the bone-implant interface.

This study aims to compare stress distribution in the maxillary bone, dental implants, and prosthetic components of upper jaw overdentures in both splinted and unsplinted designs, using QCT/FEA. The null hypothesis is that the splinted design will demonstrate

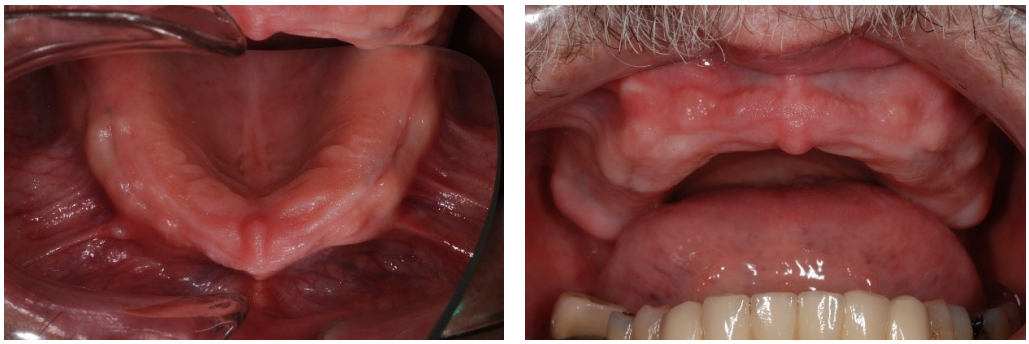

(A). Occlusal view. (B). Front view.

Figure 1. The view of the patient's residual alveolar ridge [4].

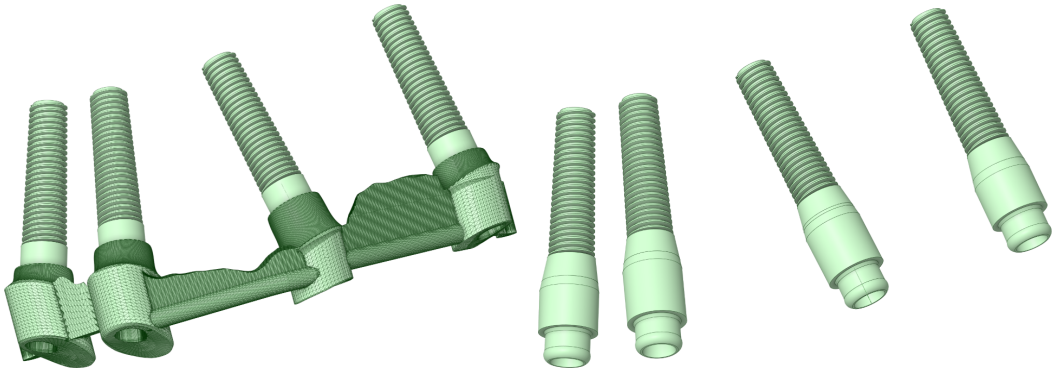

(A). The splinted, bar-supported variant. (B). The unsplinted, locator-supported variant.

Figure 2. Analyzed variants of the All-on-4 system. Assemblies designed to fit the individual patient. Geometries are identical, short of the splints [4].

superior biomechanical performance compared to the unsplinted design. To validate or refute this hypothesis, this study focuses on these two types of IODs.

Usually, other authors' analyses use a two-phase (cortical and cancellous) linearly elastic, homogeneous model. However, these assumptions do not adequately mirror the intricate nature of bone tissue [17]. The use of 3D imaging and QCT/FEA can offer more realistic simulations of bone-implant interface behavior [18]. The present study aims to provide more precise results of biomechanical performance of implant-supported upper jaw overdentures by using a more detailed model.

2. Materials and Methods

The anonymous patient who provided his 3D X-ray data for this study was a 76-year-old male with sufficient dexterity. We had obtained the patient's written consent prior to conducting the study.

All extraoral and intraoral criteria for an implant-supported overdenture in the maxilla were met [3]. Buccal inclination of the residual ridge (Figure 1) was present. The patient was predetermined for an anterior maxillary concept based on insufficient bone quality in distal regions, but sufficient quality in the frontal region.

The implants used were manufactured by Straumann (SLA RN SP Roxolid®) and placed in sites with good bone quality as follows: the upper-right first premolar (4.8 mm in diameter, 14 mm in length), upper-right first incisor (3.3 mm in diameter, 12 mm in length), upper-left second incisor (4.1 mm in diameter, 12 mm in length), and upper-left first premolar (4.1 mm in diameter, 12 mm in length). The 3D X-ray scans were acquired with Planmeca ProMax® 3D Classic.

The approach used to evaluate the patient-specific 3D X-ray scans acquired with Planmeca ProMax® 3D Classic using Romexis® 3D imaging was done using QCT/FEA. The 3D X-ray, along with the implant positions, shapes, and locations, were modeled based on data provided by the patient. For a visual representation of the analyzed implant variants, see Figure 2.

The QCT/FEA model includes both the cancellous and cortical bone. The design of the complete denture and abutments was done using Exocad (Exocad Gmbh Darmstadt, Germany) in the dental laboratory. The denture was made without a palate. For visual reference, the denture with the splinted variant is shown in Figure 3. The denture was made out of polyetheretherketone (PEEK).

2.1. Methodology

The analyses were performed using a specialized QCT/FEA software for nonlinear analysis of bone-implant interaction Mechanical Finder v. 12.0 (RCCM,

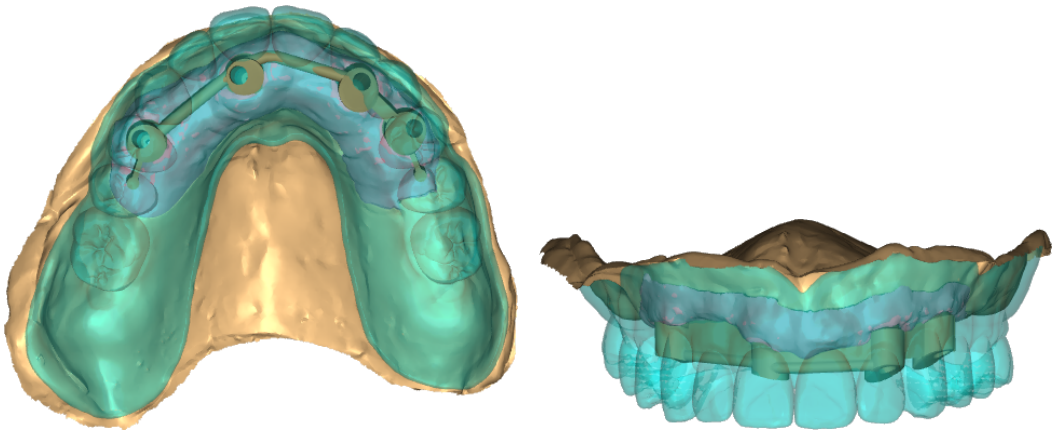

(A). Occlusal view. (B). Front view.

FIGURE 3. The view of the entire scene. The splinted variant is displayed [4].

Tokyo, Japan). The software uses sliced image data, like CT or X-ray scans. The QCT/FEA method allows for analyses using complete material inhomogeneity, where each voxel, and then finite element, possesses individual material properties specific to the individual patient's bone quality. Conventional modeling methods typically represent bone with a two-phase model (cancellous, cortical). For this study, the patient's maxilla was reconstructed from an X-ray scan, and two different implant geometries were examined.

2.2. Boundary Conditions

The loading was performed in three load cases for both analyzed variants. The first one was a 150 N force with a 35° slant in the buccolingual direction applied in the frontal region (both incisors). The second was a 600 N force with a 5° inclination applied in the distal region on both molars. The third was a 600 N force with the vertical component only, applied in the distal region on the first premolar tooth. To unify the visual appearance of the results, the color bar's upper and lower limits were normalized.

3. Results

3.1. Stress Distributions in Implants

The stress distribution in bone is similar for both alternatives in the frontal region. Moreover, the equivalent stress levels in implants show almost no difference between the two variants. Notably, even in the unsplinted alternative, the load was effectively transfered through multiple implants, thanks to the modeled denture (Figure 4a).

For the second load case (600 N force with a 5° buccolingual inclination on both molars), the splinted variant showed increased resistance to flexure. In contrast, the unsplinted design showed a significant concentration of load in the outermost implant (Figure 4b).

The results of the third load case (600 N force with a vertical component only applied on the first premolar) do not show great differences in equivalent stress distribution between the splinted and unsplinted variants. As the load is effectively transferred into the body of the implant directly beneath the first premolar, bending is minimized. Consequently, the splinting bar's contribution is diminished. The denture also helps to distribute the load, reducing disparities between the two variants (Figure 4c).

3.2. Stress Distributions in Bone

The differences in stress were more significant in bone. The distribution of minimum principal (compressive) stress for the unsplinted design had proven to be inferior to the splinted design as the load concentrated into one of the implants and the bone had a severe stress concentration at one of the implants' apices (Figure 5). This was mainly manifested in the posterior region of the maxilla.

Conversely, the splinted setup effectively prevented excessive implant displacement with the use of bars. Compressive stresses were significantly reduced for all load cases and primarily concentrated in the vicinity of the implants' axes in the posterior region (Figure 5c).

4. Conclusion

The results of this study show that the splinted variant provides a favorable, more even stress distribution. The values of stress are also lower in the analyzed load cases for the splinted variant, which confirms the null hypothesis.

Since masticatory forces are transferred through the dental restoration, splinting offers a range of benefits in implant-supported rehabilitations, including improved resistance to lateral loading and prosthetic component fractures [19].

This numerical study concludes the following:

- Stress distribution in implants loaded in the frontal region (both incisors) shows a comparable pattern for both variants with values of equivalent stress being comparable and the differences negligible.

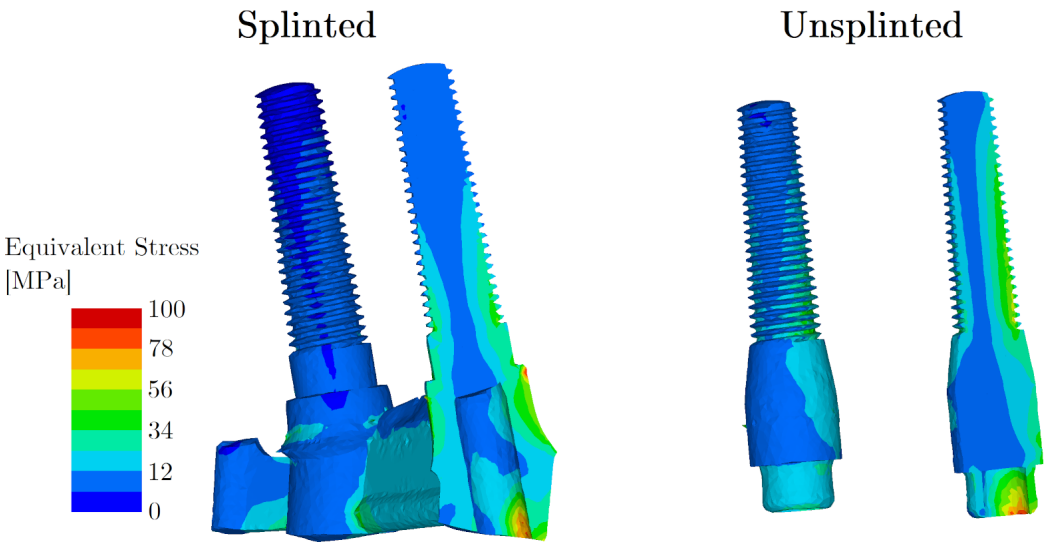

(A). First load case.

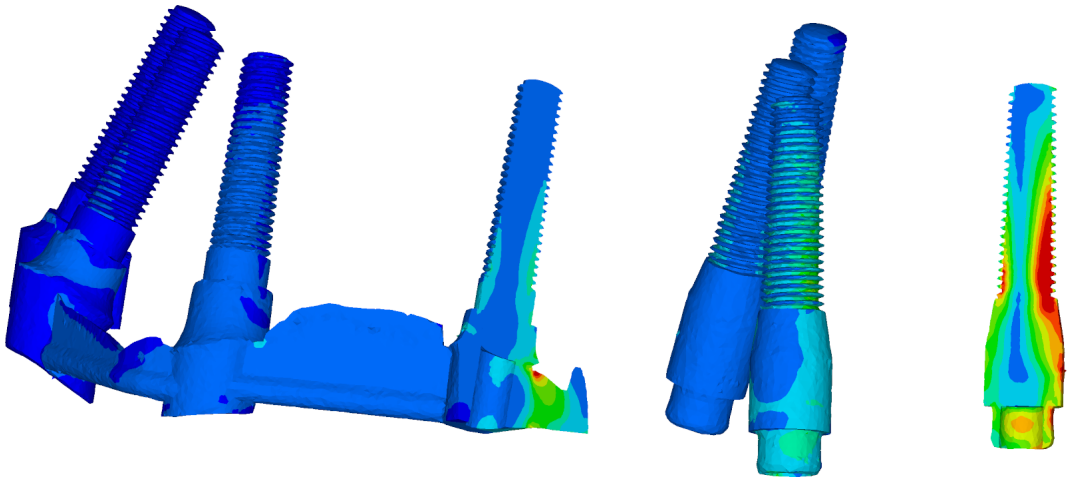

(B). Second load case.

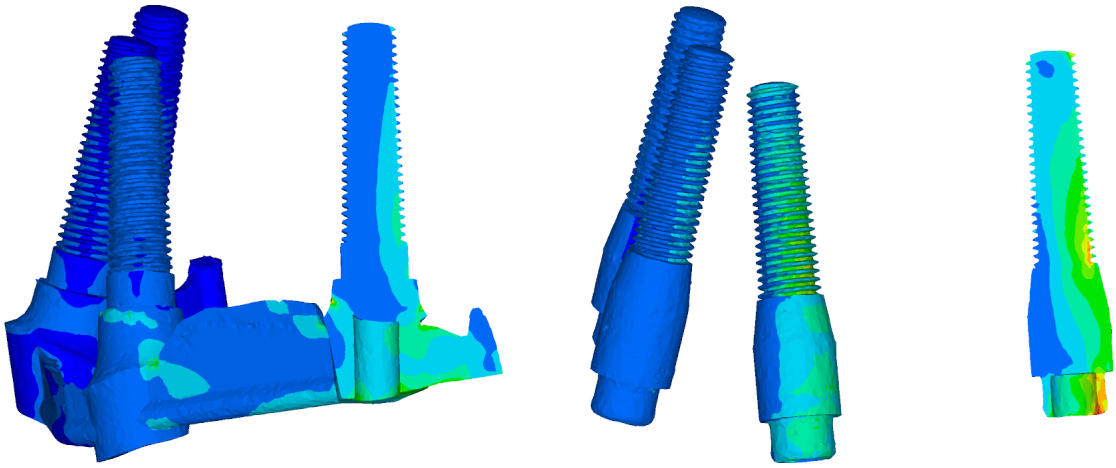

(C). Third load case.

Figure 4. Isolines of equivalent (von Mises) stress normalized across all images. Left column – the splinted variant, right column – the unsplinted variant. All images display sections of the implant assemblies [4].

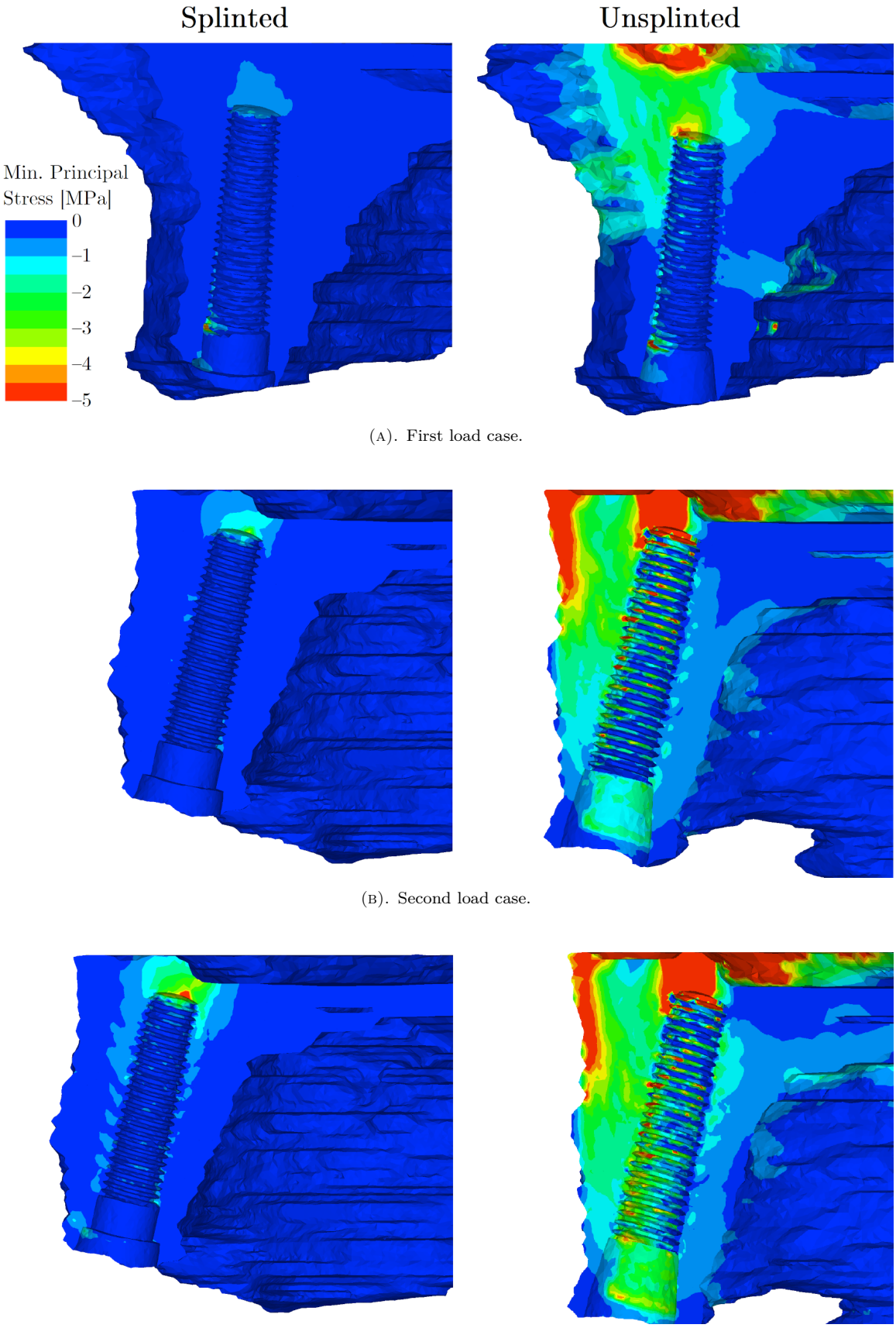

(A). First load case.

(B). Second load case.

(C). Third load case.

FIGURE 5. Isolines of minimum principal (compressive) stress normalized across all images. Left column – the splinted variant, right column – the unsplinted variant. All images display sections of bone in the buccolingual direction [4].

- Distal load applied on both molars shows the splinted variant distributes the load more evenly compared to the unsplinted variant and shows less bending in implants. On the other hand, load was concentrated to the outermost implant in the unsplinted variant.
- Force applied in the distal region on the first premolar did not create any significant stress concentrations in implants as the load was transferred solely into the body of the implant directly under the load and the effect of splinting was reduced.
- Compressive stress in the maxilla was inferior for the unsplinted variant with peaks of stress in the posterior region, namely around the implants' apices.
- The splinting effect played a significant role in preventing excessive implant displacement and bending and as a result, compressive stresses were less concentrated and had lower peaks for the splinted variant.

Acknowledgements

The financial support provided by the by the Faculty of Civil Engineering, CTU, Prague, project No. SGS23/152/OHK1/3T/11 is gratefully acknowledged.

References

[1] G. Thalji, M. Bryington, I. J. De Kok, L. F. Cooper. Prosthodontic management of implant therapy. *Dental Clinics of North America* **58**(1):207–225, 2014. https://doi.org/10.1016/j.cden.2013.09.007

[2] S. J. Sadowsky. Treatment considerations for maxillary implant overdentures: A systematic review. *The Journal of prosthetic dentistry* **97**(6):340–348, 2007. https://doi.org/10.1016/S0022-3913(07)60022-5

[3] R. D. Mericske-Stern, T. D. Taylor, U. Belser. Management of the edentulous patient. *Clinical Oral Implants Research* **11**(s1):108–125, 2000. https://doi.org/10.1034/j.1600-0501.2000.011S1108.x

[4] M. Frolo, L. Řehounek, A. Jíra, et al. Biomechanical analysis of palateless splinted and unsplinted maxillary implant-supported overdentures: A three-dimensional finite element analysis. *Materials* **16**(15):5248, 2023. https://doi.org/10.3390/ma16155248

[5] T. Aldhohrah, M. A. Mashrah, Y. Wang. Effect of 2-implant mandibular overdenture with different attachments and loading protocols on peri-implant health and prosthetic complications: A systematic review and network meta-analysis. *The Journal of Prosthetic Dentistry* **127**(6):832–844, 2022. https://doi.org/10.1016/j.prosdent.2020.12.016

[6] S. Ceraulo, A. Leonida, D. Lauritano, et al. Proposal for a clinical approach to geriatric patients with anchor need on implant for removable denture: New technique. *Prosthesis* **2**(3):185–195, 2020. https://doi.org/10.3390/prosthesis2030016

[7] P. Amornvit, D. Rokaya, S. Bajracharya, et al. Management of obstructive sleep apnea with implant retained mandibular advancement device. *World Journal of Dentistry* **5**(3):184–189, 2014. https://doi.org/10.5005/jp-journals-10015-1285

[8] M. D. Al Amri. Crestal bone loss around submerged and nonsubmerged dental implants: A systematic review. *The Journal of Prosthetic Dentistry* **115**(5):564–570, 2016. https://doi.org/10.1016/j.prosdent.2015.11.002

[9] S. M. Heckmann, M. G. Wichmann, W. Winter, et al. Overdenture attachment selection and the loading of implant and denture-bearing area. Part 2: A methodical study using five types of attachment. *Clinical Oral Implants Research* **12**(6):640–647, 2001. https://doi.org/10.1034/j.1600-0501.2001.120613.x

[10] M. A. Elsyad, M. M. Alokda, A. A. Gebreel, et al. Effect of two designs of implant-supported overdentures on peri-implant and posterior mandibular bone resorptions: A 5-year prospective radiographic study. *Clinical Oral Implants Research* **28**(10):e184–e192, 2017. https://doi.org/10.1111/clr.12984

[11] J. F. Martínez-Lage-Azorín, G. Segura-Andrés, J. Faus-López, R. Agustín-Panadero. Rehabilitation with implant-supported overdentures in total edentulous patients: A review. *Journal of Clinical and Experimental Dentistry* **5**(5):e267–e272, 2013. https://doi.org/10.4317%2Fjced.50817

[12] V. A. R. Barão, W. G. Assunção, L. F. Tabata, et al. Effect of different mucosa thickness and resiliency on stress distribution of implant-retained overdentures-2D FEA. *Computer Methods and Programs in Biomedicine* **92**(2):213–223, 2008. https://doi.org/10.1016/j.cmpb.2008.07.009

[13] M. Roccuzzo, F. Bonino, L. Gaudioso, et al. What is the optimal number of implants for removable reconstructions? A systematic review on implant-supported overdentures. *Clinical oral implants research* **23**(s6):229–237, 2012. https://doi.org/10.1111/j.1600-0501.2012.02544.x

[14] G. M. Raghoebar, H. J. Meijer, W. Slot, et al. A systematic review of implant-supported overdentures in the edentulous maxilla, compared to the mandible: How many implants. *European Journal of Oral Implantology* **7**(Suppl 2):S191–S201, 2014.

[15] V. Jagota, A. P. S. Sethi, K. Kumar. Finite element method: an overview. *Walailak Journal of Science and Technology (WJST)* **10**(1):1–8, 2013.

[16] J.-P. Geng, K. B. C. Tan, G.-R. Liu. Application of finite element analysis in implant dentistry: A review of the literature. *The Journal of Prosthetic Dentistry* **85**(6):585–598, 2001. https://doi.org/10.1067/mpr.2001.115251

[17] J. B. Brunski. Biomechanical aspects of the optimal number of implants to carry a cross-arch full restoration. *European Journal of Oral Implantology* **7**(Suppl 2):S111–S131, 2014.

[18] M. Prado, S. Khosla, C. Chaput, H. Giambini. Opportunistic application of phantom-less calibration methods for fracture risk prediction using QCT/FEA. *European radiology* **31**(12):9428–9435, 2021. https://doi.org/10.1007/s00330-021-08071-w

[19] C. E. Misch. *Dental implant prosthetics*. Elsevier Health Sciences, 2004. ISBN 9780323078962.

IMAGE-BASED RANDOM FIELDS IN NUMERICAL MODELING OF HETEROGENEOUS MATERIALS

David Šilhánek, Jan Sýkora*

Czech Technical University in Prague, Faculty of Civil Engineering, Department of Mechanics, Thákurova 7, 160 00 Prague, Czech Republic

* corresponding author: jan.sykora.1@fsv.cvut.cz

Abstract. Modeling of spatial variability using random fields is nowadays standard in computational modeling of heterogeneous materials. The only difficulty remains in determining the input parameters of the random field in order to represent the modeled material morphology as accurately as possible. The most frequent method of constructing a random field relies on various covariance kernels that primarily use as input the values of the correlation lengths, which are typically estimated ad-hoc. However, another possibility is to extract input parameters from the modeled material morphology. Moreover, this approach enables to calculate the covariance kernel itself. The performance of the image-based procedure is compared with standard methods of random field construction on the response of the two-phase elastic material.

Keywords: Karhunen-Loève expansion, random field, Monte Carlo, two-phase elastic material.

1. Introduction

The stochastic finite element method is an extension of the deterministic finite element method that introduces randomness into the computational scheme, see [1, 2]. Mostly, the input parameters are cast in a probabilistic setting, and random fields (see [3–5]) play a crucial role in this because they allow us to incorporate randomness and spatial variability. So, our goal is to investigate the efficiency of constructing a random field using several different strategies on the material response, which is here represented by the elastic problem of the two-phase medium.

2. Estimation of the RVE cell

The first step in our work is estimating the dimensions of the representative volume element (RVE), which means an area with statistically homogeneous properties or at least with properties insignificantly affected by a particular choice. Let us consider a two-dimensional heterogeneous composite material with two phases represented by an integer matrix containing only 0 (black color) and 1 (white color), see Figure 1 depicting several cut-outs of the original medium. Each matrix member corresponds to one pixel in the image and simultaneously to one rectangular element in the finite element mesh. The domain under the study contains different-sized circular white-labeled inclusions with the following prescribed grain-size distribution curve: diameter 2 px (10 %), 4 px (10 %), 8 px (15 %), 16 px (20 %), 24 px (20 %), and 32 px (25 %). Its overall dimensions are 10 000 × 10 000 px, and the volume fraction of inclusions is $c^1 = 0.5$.

Here, the determination of the RVE size stems from an engineer's approach a priori estimating the dimensions based on easily observable parameters, namely the volume fraction of the white phase and the optimal correlation lengths. Authors are aware of a more correct approach to identifying RVE size from the statistical analysis of model responses. However, this does not have to be always possible and brings ob-

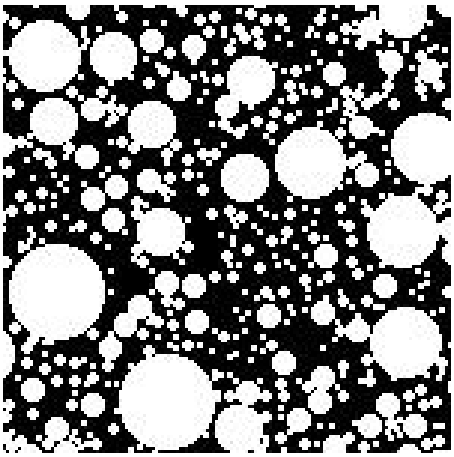

(a). 150 × 150 px

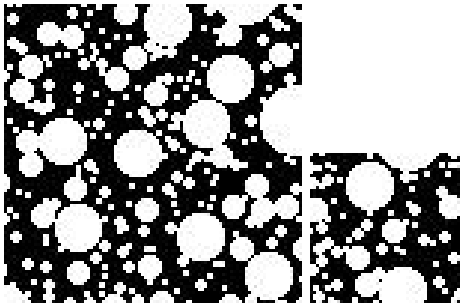

(b). 100 × 100 px (c). 50 × 50 px

Figure 1. Samples of the windows with predefined dimensions taken randomly from the original domain.

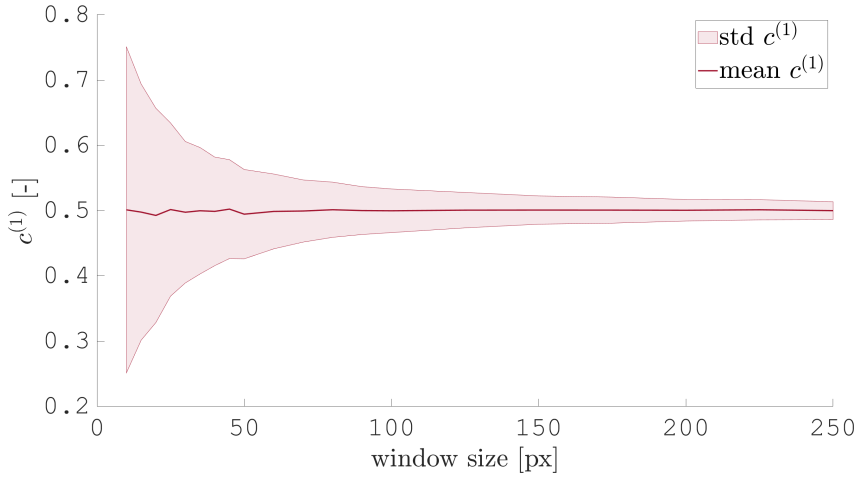

Figure 2. The convergence graph computed for the volume fraction of the inclusions as a function of the window size. The solid line denotes the mean and the light-hatched area represents the ± standard deviation.

stacles, especially for the time-demanding numerical simulations.

The first study addressing the optimal RVE size is built upon the parameter of volume fraction. A window of predefined dimensions is randomly placed 1 000 times in the original medium. Consequently, the difference in the studied properties and their statistical moments are then evaluated on the obtained dataset. The entire procedure is repeated for various dimensions of the placed window. The plotted graphs serve for the visual determination of optimal RVE dimensions. The results obtained from the first study are shown in Figure 2. The mean of the volume fraction is almost constant for all predefined window sizes, contrary to the standard deviation, which steeply converges with increasing dimensions, and the values around the window size of 100×100 px reach the final plateau. So, optimal RVE sizes in the view of the volume fraction are the dimensions above 100×100 px.

The second study focuses on estimating the RVE size based on the optimal correlation lengths (L_x, L_y). The algorithmic procedure is similar to the previous case, except that an additional step of identifying the correlation lengths for every placed window with predefined dimensions is added to the calculation. This step does not significantly increase the computational costs, since the relatively small window sizes enter the optimization process of correlation lengths. The built-in Matlab function is used as an optimizer for minimizing the value of error $\varepsilon_{L_{\text{opt}}}$ between the correlation functions C_G and C_{TPP}:

$$\varepsilon_{L_{\text{opt}}} = \frac{1}{n_x \cdot n_y} \sum_{i=1}^{n_x} \sum_{j=1}^{ny} |C_{TPP,ij} - C_{G,ij}(L_x, L_y)|, \tag{1}$$

where

n_x denotes the window dimension in x-direction,

n_y denotes the window dimension in y-direction,

C_{TPP} is the image-based correlation kernel stored as a matrix and enumerated according to Equation (4),

C_G is the Gaussian correlation kernel based on Equation (3).

The optimal correlation lengths are plotted in Figure 3. As we can notice, the values of optimal correlation length become constant for window dimensions greater than 70×70 px. Moreover, the mean values of correlation length for the same threshold also correspond to the optimal values computed for the entire original domain ($10\,000 \times 10\,000$ px), as one can ensure from Figure 4, where the absolute values of the error are plotted. The optimal values of correlation length are primarily affected by the spatial distribution of inclusions, the sizes of the inclusions, and the value of the volume fraction. So, the observed evolution of error curves coincides with the study findings examining the effect of volume fraction on the window size. Consequently, the influence of window size on optimal correlation lengths is negligible for dimensions above 100×100 px and almost disappears for the window sizes above 150×150 px.

Usually, the S_2 function is computed using the discrete fast-Fourier transform algorithms (DFT) [5] to save an enormous amount of computational time. However, this procedure requires the periodic medium as an input, which is not our case of windows randomly placed into the original medium, thus the effect of the non-periodic domain on the final S_2 DFT-based values needs to be carefully investigated. For this reason, the algorithm computing S_2 values for the non-periodic medium has been implemented as a comparison tool with DFT-based values. The computational testing protocol is the same as in previous studies and the observed values of error are obtained from the following equation as:

$$\varepsilon_{S_{2,p},S_{2,np}} = \frac{1}{n_x \cdot n_y} \sum_{i=1}^{n_x} \sum_{j=1}^{n_y} |S_{2,ij}^{\text{periodic}} - S_{2,ij}^{\text{nonperiodic}}|, \tag{2}$$

where

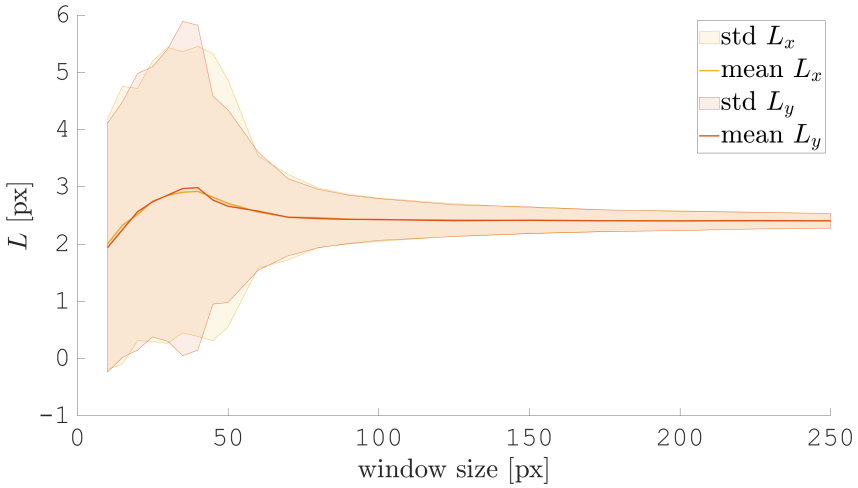

FIGURE 3. The convergence of optimal correlation lengths as a function of the window size. The solid line denotes the mean and the light-hatched area represents the ± standard deviation.

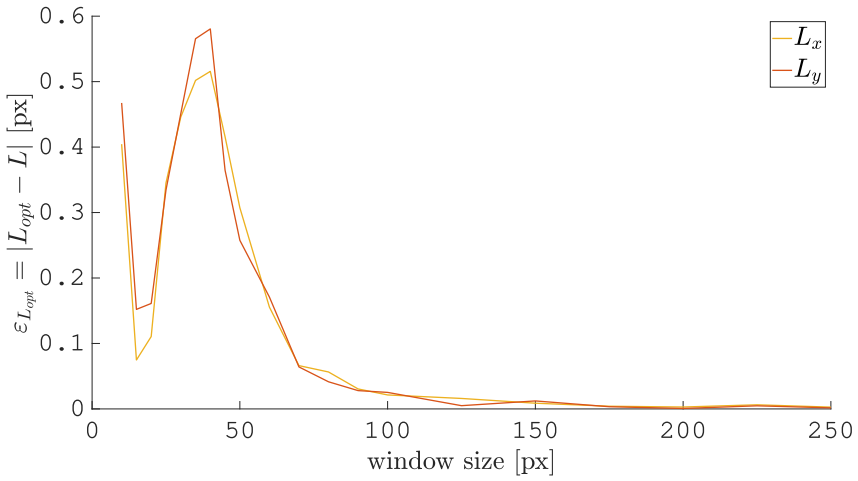

FIGURE 4. The difference between the optimal correlation length obtained from the entire original domain and mean values of the correlation length computed for the various dimensions of the placed window.

n_x denotes the window dimension in x-direction,

n_y denotes the window dimension in y-direction,

$S_{2,ij}^{\text{periodic}}$ is the i,j-th element of two-point probability matrix computed with the assumption of periodicity according to Equation (5), and i,j-th element of two-point probability matrix obtained for the non-periodic medium with the help of Equation (7).

As expected, the curves in Figure 5 show good convergence of values of error with higher window sizes. Therefore, the effect of the periodic assumption on the optimized values of correlation lengths is negligible for the window sizes of our interest, and the fast evaluation of the two-point probability based on the DFT algorithm can be performed in our computational scheme.

Considering the outcomes mentioned above, we decided to proceed further with an RVE size of 100×100 px. It is a reasonable compromise between the obtained results – the variance of the volume fraction and the optimized correlation length – and computational cost. Another enlarging of the window area would not bring a huge benefit since the values of mean computed for the correlation length and volume fraction are further invariable, and their standard deviations reach almost the plateau.

3. Numerical Example

This numerical example is devoted to the assessment of several proposed techniques of random field constructions in stochastic material modeling. Since the efficiency of the random fields is demonstrated mostly on the model inputs, the emphasis is here mainly on checking the quality of the prediction of material behavior. To begin with, the ideal elastic model simulating the mechanical behavior is employed for both material phases. Their material properties – E Young's modulus and ν Poisson's ratio – differing by an order of magnitude, are summarized in Table 1.

The geometrical domain with applied boundary conditions is depicted in Figure 6. The Dirichlet boundary conditions are imposed on the left side of the domain as $u_x = 0$, on the right side as incrementally increasing up to $u_x = 1.5 \cdot 10^{-6}$ m, and

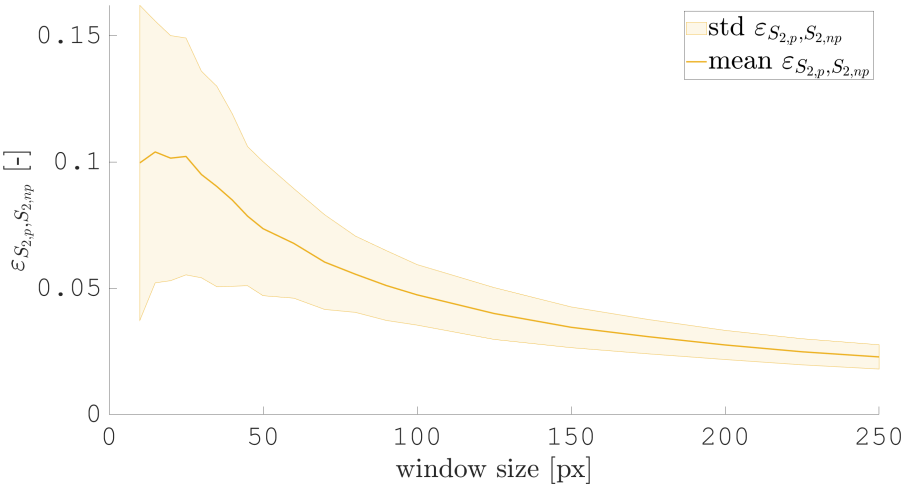

Figure 5. The comparison of the periodic and non-periodic assumptions on the values of S_2 function.

Phase	$\boldsymbol{E}$ **[MPa]**	$\boldsymbol{\nu}$ **[-]**
Black phase, 0	1 325	0.43
White phase, 1	25 000	0.20

Table 1. Elastic properties of black and white phase representing the material constants of polypropylene composite materials [6].

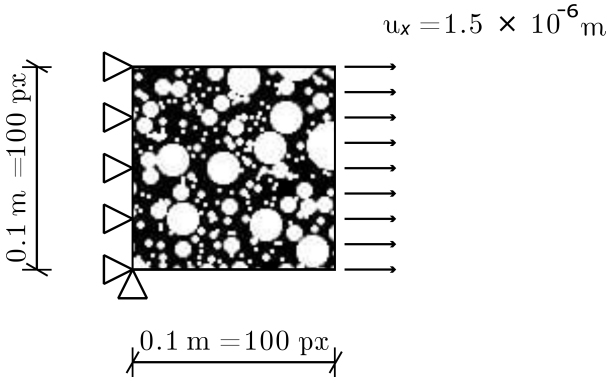

Figure 6. A scheme of the tensile st problem.

finally $u_y = 0$ at bottom left corner. The entire domain with dimensions of 100×100 px is discretized into 10 000 finite rectangular elements. The observed responses are displacements u_x, u_y, and average stresses σ_x.

3.1. Random field

The spatial variability of material properties is modeled here by the random fields, which are essentially dependent on the auto-covariance function. Since the correct determination of the auto-covariance function plays a crucial role, several methods of constructing this key function are tested within this study. The classical approach, published in literature [4, 5, 7], is based on the approximation of the covariance function by the Gaussian correlation kernel, which is a function of a material variance σ^2, correlation lengths L_x, L_y, and the vector of relative position $\boldsymbol{r} = (x - x_0, y - y_0)$, where (x_0, y_0) are coordinates of an arbitrarily chosen point (pixel in our case). The Gaussian kernel is then expressed as:

$$C_G(\boldsymbol{r}) = \sigma^2 \cdot \exp\left(- \frac{(x - x_0)^2}{2 \cdot L_x^2} - \frac{(y - y_0)^2}{2 \cdot L_y^2} \right). \quad (3)$$

The input correlation lengths are chosen based on the expert's guess or their values can be estimated from the optimization process minimizing the absolute difference between the Gaussian covariance kernel (see Equation (3)) and image-based covariance kernel, see [5], derived from a two-point probability function. The latter-mentioned approach represents relatively new concepts of extracting the spatial covariance from images according to the following formula:

$$C_{TPP}(\boldsymbol{r}) = (\kappa^0 - \kappa^1)^2 \cdot (S_2^1(\boldsymbol{r}) - (c^1)^2), \quad (4)$$

where

κ^f is the selected material property (e.g. Poisson's ratio) of given phase f,

c^1 denotes the volume fraction of the white phase,

S_2^1 is the two-point probability function computed by the Fast Fourier Transformation, see [7], as:

$$S_2^f(\boldsymbol{r}) = \frac{\mathrm{IDFT}\{\mathrm{DFT}\{\chi^f(\boldsymbol{r})\}\overline{\mathrm{DFT}\{\chi^f(\boldsymbol{r})\}}\}}{n_x \cdot n_y}, \quad (5)$$

where

DFT is the Discrete Fourier Transformation,

IDFT is the inverse Discrete Fourier Transformation,

$\overline{\cdots}$ stands for the complex conjugate,

$n_x \cdot n_y$ is the image area,

f is the given phase,

χ^f is the characteristic function defined as:

$$\chi^f(\boldsymbol{x}) = \begin{cases} 1 & \text{if the point } \boldsymbol{x} \text{ lies in the phase } f, \\ 0 & \text{otherwise.} \end{cases} \quad (6)$$

If the non-periodic medium is considered, the formula used for the evaluation of a two-point probability function arises directly from its definition:

$$S_2^f(\boldsymbol{x}, \boldsymbol{x}') = \frac{\sum_{x=0}^{(2\cdot n_x - d_x - 1)} \sum_{y=0}^{(2\cdot n_y - d_y - 1)} \chi^f(\boldsymbol{x}) \chi^f(\boldsymbol{x}')}{(2n_x - d_x) \cdot (2n_y - d_y)}, \tag{7}$$

where

$\boldsymbol{x} = (x, y)$ are the coordinates of the starting point,

$\boldsymbol{x}' = (x + d_x, y + d_y)$ are the coordinates of the ending point.

Finally, the auto-covariance matrix entering the random field construction is obtained as a resulting covariance computed from Equations (3) or (4), which is further reassembled into the row vector. Then, this reshaped product determines the first row in a symmetric square Toeplitz matrix representing the auto-covariance matrix such that $C_{i,j} = C_{i+1,j+1}$. Another possibility of computing the auto-covariance matrix is directly from the definition itself. Based on the assumption that our original domain is sufficiently large enough, many independent samples are collected via a window of predefined dimensions randomly placed in the original structure. Each of these cut-outs can be then rearranged into a row vector, and subsequently, the auto-covariance is calculated as follows:

$$C_S(\boldsymbol{X}, \boldsymbol{X}') = \mathbb{E}[(\boldsymbol{X} - \mathbb{E}(\boldsymbol{X}))(\boldsymbol{X}' - \mathbb{E}(\boldsymbol{X}'))]. \tag{8}$$

3.1.1. Karhunen-Loève Expansion

The Karhunen-Loève expansion is an extremely useful tool representing the stochastic process as an infinite linear combination of orthogonal functions. Based on the spectral decomposition of the discretized form of the auto-covariance function $C(\boldsymbol{X}, \boldsymbol{X}')$, and the orthogonality of eigenfunctions $\boldsymbol{\phi}_i$, the Gaussian random field of parameter $\boldsymbol{\kappa}(\omega)$ can be written as:

$$\boldsymbol{\kappa}(\omega) \approx \kappa_\mu + s \sum_{i=1}^{n_\phi} \sqrt{\varphi_i} \boldsymbol{\phi}_i \xi_i(\omega), \tag{9}$$

where

$\xi_i(\omega)$ is the standard independent and identically distributed random variable,

κ_μ is the mean of material parameters,

s is the standard deviation of material parameters,

φ_i represents a corresponding eigenvalue,

n_ϕ is the number of eigenmodes.

Smaller values of n_ϕ lead to more significant dimensionality reduction, and oppositely, higher values give better descriptions of the resulting random field. The log-normal formulation of the random field $\boldsymbol{\kappa}_{ln}(\omega)$ stemming from the Gaussian expression is given by:

$$\boldsymbol{\kappa}_{ln}(\omega) \approx \exp\left(\kappa_{\mu,g} + s_g \frac{\sum_{i=1}^{n_\phi} \sqrt{\varphi_i} \boldsymbol{\phi}_i \xi_i(\omega)}{\sqrt{\sum_{i=1}^{n_\phi} (\sqrt{\varphi_i} \boldsymbol{\phi}_i)^2}}\right), \tag{10}$$

Tag	Label	Cov. kernel	Correlation length	Trimmed
#1	Gauss	(3)	L_{opt}	No
#2	Gauss T	(3)	L_{opt}	Yes
#3	TPP	(4)	–	No
#4	TPP T	(4)	–	Yes
#5	S	(8)	–	No
#6	S T	(8)	–	Yes
#7	Gauss +	(3)	$2 \cdot L_{\text{opt}}$	No
#8	Gauss + T	(3)	$2 \cdot L_{\text{opt}}$	Yes
#9	Gauss ++	(3)	$10 \cdot L_{\text{opt}}$	No
#10	Gauss ++ T	(3)	$10 \cdot L_{\text{opt}}$	Yes
#11	Gauss −	(3)	$\frac{1}{2} \cdot L_{\text{opt}}$	No
#12	Gauss − T	(3)	$\frac{1}{2} \cdot L_{\text{opt}}$	Yes
#13	Gauss −−	(3)	$\frac{1}{10} \cdot L_{\text{opt}}$	No
#14	Gauss −− T	(3)	$\frac{1}{10} \cdot L_{\text{opt}}$	Yes

Table 2. Description of all tested random field constructions. The first six versions #1–#6 characterized the main approaches of constructing random fields. The rest of them #7–#14 served for simulating the wrong initial guess of experts about correlation lengths.

where $\kappa_{\mu,g}$ and s_g are the Gaussian mean and standard deviation, respectively, computed from their log-normal counterparts ($\kappa_{\mu,ln}$, s_{ln}) according to the following equations, see [2]:

$$\kappa_{\mu,g} = \ln\left(\kappa_{\mu,ln}\right) - \frac{1}{2} s_{ln}^2, \tag{11}$$

$$s_g = \sqrt{\ln\left(\left(\frac{s_{ln}}{\kappa_{\mu,g}}\right)^2 + 1\right)}. \tag{12}$$

3.1.2. Description of tested random field

All tested versions of random field constructions are summarized in Table 2. Overall, 14 different versions have been examined with the following specifications: The labels – Gauss, TPP, S – refer to the equations employed for assembling the covariance kernels and auto-covariance. Since the Karhunen-Loève expansion delivers the real-valued random fields, the additional label – T – is introduced as another option referring to value filtering. It means that real-valued random fields are trimmed back to the binary values preserving the volume fraction. Finally, the correlation lengths indicate the values entering the covariance kernels. The versions with the labels – plus and minus – serve for simulating the wrong initial guess of experts, i.e. the underestimations and overestimations of correlation lengths, respectively.

3.2. Homogenization bounds

Since the initial guess of experts about the inputs entering the covariance kernels is missing here, the theoretical homogenization bounds are exploited for the comparison of our proposed techniques with easily

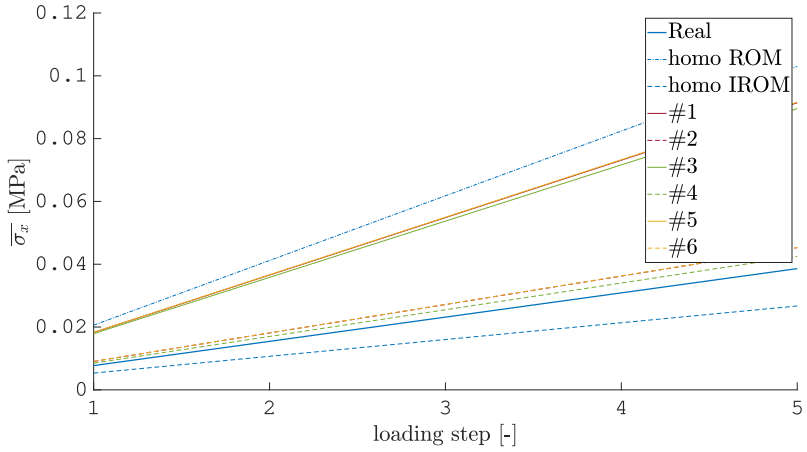

Figure 7. The evolution of average stresses as a function of loading steps, $n_\phi = 50$.

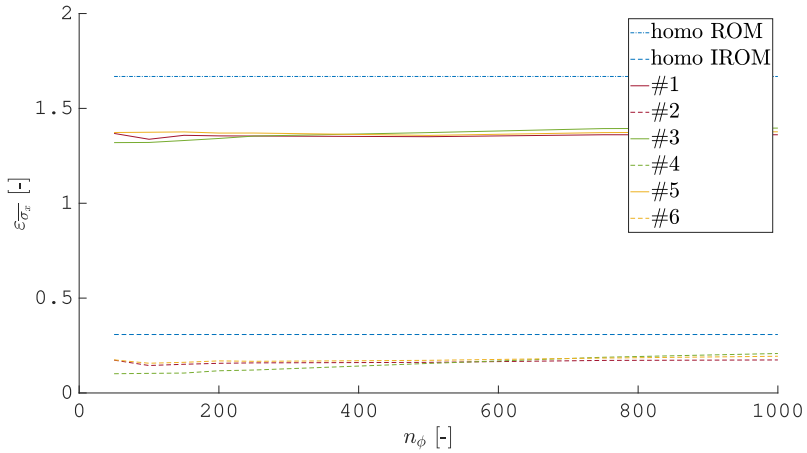

Figure 8. The values of error computed for the average stress as a function of the number of eigenmodes.

computed rules. The first homogenization bound is the rule of mixtures, which is given by:

$$\kappa_{\text{hom}} = \kappa^1 \cdot c^1 + \kappa^1 \cdot (1 - c^1), \tag{13}$$

and the inverse rule of mixtures is defined as:

$$\kappa_{\text{hom}} = \left(\frac{c^1}{\kappa^1} + \frac{1 - c^1}{\kappa^0} \right)^{-1}. \tag{14}$$

κ_{hom} is the homogenized material property, and the results stemming from these two equations are labeled as ROM and IROM, respectively.

4. Results

For the comparison, it is necessary to introduce the metrics of error. They represent the absolute values calculated as a difference between the reference set of material responses, and the response set having the random fields as an input. The equations evaluating the values of error for the average stress $\overline{\sigma_x}$ and its variance $\text{var}(\overline{\sigma_x})$ are expressed as:

$$\varepsilon_{\overline{\sigma_x}} = \left| \frac{\overline{\sigma_x}_{,\text{real}} - \overline{\sigma_x}_{,\text{RF}}}{\overline{\sigma_x}_{,\text{real}}} \right|, \tag{15}$$

and:

$$\varepsilon_{\text{var}(\overline{\sigma_x})} = \left| \frac{\text{var}(\overline{\sigma_x}_{,\text{real}}) - \text{var}(\overline{\sigma_x}_{,\text{RF}})}{\text{var}(\overline{\sigma_x}_{,\text{real}})} \right|, \tag{16}$$

where the subscript $_{\text{real}}$ represents the reference set assembled from 1 000 Monte Carlo simulations with a domain size of 100×100 px, which is randomly taken from the original structure. Then, the subscript $_{\text{RF}}$ refers to set collected for the 1 000 Monte Carlo simulations utilizing the random fields as an input.

The first graph (Figure 7) illustrates the evolution of average stresses as a function of loading steps for different constructions of random fields. The results are plotted for the fixed number of eigenmodes, which is equal to 50. The true values of the average stresses computed from the reference set are shown by the solid blue line and the homogenization bounds are depicted as dashed blue lines. The first six versions #1–#6 of random field construction are only compared for the sake of clarity. From the presented graph we can see that the trimmed versions show good correspondence with the reference values, in contrast to values carried out for real-valued random fields, which shift to the upper homogenization bound. A similar conclusion is observed from Figure 8 depicting the values of error computed for the average stress depending on the number of eigenmodes. As we can see from this graph, including more eigenmodes in the Karhunen-Loève expansion does not tend to have smaller values of error; however, it has a significant impact on values of error

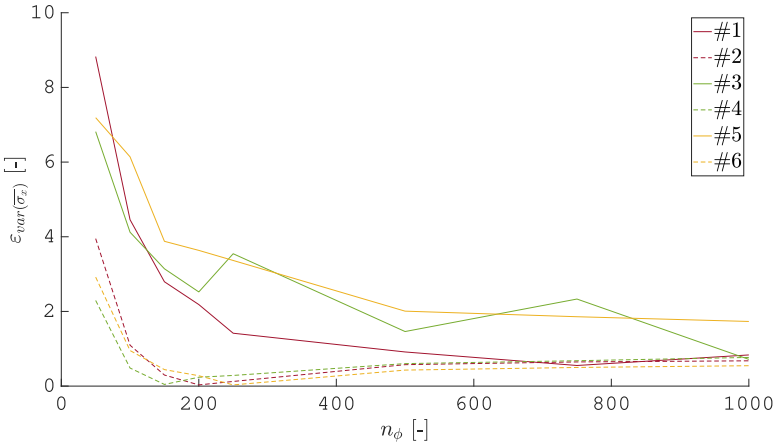

FIGURE 9. The variance error in dependence on the number of eigenvectors included in KLE.

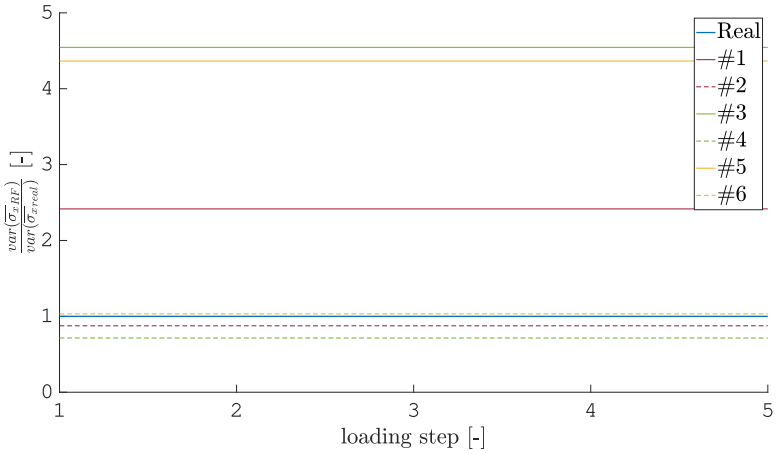

FIGURE 10. The ratio of the variances computed for the average stresses of the reference set and set assembled from the random field-based simulations #1–#6, $n_\phi = 250$.

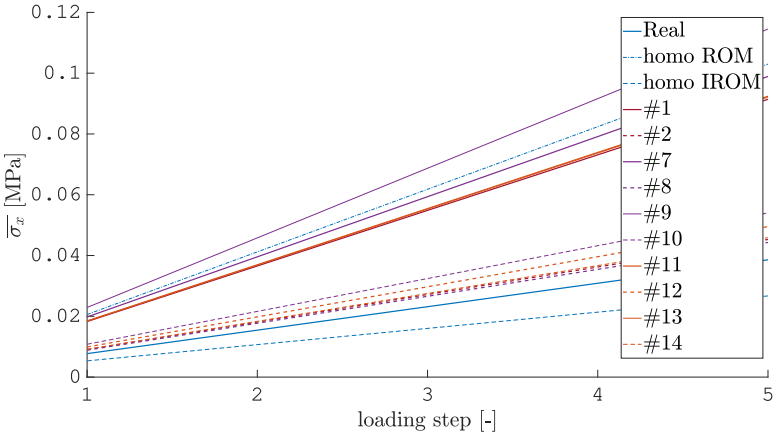

FIGURE 11. The average stress for RF with arbitrarily chosen correlation lengths $n_\phi = 50$.

computed for the stress variance illustrated in Figure 9. All trimmed versions achieve the minimum values for $n_\phi = 200$, while the real-valued versions converge with the higher number of involved eigenmodes. The last comparison is finally depicted in Figure 10 showing the ratio between the variances of average stresses determined from the reference set and set assembled from the random field-based simulations, respectively.

Other interesting findings arise from the study of the wrong-determined input correlation lengths caused by the expert guess. It can be seen from Figures 11 and 12 that the random fields with the incorrect correlation lengths as an input can have fatal consequences on the material response and can bring no benefit to the probabilistic analysis of the studied problem. From the predicted lines, the splitting into the real-valued and trimmed groups is more observed than the clustering based on the different covariance kernels.

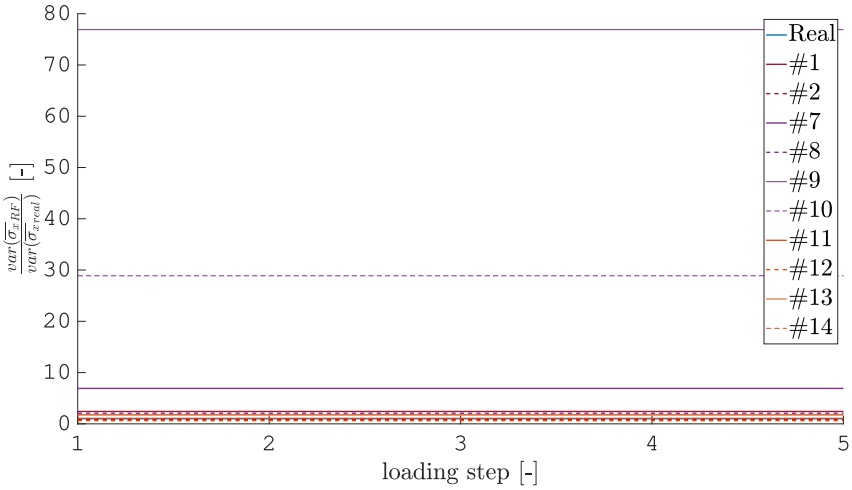

Figure 12. The ratio of the variances computed for the average stresses of the reference set and set assembled from the random field-based simulations #7-#14, $n_\phi = 250$.

Taken together, the values of error for the real-valued random fields are large in comparison to other methods, and therefore they do not appear to be adequate approaches for simulating such type of material.

5. Conclusion

Within this contribution, the efficiency of the image-based procedure of random field construction was studied with classical methods on the elastic problem of the two-phase material. Good results have been obtained for trimmed versions of random fields. Here, our proposed techniques for identifying properties from images, e.g. correlation lengths or image-based covariance, are beneficial and can be applied to such problems. Unfortunately, these random field constructions can no longer exploit the potential of the Karhunen-Loève expansion, and their contribution to the stochastic finite method in terms of acceleration is not significant.

Acknowledgements

The authors are thankful for financial support from the Student Grant Competition of CTU, project No. SGS23/152/OHK1/3T/11 and the Czech Science Foundation, project No. 22-35755K.

References

[1] R. G. Ghanem, P. D. Spanos. *Stochastic finite elements: A spectral approach*. Springer New York, USA, 1991. https://doi.org/10.1007/978-1-4612-3094-6

[2] B. Rosić, H. G. Matthies. Computational approaches to inelastic media with uncertain parameters. *Journal of the Serbian Society for Computational Mechanics* **2**(1):28–43, 2008.

[3] R. J. Adler, J. E. Taylor. *Random fields and geometry*. Springer-Verlag New York, USA, 2007. https://doi.org/10.1007/978-0-387-48116-6

[4] J. Havelka, A. Kučerová, J. Sýkora. Dimensionality reduction in thermal tomography. *Computers & Mathematics with Applications* **78**(9):3077–3089, 2019. https://doi.org/10.1016/j.camwa.2019.04.019

[5] M. Lombardo, J. Zeman, M. Sejnoha, G. Falsone. Stochastic modeling of chaotic masonry via mesostructural characterization. *International Journal for Multiscale Computational Engineering* **7**(2):171–185, 2009. https://doi.org/10.1615/IntJMultCompEng.v7.i2.70

[6] J.-H. Yun, Y.-J. Jeon, M.-S. Kang. Analysis of elastic properties of polypropylene composite materials with ultra-high molecular weight polyethylene spherical reinforcement. *Materials* **15**(16):5602, 2022. https://doi.org/10.3390/ma15165602

[7] J. Havelka, A. Kučerová, J. Sýkora. Compression and reconstruction of random microstructures using accelerated lineal path function. *Computational Materials Science* **122**:102–117, 2016. https://doi.org/10.1016/j.commatsci.2016.04.044

RECONSTRUCTION OF CONCRETE MORPHOLOGY USING DEEP LEARNING

ONDŘEJ ŠPERL, JAN SÝKORA*

Czech Technical University in Prague, Faculty of Civil Engineering, Department of Mechanics, Thákurova 7, 160 00 Prague, Czech Republic

* corresponding author: jan.sykora.1@fsv.cvut.cz

ABSTRACT. In this contribution, the concrete morphology is reconstructed with a simple algorithm selecting a pixel value based on the small set of surrounding pixels. A deep neural network (DNN) is used as a classifier, and the authors focus on studying different DNN architectures. The performance of the proposed algorithm is evaluated on several statistical descriptors and the grain size distribution curve.

KEYWORDS: Reconstruction, concrete, deep learning, convolutional neural network.

1. INTRODUCTION

The reconstruction of material morphology has become an essential part of the numerical computational modeling of heterogeneous materials. The first reconstruction algorithms employed optimization routines to minimize selected statistical descriptors, see [1–4]. The drawback of such an approach is the exhaustive computational time caused by sequential pixel-by-pixel replacement with subsequent evaluation of statistical descriptors. The second strategy concentrated on material description using random fields with optimized image-based correlation kernels, see [5]. This method dramatically reduces the dimensionality of the problem [6], however, it has the disadvantage of preserving maximal second-order statistical moments. The last approach is texture synthesis, which exploits the relatively simple principle of texture locality and stationarity for material reconstruction, see [7–9]. Locality means that a random pixel inside the texture is related only to a small set of surrounding pixels (see [10]), and stationarity can be explained by the following example. Assume a movable window placed in different positions in the texture. The regions of texture marked by the movable window seem to be always similar contrary to the situation of the general image, where the observed regions are clearly different. Our aim is to reconstruct the image using the latter-mentioned approach, focusing on different DNN architectures, see [11], and the influence of their hyperparameters on the resulting concrete morphology. The authors are aware of more progressive techniques, such as generative adversarial networks or diffusion models, see [12–14], requiring a relatively rich dataset of images used for their training process, that might not always be available.

2. METHODOLOGY

The reconstruction of the concrete cross-section is based on the algorithm shown in Figure 1. As an input to the computation, we use a sample of the concrete cross-section characterized by a two-dimensional image, introduced in the algorithm by a matrix of values 0 and 1 representing the black and white colors. The input and output data used for training the model are generated from the original image. The size of the dataset depends on the parameters of the computation; however, it can be estimated that for images ranging from 200×200 to 400×400 px, the size of the dataset is around tens of thousands. The model here is defined as a classification tool determining, based on a given pixel neighborhood, whether a pixel at a given position has a value of 0 or 1. The reconstruction algorithm then uses the trained classifier and the edges of the original image for the prediction of a new concrete cross-section. The quality of the new morphology is evaluated on our selected statistical descriptors. The aim of the reconstruction is to generate a similar sample with a statistically and physically equivalent structure with respect to the studied medium.

The pixel neighborhood is an important parameter of the reconstruction algorithm. Figure 2 shows the template as a function of the parameters w and h. These two parameters define its dimension, which significantly affects the properties of the entire reconstruction. The pixel neighborhood has two major features:

(1.) It specifies the number of input values of pixels needed for the output value. Yellow-labeled pixels in the scheme are our input values, and the red-labeled pixel is the output value. Since the values of the yellow-labeled pixels have to be known, the reconstruction algorithm must always have the edges of the original image enabling the prediction of the first red pixel. Thus, the parameters w and h also characterize the sizes of the boundary regions of the original image, which are needed for the start of the reconstruction algorithm.

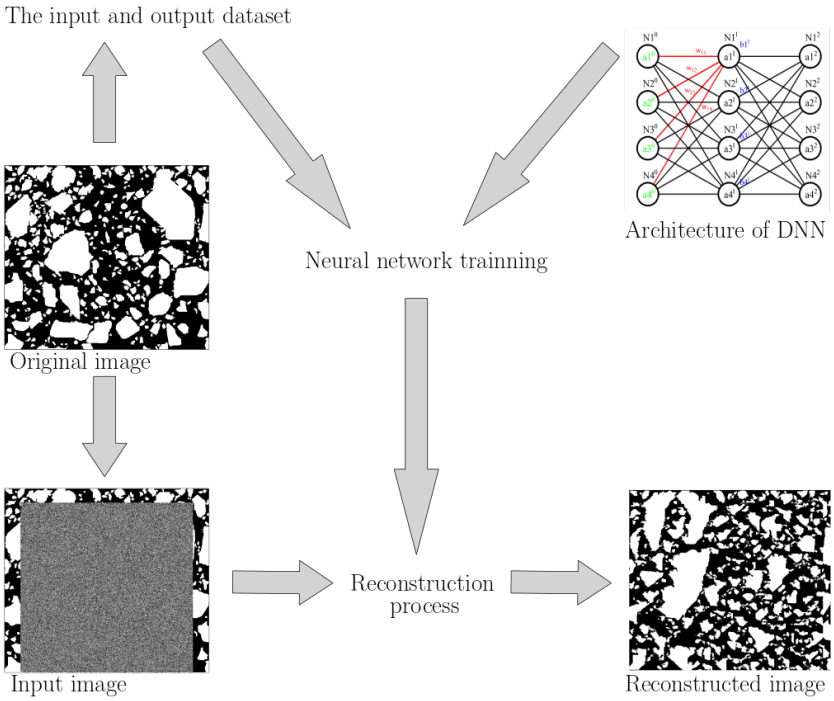

Figure 1. Algorithmic framework.

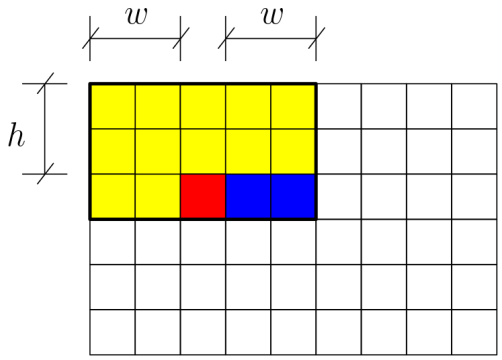

Figure 2. Template determining set of surrounding pixels.

(2.) Moreover, it defines a template that moves pixel-by-pixel within the reconstructed image and predicts the value of the red-labeled pixel. It can be seen from the scheme that the rectangle of size $(2w+1)\cdot(h+1)$ is used as a template, and for this reason, we have to use blue-labeled and red-labeled pixels as input values. These are the values that are not taken from the original image but are randomly and independently generated from a uniform distribution satisfying the volume representation of 0 and 1 values in the original image.

Once the pixel neighborhood is set and the classifier is trained, the reconstruction algorithm starts the execution with the given template from the upper left corner of the initial image. The initial image is shown in Figure 1, with the edges representing the morphology of the original media and the rest being randomly determined pixels so as to preserve the volume representation. The red-labeled pixel is computed with the help of the classifier specifying the probability of 0 and 1 for a given vicinity and the pseudo-random number generator determining the final value. The newly determined red-labeled pixel becomes the yellow-labeled pixel, and then the template is shifted one pixel further to the right. The value of all reconstructed pixels is successively identified in this fashion. The reconstruction algorithm terminates in the lower right corner of the image. Subsequently, the metrics of the statistical and physical descriptors are evaluated.

2.1. Architecture of DNN

Deep neural learning is the subclass of machine learning using DNN as a tool for solving complex problems. Each DNN has multiple layers of interconnected nodes enabling one to learn complex representations of data by discovering hierarchical patterns and features, see [15]. The regular DNN is composed of three types of layers:

(1.) Input layer processing input data into the model,

(2.) hidden layers representing the key part of DNN and applying weights to the inputs and directing them through an activation function as the outputs,

(3.) output layer is the last layer in the neural network calculating the final probability scores of desired outputs.

The special case of DNN is the convolutional neural network (CNN) developed for image classification and data visual interpretation, see [16]. It is based on the principles of mathematical convolution extracting the important features from the image with the help of learnable filters. The CNN is primarily composed of

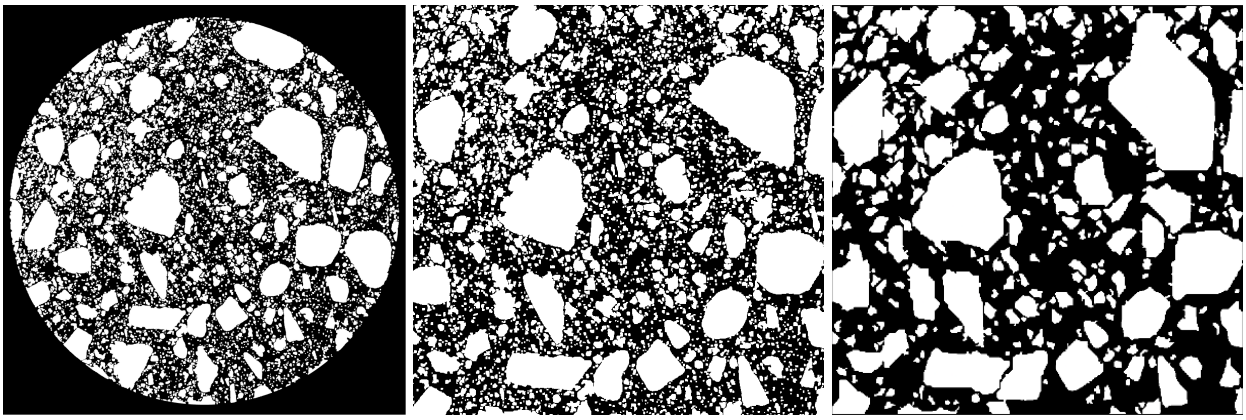

(A). Original segmented image – 1 200 × 1 225 px.

(B). The largest possible square image cut from the original segmented image – 816 × 816 px.

(C). The final image adjusted for redundant pores – 400 × 400 px.

FIGURE 3. Input image preparation.

convolutional layers and max pooling layers reducing the number of weights in the neural network. Our designed classifiers are built upon the standards of DNN and CNN architectures.

3. EXAMPLE

The example devoted to the reconstruction of the concrete structure using deep learning techniques is illustrated in this section. The sample of concrete morphology that is being reconstructed is depicted in Figure 3a. It is a CT scan of the concrete transformed by a segmentation algorithm into a monochrome image. The white pixels indicate the aggregates and the pores, while the cementitious binder in between is represented by black pixels. The sample image was captured on a 74 mm diameter concrete cylinder. For algorithmic simplicity, the largest possible square image with dimensions of 816×816 px is selected from the original segmented image, see Figure 3b. Although the training process of our computational model is accelerated on a graphics card (Nvidia GeForce RTX 2060), it turns out that it is not possible to work with such a huge dataset collected from the largest possible square image. Therefore, we reduced the image to a final resolution of 400 × 400 px minimizing the work with large data files. Unfortunately, the segmentation algorithm does not allow to identify between the pore and the aggregate and labels both phases identically as white pixels. Since the original grain size distribution curve is known, a portion of the small white pixels has been removed so that the grain size distribution curve is as close as possible to the original mixture curve of the concrete sample. The histogram shows the grain size distribution curve of the final image determined by the principal component analysis (PCA) and Feret's characteristics (Feret), and the real volume distributions of aggregates in the investigated concrete, see Figure 4. The imperceptible differences in the histogram are probably mainly caused by the absence of the third grain dimension in the calculation of the grain size distribution curves. The final 400 × 400 px image, adjusted for redundant pores, is shown in Figure 3c.

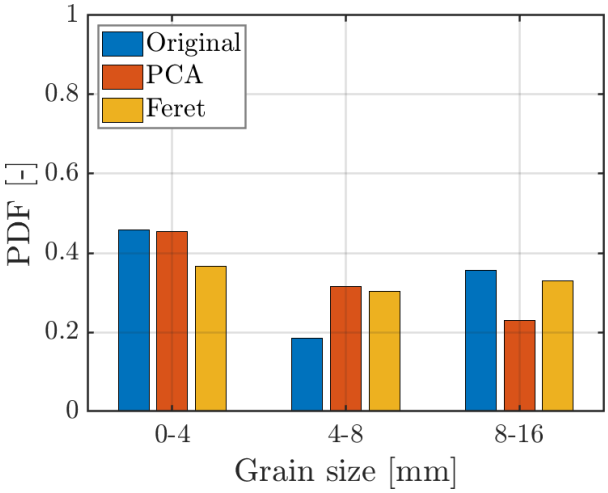

FIGURE 4. Grain size distribution curve of final image utilized for the reconstruction process. The original data (blue-labeled) represents the concrete mixture used for the CT scanning. The red-labeled and orange-labeled grain size distribution curves display the results computed for the PCA and Feret's algorithm, respectively.

The computational image reconstruction algorithm offers various solutions with different success rates influenced by several variables. The variables affecting the reconstruction process are mainly:

(1.) Hyper-parameters of the model. These are the parameters controlling the neural network architecture, and some of their aspects are examined here in detail. In particular, the type of neural network layer and its input parameters such as the number of neurons, the composition of the layers in a sequence, or the total number of layers.

(2.) The size of the pixel neighborhood is the second essential parameter that significantly affects

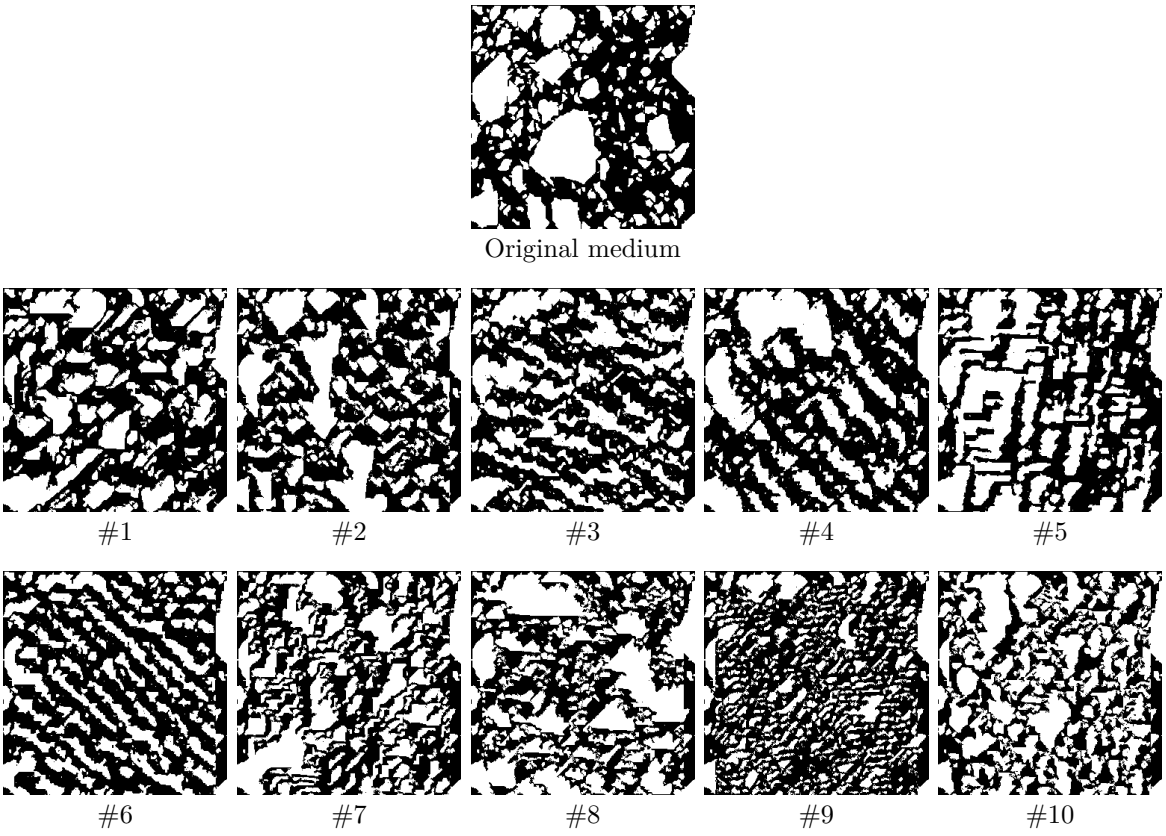

Figure 5. The original and resulting reconstructed images (#1–#10).

Model ID	Architecture of DNN
#1	15x15_c(16,3x3)_c(16,3x3)_m(2x2)_d(64)_d(64)_d(64)
#2	15x15_c(16,3x3)_c(16,3x3)_m(2x2)_d(128)_d(128)_d(128)
#3	15x15_c(32,3x3)_c(32,3x3)_m(2x2)_d(64,l1_0.01)_d(64)_d(64)
#4	15x15_d(128)_d(128)_d(128)
#5	15x15_d(128)_d(128)
#6	15x15_d(64)_d(64)_d(64)
#7	15x15_c(16,3x3)_c(16,3x3)_m(2x2)_d(128)_d(128)_d(128)
#8	15x15_c(16,3x3)_c(16,3x3)_m(2x2)_d(128)_d(128)
#9	15x15_c(8,3x3)_c(8,3x3)_m(2x2)_d(128)_d(128)_d(128)
#10	15x15_c(8,3x3)_c(8,3x3)_m(2x2)_d(64)_d(64)_d(64)

Table 1. Model ID's and abbreviated names of DNN architecture: For illustration, 15×15 stands for the pixel neighborhood, i.e. the dimensions of w and h in pixels, c(16,3x3) is the convolutional layer with 16 filters of spatial size 3x3, m(2x2) is the max pooling layer with 2x2 filter, and d(64) is the dense layer with 64 neurons.

the success rate of the entire model. This parameter has also been investigated; however, due to the limited space of the paper, we limit ourselves to claiming that for the problem illustrated here, a pixel neighborhood of 15×15 px seems optimal.

The hyper-parameters of the model are investigated on the image with dimensions of 300×300 px, see Figure 5. The reason for reducing the image to acceptable dimensions is again the higher computational effort of the entire study, which is performed on a series of 10 architectures of the neural network with differently composed convolutional, dense, and max pooling layers. The model ID's and abbreviated names of DNN architecture are summarized in Table 1. It is obvious that the possibility of designing the DNN architecture is enormous, especially in terms of filter size or number of neurons; thus this study is limited more to the comparison between the CNN and DNN architectures.

The resulting reconstructed images for ten different DNN architectures are depicted in Figure 5. Besides the visual comparison, the following table (Table 2) displays the values of errors in the statistical descriptors computed for the original and reconstructed structures. From the wide range of statistical descriptors, three fundamental metrics are selected for our study – the volume fraction (ϕ), the two-point proba-

Model ID	$\epsilon_{\phi}^{\text{white}}$	$\epsilon_{S2}^{\text{white}}$	$\epsilon_{S2}^{\text{black}}$	$\epsilon_{L2}^{\text{white}}$	$\epsilon_{L2}^{\text{black}}$
#1	0.001797	0.000157	0.000158	0.000171	0.000106
#2	0.009209	0.000185	0.000220	0.000205	0.000117
#3	0.010342	0.000238	0.000284	0.000202	0.000148
#4	0.011240	0.000247	0.000303	0.000213	0.000153
#5	0.054454	0.002175	0.002939	0.000796	0.000557
#6	0.055820	0.001978	0.003782	0.000727	0.000627
#7	0.060252	0.002672	0.003554	0.000884	0.000614
#8	0.092767	0.006558	0.007819	0.001403	0.000919
#9	0.094060	0.004631	0.010755	0.001173	0.001081
#10	0.113770	0.010151	0.011235	0.001756	0.001106

TABLE 2. The resulting values of errors calculated for the volume fraction, the two-point probability function, and the lineal path function.

bility function ($S2$), and the lineal path function ($L2$). These statistical descriptors have been used in reconstruction problems for a significant period and have become an essential part of numerical studies devoted to material morphology. Their particular formulations are skipped here, and the interested reader referred to, e.g., [17] or [2] providing basic characteristics, illustrative examples, and implementation strategies. The values of errors are calculated according to the following formulas expressing the differences between values of selected statistical descriptors calculated for the original and reconstructed image:

$$\epsilon_{\phi}^{\text{phase}} = \phi_{\text{orig}}^{\text{phase}} - \phi_{\text{rec}}^{\text{phase}}, \tag{1}$$

where

$\phi_{\text{orig}}^{\text{phase}}$ is the volume fractions of a given phase corresponding to the original image,

$\phi_{\text{rec}}^{\text{phase}}$ is the volume fractions of a given phase corresponding to the reconstructed image.

The values of errors for complex statistical descriptors are evaluated as:

$$\epsilon_{p}^{\text{phase}} = \frac{\sum_{r=1}^{R}\sum_{s=1}^{S}(p_{rs,\text{orig}}^{\text{phase}} - p_{rs,\text{rec}}^{\text{phase}})^2}{SR}, \tag{2}$$

where

R and S are the image dimensions,

p is the chosen statistical descriptor, here $p = \{S2, L2\}$.

From the resulting values of errors and comparison of the reconstructed images, two models #1 and #2 have been studied in detail and more runs of reconstruction algorithm have been performed focusing on the statistical moments of error analysis. The most stable classifier is model #2, which is further utilized for reconstructing the larger image of the concrete cross-section in the following paragraph.

3.1. Large image Evaluation

The final reconstruction is carried out on an image of dimensions 400×400 px, the original image is shown in Figure 6a, and the reconstructed result is in Figure 6b. It is apparent that the reconstruction algorithm is quite successful from the visual comparison of these two images. However, some irregularities are observed in the shape of the grains compared to the original image. From the perspective of statistical descriptors, the following values of errors – $\epsilon_{\phi}^{\text{white}} = 0.001046$, $\epsilon_{S2}^{\text{white}} = 0.000171$, and $\epsilon_{L2}^{\text{white}} = 0.000069$ – indicate

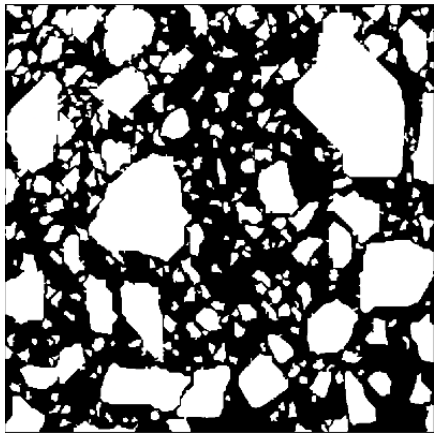

(A). Original image – 400×400 px.

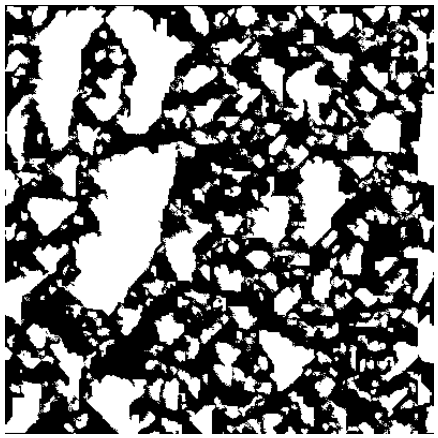

(B). Reconstructed image obtained with the model #2 – 400×400 px.

FIGURE 6. Final image reconstruction.

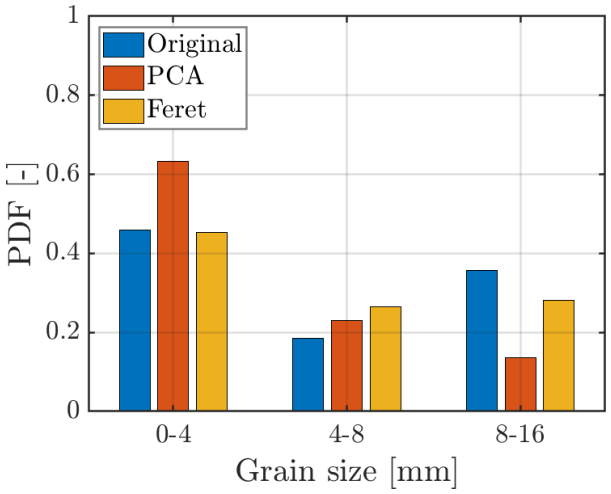

Figure 7. Comparison of grain size distribution curves obtained for the original and reconstructed concrete cross-sections.

again good performance of proposed strategy. The last comparison (see Figure 7) shows the grain size distribution curves of original and reconstructed images computed for the algorithm using Feret diameters (Feret) and principal component analysis (PCA). In the case of the PCA evaluation, the original and reconstructed images differ in the representation of the individual grain size as follows: size range of 0–4 mm – 17.7 %, 4–8 mm – 8.6 %, and 8–16 mm – 9.1 %. In the case of the Feret diameters, the grain size distribution differs as follows: size range of 0–4 mm – 8.6 %, 4–8 mm – 3.9 %, and 8–16 mm – 4.7 %. Thus, the reconstructed image contains more aggregates of 0–4 mm since both methods result in a higher volume percentage, and conversely, size ranges of 4–8 mm and 8–16 mm are less observed in the reconstructed image. From the perspective of the grain size distribution curve, the reconstruction process of concrete morphology is less effective.

4. Conclusion

The reconstruction of the concrete cross-section area using deep learning techniques is illustrated in this paper. The proposed model can generate reasonably accurate samples of concrete morphology in terms of the selected statistical descriptors. Some limitations are observed in the results of the grain size distribution curve, and the shapes of the aggregates which appear to be more irregular. Taking into account that the computational hardware has some limitations and also the fact that we only handled one image, the obtained result can be evaluated positively.

Acknowledgements

The authors are thankful for financial support from the Student Grant Competition of CTU, project No. SGS23/152/OHK1/3T/11 and the Czech Science Foundation, project No. 22-35755K.

References

[1] C. L. Y. Yeong, S. Torquato. Reconstructing random media. *Physical review E* **57**(1):495, 1998. https://doi.org/10.1103/PhysRevE.57.495

[2] J. Havelka, A. Kučerová, J. Sýkora. Compression and reconstruction of random microstructures using accelerated lineal path function. *Computational Materials Science* **122**:102–117, 2016. https://doi.org/10.1016/j.commatsci.2016.04.044

[3] R. Bostanabad, Y. Zhang, X. Li, et al. Computational microstructure characterization and reconstruction: Review of the state-of-the-art techniques. *Progress in Materials Science* **95**:1–41, 2018. https://doi.org/10.1016/j.pmatsci.2018.01.005

[4] M. V. Karsanina, K. M. Gerke. Stochastic (re)constructions of non-stationary material structures: Using ensemble averaged correlation functions and non-uniform phase distributions. *Physica A: Statistical Mechanics and its Applications* **611**:128417, 2023. https://doi.org/10.1016/j.physa.2022.128417

[5] M. Lombardo, J. Zeman, M. Sejnoha, G. Falsone. Stochastic modeling of chaotic masonry via mesostructural characterization. *International Journal for Multiscale Computational Engineering* **7**(2):171–185, 2009. https://doi.org/10.1615/IntJMultCompEng.v7.i2.70

[6] J. Havelka, A. Kučerová, J. Sýkora. Dimensionality reduction in thermal tomography. *Computers & Mathematics with Applications* **78**(9):3077–3089, 2019. https://doi.org/10.1016/j.camwa.2019.04.019

[7] R. Bostanabad, A. T. Bui, W. Xie, et al. Stochastic microstructure characterization and reconstruction via supervised learning. *Acta Materialia* **103**:89–102, 2016. https://doi.org/10.1016/j.actamat.2015.09.044

[8] J. Fu, S. Cui, S. Cen, C. Li. Statistical characterization and reconstruction of heterogeneous microstructures using deep neural network. *Computer Methods in Applied Mechanics and Engineering* **373**:113516, 2021. https://doi.org/10.1016/j.cma.2020.113516

[9] K. Latka, M. Doškář, J. Zeman. Microstructure reconstruction via artificial neural networks: A combination of causal and non-causal approach. *Acta Polytechnica CTU Proceedings* **34**:32–37, 2022. https://doi.org/10.14311/APP.2022.34.0032

[10] L.-Y. Wei, M. Levoy. Fast texture synthesis using tree-structured vector quantization. In *Proceedings of the 27th annual conference on Computer graphics and interactive techniques*, pp. 479–488. 2000. https://doi.org/10.1145/344779.345009

[11] V. Sze, Y.-H. Chen, T.-J. Yang, J. S. Emer. Efficient processing of deep neural networks: A tutorial and survey. *Proceedings of the IEEE* **105**(12):2295–2329, 2017. https://doi.org/10.1109/JPROC.2017.2761740

[12] K.-H. Lee, G. J. Yun. Microstructure reconstruction using diffusion-based generative models. *Mechanics of Advanced Materials and Structures* **31**(18):4443–4461, 2024. https://doi.org/10.1080/15376494.2023.2198528

[13] C. Düreth, P. Seibert, D. Rücker, et al. Conditional diffusion-based microstructure reconstruction. *Materials Today Communications* **35**:105608, 2023. https://doi.org/10.1016/j.mtcomm.2023.105608

[14] X. Lyu, X. Ren. Microstructure reconstruction of 2D/3D random materials via diffusion-based deep generative models. *Scientific Reports* **14**(1):5041, 2024. https://doi.org/10.1038/s41598-024-54861-9

[15] F. Chollet. *Deep learning with Python*. Manning, 2021. ISBN 9781617296864.

[16] Z. Li, F. Liu, W. Yang, et al. A survey of convolutional neural networks: Analysis, applications, and prospects. *IEEE Transactions on Neural Networks and Learning Systems* **33**(12):6999–7019, 2022. https://doi.org/10.1109/TNNLS.2021.3084827

[17] J. Zeman. *Analysis of composite materials with random microstructure*. Ph.D. thesis, Czech Technical University, 2003. https://doi.org/10.13140/RG.2.1.2399.0004

TRANSFORMING POINT CLOUD DATA INTO 3D BIM MODELS: A CASE STUDY ON SLABS

Slávek Zbirovský*, Václav Nežerka

Czech Technical University in Prague, Faculty of Civil Engineering, Department of Physics, Thákurova 7, 166 29 Prague, Czech Republic

* corresponding author: slavek.zbirovsky@fsv.cvut.cz

Abstract. We explore the automatized transition of point cloud data into a Building Information Model (BIM), an essential task for reconstructions, demolition plans, or auditing. In this study, we use point cloud data generated by 3D laser scanning. The research elaborates on the process of segregating and segmenting floor slabs from point clouds and the developed algorithms categorize point cloud subsets based on different height parameters (z-coordinates). Once slabs are identified, a function is applied to create envelopes for each slab level, accommodating any convex or concave shape. The resulting geometry, along with relevant auxiliary data, is exported in the Industry Foundation Classes (IFC) format, a standard for BIM data exchange. The exported entities can then be further processed using prevalent software such as Revit or ArchiCAD.

Keywords: BIM, pointcloud, automatization, IFC.

1. Introduction

The conversion of point cloud data into 3D Building Information Model (BIM) has been predominantly accomplished through manual methods, which have served as a fundamental technique in the industry for the last decades. These manual methods involve precise tracing of the outlines of objects and structures within the point cloud data to create a comprehensive 3D model. While this process allows for greater control over individual elements and ensures the overall integrity of the model, it is time-consuming. Moreover, manual methods are often constrained by the expertise of the user, the limitations of the software, and the scale and intricacy of the scanned point cloud.

In recent years there has been significant progress in automated methods of transforming point cloud data into 3D models. These automated techniques use sophisticated algorithms and computer software to process data from the point cloud, greatly reducing the need for human intervention in acquiring data for a BIM model. By minimizing manual intervention, automated methods offer higher processing speeds. Nonetheless, they can also introduce a greater number of errors compared to traditional manual modelling techniques. Commercial solutions, such as Pointfuse, Faramoon, Aurivus [1–3], have emerged in the market, providing semi-automatic conversion capabilities for transforming point cloud data into accurate 3D models. Also, there was published many solutions which integrate state-of-the-art algorithms such as RANSAC [4–7].

In this work, we describe a methodology that utilizes all the past developments in the area and enables the extraction of 3D entities along with auxiliary data. The flowchart of this procedure is provided in Figure 1 and described in the following sections.

1.1. Building information modeling

Building Information Modeling (BIM) is a process that has a major impact on how construction projects are planned, designed, constructed, managed, or what happens to them after their lifetime. BIM integrates various aspects of a construction project into a comprehensive 3D information model, including architectural, structural, and MEP (mechanical, electrical, and plumbing) systems.

The 3D model provides information that facilitates cooperation between construction participants, the investor, and building management throughout the project's life cycle. BIM enables accurate visualization, analysis, and simulation of building performance, leading to better decision-making, reduced errors, and increased efficiency. With BIM, all professions can access real-time information, coordinate designs, reduce collisions, generate detailed documentation, and simulate the construction sequence. Suppose there is no BIM model available at the end of the life cycle of a building. In that case, it can pose challenges and limitations for effective planning and decision-making during the deconstruction, demolition, or adaptive reuse process. For these reasons, it is good to create at least a partial BIM model containing as-built constructions and their materials. Conventional methods of creating 3D models from as-built documentation tend to be inaccurate, which is why digital scan technologies have begun to be used in recent decades.

1.2. Point clouds

Point clouds are large data sets that describe an object or space in a coordinate system using individual points. These points usually represent the surfaces of scanned objects and are described by coordinates

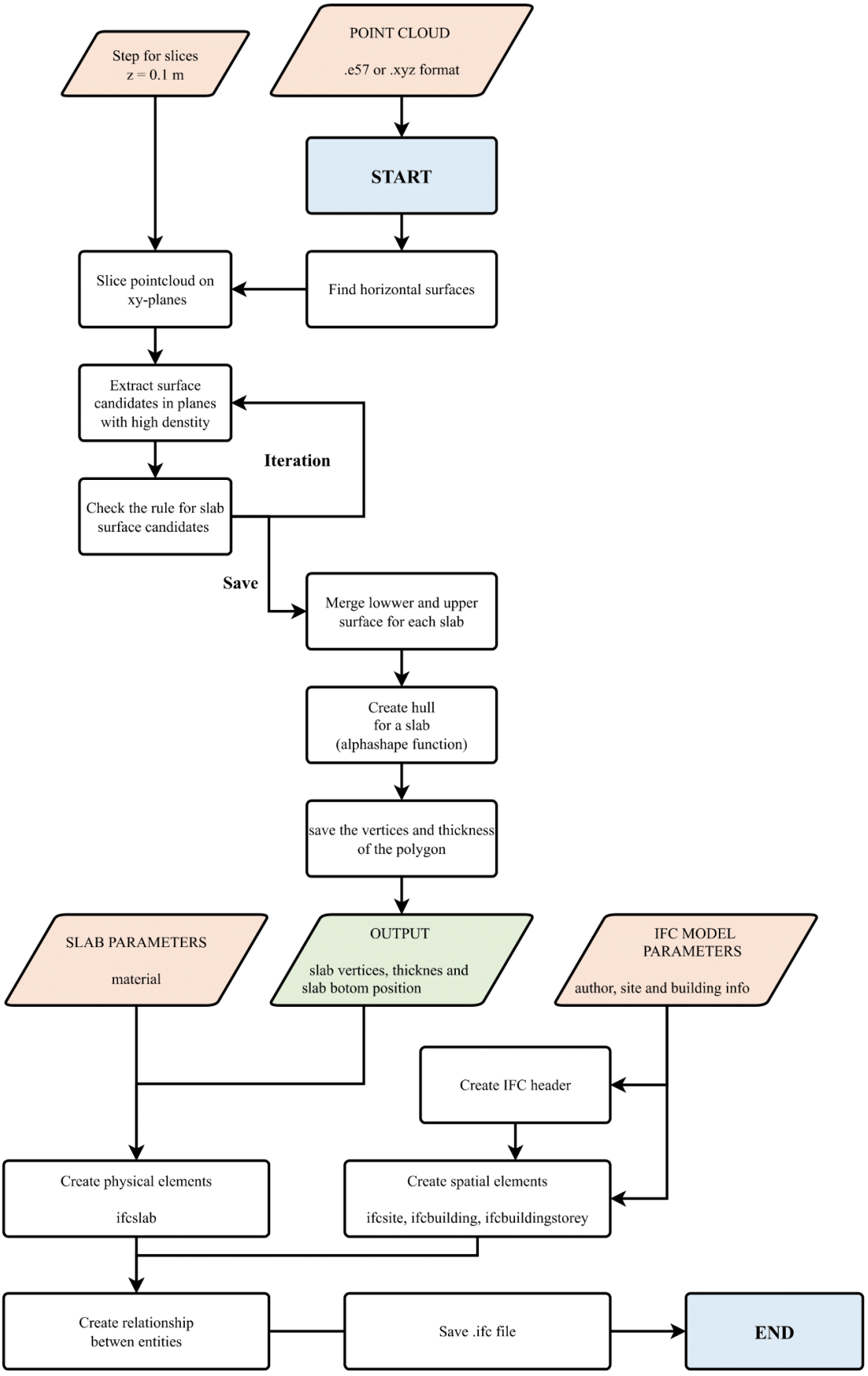

FIGURE 1. Flow chart diagram of the Python script used for extraction of floor elements from point clouds and their formatting into the IFC format.

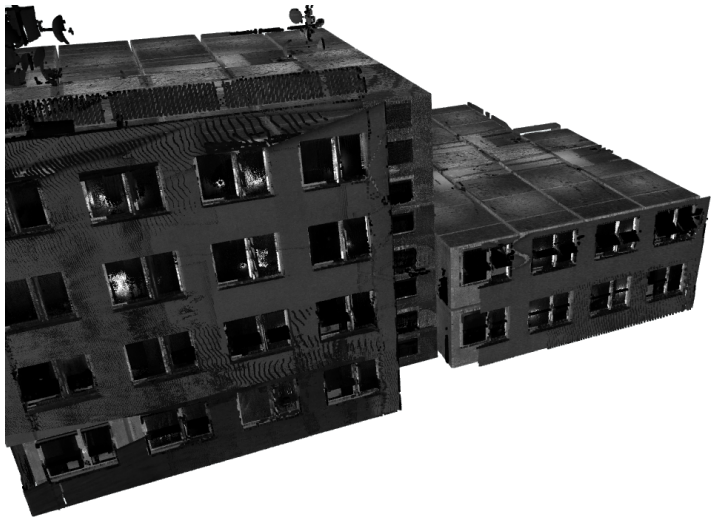

Figure 2. Laser-scanned data (point cloud) of a building that was used for testing of the presented algorithms.

(X,Y,Z), RGB values or brightness intensities. Figure 2 shows an example of a common point cloud containing a building. The essential parameter of each point cloud is the density, with a higher density value, texture, and finer details can be distinguished on the scanned surface. But this parameter also negatively enables the speed of the scan itself, the requirements for the computing power of the device on which the point cloud will be processed, and the resulting large file.

The most common way to obtain the point cloud is LiDAR (Light detection and ranging) technology. It works on the principle of the spatial polar method, which evaluates the position of individual points based on elevation angles and distances. The second method, also commonly used in surveying, is photogrammetry, exploiting images taken from different angles and positions [8, 9].

1.3. IFC

IFC was developed by the International Alliance for Interoperability (IAI), now known as buildingSMART International, with the aim of improving collaboration and communication among different software applications used throughout the life cycle of a building or infrastructure project.

IFC defines a common data schema and a standardized set of object classes, properties, and relationships to represent various aspects of a building project, such as building elements, spaces, materials, quantities, schedules, and more. The data model is based on a semantic representation, meaning that it captures not only geometric information but also the meaning and behaviour of the objects and their relationships.

2. Algorithms

The algorithms for creating and placing slabs within a building can be divided into several parts. In the first step, the point cloud is divided into strips, which are planes parallel to the x-y axes, and those strips with a point density on the histogram higher than a certain percentage (set to 50 % in our study) of the strip with the highest number of points are extracted. Figure 3 shows a section of the point cloud and a histogram on which individual horizontal surfaces are visible in places with maximum histogram values. In these strips, the median z-coordinate is taken based on the index and subsequently labelled as the lower or upper surface. Then, neighbouring surfaces formed by points are unified, creating the top and bottom surfaces of the slab.

The final step involves calling the function *create_hull_alphashape*. The alphashape function for a hull creation takes a set of 2D points as input and performs a Delaunay triangulation. It then removes edges longer than a specified alpha value, resulting in a non-convex polygon. The remaining edges form the boundaries of the hull polygon, and the function returns the set of vertices and edges that define the polygon [10]. An example of the Delaunay triangulation and the Alpha shape function with $\alpha = 5$ can be seen in Figure 4.

3. IFC file ganeration

The IFC files presented in this study were generated according to the *IFC4_ADD2_TC1 structure* [11]. The library for Python, *Ifcopenshell 0.7.0*, was used to generate an *output.ifc* file [12]. The structure of an IFC file can be divided into two main parts. The first, which is called a header, contains basic information such as name, author, view definition, implementation level, and file schema. The example of the file header section in STEP (Standard for the Exchange of Product model data) format can be seen in Figure 5. The second part of the file is data section it is the main part of the IFC file and contains the actual data in a structured format. It consists of the IFC entities representing building elements, relationships, and properties.

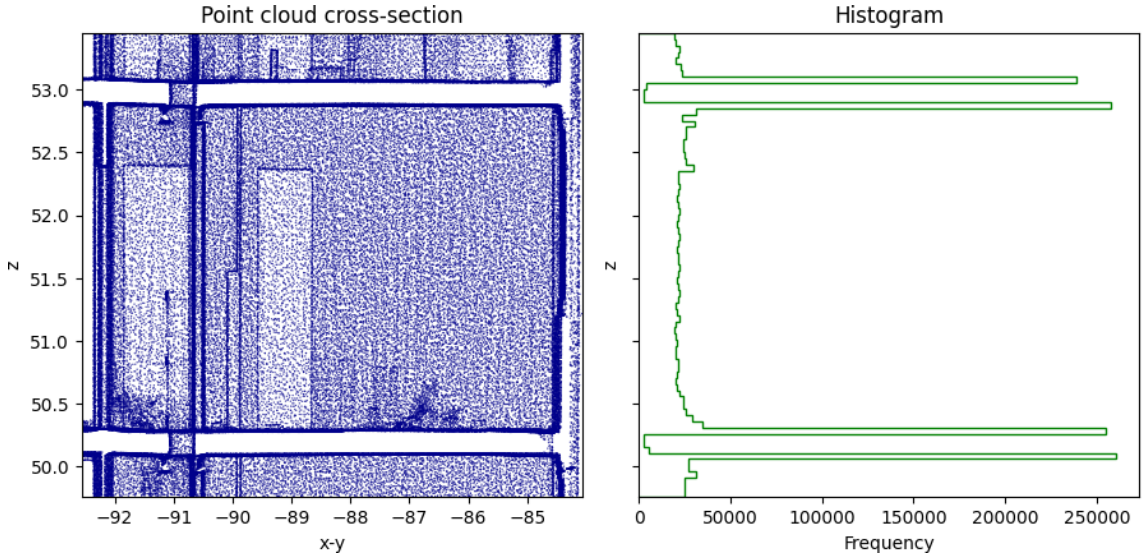

FIGURE 3. A z-coordinate histogram of point cloud data to detect slab surface candidates.

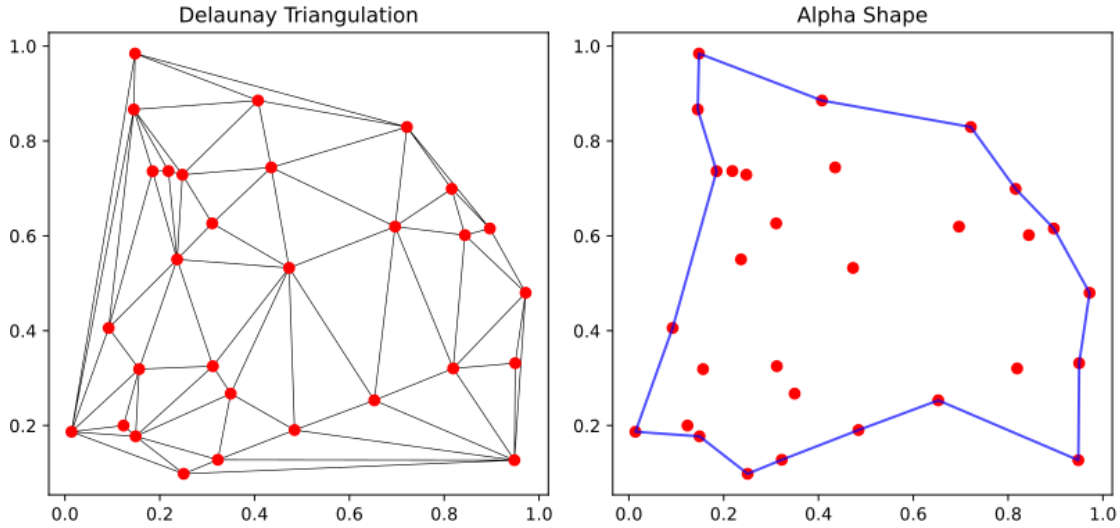

FIGURE 4. Alpha shape of a set of 2D points from the Delaunay triangulation; $\alpha = 5$.

```
ISO-10303-21;
HEADER;
FILE_DESCRIPTION(('ViewDefinition [DesignTransferView_V1.0]'),'2;1');
FILE_NAME('output-2.ifc','2023-07-03T13:32:25.969496',
('Slavek Zbirovsky'),('CTU in Prague'),'IfcOpenShell v0.7.0-476ab506d',
'Cloud2BIM','None');
FILE_SCHEMA(('IFC4'));
ENDSEC;
```

FIGURE 5. Example of the IFC STEP file header section structure.

In addition to the slab geometry, the data part also describes the structure of the project. An essential part of every ifc file is the *ifcproject*. This instance represents the main project entity. It is a fundamental concept within the IFC schema that serves as a container for various building-related information and acts as a starting point for organizing and representing the entire building or construction project. The tree structure *ifcproject* > *ifcsite* > *ifcbuilding* > *ifcstorey* is created in the file. This structure makes it possible to place and assign individual elements to different buildings and floors. The generated floor structures can be seen in Figure 6.

4. SLAB IFC GEOMETRY

By combining the profile definition and the extrusion parameters, the *IfcExtrudedAreaSolid* entity creates a 3D solid geometry that represents the slab. The profile shape which is described by *IfcArbitraryClosedProfileDef* entity is extruded along the specified direction to form the solid shape. The resulting solid represents the volume of the slab in the specified dimensions and position. The main IFC entities for the slab are provided in Figure 7.

5. CONCLUSION

In this study, an algorithm was developed to automate the conversion of point cloud data into a 3D BIM model, with a specific focus on slabs. The code was implemented in Python and at the moment it

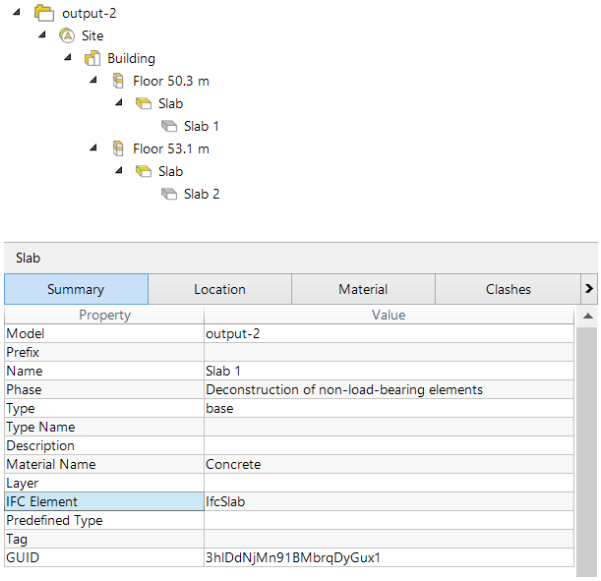

Figure 6. IFC tree structure with assigned slabs.

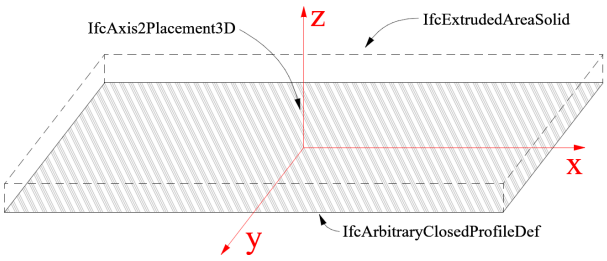

Figure 7. IFC entities used to create the slab geometry.

is capable of autonomously assessing individual floor levels in a point cloud and identifying floor slabs. Subsequently, the information about these slabs is written into an IFC structure, enabling compatibility with commercial software such as ArchiCAD, Revit, and other user-friendly software tools. This algorithm significantly expedites the process of working with point cloud data during the creation of a 3D BIM model for existing buildings.

This research showcases the successful development and implementation of a Python-based algorithm that automates the conversion of point cloud data into 3D BIM models, with a particular emphasis on slabs. The seamless integration of this algorithm with commercial BIM software makes it a valuable asset for streamlining the modelling process of existing structures. The significance of this advancement lies in its potential to save time, reduce manual effort, and enhance the overall accuracy of 3D BIM models, ultimately contributing to the advancement of the industry.

List of symbols

BIM Building information modeling

LiDAR Light detection and ranging

IFC Industry foundation classes

IAI International Aliance for Interoperability

STEP Standard for the Exchange of Product model data

Acknowledgements

This work was supported by the Faculty of Civil Engineering at CTU in Prague, grant number SGS23/004/OHK1/1T/11 and by the European Union's Horizon Europe Framework Programme (call HORIZON-CL4-2021-TWIN-TRANSITION-01-11) under grant agreement No. 101058580, project RECONMATIC (Automated solutions for sustainable and circular construction and demolition waste management).

We would like to express our gratitude to Cegra and Graphisoft for facilitating the provision of a complimentary ArchiCAD software license, a crucial tool employed in the processing of point cloud data and the visualization of the automatically generated Building Information Model (BIM) in this research.

References

[1] Autodesk.com. Pointfuse, 2023. [2023-07-06]. https://pointfuse.com/

[2] Faramoon, 2023. [2023-07-06]. https://www.faramoon.io/

[3] Aurivus, 2023. [2023-07-06]. https://aurivus.com/

[4] M. A. Fischler, R. C. Bolles. Random sample consensus: A paradigm for model fitting with applications to image analysis and automated cartography. *Readings in Computer Vision* pp. 726–740, 1987. https://doi.org/10.1016/b978-0-08-051581-6.50070-2

[5] Z. Li, J. Shan. RANSAC-based multi primitive building reconstruction from 3D point clouds. *ISPRS Journal of Photogrammetry and Remote Sensing* **185**:247–260, 2022. https://doi.org/10.1016/j.isprsjprs.2021.12.012

[6] T. Doougphummet. *3D building internal structural component segmentation from point cloud data using DBscan and modified RANSAC with normal deviation conditions*. Master's thesis, Chulalongkorn University, 2022. https://doi.org/10.58837/chula.the.2022.13

[7] W. Yue, J. Lu, W. Zhou, Y. Miao. A new plane segmentation method of point cloud based on mean shift and RANSAC. In *2018 Chinese Control And Decision Conference (CCDC)*, pp. 1658–1663. 2018. https://doi.org/10.1109/ccdc.2018.8407394

[8] Q. Wang, Y. Tan, Z. Mei. Computational methods of acquisition and processing of 3D point cloud data for construction applications. *Archives of computational methods in engineering* **27**(2):479–499, 2020. https://doi.org/10.1007/s11831-019-09320-4

[9] F. Remondino. Point cloud acquisition & structuring, 2018. [2023-06-19]. https://3d.bk.tudelft.nl/pdfs/pcp2018/pcp2018_FabioRemondino.pdf

[10] H. Edelsbrunner, D. Kirkpatrick, R. Seidel. On the shape of a set of points in the plane. *IEEE Transactions on Information Theory* **29**(4):551–559, 1983. https://doi.org/10.1109/tit.1983.1056714

[11] BuildingSMART. IFC4_ADD2_TC1 – 4.0.2.1 Official, 2022. [2023-05-31]. https://standards.buildingsmart.org/IFC/RELEASE/IFC4/ADD2_TC1/HTML

[12] D. Moult. Ifcopenshell 0.7.0 documentation, 2023. [2023-07-06]. https://pypi.org/project/ifcopenshell/

FORMULATION AND IMPLEMENTATION OF NONLINEAR ELASTICITY IN ADVANCED CONSTITUTIVE MODELS IN GEOMECHANICS

Tereza Žalská[a,*], Michal Šejnoha[b], Tomáš Janda[b], Alena Zemanová[a]

[a] *Czech Technical University in Prague, Faculty of Civil Engineering, Department of Geotechnics, Thákurova 7, 166 29 Prague, Czech Republic*

[b] *Czech Technical University in Prague, Faculty of Civil Engineering, Department of Mechanics, Thákurova 7, 166 29 Prague, Czech Republic*

[*] corresponding author: tereza.zalska@fsv.cvut.cz

Abstract. Several formulations of a nonlinear elastic behavior within the yield surface of the selected advanced constitutive models are described and compared. Since concentrating on geotechnical applications the accompanied numerical simulations are limited to basic laboratory tests such as isotropic compression, oedometer, and drained triaxial compression. The results show a significant influence of the size of the initial load step on final predictions particularly when starting from a very low initial stiffness associated with the assumed zero initial stress. Differences in the predicted response arising from different formulations are also discussed. These might be quite significant and the design engineer should be aware of that when choosing a particular computational software.

Keywords: Hardening soil model, generalized cam clay model, soft soil model, nonlinear elasticity, oedometer, isotropic compression, triaxial compression.

1. Introduction

Constructing underground structures in densely populated areas, preventing large scale landslides, as well as being able to accurately simulate a complex response of soils observed experimentally, opens the door to the application of advanced constitutive models [1, 2]. Grounding on experimental evidence such models attempt to address a nonlinear response of soils already at initial stages of loading. An illustrative example are the critical state models [1, 3] where the nonlinear stress-strain behavior within the yield surface arises naturally. A large group of formulations introduce such a behavior in the spirit of Duncan and Chang hyperbolic model [4–7]. While their appearance in available commercial software is common [8–10] (to cite a few), the details on their numerical implementation within a given constitutive model may differ. This in turn may result in predictions, which are considerably influenced by the initial load increment. In some formulations, the load step dependence yields loading-unloading curves which deviate even for loading conditions that do not exceed the yield limit, often resulting in an artificial residual strain. It is therefore crucial to understand such potential drawbacks and the user should be aware of that when creating the computational model for a given geotechnical construction.

The present paper revisits this issue in light of three popular constitutive models implemented in the above mentioned commercial codes. In particular, the Hardening Soil Model [5, 6], the Generalized Cam clay model [10, 11], and the Soft soil model [12] are examined in Section 2 with emphasis on the implementation of the associated nonlinear elastic constitutive model. The results of numerical simulations together with a thorough discussion are presented in Section 3. All calculations are carried out using the GEO5 FEM software [10].

2. Advanced constitutive models

The present section provides details on the formulation of nonlinear elasticity of the selected constitutive models, while the plasticity issues will be presented only briefly with details available in the above mentioned references.

2.1. Hardening soil model

The Hardening soil (HS) model developed in [5] and later extended in [6] to account for small strain yielding is plotted in Figure 1. As seen in Figure 1a it combines two yield surfaces where the shear part, bounded by a limiting yield surface of the Mohr-Coulomb type, is derived on the assumption of the hyperbolic stress-strain response in triaxial compression as depicted in Figure 1c with ε_1 being the major principal strain and q representing an equivalent deviatoric stress measure. In the formulation implemented in GEO5 FEM, both the shear yield surface and the cap yield surface, which is assumed elliptic and centered at the origin of the meridian plane, plot as a smooth hexagon in the deviatoric plane in the spirit of the Matsuoka-Nakai (MN) yield surface [13], see Figure 1b. The evolution (hardening) of both surfaces is controlled by the current value of the equivalent deviatoric plastic strain γ and preconsolidation pressure p_c, respectively.

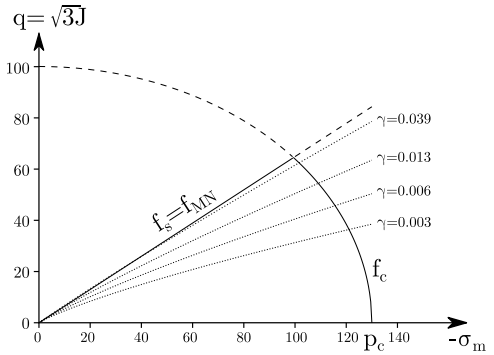

(A). Yield surface with zero cohesion in meridian plane.

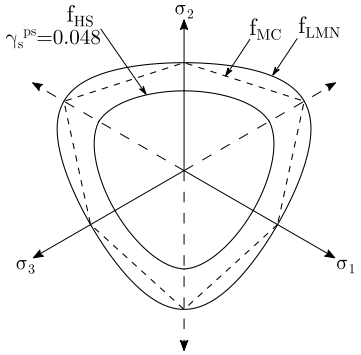

(B). Yield surface in deviatoric plane.

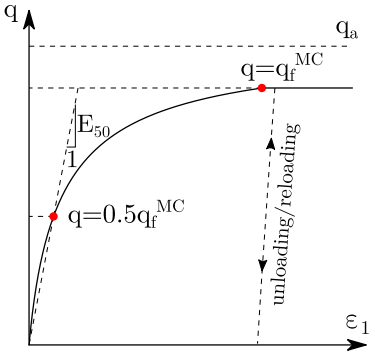

(C). Response in triaxial compression.

FIGURE 1. Graphical representation of Hardening soil model.

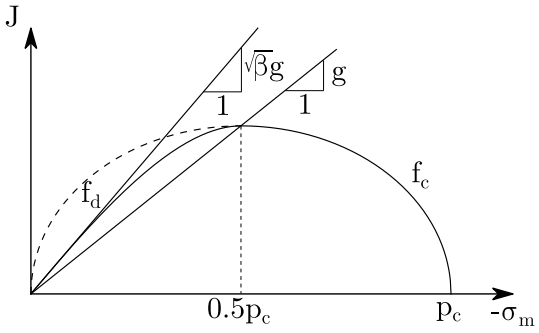

(A). Yield surface in meridian plane.

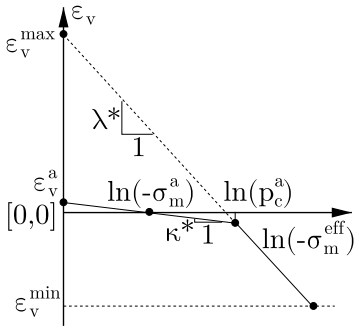

(B). Behavior under isotropic compression.

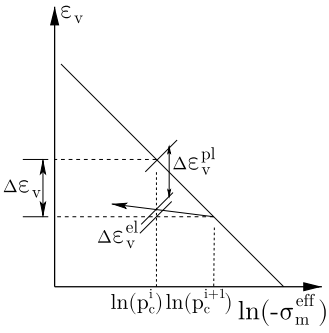

(C). Elastic and plastic part of total strain increment.

FIGURE 2. Graphical representation of Generalized Cam clay model.

The nonlinear elastic model due to Vermeer [14] writes the elastic modulus E_{ur} in the form of a power law as a function of the current value of mean effective stress σ_m as:

$$E_{ur}(\sigma_m) = E_{ur}^{\mathrm{ref}} \left(\frac{\sigma_m - c\cot\varphi}{\sigma_m^{\mathrm{ref}} - c\cot\varphi} \right)^m, \qquad (1)$$

where

E_{ur}^{ref}, σ_m^{ref}, m are model parameters,

c, φ are the shear strength parameters, the cohesion and the angle of internal friction, respectively.

In particular, E_{ur}^{ref} is the reference elastic modulus for a reference stress σ_m^{ref} typically equal to $-100\,\mathrm{kPa}$. Note that the standard elasticity sign convention is adopted with tension being positive. For simplicity, we shall now consider the volumetric response only and assume a linear variation of the mean stress σ_m over a given load increment as:

$$\sigma_m = \eta\sigma_m^i + (1-\eta)\sigma_m^{i+1}. \qquad (2)$$

Setting $\eta = 1$ gives fully explicit formulation (forward Euler (FE) method, $\sigma_m = \sigma_m^i$ in Equation (1)) while $\eta = 0$ renders fully implicit (backward Euler (BE) method, $\sigma_m = \sigma_m^{i+1}$ in Equation (1)). Henceforth, the former formulation will be referred to as the constant elasticity (CE) return while the latter formulation will be termed the variable elasticity (VE) return. Further distinction is made by considering either secant formulation in the form:

$$\sigma_m^{i+1} = K_{ur}(\sigma_m(\eta))(\varepsilon_v^i + \Delta\varepsilon_v), \qquad (3)$$

or incremental formulation provided by:

$$\sigma_m^{i+1} = \sigma_m^i + K_{ur}(\sigma_m(\eta))\Delta\varepsilon_v, \qquad (4)$$

where K_{ur} is the elastic bulk modulus given by:

$$K_{ur} = \frac{E_{ur}}{3(1-2\nu_{ur})}. \qquad (5)$$

In particular, cases with $\eta = 1$ (FE), $\eta = 0$ (BE), and so called mid-point rule (MP), i.e., $\eta = 0.5 \rightarrow \sigma_m(\eta) = 0.5(\sigma_m^i + \sigma_m^{i+1})$, will be examined in Section 3.

2.2. Generalized Cam clay model

The Generalized Cam clay (GCC) model has been introduced to reconcile the principal drawback of the Modified Cam clay (MCC) model associated with overestimating the shear strength and consequently an excessive softening of highly overconsolidated soils. To this end, the supercritical (dilation) part of the MCC model was suitably adjusted, see Figure 2a, resulting in the dependence on both the critical friction angle φ_{cs} and peak friction angle φ via parameter β given by:

$$\beta = \left(\frac{\sin\varphi}{\sin\varphi_{cs}} \frac{3-\sin\varphi_{cs}}{3-\sin\varphi} \right)^2. \qquad (6)$$

Similar to the HS model, the MN yield surface represents the projection into a deviatoric plane.

The nonlinear elastic constitutive model derives from the assumed response in isotropic compression shown in Figures 2b and 2c. When moving along the unloading-reloading κ-line the rate form of the stress-strain law is provided by:

$$\dot{\sigma}_m = -\frac{\sigma_m}{\kappa^*}\dot{\varepsilon}_v^{el},\ \kappa^* = \frac{\kappa}{1+e}, \tag{7}$$

where

κ is called the swelling modulus,

e is the void ratio.

Integrating over a given time increment gives the evolution of the mean effective stress in the form:

$$\sigma_m^{i+1} = \sigma_m^i \exp\left[\frac{-\Delta\varepsilon_v^{el}}{\kappa^*}\right]. \tag{8}$$

Next, writing the stress increment $\Delta\sigma_m$ as:

$$\begin{aligned}\Delta\sigma_m &= \sigma_m^{i+1} - \sigma_m^i \\ &= \sigma_m^i\left(\exp\left[\frac{-\Delta\varepsilon_v^{el}}{\kappa^*}\right] - 1\right) = \overline{K}_s\Delta\varepsilon_v^{el},\end{aligned} \tag{9}$$

allows us to express the secant bulk modulus $\overline{K}_s$ as:

$$\overline{K}_s = \sigma_m^i\frac{\exp\left[-\dfrac{\Delta\varepsilon_v^{el}}{\kappa^*}\right] - 1}{\Delta\varepsilon_v^{el}}. \tag{10}$$

The analysis may simplify if leaving the concept of variable elasticity return represented by Equation (10) and assume the bulk modulus:

$$K^i = -\frac{\sigma_m^i}{\kappa^*}, \tag{11}$$

to be constant over the load increment (constant elasticity return), recall Equation (7).

2.3. Soft soil model

In the original MCC model the shear strength depends solely on the slope of the critical state line g which for the triaxial compression reads:

$$g = \frac{2\sqrt{3}\sin\varphi_{cs}}{3-\sin\varphi_{cs}}. \tag{12}$$

Brinkgreve showed in [12] that it is not possible to simulate both the oedometer stress path and full triaxial compression path with good accuracy using the same value of g. This let to the formulation of a Soft soil (SS) model combining the cap yield surface in the form of MCC model to predict a correct K_0-path and the shear yield surface, here again assumed in the form of MN model, to ensure a correct shear strength. Such a yield surface is plotted in Figure 3 where M_c for triaxial compression is given in terms of the coefficient of lateral earth pressure of normally consolidated

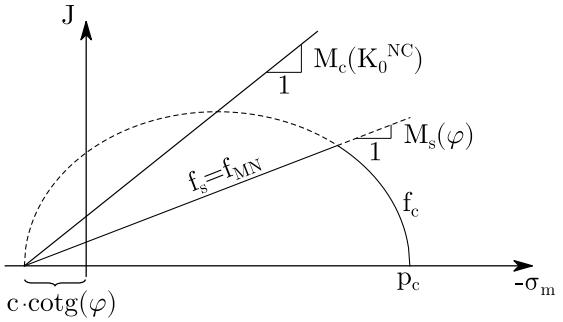

FIGURE 3. Yield surface of Soft soil model in meridian plane.

soils K_0^{NC} [12] whereas M_s follows from the solution of nonlinear MN yield function [13].

While the shear yield surface represents a response of an elastic perfectly plastic material, the cap yield surface may undergo isotropic hardening. To avoid potential softening within the cap model, which is not allowed in the present implementation, the M_c-value should be larger than the slope of the Matsuoka-Nakai failure surface M_s.

Considering the nonlinear elastic response, we follow the implementation in [8] and limit attention to the constant elasticity return of Equation (11). As suggested in [12] it is possible to relate Equation (11) to Equation (1) by writing:

$$K(\sigma_m) = K^{\text{ref}}\left(\frac{\sigma_m}{\sigma_m^{\text{ref}}}\right)^m. \tag{13}$$

When setting $m = 1$, the logarithmic compression law is recovered with:

$$\frac{1}{\kappa^*} = -\frac{K^{\text{ref}}}{\sigma_m^{\text{ref}}}. \tag{14}$$

3. Simulation of simple laboratory tests

Numerical simulation of three basic laboratory tests is performed in this section to examine and compare individual formulations presented in the previous section. In all cases, the computational model consists of two constant strain triangular elements. While the oedometric test is run in plane strain regime, the axisymmetric state of stress is assumed for isotropic and triaxial compression. The loading and boundary conditions are displayed in Figure 4 for individual cases. All simulations assumed zero initial stress.

3.1. Hardening soil model

The response in isotropic compression and oedometer is simulated to compare the secant and incremental formulation represented by Equations (3) and (4). As for Equation (2), only the cases with $\eta = 0$ (BE) and $\eta = 0.5$ (MP) are tested. Although purely elastic behavior is addressed, the nonzero values of $c = 10\,\text{kPa}$ and $\varphi = 30°$ are adopted together with $E_{ur}^{\text{ref}} = 30\,\text{MPa}$

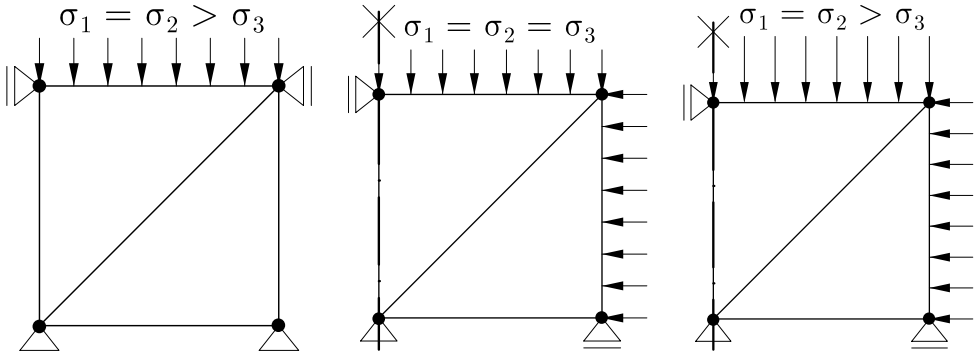

(A). Oedometer. (B). Isotropic compression. (C). Drained triaxial compression.

Figure 4. Computational models of simple laboratory tests.

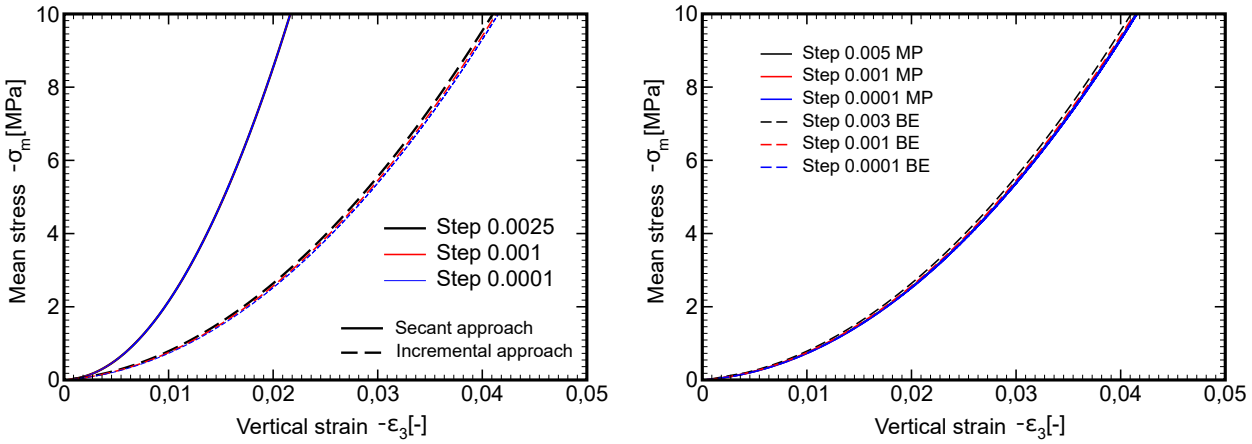

(A). Comparing predictions provided by secant and incremental (BE) formulations.

(B). Comparing predictions provided by MP and BE implementation of incremental formulation.

Figure 5. Response of HS model in isotropic compression.

and $\sigma_m^{\text{ref}} = -100\,\text{kPa}$ to set the initial stiffness of $E_{ur}(\sigma_m = 0)$ according to Equation (1).

The results for isotropic compression appear in Figure 5. Point out that achieving convergence of the underlying nonlinear equation with $\overline{\sigma}_m(\eta)$ provided by Equations (2)–(4):

$$R = \sigma_m^{i+1} - \overline{\sigma}_m(\eta), \tag{15}$$

required a relatively small initial load increment. So only a minor difference in the nonlinear elastic response is observed for incremental formulation for the tested load steps. On the other, the secant formulation shows response, see Figure 5a, which is step size independent. This conclusion is further supported via results presented in Figure 6a. Point out that both formulations adopt in the present study the same model parameters in the calculation of E_{ur}. However, it is clear from Figure 5a that arriving at identical predictions would require adjusting at minimum the power law coefficient m for individual formulations based on the experimental measurements.

Figure 5b compares the results associated with MP and BE implementation of Equation (1) in the framework of incremental formulation. It appears that MP approach is less sensitive to the size of the loading step. This approach is further promoted by predicting an identical stress-strain curve in both loading and unloading if keeping the same load increment. Note that such an approach is implemented in [8] and currently also in [10].

The above discussion is fully supported by simulating an oedometric test as seen in Figure 6. The influence of the load step size, particularly for BE approach, is clearly evident.

3.2. Comparing generalized Cam clay and soft soil models

This section demonstrates potential differences between the variable elasticity approach, adopted with GCC model, and the constant elasticity approach, adopted with SS model, in light of incremental formulation. The material data were set such as to arrive at identical predictions in isotropic compression when enforcing the constant elasticity return also with GCC model. The material parameters used in all subsequent simulations are: $\kappa^* = 0.0094$, $\lambda^* = 0.0678$, $\nu = 0.26$ and $g = M_c = 1.074$. The initial value of $K_0 = \frac{1}{\kappa^*}$ was considered.

Before proceeding with our discussion on individual results it is worth mentioning that the GEO5 FEM

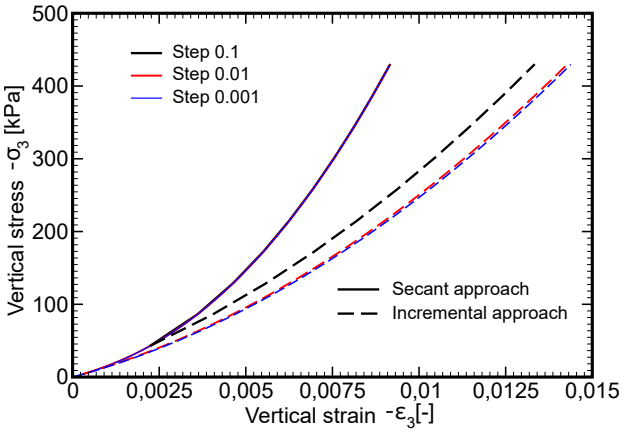

(A). Comparing predictions provided by secant and incremental (BE) formulations.

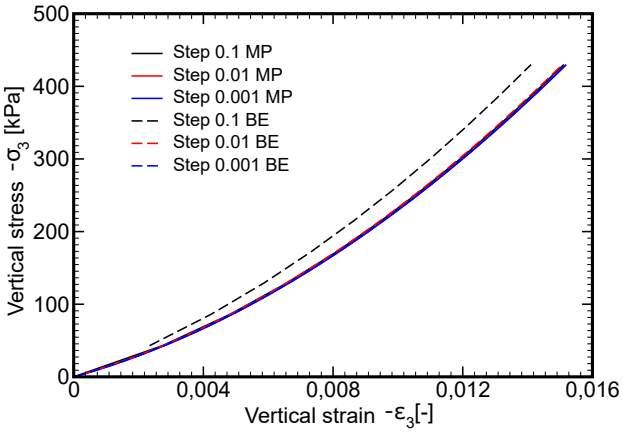

(B). Comparing predictions provided by MP and BE implementation of incremental formulation.

FIGURE 6. Response of HS model in oedometer.

software allows for gradually increasing the initial size of the load step with a number of iterations needed to achieve global equilibrium. In the present study, the elastic simulations essentially adopted two times larger step size with every new load step when this option, denoted here as VS, was exploited. In this case, the parameter step_0, see e.g. Figure 7, represents just the initial step being gradually increased in the course of analysis. All other calculations considered constant step size throughout the analysis.

Exposition to the derived results begins with Figure 7 to show the importance of a relatively small initial load step size to avoid excessive strains attributed to initially very low stiffness.

The influence of stiffness variation over the load increment (VE), Equation (10), in comparison to CE return, Equation (11), appears for isotropic compression in Figure 8. Note that the $*$-lines require 10 steps only in comparison to 100 and 1 000 steps associated with red and blue simulations, respectively.

Promoting VE return over CE return might seem justifiable when leaving purely elastic response and allowing for plasticity as shown in Figure 8b where simulations based on variable step size match those with the constant step size in the case of VE rather well.

Similar conclusions can be drawn from the results in Figure 9 derived for oedometer. Figure 9a further shows that, unlike the HS model, the assumed stiffness evolution leads to artificial residual strains upon complete unloading even in the case of pure elasticity, which may become significant for larger load steps. On the other hand, this issue will become less important when loading the soil beyond its relatively low elastic limit, because the generated permanent plastic strains will then well exceed their elastic counterparts.

The last simulations are concerned with the plastic response predicted by the GCC and SS models for the drained triaxial compression test. As seen in Figure 10 the analysis begins with isotropic compression, Figure 4b, when the specimen is first loaded to acquire

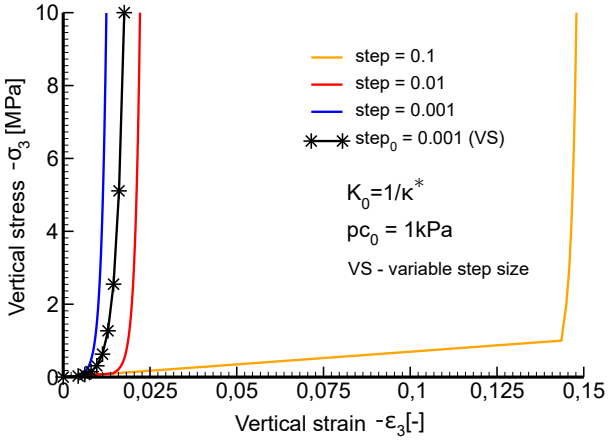

FIGURE 7. Nonlinear elastic response of GCC model in isotropic compression: influence of initial step size.

an initial pressure of 50 kPa. Clearly, no deviatoric stresses are generated during this loading stage. The evolution of deviatoric stresses begins with the second stage of loading corresponding to triaxial compression, Figure 4c. Note that the deviatoric stress measure J is defined as the square root of the 2nd invariant of deviatoric stresses s_{ij} as:

$$J = \sqrt{\frac{1}{2} s_{ij} s_{ij}}. \tag{16}$$

Similarly to previous studies the CE predictions linked to variable step size (VS) slightly deviate from those obtained with the constant step size. This is not the case for the approach based on VE return. However, it is fair to mention, that smooth convergence with VE required a slightly larger number of iterations, thus a smaller load step size, in contrast to CE return (star and diamond symbols identify individual load steps). Also note that for sufficiently small load steps the difference between the two approaches becomes insignificant.

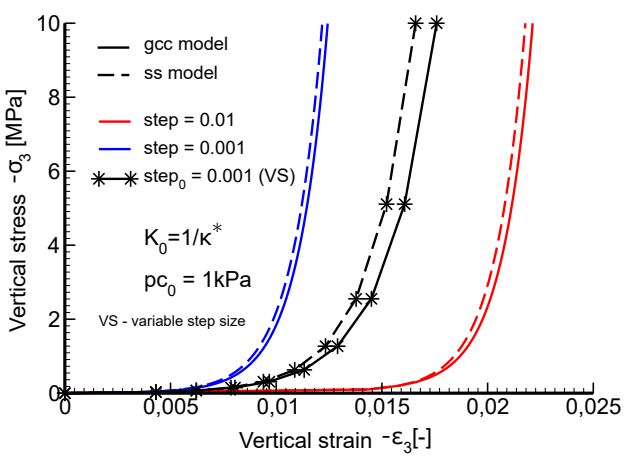

(A). Nonlinear elastic response.

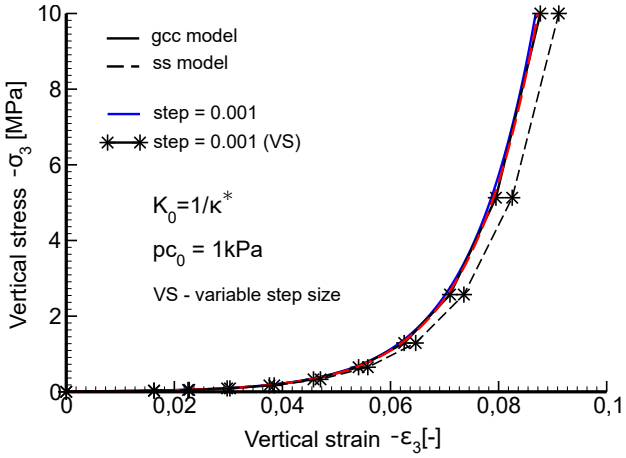

(B). Plastic response.

Figure 8. Comparing GCC and SS models in isotropic compression.

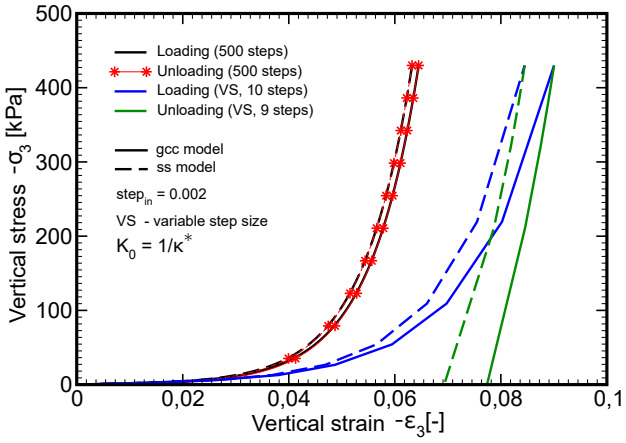

(A). Nonlinear elastic response.

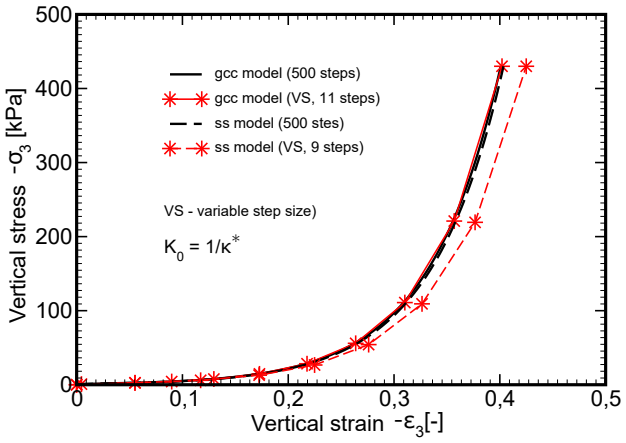

(B). Plastic response.

Figure 9. Comparing GCC and SS models in oedometer.

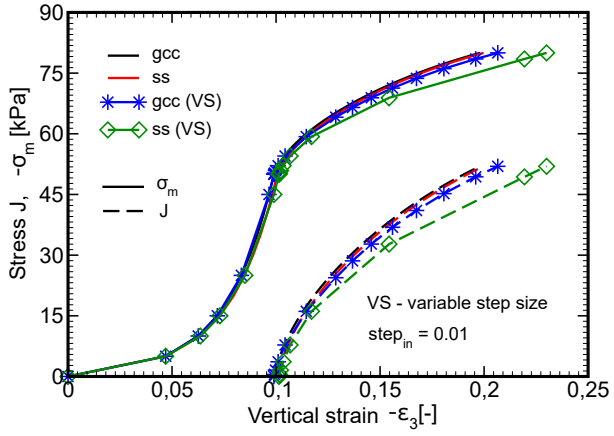

Figure 10. Comparing GCC and SS models in drained triaxial compression.

4. Conclusion

The paper presented several illustrative examples via simulations of simple laboratory tests to show differences in the implementation of nonlinear elastic constitutive laws arising in the formulation of three particular advanced plasticity models.

It has been confirmed that the chosen method of implementation may considerably affect the predicted response. The user of a given commercial software should be aware of that, since using the same model in different softwares does not assure the same results. Common to all examined models is their dependence on the mean effective stress which may generate a very low initial stiffness when starting from zero initial stress. This in turn leads to excessive strains providing the initial load steps are not sufficiently small. To avoid a large number of loading steps to reach the prescribed load the program GEO5 FEM allows for a gradual increase of the initially small step size in dependence on the number of iterations needed to converge for the previous load increment.

It has also been observed that with the GCC and SS models irreversible elastic strains occur as the stiffness at the end of the loading and at the beginning of unloading is different. On the other hand, this issue does not seem to play a major role as the influence of irreversible elastic strains become negligible in plastic analyses. In this regard, the approach based on variable elasticity return provides response which

seems less dependent on increasing the load step in simulations adopting the variable step size (VS).

To conclude we remind that the GEO5 FEM software, adopts, similar to [8], the incremental formulation with MP approach for the HS model and the concept of constant elasticity return for the SS model. On the other hand, the MCC and GCC models employ the variable elasticity return approach.

Acknowledgements

The support provided by the SGS project No. SGS23/032/OHK1/1T/11 and by the GAČR grant No. 22-12178S is gratefully acknowledged.

References

[1] K. H. Roscoe, J. B. Burland. On the generalised stress-strain behaviour of 'wet' clay. In J. Heyman, F. A. Lechie (eds.), *Engineering plasticity*, pp. 535–609. Cambridge University Press, 1968.

[2] D. Mašín. A hypoplastic constitutitve models for clays. *International Journal for Numerical and Anlytical Methods in Geomechanics* **29**(4):311–336, 2005. https://doi.org/10.1002/nag.416

[3] D. M. Potts, L. Zdravkovič. *Finite element analysis in geotechnical engineering: Volume one – theory*. Thomas Telford Publishing, UK, 1999. https://doi.org/10.1680/feaiget.27534

[4] J. M. Duncan, C.-Y. Chang. Nonlinear analysis of stress and strain in soils. *Journal of the Soil Mechanics and Foundations Division* **96**(5):1629–1653, 1970. https://doi.org/10.1061/JSFEAQ.0001458

[5] T. Schanz, P. A. Vermeer, P. G. Bonnier. The hardening soil model: Formulation and verification. In R. B. J. Brinkgreve (ed.), *Beyond 2000 in Computational Geotechnics*, pp. 281–290. 1999. https://doi.org/10.1201/9781315138206-27

[6] T. Benz. *Small-strain stiffness of soils and its numerical consequences*. Ph.D. thesis, University of Stuttgart, 2007.

[7] J. Veselý. *The use of the advanced material models for the numerical modelling of the underground structures in clays*. Ph.D. thesis, CTU in Prague, Faculty of Civil Engineering, 2016.

[8] Seequent.com. PLAXIS. [2023-11-03]. http://www.plaxis.nl/

[9] ZSOIL. [2023-11-03]. http://www.zsoil.com/

[10] Fine.cz. GEO5 FEM. [2023-11-03]. http://www.fine.cz/

[11] T. Janda, M. Šejnoha. Formulation of generalized Cam clay model. *Engineering Mechanics* **13**(5):367–384, 2006.

[12] R. B. J. Brinkgreve. *Geomaterial model and numerical analysis of softening*. Ph.D. thesis, Delft University of Technology, 1994.

[13] J. P. Bardet. Lode dependences for isotropic pressure-sensitive elastoplastic materials. *Journal of Applied Mechanics* **57**(3):498–506, 1990. https://doi.org/10.1115/1.2897051

[14] P. A. Vermerr. *Formulation and analysis of sand deformation problems*. Ph.D. thesis, Delft University of Technology, 1980.